Distinguishing Stress-Induced Anisotropy from Fracture-Induced Anisotropy, and the Implications of Stress-Induced Anisotropy for Time-Lapse Seismic

Houshang Mansouri Rostamabad

A Thesis Submitted for the Degree of Doctor of Philosophy

Institute of Petroleum Engineering, Heriot-Watt University,

Edinburgh, Scotland, UK

November 2006

In the name of God the most compassionate the most merciful

Abstract

A clear understanding of stresses in terms of their magnitude and direction plays a vital role in hydrocarbon exploration and production; reservoir characterization and management; drilling; and many other related aspects. Ignoring reservoir stresses may lead to various mishaps, thus endangering the sustainability of the reservoir. Open and fluid-conducting fractures will make it economic to exploit reservoirs.

In order to separate the contributions of stresses from those of fractures, I will present a methodology to compute and compare stress-induced anisotropy and fracture-induced anisotropy, using the fact that both differential horizontal stresses and vertical fractures result in horizontal transverse isotropy. I will make a direct comparison of these types of anisotropies and an indirect analysis of several seismic attributes such as compressional- and shear-wave reflectivities, AVO gradient and curvature.

I will also review the common practice of today's 4D techniques, under the isotropic assumption of seismic-wave velocity, and will illustrate the differences while utilizing stress-induced anisotropy. The results suggest that taking stress-induced anisotropy into account may significantly reduce the risk of errors in detecting the oil–water contact and water encroachment. As another implication of the induced anisotropy, I will modify a two-way travel-time method of compaction estimation; extend it to non-zero offset; and examine it in the presence of the seismic-wave velocity anisotropy in overburden and reservoir rocks.

This study illustrates that in stress-sensitive sand reservoirs the stress-induced anisotropy may be larger than the fracture-induced anisotropy. The types of anisotropy being studied produce different AVO gradients and curvatures. Different fluid types produce the same stress-induced anisotropy for shear-wave velocity, while fracture-induced anisotropy is illustrated to decrease with the fluid bulk modulus within the framework utilized in this study. Conventional time-lapse studies using isotropic assumptions can be improved significantly by considering velocity anisotropy. Taking into account the velocity anisotropy of reservoir and overburden rocks is demonstrated to improve estimation of the reservoir's geomechanical compaction.

To my loved ones: my wife Laleh, our son Neema, and our families

Acknowledgements

I offer all praise to Allah, God the Almighty. Moreover, I am eternally grateful to my supervisor, Professor Colin MacBeth, for his brilliant ideas, excellent interaction and unique professional standards. Assistance, and valuable and constructive comments from my external examiner, Dr Enru Liu, and my internal examiner, Dr Jim Somerville, are very much appreciated. Deputy of Iranian Petroleum Minister and NIOC Managing Director, Mr Gholam Hossein Nozari is sincerely appreciated. My research offered a valuable opportunity to attend the profound and informative courses run by Leon Thomsen and Mike Schoenberg.

I am very grateful for the assistance of the National Iranian Oil Company (NIOC), my sponsor, of its Petroleum University of Technology and of NIOC Central Training Department, which coordinated Tarh_e_Zarbati PhD Scholarship Scheme. More specifically, I wish to thank Director of NIOC Administration Affairs, Mr Mohammad Sadegh Bakhshiyan, Head of NIOC Central Training Department, Mr Seyed Hadi Mousavi, Mr Za'farani, and Mr Ezatinia. I also thank Ms Aghababaie, Dr Alireza Alizadeh Attar, Dr Hamid Hatamian (the NIOC representative-adviser), Mr Firooz Nikpour, Dr Mousavi Zadeh and Ms Taghi Zadeh.

I also wish to thank my referees: Dr Nasser Hosseinzadeh Gooya, Dr Abdolrahim Javaherian, Mr Mohammad Bagher Farshid Nasab, Dr Ali Mohamad Riahi, and Mr Seyed Mahmoud Tabatabei.

I am indebted to my wife, my son, and our families, especially my sister-in-law, Susan.

Support of my OEOC colleagues including Mr Mohammad Taghi Bahrehvar, Ms Zari Bayat, Mr Majid Dangar, Mr Hassan Masoomzadeh, Ms Noosha Heidari Monfared and Mr Mehdi Moradi, before joining HW was great. (The most sorrowful time that my wife and I had, was the tragic demise of our family friend and my dear colleague Ms Noosha Heidari Monfared along with her mother).

I would also like to thank all my friends, especially Mr Babak Adibi, Dr Soheil Asgarpour, Mr Reza Hosseyni and Mr Greg Noval. The friendly atmosphere of my office promoted learning, understanding and cooperation. I was privileged to share the office with Alex Druzhinin, Hartmut Schuett, Fiona Reid, Mark Harrison, Yahya Al-Maskari,

Faisal Al-Kindi, Sean Wagner, Juan Carlos Soldo, Said Al-Busaidi, Mariano Floricich, Neil Hodgson and Otelindo Medina. Steve Hall, Asghar Shams, Ali Al-Naamani, Alex Bertrand, Christophe Ribeiro, Margarita Corzo, Jesus Nunez and Hansel Gonzalez were valuable members of my group.

My friendships with Jahan Arjmandi, Rahim Attaei, Alireza Bahramian, Mahmoud Jamiolahmady, Rahim Masoudi, Amir Hossein Mohammdi, Hashem Monfared, Hessam Najibi and Mehran Sohrabi are very much appreciated. I am also thankful for the companionship of my Muslim friends, including Mohammad Al-Abri and Naeem Al-Jabari. I am grateful for computer support from Alan Brown, Ian Chis, Nasser Khan, Andrew Kidd, Andy Tunnicliffe and Robert Stables; and for secretarial and administrative support from Brenda Laidlaw, Ann Mathers, Hazel Michael, Juergen Munz, Angela Nelson, Pamela Peindreigh, Jill Prior and Jane Wells.

During correction of my first draft in Tehran, I received enormous support from the Managing Director of the Oil Exploration Operations Company (OEOC), Mr Hassan Mohammadi Moghadam; the OEOC Exploration Director, Mr Moezedin Khazeni Zadeh; the Head of the Geophysics Department, Mr Ali Asghar Pazoki; the Head of the Processing Centre, Mr Mohammad Bagher Farshid Nasab; and my colleagues: Mr Hossein Abbassian, Mr Naghi Ahangarian, Mr Abolfazl Ansari, Mr Rahim Bakhshi, Mr Reza Fayyaz, Mr Mohammad Ghaffari, Mr Reza Ghapanoori, Ms Shadi Ghavami, Mr Amir Ja'fari, Mr Mehdi Khabazi, Ms Azadeh Ma'roofi, Mr Mehran Morshedi, Mr Abolfazl Moslemi, Ms Najdeh Mossaedian, Mr Hassan Nezam-ol-Eslami, Mr Mohammad Rafigh, Mr Abbass Shirkavand, Ms Mahzad Sorooshi and Mr Seyed Mahmoud Tabatabei.

Declaration

I, Houshang Mansouri Rostamabad, confirm that this work submitted for assessment is my own and is expressed in my own words. Any uses made within it of the works of other authors in any forms (*e.g.* ideas, equations, figures, text, tables, programs) are properly acknowledged at the point of their use. A list of the references employed is included.

Signature: H. Mansouri R.

Date: 04/12/2006

ACADEMIC REGISTRY

Research Thesis Submission

Name:	HOUSHANG MANSOURI ROSTAMABAD		
School/PGI:	Institute of Petroleum Engineering		
Version: *(i.e. First, Resubmission, Final)*	Final	Degree Sought:	PhD

Declaration

In accordance with the appropriate regulations I hereby submit my thesis and I declare that:

1) the thesis embodies the results of my own work and has been composed by myself
2) where appropriate, I have made acknowledgement of the work of others and have made reference to work carried out in collaboration with other persons
3) the thesis is the correct version of the thesis for submission*.
4) my thesis for the award referred to, deposited in the Heriot-Watt University Library, should be made available for loan or photocopying, subject to such conditions as the Librarian may require
5) I understand that as a student of the University I am required to abide by the Regulations of the University and to conform to its discipline.

* *Please note that it is the responsibility of the candidate to ensure that the correct version of the thesis is submitted.*

Signature of Candidate:	H. Mansouri R.	Date:	4 December 2006

Submission

Submitted By *(name in capitals)*:	HOUSHANG MANSOURI ROSTAMABAD
Signature of Individual Submitting:	H. Mansouri R.
Date Submitted:	04 / 12 / 2006

For Completion in Academic Registry

Received in the Academic Registry by *(name in capitals)*:	VAL MURDOCH				
Method of Submission *(Handed in to Academic Registry; posted through internal/external mail)*:	By hand				
Signature	Valerie A Murdoch	Date:	4	12	06

Table of Contents

List of Tables

List of Figures

Nomenclature

4D	Four-dimensional or time-lapse seismic survey
α	Crack aspect ratio
δ	Anisotropy parameter
δ_∞	Asymptote value for anisotropy parameter
δ_{HTI}	Anisotropy parameter for HTI media
δ_{VTI}	Anisotropy parameter for VTI media
ΔS_{ijkl}	Excess compliance tensor
ε	Anisotropy parameter
ε	Strain
ε_∞	Asymptote value for anisotropy parameter
ε_{HTI}	Anisotropy parameter for HTI media
ε_{VTI}	Anisotropy parameter for VTI media
ϕ	Porosity
ϕ	Azimuth in degrees
ϕ_c	Crack porosity
ϕ_∞	Porosity asymptote at high pressure
γ	Anisotropy parameter
γ_0	Ratio of heat capacity at constant pressure to that at constant volume
γ_∞	Asymptote value for anisotropy parameter
γ_{HTI}	Anisotropy parameter for HTI media
$\gamma^{(V)}$	Anisotropy parameter for vertical fractures
γ_{VTI}	Anisotropy parameter for VTI media
η	Anisotropic NMO parameter
η_{Dry}	Dry-frame rock velocity ratio
η_f	Fluid velocity ratio
η_g	Gas velocity ratio
η_{Sat}	Saturated rock velocity ratio
η_r	Velocity ratio
κ	Bulk modulus in GPa

κ'	Bulk modulus of inclusion material
κ_∞	Bulk modulus asymptote at high pressure
κ_b	Brine bulk modulus
κ_d	Bulk modulus of dry frame
κ_f	Fluid bulk modulus
κ_g	Gas bulk modulus
κ_g	Mineral or grain bulk modulus
κ_N	Normal specific stiffness of fractures
κ_o	Oil bulk modulus
κ_{Sat}	Bulk modulus of saturated rock
κ_T	Tangential specific stiffness of fractures
λ	Wavelength in m
λ	Rock elastic parameter
μ	Shear modulus in GPa
μ	Viscosity of following fluid in cp (centipoise) or Nsec/m^2
μ'	Shear modulus of inclusion material
μ_∞	Shear modulus asymptote at high pressure
μ_b	Brine shear modulus
μ_d	Shear modulus of dry frame
μ_f	Fluid shear modulus
μ_g	Gas shear modulus
μ_o	Oil shear modulus
μ_{Sat}	Shear modulus of saturated rock
ν	Poisson's ratio
θ	Incidence angle in degrees
ρ	Density in kg/m^3 or g/cm^3
ρ_b	Brine density
ρ_d	Density of dry frame
ρ_f	Fluid density
ρ_g	Gas density

ρ_m	Mineral or grain density
ρ_o	Oil density
ρ_{Sat}	Density of saturated rock
ρ_W	Water density
σ	Effective stress in MPa
σ_0	Isotropic stress
σ_H	Maximum horizontal effective stress
σ_h	Minimum horizontal effective stress
σ_r	Reference isotropic loading stress
σ_U	Uniaxial stress
σ_V	Vertical effective stress
τ	Two-way travel time in ms
τ_{PP}	P-wave two-way travel time
τ_{PS}	S-wave two-way travel time
A	Area in m^2
a	Crack length in m
a	Crack radius
API	American Petroleum Institute
AVO	Amplitude variation with offset or amplitude versus offset
AVOAZ	Amplitude variation with offset and azimuth
BHTV	Borehole televiewer
C	Stiffness in GPa
C_{ijkl}	General stiffness tensor
C'_{ijkl}	Rotated general stiffness tensor
C_{IJ}	General stiffness matrix
C_{ijkl}^{Eff}	General stiffness tensor
C_{ijkl}^{Dry}	Stiffness tensor of dry frame
C_{ijkl}^{Sat}	Stiffness tensor of saturated rock
c	Crack width
D	Maximum depth of the reservoir in m
dh	Compaction

dh	Depth increment
dp/dl	pressure gradient in the flow direction in atm/cm
e	Crack density
E_ϕ	Characteristic pressure function
E_κ	Characteristic pressure function
E_μ	Characteristic pressure function
EOR	Enhanced oil recovery
FIA	Fracture-induced anisotropy
FMI	Formation micro-imager
FMS	Formation micro-scanner
f	Frequency in Hz
G	Shear modulus
g	Gravitational acceleration in m/sec^2
H	Fracture spacing
HPHT	High-pressure–high-temperature
HTI	Transverse isotropy with horizontal axis of symmetry
h_f	Volume fraction of fractures
IOR	Increased oil recovery
ISIP	Instantaneous shut-in pressure
k	Permeability in Darcies or mDarcies
L	Length in m
LOT	Leak off test
LWD	Logging while drilling
MOWC	Moved oil–water contact
MWD	Measurement while drilling
N	Number of cracks
OWC	Oil–water contact
OOWC	Original oil–water contact
p	Ray parameter
P	Pressure in MPa
P_κ	Characteristic pressure constant
P_μ	Characteristic pressure constant
P_ϕ	Characteristic pressure constant

P_P	Fluid pore pressure
PP	P-P wave mode
PS	Converted S-wave
P_r	Reflected compressional wave
P_t	Transmitted compressional wave
PWD	Pressure while drilling
q	Flow rate in cm^3/sec
R	Reflectivity
R_P	P-wave reflectivity
R_{PS}	Reflectivity of converted S-wave
R_S	S-wave reflectivity
R_{S_H}	Reflection coefficient of horizontally polarized shear wave
R_{S_V}	Reflection coefficient of vertically polarized shear wave
R_P^{sym}	Reflection coefficient of compressional wave in symmetry plane
S	Saturation
S_κ	Stress-sensitivity factor
S_μ	Stress-sensitivity factor
S	Compliance in 1/GPa
S_h	Minimum horizontal stress
S_H	Horizontally polarized shear wave
S_H	Maximum horizontal stress
S_{HYD}	Hydrostatic stress
SIA	Stress-induced anisotropy
S_{IJ}	General compliance matrix
S_{ijkl}	General compliance tensor
S_{ijkl}^0	Background compliance tensor
S_{ijkl}^{Dry}	Compliance tensor of dry frame
S_{ijkl}^{Eff}	Effective compliance tensor
S_{ijkl}^{Sat}	Compliance tensor of saturated rock
S_G	Gas saturation
S_O	Oil saturation

S_{OR}	Residual oil saturation
S_r	Reflected shear wave
S_t	Transmitted shear wave
S_V	Vertical stress
S_V	Vertically polarized shear wave
S_W	Water saturation
S_{WC}	Connate water saturation
stb	Short barrel
t	Time in sec or ms
T	Temperature in °C
TI	Transverse isotropy
TTI	Tilted transverse isotropy
TVDSS	True vertical depth sub-sea in m
TWT	Two-way travel-time in ms
U_1	Function of Lamé constants
U_3	Function of Lamé constants
u	Displacement in m
V	Volume in m^3 or cm^3
V_B	Bulk volume
V_P	Compressional-wave velocity in km/s or m/s
V_{P0}	Normal-incidence compressional-wave velocity
V_{Pf}	Compressional-wave velocity of fluid
V_S	Shear-wave velocity
V_{S0}	Normal-incidence shear-wave velocity
V_{S_H}	Velocity of horizontally polarized shear wave
V_{SP}	Sphere volume
VSP	Vertical seismic profile
V_{S_V}	Velocity of vertically polarized shear wave
V_{VS}	Void space volume
VTI	Transverse isotropy with vertical axis of symmetry
X	Source–receiver offset in m
z	Depth of a studied point in the reservoir

Z	Acoustic impedance
Z_N	Normal compliance
Z_N^f	Fracture normal compliance
Z_S	Shear-wave acoustic impedance
Z_T	Tangential compliance
Z_T^f	Fracture tangential compliance

Chapter 1

Introduction

1.1 Introduction

Almost all stages of exploration and production for the oil industry are highly dependent on an adequate understanding of subsurface stresses. Indeed, there is no related study in this field that does not require a knowledge of stress. Numerous mishaps are likely to occur unless a comprehensive study of stress states is carried out. For example, verifying the stress regimes of a region may minimize the risk of borehole collapse, deviation of drilling from the desired direction, and other mishaps that can occur when sinking a well or at the production stage. The extraction of large amounts of hydrocarbons from underground reservoirs causes imbalances and disturbs the effective overburden stress. The pressure decrease associated with such production leads to an increase in reservoir effective stress. In addition, fluid injection; drilling; consolidation; and other exploration, exploitation, production and development projects imposed on the reservoir – or any other possible forms of in-equilibrium (lack of equilibrium) – may lead to the same undesirable circumstances, endangering life and the economy of the hydrocarbon field. Stress prediction is thus of great assistance to the industry.

A relatively comprehensive knowledge of stress and stress fields plays a vital role in the production and stability of a hydrocarbon reservoir. Ambiguity in understanding stress may cause projects to encounter problems, such as: reservoir compaction, surface subsidence, borehole instability, failure, collapse, breakout, sand production, and

hydrocarbon leakage and migration. The weight of the overlying strata imposes large stresses on the reservoir formations. The fluid filling the pore spaces, and the solid framework of the rocks themselves, help to support this weight. Because of the presence of high stresses in a reservoir and the variation in the effective stresses, various scenarios can occur. For instance, the accumulation of large shear stresses can cause failure. Similarly, when the contrast between the radial and tangential compressive stresses around a borehole is high, failure may occur, and drilling, log measurements and other activities may be halted. Reliable prediction of the *in situ* stresses in a field is necessary for successful reservoir management. A comprehensive study of stress regimes and fractures can lead to substantial economic benefits throughout the lifetime of a prospect. In assisting reservoir management, such analyses have been found to substantially decrease the financial risks involved in each stage of the work.

As there are no direct methods of measuring *in situ* stresses in a reservoir, and the current methods are of limited use in quantifying the entire stress field of a reservoir, for example, core analysis can provide information at only a few points along a well, so, ideally, it is more desirable in terms of reservoir management to map the magnitude and orientation of stresses in the reservoir under study. Available approaches to reservoir stress management are constrained to one principal stress, for instance by analysing borehole breakouts, the minimum principal stress can be found, whereas the hydrofracture method gives the maximum principal stress only. Other methods, such as strain release, fault-plane solutions (earthquakes) and fault slip analysis have their own difficulties and limitations. Stress and stress release have significant effects on stress measurement while using cores and logs (sonic logs and nuclear magnetic/quadrupole resonance logs), rendering the results unreliable, as, for example, once a core is drilled, the rock becomes separated from the surrounding formations, so the results can deviate from the true values.

Indirect methods, such as those based on the induced seismic azimuthal anisotropy, are of immense value for characterizing such reservoir stresses and mapping their spatial distribution. Time-lapse surveys can also detect such stress variations by monitoring fluid-flow movements. Seismic waves show varying velocities at different azimuths with regard to the orientation of the principal stresses, as the velocities are sensitive to stress; *i.e.* the velocities increase as the stress increases. Rocks are made up of the matrix and numerous planes of weakness, such as microcracks, grain boundaries and contacts; and also pores that may be filled by fluids. As a block of rock containing planes of weakness,

flaws and defects, is subjected to a stress, the cracks or void spaces made up of these planes of weakness, *etc.*, oriented perpendicular to the direction of stress, start to close, making the rock stiffer and hence increasing the velocity in the stress direction. As the stress increases, new cracks start to form in other directions. The minimum velocity will be observed in the direction perpendicular to that of the stress.

1.2 The Motivation for the Research

Unfortunately, the seismic azimuthal anisotropy approach also senses aligned open and fluid-conducting reservoir fracturing, and this, therefore, leads to interpretational and reservoir management ambiguities(Of course it is fortunate that seismic anisotropy can characterize open/fluid-conducting fractures and keep us on business). Such fractures are often considered as 'sweet spots' in exploration, for they can be area of unusually high reservoir productivity, rendering tight reservoirs economic. However, fractures can also dominate reservoir-rock permeability and can act as thief zones in some circumstances. Thus, their existence, location, intensity, orientation, distribution, openness and fluid content (gas, oil, brine) necessitate detailed investigation. The detection of fractures in terms of their density and orientation is of great significance. Fracturing may lead to drilling and completion difficulties. Drilling in a direction perpendicular to that of the fractures can, however, maximize production. It is very true that stresses and fractures are associated or coupled in the whole rock blocks and they cannot be totally separated and dealt with, however, distinguishing the effects of stress from those of fractures is of great significance in exploration, extraction, field development, and production optimization, but also more generally in mining, construction, water and wastewater projects and earthquake seismology.

Another area of consideration with regard to stress-related issues is the understanding of time-lapse seismic data. These studies are considered to be an enormous source of information for reservoir management. Time-lapse seismic surveys are providing a wide range of valuable information on fluid pressure, saturation, temperature, movement, reservoir stresses and several other time-variant factors. A 4D or time-lapse study comprises a 3D survey acquired at the beginning, and at least one further 3D survey acquired several years later at the end of the study. The first 3D survey is also known as a base survey, and the second 3D survey is known as a monitor survey. In a time-lapse study, the variations of one or several seismic attributes in the monitor survey and in the

base survey are measured and interpreted, and these can be stated simply as, for example, the seismic amplitude of the base survey subtracted by seismic amplitude of the monitor survey. As these 3D analyses are usually carried out using the assumption that subsurface strata are isotropic, *i.e.* the velocities of the propagated seismic waves are the same in all directions, so that in areas where the behaviour of the subsurface strata is far from isotropic, using the simplified relations of wave propagation (based on the isotropic assumption), may cause a significant error in the time-lapse response of the reservoir. Due to the isotropic assumptions utilized in the study of seismic-wave propagation in rocks, the resulting 4D response may be erroneous, making the information derived from it unreliable. Hence, the application of the anisotropy of seismic-wave velocity can cut or minimize the error risk of the time-lapse studies. The same erroneous situation may occur when estimating a reservoir's geomechanical compaction, which could be prevented by applying an anisotropic correction. In unconsolidated reservoirs, compaction can cause well failure, surface subsidence and platform sinking. The estimation of compaction is meant to provide reservoir management with guidelines to mitigate the probable undesirable consequences of reservoir geomechanical compaction. Here again, taking the anisotropic behaviour of rock formations into account may improve our estimate.

Due to the importance of stress in all aspects of oil and gas industry, a couple of examples regarding stress threshold and stress prediction for drilling will be discussed briefly. The formation stress in any reservoir can be defined by the magnitude and orientation of the vertical stress S_V, the maximum horizontal stress S_H, and the minimum horizontal stress S_h. Depletion associated with pore-pressure changes in a reservoir might cause an imbalance in the formation stresses. For example, in the North Sea, many dry holes could be avoided by taking into account a threshold effective minimum horizontal stress σ_h ($S_h - P_P$ = the difference between the minimum horizontal stress and the pore pressure), (Gaarenstroom *et al.*, 1993; Borgerud and Svare, 1995), (Figure 1.1).

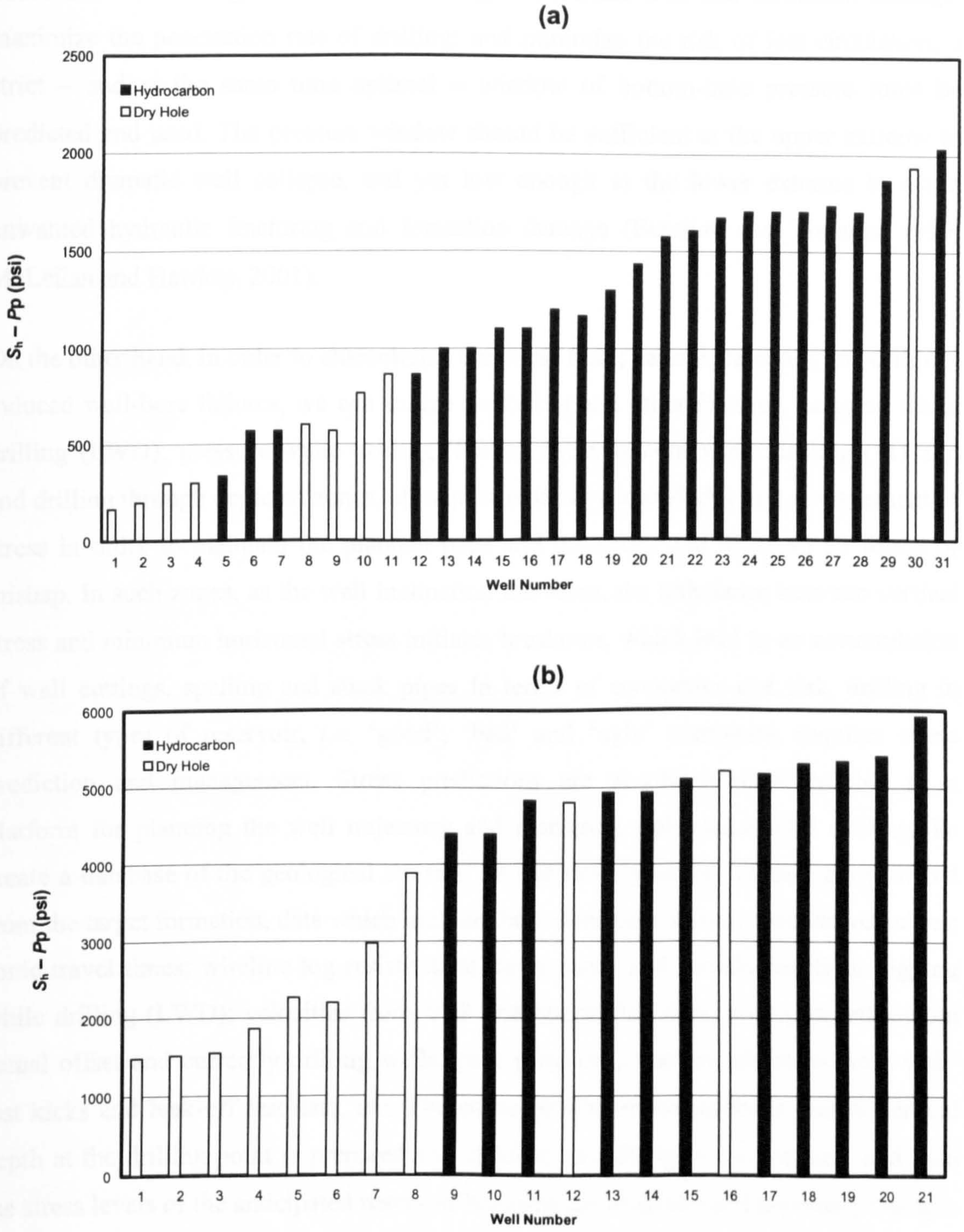

Figure 1.1: Successful and unsuccessful (dry) wells versus minimum effective horizontal stress in the North Sea: (a) in the Central Graben, threshold = 1000 psi (Gaarenstroom et al., 1993), and (b) on the Halten Terrace, threshold = 3000 psi (Borgerud and Svare, 1995).

For the various drilling scenarios, a good knowledge of stress magnitude and directions is indispensable. Drilling in high-pressure–high-temperature or HPHT reservoirs (a wellhead shut-in pressure in excess of 70 MPa, and a reservoir temperature in excess of 150 °C) requires a comprehensive study of realistic *in situ* stresses, pore pressures, and stress variations due to production and other activities (Skomedal *et al.*, 2002). In

underbalanced drilling, which aims to mitigate borehole wall and formation damage; maximize the penetration rate of drilling; and minimize the risk of lost circulation, a strict – and at the same time optimal – window of bottom-hole pressure must be predicted and used. The pressure window should be sufficient at the upper extreme to prevent dramatic well collapse, and yet low enough at the lower extreme to avoid unwanted hydraulic fracturing and formation damage (Bennion and Thomas, 1999; McLellan and Hawkes, 2001).

On the other hand, in order to characterize the stress field; natural fractures; and drilling-induced well-bore failures, we can utilize fracturing and other features. Logging while drilling (LWD); pressure while drilling (PWD); measurement while drilling (MWD); and drilling through depleted zones, all require extensive knowledge and management of stress in order to maintain the planned pace and trajectory and to avoid all forms of mishap. In such zones, as the well inclination increases, the imbalance between vertical stress and minimum horizontal stress initiates breakouts, which lead to an accumulation of wall cuttings, spalling and stuck pipes In terms of economics and risk, drilling in different types of reservoir, *i.e.* 'good', 'bad' and 'ugly' reservoirs, requires stress prediction and management. Stress predictions are absolutely indispensable as a platform for planning the well trajectory and managing safe and careful drilling. To create a database of the geological stresses for the field, a variety of data are gathered from the target formation, data which include: bulk densities; seismic interval velocities; sonic travel times; wireline log resistivities; travel times and resistivities from logging while drilling (LWD); velocities from VSP and check shot data; rock properties from actual offset and currently drilling wells; pore pressures; fracture pressures from well-test kicks and leak-off test data, *etc.* The stress profile of the reservoir versus vertical depth at the drilling point is prepared and checked as drilling is commenced, and then the stress levels of the anticipated reservoir horizons are analysed and necessary changes in the drilling plan are considered, while at the same time the real-time drilling activity can be monitored via a modem communication instrument to modify stress prediction in order to guide even a 'bad' or 'ugly' well towards successful completion (Eaton, 1998).

The porosity and permeability of porous and fractured media decrease with the exploitation of formation fluids. This may result in ground subsidence and a decrease in the recovery of petroleum and natural gas. Therefore, an evaluation of the behaviour of permeability and porosity, under formation fluid-pressure changes, is important to the petroleum industry. During the pumping of oil or natural gas from fractured or porous

formations, a problem occurs when, due to the drawdown created by the well, the pressure in the adjacent formation is not sufficient to keep fractures or pore spaces open. If fractures collapse, then the permeability of the rock decreases – and with it the productivity of the well, and thus the sustainability of production is endangered. The hydraulic properties of the rock – properties that are controlled by fractures and faults, are very effective in providing permeable conduits for hydrocarbons.

1.3 Plans and Strategies for the Research

I will first discuss the importance and role of stress in dealing with oil and gas reservoirs. After defining anisotropy and induced anisotropy, I will investigate stress-induced anisotropy and present a workflow to parameterize it. I will review and utilize fracture theories in order to quantify fracture-induced anisotropy. I will then compare these induced anisotropies directly to one another, as well as compare and illustrate their effects on some seismic attributes. I conducted isotropic and anisotropic time-lapse analyses in the Nelson Field to illustrate the influence of stress-induced anisotropy on the 4D response of the reservoir. The geomechanical compaction of a producing reservoir will be estimated using the two-way travel-time method, with and without the presence of the seismic-wave velocity anisotropy.

In this work, stress-induced velocity anisotropy is proposed as a way of determining variations in the stress field in reservoirs. This concept is used in the monitoring of the anisotropic amplitude variations with offset and azimuth; and also in the analysis of time-lapse data.

A comparison of isotropic with anisotropic AVO and 4D responses hence provides an estimate of the error caused by ignoring the presence of stress-induced anisotropy in the reservoirs. Meanwhile, as another objective is to distinguish between the anisotropic responses caused by stress and fracturing, fracture-induced anisotropy is computed and compared to that induced by stress changes in the reservoirs. Some estimations of reservoir compaction after several years of production are also made, assuming the isotropic/anisotropic responses of both overburden and reservoir rocks.

1.4 Scope and Summary of the Thesis

The following chapters form the main structure of this thesis:

Chapter 2: The background and concepts that will be necessary for understanding and studying reservoir stresses are discussed in sufficient detail to cover reservoir stress-sensitivity; stress orientation in reservoirs; stress types and states; and the resultant faulting systems. Some stress characterization methods are introduced, before giving a review of the seismic anisotropy. As a major part of this study focuses on anisotropy induced either by stress or fracture, other types of anisotropy are merely mentioned, followed by a review of the measurement of stress-induced anisotropy; important factors affecting fractured reservoirs; and effective medium and fracture theories.

Chapter 3: The isotropic dry-frame rock dependence on stress is used as an initiator to introduce stress change in a reservoir rock, and by following a procedure; the resulting induced anisotropy is parameterized. Afterwards, anisotropy changes due to saturation are calculated using an anisotropic version of Gassmann's equation. Approximations to the stress-dependent anisotropy parameters are also introduced at the end.

Chapter 4: Hudson's and Schoenberg-Muir's fracture theories are utilized as a basis to calculate fracture-induced anisotropy. Then the results are compared to stress-induced anisotropy, both directly – according to their behaviours and magnitudes, and indirectly – according to their effects on reflectivity and AVO gradient and curvature.

Chapter 5: As common time-lapse seismic studies are carried out assuming that the subsurface layers have an isotropic response, predicting anisotropic counterparts could shed light on our understanding of reservoirs. After comparison of two types of induced anisotropies, values of stress-induced anisotropy are inputted in order to study the variation of reflectivity in both isotropic and anisotropic media, and the consequent AVO responses, and also time-lapse signatures. An error in estimating the oil–water contact will be detected by comparing isotropic with anisotropic time-lapse seismic scenarios.

Chapter 6: The importance of geomechanical compaction in oil and gas reservoirs is discussed. During the life of a reservoir, fluctuations in the stress field impose deformations on the reservoir that may result in compaction and surface subsidence. Several methods for estimating compaction are mentioned, and the two-way travel-time method is utilized and modified and further shown to improve the estimate by considering the anisotropy of seismic-wave velocity in the reservoir and overburden.

Chapter 7: The results achieved, and the assumptions and limitations involved, are presented. In the partition (division) of stress-induced anisotropy (SIA), which takes up a large proportion of this thesis, conclusions are drawn about the potential impact of SIA on: reflectivity, variations of seismic amplitude with offset and azimuth and time-lapse signatures. In the section of the thesis dealing with fracture-induced anisotropy, the concept is investigated. The results of comparison between the two types of induced anisotropy are discussed, and contribution of – or need for – stress-induced anisotropy in the estimation of compaction forms the final part of the conclusions, together with a few recommendations for further studies.

Chapter 2

Reservoirs, Stress and Seismic Anisotropy

2.1 Introduction

A classification of stresses illustrates that many artificial stresses or their variants fall into a broad category, namely 'induced stresses'. Here, important elements of *in situ* (virgin) stresses will be mentioned. Considering the different stress states leads to the three main faulting systems. Several methods for characterizing reservoir-rock stresses will be discussed briefly. In this chapter, reservoir stress-sensitivity will be discussed in detail, followed by different ways of indicating stress orientation. Due to its connection with stress measurement, the concept of seismic anisotropy is reviewed. As a large proportion of this thesis deals with stress, what follows is a basis for the calculation of stress-induced anisotropy, and a review of past work and measurement of stress-induced anisotropy. This chapter also covers fractures and fractured reservoirs and their important features, before dealing with the topic of effective medium and fracture theories.

2.1.1 Stress States and Faulting Systems

Stress intensity within the body of a component is expressed as one of three basic types of internal load. These are known as tensile, compressive, and shear. More importantly, rock stresses can be classified into two main categories: *in situ* stresses and induced stresses. *In situ* stresses are also called virgin, contemporary, natural, or primitive stresses. Induced stresses might be thought of as artificial or secondary stresses as well.

In situ stresses exist prior to any disturbances in the rock, while induced stresses appear after artificial disturbances resulting from unbalancing the natural equilibrium within rock blocks. The former are described as the cumulative products of entire events accumulated during the geological life time of a rock. The latter are postulated as a variety of changes brought about by either direct or indirect human involvement in one or a combination of activities such as civil engineering mining, excavation, hydrocarbon exploitation, *etc.* The important types of stresses are tabulated in Table 2.1.

The tectonic history of any region is regarded as a foundation for almost any study. Faults, folds, *etc.* are of great significance in this regard. Stress states are revealed through determining the direction of the principal stresses at the time that the faults were formed. The occurrence of three types of faults: normal, reverse and strike-slip, is postulated as evidence for the existence of three-dimensional stress fields. As underground rocks might never have undergone equal principal stresses, isotropic three-dimensional stresses, if measured *in situ*, may only be a transitory feature in a dynamic equilibrium state. Therefore a rock block in the crust or near the surface is believed to be subjected to a vertical stress, S_V; a maximum horizontal stress, S_H; and a minimum horizontal stress, S_h. Near the surface, the observed *in situ* stresses often exhibit different horizontal stresses. The main types of faults may be summarized depending on the magnitude of the vertical and horizontal stresses. Normal faults occur when the vertical stress is the greatest. Reverse faults or thrusts are caused by conditions in which the horizontal stresses are greater than the vertical stress. And finally, when the vertical stress is smaller than the maximum horizontal stress and larger than the minimum horizontal stress; the rock block yields to strike-slip faulting.

Figure 2.1 shows the various faults caused by different stress states. The *in situ* stress state in the Earth can cause a combination of the fault systems illustrated briefly in this section. Obviously, pure systems do not appear on their own in reality, but, for the sake of simplicity, they are explained briefly. Normal faults result from tensional forces. The block of rock is broken into two parts, and one part falls down relative to the other, along the fault plane. The overall length of the two blocks becomes more than that of the original block, *i.e.* there is extension in the direction normal to the strike of the fault. Normal faults may also be known as normal-slip, tensional or gravity faults. In contrast to normal faults, in reverse faults one block moves up relative to the other, along the fault plane, as compressional forces are applied to the rock and hence cause a reduction in the overall length of the blocks. Reverse faults are also known as compressional

faults. Unlike previous two systems, where the movement of the rock is vertical, in strike-slip faults the movement is horizontal, one block moves back relative to the other along the fault plane. Strike-slip faults are caused by shear forces, and so are also known as transcurrent, lateral, tear, and wrench faults.

Table 2.1: Classification of rock stresses (Amadei and Stephansson, 1997).

Induced Stresses (mining, excavation, drilling, pumping, injection, energy extraction, applied loads, swelling, *etc.*)

In situ **(Virgin) Stresses**

- Gravitational stresses (the effects of flat ground surface and of a varied topography)
- Tectonic stresses
  - ➢ Active tectonic stresses
    - Broad scale (shear traction, slab pull, ridge push, trench suction, membrane stress)
    - Local (bending, isostatic compensation, down-warping of the lithosphere, volcanism, and heat flow)
  - ➢ Remnant tectonic stresses (these are the same as residual stresses but tectonic activity is involved, such as folding, faulting, jointing and boudinage)
- Residual stresses (diagenesis, metasomatism, metamorphism, magma cooling, changes in pore pressure)
- Terrestrial stresses (seasonal temperature variation, Moon pull: *i.e.* tidal stresses, Coriolis force, diurnal stresses)

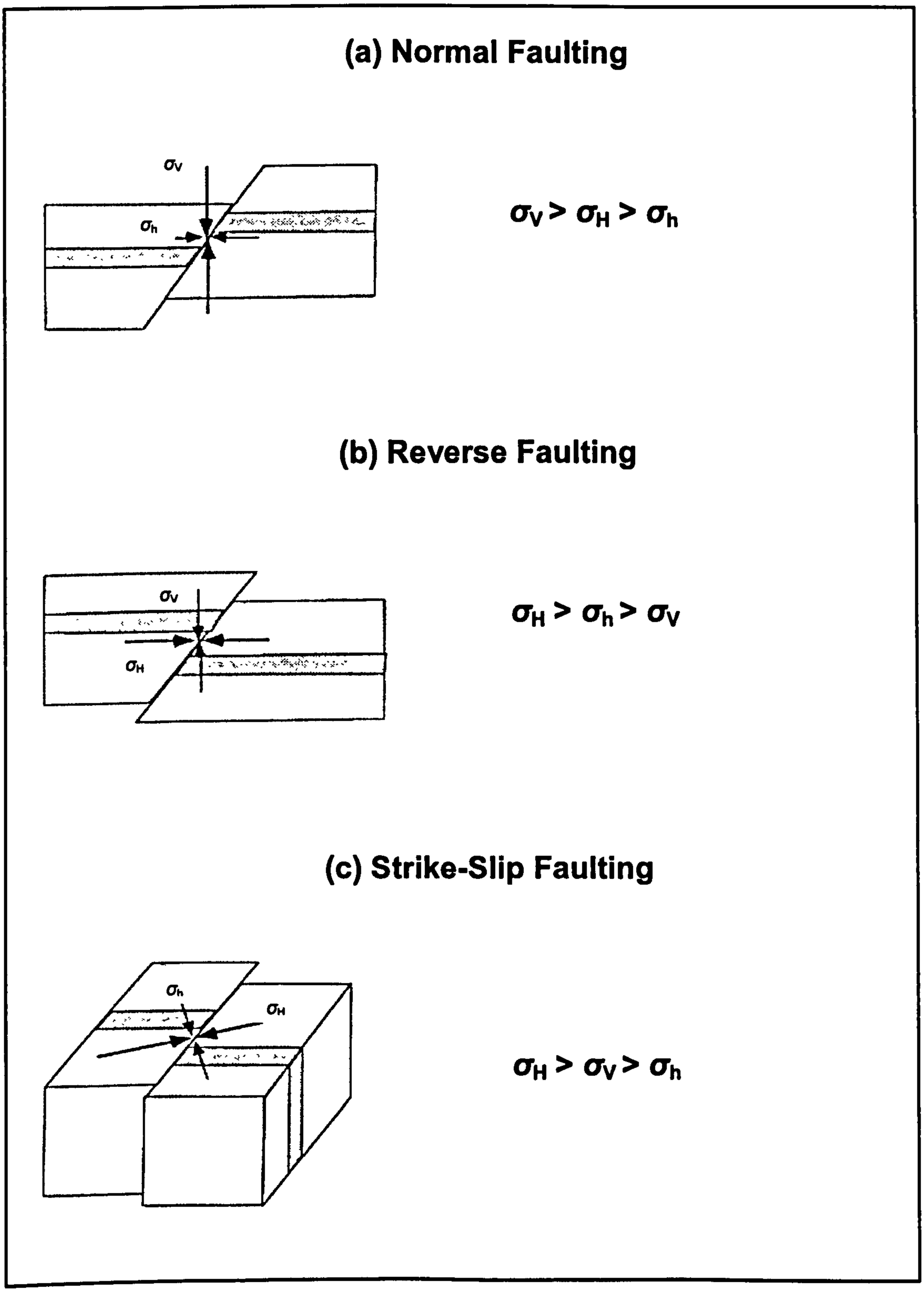

Figure 2.1: Different combinations of the three principal stresses and the corresponding faulting: (a) normal, (b) reverse, and (c) strike-slip faulting systems (Seiki et al., 1997).

2.1.2 Methods for Stress Characterization

Attempts have been made to map and identify the principal stresses in some regions of the world. Zoback and Peska (1995) characterized the maximum horizontal stress, in terms of magnitude and orientation, in the South Eugene Island (SEI), offshore Gulf of

Mexico, through fracture closure pressure, pore pressure and borehole breakouts, using dip-meter caliper logs. A borehole televiewer (BHTV) is also used to constrain *in situ* stresses in reservoirs (Finkbeiner *et al.*, 1996). Data from borehole breakouts can be utilized to determine S_H in the wells, which can in turn be correlated to regional earthquake focal mechanisms. Prensky (1992) defines borehole breakout as 'enlargement and elongation of a borehole in a preferential direction which are formed by spalling of fragments of the well-bore in a direction parallel to the minimum horizontal stress (S_h)'. He also noted that hydraulic (induced) fracturing occurs perpendicular to S_h.

Here I will explain ways of indicating the magnitude of all the stress elements. Vertical (lithostatic or overburden) stress can be calculated as the weight of the column of rock layers over the desired point in the reservoir, divided by the unit of area. It is also computed from integrated density logs as the weight of rock column above the measurement point:

$$S_V = \rho g z = \int_0^D \rho g \mathrm{d}h \tag{2.1}$$

where ρ, g, z, dh and D are rock density, gravitational acceleration, the depth of the studied point in the reservoir, the depth element (increment), and the maximum depth, respectively. The other way of expressing the overburden stress is to state it as the average overburden gradient, for instance, 1.05 psi/ft. Following Biot's theory of poro-elasticity (Biot, 1962) the effective vertical stress (σ_V) can be expressed in terms of vertical stress (S_V) and pore pressure (P_P):

$$\sigma_V = S_V - P_P \tag{2.2}$$

The maximum horizontal stress S_H is obtained using several techniques in breakout and drilling-induced fracture studies, such as the four-arm caliper, the formation micro-imager (FMI), the formation micro-scanner (FMS), the borehole televiewer (BHTV), STAR – an electrical image, and UBI – an acoustic image. The techniques used to determine the magnitude of maximum horizontal stress are also used to verify the orientations of all of the stresses. The minimum horizontal stress S_h can be obtained in several ways. A minifracture study, known as the 'MiniFrac', is a way to do so in a fracturing process during well-bore pressurization. Pressure–time curves in well instantaneous shut-in pressure (ISIP) and leak off test (LOT) are other tools for showing

the minimum horizontal stress or its gradient. S_h is given by the following relation as a function of S_v:

$$S_h = \frac{\nu}{1-\nu} S_v \tag{2.3}$$

where ν is the Poisson's ratio of rock. Figure 2.2 shows different pressure gradients within a typical reservoir.

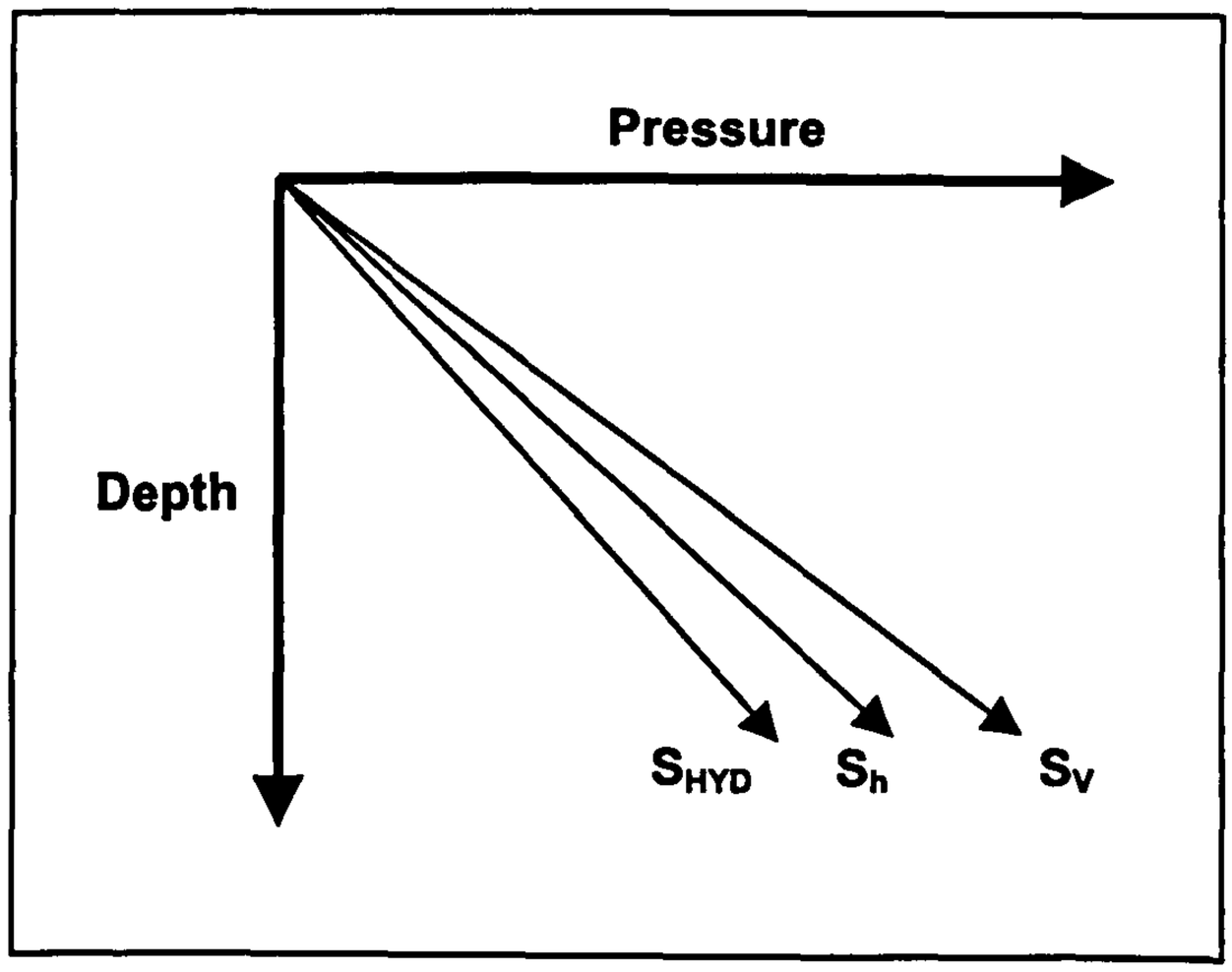

Figure 2.2: Variations of pressure gradients in a reservoir with depth, vertical, minimum horizontal and hydrostatic stresses.

Other terms that we may encounter in a reservoir pressure study are normal and abnormal pressures. When a reservoir shows pressure gradients in the range 9.8 to 11 kPa/m (0.43–0.48 psi/ft), this is known as normal pressure. An overpressured reservoir has a gradient higher than 11 kPa/m (0.48 psi/ft). This overpressure occurs when impermeable strata are compacted so rapidly that the pore fluid has no chance to escape, leading to abnormally high-pressure conditions, which in turn cause a well to become uncontrollable while drilling, or to blow out. The pressure gradient of an underpressured reservoir is less than 9.8 kPa/m (0.43 psi/ft). The drill pipe may stick to the well as the result of the underpressured conditions. The hydrostatic pressure gradient is 0.43–0.48 psi/ft (9.8–11 kPa/m).

2.2 Reservoirs and Stress

It is well known that the velocities of elastic waves propagating through reservoir rocks increase with the application of compressive stress. Measurements made on reservoir rocks up to a value of stress called the yield stress, give the elastic behaviour of the rocks being studied, whereas, upon exceeding the yield stress, the reservoir rocks undergo elastic–plastic deformation and experience geomechanical failure. Here elastic velocities start to decrease. After several years of production, the reservoir pore pressure depletes dramatically and the effective stresses on the reservoir formations increase. With further pressure depletion, reservoir rocks that have previously behaved elastically start deforming plastically. The velocities of the seismic waves may increase with elastic deformation, and may decrease while undergoing plastic deformation (Sinha and Plona, 2001).

Winkler and Murphy III (1995) studied the acoustic velocities of rocks subjected to stresses, and attributed the difference between the resulting static and dynamic moduli of the rocks to the stress dependence of the observed velocities. Static moduli can be obtained from direct measurement of stress and strain, for strain over 10^{-6}. Static moduli are conversely proportional to the size of the stress cycle, *i.e.* they decrease with an increase in the stress. The dynamic moduli are derived from propagating acoustic waves with strains generally much less than 10^{-6}. Dynamic moduli are several (typically 5–10) times larger than static moduli at small ranges of effective stresses (Holt and Fjaer, 1987). In the following subsections, I will explain the behaviour of reservoir rocks when subjected to differential stresses, review the resulting geomechanical deformations and illustrate the consequent changes in aspects of the rock physics.

2.2.1 Stress-Sensitivity of Reservoirs and Reservoir Rocks

Not all types of rocks: igneous, metamorphic or sedimentary, will behave in the same manner when placed in different environments when they are being deformed. Deeply buried rocks exposed to large confining pressures become more ductile than when they are deformed at shallow depths under low confining pressures. Regardless of the environment, some rocks are inherently weak and others are very strong. The nature and direction of the applied stresses also affects the way that the various rocks behave. Each rock type, when deformed, displays a different response to stress. These differences can be represented by variously defined moduli. Each modulus describes the various types of physical responses of the sample. As the sample deforms, it passes through three different types of behaviour: elastic (recoverable) strain; ductile/plastic (non-

recoverable) strain; and finally failure, where cohesion is lost between the components of the rock. The contemporary state of reservoir-rock stress is the result of complex geological and tectonic activity; the stress conditions are also, to a considerable extent, influenced by a variety of operations (such as drilling, excavation, injection, *etc.*) common in the oil industry. The *in situ* reservoir stresses control the initiation, direction and reopening of fractures, as well as the propagation pressures and the direction of the induced hydraulic fractures.

The propagation of acoustic waves is also known to be sensitive to stress and stress directions, and hence there will obviously be a potential to use seismic methods, log and core data for stress analyses. For this purpose, stress conditions and stress history, and their effects on wave velocities should be considered (Fjaer and Holt, 1999; Al-Sughayer, 1999).

Several years of oil and/or gas production from a reservoir leads to a huge drop in pore pressure and a dramatic increase in the effective stress. The geological deformation of the rocks and, in terms of rock physics, changes in the pore geometry and bulk and shear moduli of the reservoir rocks, are direct and indirect consequences of such an increase in effective stress. Figure 2.3 illustrates compaction in the Ekofisk Field in the Norwegian sector of the North Sea. Several metres of platform sinking are obvious. The deformation of the structure, shear failure of the casing, and buckling, are also depicted. Maps of subsidence and compaction versus time for the Ekofisk Formation are displayed in Figure 2.4. Figure 2.5 shows the equivalent seismic-derived compaction map of the field.

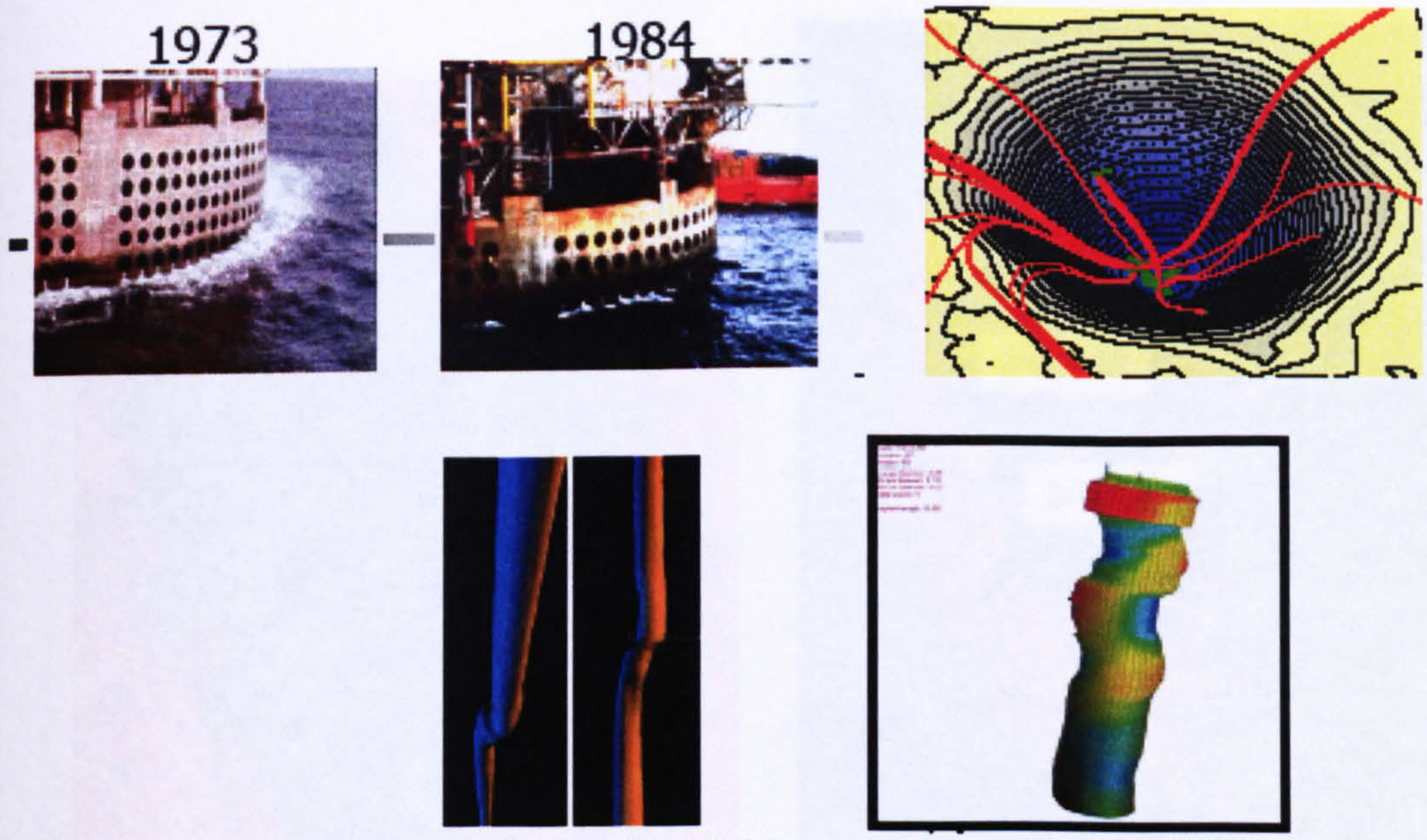

Figure 2.3: Compaction in the Ekofisk Field. Top left: platform in 1973; middle: in 1984, showing several metres of sinking; and right: a structure map after compaction. Bottom: casing deformation; left: shear failure and right: casing buckling resulting from compaction (Chin et al., 2003).

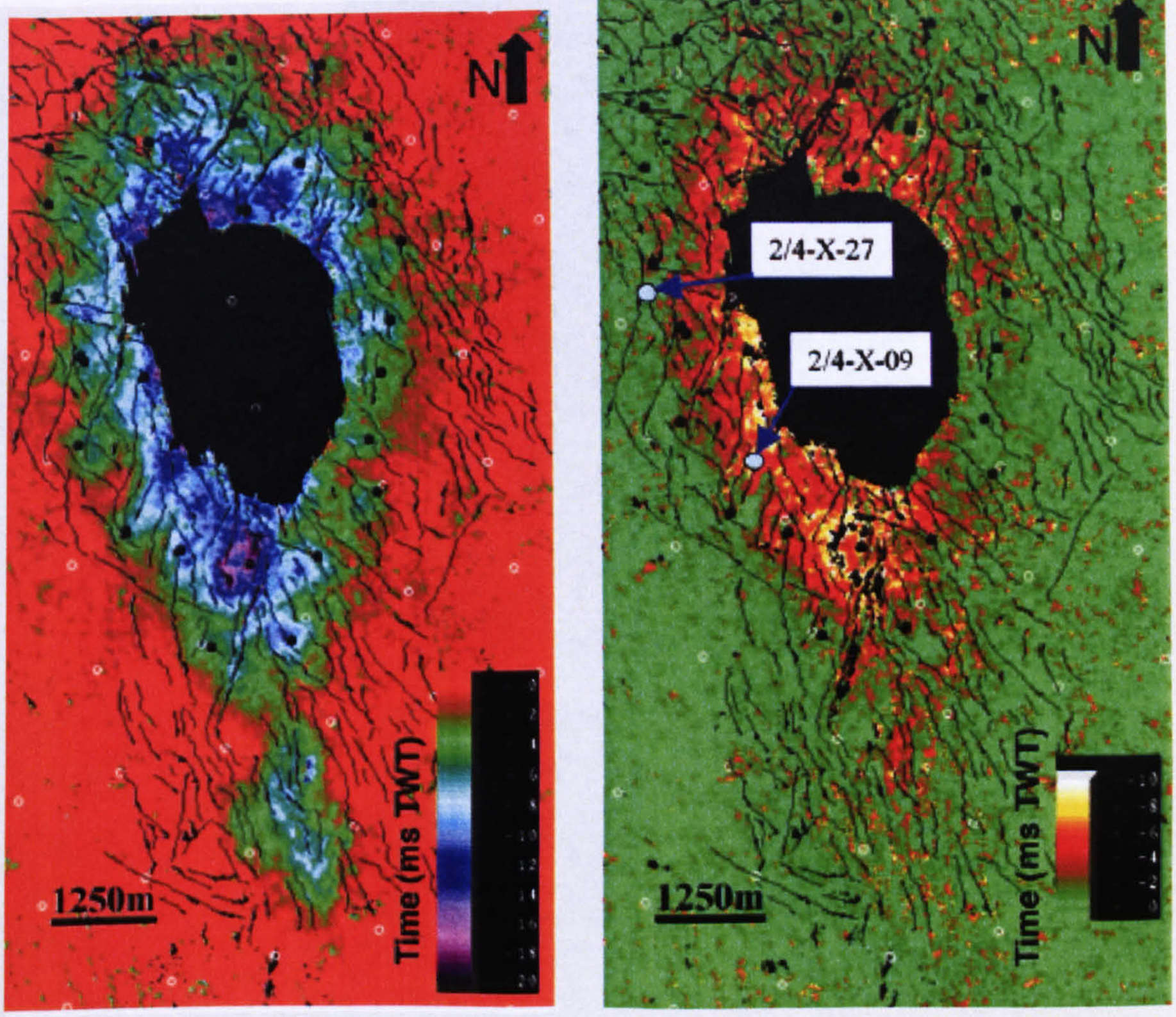

Figure 2.4: Left: time subsidence map for the top of the reservoir (Ekofisk Field) and right: time compaction map for the Ekofisk Formation. The fault pattern of the top chalk and the positions of the water injection wells are shown in black. The gas cloud in the centre of the reservoir is also displayed in black (Guilbot and Smith, 2002).

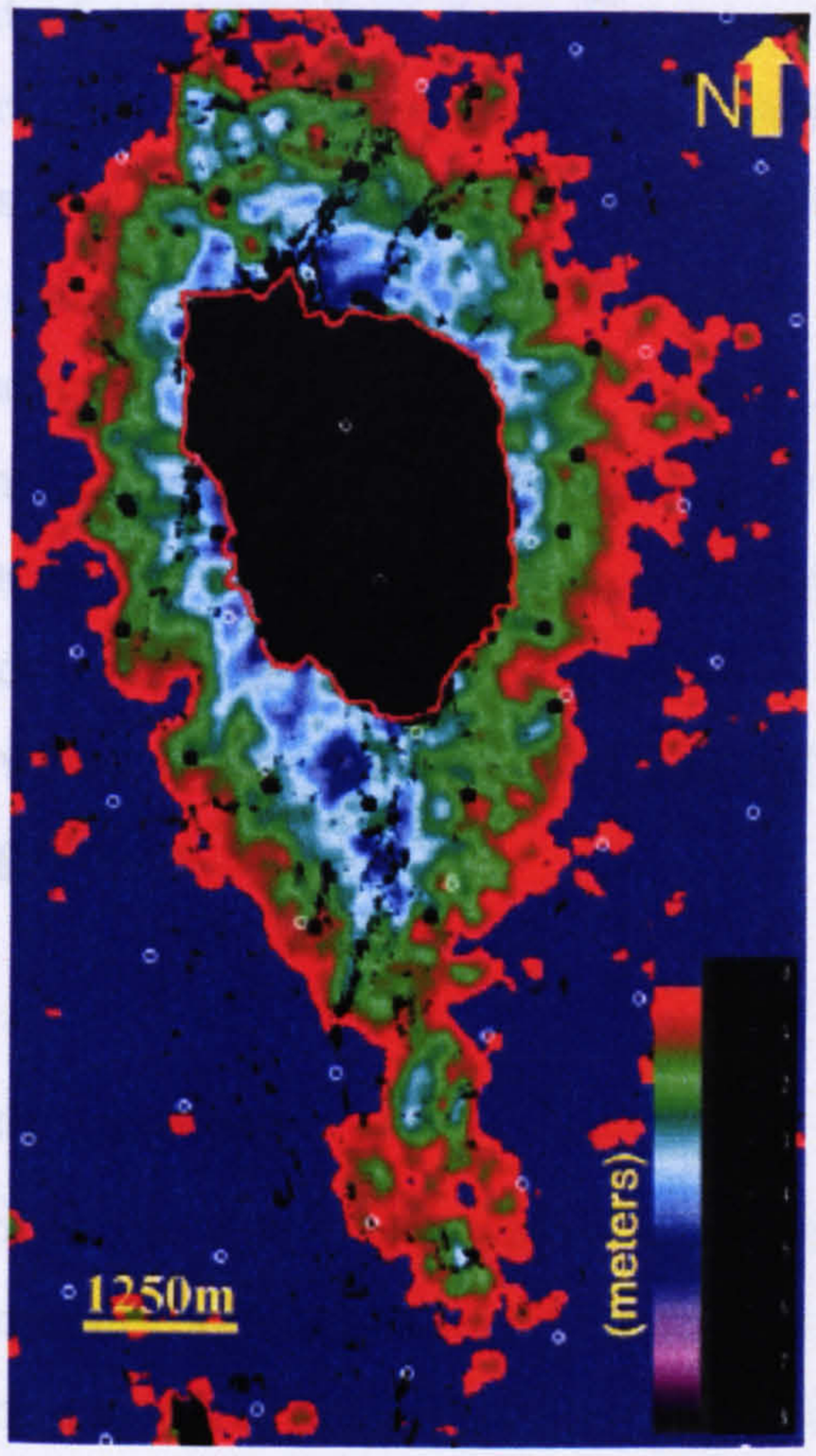

Figure 2.5: Seismic-derived compaction map of the Ekofisk Field (Guilbot and Smith, 2002).

2.2.2 Stress Orientation in Reservoirs

Stress orientation in a reservoir is studied in order to avoid mishaps in the reservoir throughout its lifespan, from exploration, to drilling, completion, development, exploitation, and abandonment. Obviously, as the orientation of the vertical stress is downwards, only the azimuths of horizontal stresses are considered. Along with the magnitude of the maximum horizontal stress, its orientation is also important for specifying the mud weight during drilling, in order to prevent lost circulation, unintentional fractures, well-bore collapse, spalling, stuck pipe, pack-off, *etc.* On the other hand, as well-bore stability and the propensity to form unwanted fractures depend upon the inclination and azimuth of the well, a priority in horizontal completion is to determine the stress orientation.

Sand production during production is another problem that may occur after damage by a concentration of stress around the well-bore. Several parameters show a variation with the direction of stress. Fracture orientation and effective widths in both natural and artificial fractured reservoirs are also related to stress characteristics. Based on Heffer *et al.* (1997) several water-flood analyses show that the direction of maximum horizontal

stress is the same as that of reservoir fluid flow. The magnitude and direction of the stress in many reservoirs vary with depth, structural, lithological, and stratigraphic features. Burial history, surface topography, local structures, bedding, foliation, lateral heterogeneity, dip, and many other factors, affect stress orientation. Bruno and Winterstein (1994) investigated the influences of stratigraphy and folds on stress orientations. In their numerical modelling, they illustrate that the azimuth of maximum horizontal stress depends on the depth and location in the subsurface structure. It is assumed that the direction of maximum horizontal stress is the same as that of the polarization of fast shear waves. (Shear-wave splitting, fast and slow shear waves will be dealt with in the following sections.)

2.3 Overview of Seismic Anisotropy

In 1856, Thomson described the anisotropic elastic tensor using the key concepts of 'parallel-ity' and 'orthogonal-ity' of stresses and strains, regardless of any external co-ordinate systems, while the concept of tensors was not known and the concepts of stress and strain were only one year old (Helbig, 1996). Since early in the history of the seismic exploration, it has been realized that the simplified assumption of isotropic behaviour of the Earth is not always justified. The velocities of seismic waves in the upper part of the Earth's crust have been found in several instances to vary with the direction of propagation (Postma, 1955). Uhrig and Van Melle (1955) mention surveys done in 1944, 1948 and 1953 to measure the oblique times from shots spaced at large distances from a well to a seismometer in the well; the results could be explained only by velocity anisotropy. They also gave a method to quantitatively measure the velocity anisotropy. Their anisotropy factor A is defined as the ratio of the velocity along the layers, to the velocity perpendicular to the layers. They conclude that the velocity anisotropy is probably the result of three effects: homogeneous anisotropy in individual rock layers; transversely isotropic rock layers; and for the oblique paths, quasi-anisotropy caused by time differences between straight-line and minimum-time paths, assuming a sequence of isotropic formations through which the waves travelled at different speeds.

2.3.1 Definition and Concepts

Seismic anisotropy may be defined as the angle-dependency of seismic velocity (Thomsen, 2002). An isotropic medium is one in which physical properties are the same

in all directions. Hence, when a physical property differs in various directions, the medium is considered to be anisotropic. To clarify the concept, I will now review the definitions given by several authors. Winterstein (1990) believes that it is appropriate to use the definition of anisotropy to mean something less than its broadest scope, although it is quite useful to distinguish anisotropy from the related concept of inhomogeneity. In an inhomogeneous material, the physical properties, when measured in the same direction, will change with location. Winterstein uses anisotropy only in a limited sense to mean the variation of the properties of homogeneous materials with direction.

Based on Crampin (1989), uniform materials with an internal structure like a crystal or a set of aligned cracks, are elastically anisotropic, because the elastic properties vary with direction. Variation in the properties of purely elastic solids, such as crystals, may be well described by a fourth-order tensor of anisotropic elastic constants. For compound materials with an internal structure, akin to a solid made up of periodic thin layers or containing aligned cracks, the structure can also be simulated by anisotropic elastic constants. Thomsen (2002) includes all waves ranging from 1 Hz to many MHz in the definition of 'seismic', rather than limiting it to merely primary and shear waves.

All points of a continuum can be assigned scalar, vectorial or tensorial parameters. If the studied parameter is the same everywhere in a region, the region will be called homogeneous with respect to that parameter. If the parameter depends upon the direction of the measurement, then the region is called anisotropic with respect to that parameter (Helbig, 1984, 1994). All anisotropy originates in inhomogeneity, and all inhomogeneous materials also show anisotropy at some scale (Winterstein 1990). Materials may or may not be homogeneous, depending on the scale of the study. The scales include atomic, grain, fabric, texture and structure. Materials that show inhomogeneity on the scale of the probing wavelengths are anisotropic. In geophysics, the pertinent scale varies, and is related to the applied wavelengths. For seismic bandwidths ranging from 1 to 100 Hz, the scale may be in tens of metres; for sonic bandwidths (1 to 25 Hz), it is in the order of decimetres; and for the ultrasonic bandwidth of 1 kHz to MHz in laboratory measurements, it is a few millimetres.

2.4 Basis for the Calculation of Stress-Induced Anisotropy

2.4.1 Stress–Strain Relation

The mathematical basis of elastic-wave propagation in an anisotropic medium has been discussed by Love (1934). Some physical laws are utilized as the basis of calculations of all categories of deformation in a continuum, due to propagation of seismic waves. These theorems of conservation include conservation of energy, conservation of mass, conservation of linear momentum, and conservation of angular momentum. Let x_1, x_2 and x_3 be spatial co-ordinates, and u_1, u_2 and u_3 be the displacement components of an elastic wave in the rock. If the stress tensor is σ_{ij} and the normal strain tensor is related to the displacements by:

$$\varepsilon_{ii} = \frac{\partial u_i}{\partial x_i}, \text{ for } i = 1, 2 \text{ and } 3. \tag{2.4}$$

and for shear strain:

$$\varepsilon_{ij} = \frac{\partial u_i}{\partial x_j} + \frac{\partial u_j}{\partial x_i}, \text{ for } i \text{ and } j = 1, 2 \text{ and } 3. \tag{2.5}$$

The generalized Hooke's law is the starting point of our analysis. As shown in Aki and Richards (1980), a linearly elastic medium behaves so that each component of applied stress is linearly dependent on every component of strain. Or, in other words, an elastic medium possesses a constitutive relation between the applied stress and the resultant strain, which is one-to-one and time-independent. Stressed sandstone treated in a Hooke cell is expected to follow the stress–strain rule that reads:

$$\sigma_{ij} = C_{ijkl}\varepsilon_{kl} \tag{2.6}$$

where σ_{ij} is the second-order tensor of stress, ε_{kl} is the second-order tensor of strain, and C_{ijkl} is the fourth-order tensor of elastic modulus or stiffness. Writing the relation in another way, the fourth-order compliance tensor emerges:

$$\varepsilon_{ij} = S_{ijkl}\sigma_{kl} \tag{2.7}$$

where compliance is the inverse of stiffness, *i.e.* $S_{ij} = C_{ij}^{-1}$.

Conservation of angular momentum results in the symmetry of the stress tensor, hence:

$$\sigma_{ij} = \sigma_{ji} \tag{2.8}$$

and

$$\varepsilon_{kl} = \varepsilon_{lk} \tag{2.9}$$

So equations (2.6) and (2.7) can be expressed in terms of tensors as:

$$\sigma_{ij} = C_{ijkl}\varepsilon_{kl}, \text{ for } i, j, k \text{ and } l = 1, 2 \text{ and } 3: \tag{2.10}$$

or

$$\varepsilon_{ij} = S_{ijkl}\sigma_{kl}, \text{ for } i, j, k \text{ and } l = 1, 2 \text{ and } 3: \tag{2.11}$$

in which σ_{ij} is the ij-element of the symmetrical second-order stress tensor; ε_{kl} is the kl-element of the symmetrical second-order strain tensor, C_{ijkl} is the $ijkl$-element of the fourth-order stiffness tensor, and S_{ijkl} (the inverse of C_{ijkl}) is the corresponding compliance tensor. (For further reading, see Appendix 1.) C_{ijkl} comprises 81 components, which reduce to only five components for a VTI medium. (Appendix 2 gives a detailed treatment of symmetry systems.)

So the familiar stiffness tensor of a VTI medium in two-subscript notation emerges as:

$$C_{IJ} = \begin{bmatrix} C_{11} & C_{11}-2C_{66} & C_{13} & 0 & 0 & 0 \\ C_{11}-2C_{66} & C_{11} & C_{13} & 0 & 0 & 0 \\ C_{13} & C_{13} & C_{33} & 0 & 0 & 0 \\ 0 & 0 & 0 & C_{44} & 0 & 0 \\ 0 & 0 & 0 & 0 & C_{44} & 0 \\ 0 & 0 & 0 & 0 & 0 & C_{66} \end{bmatrix} \tag{2.12}$$

where there are only five independent elements: C_{11}, C_{33}, C_{44}, C_{66} and C_{13}.

Figure 2.6 shows a VTI medium. The Thomsen's type anisotropy parameters of a VTI medium are as follows:

$$\varepsilon = \frac{C_{11}-C_{33}}{2C_{33}} \tag{2.13}$$

$$\delta = \frac{(C_{13}+C_{55})^2-(C_{33}-C_{55})^2}{2C_{33}(C_{33}-C_{55})} \tag{2.14}$$

$$\gamma = \frac{C_{66}-C_{55}}{2C_{55}} \tag{2.15}$$

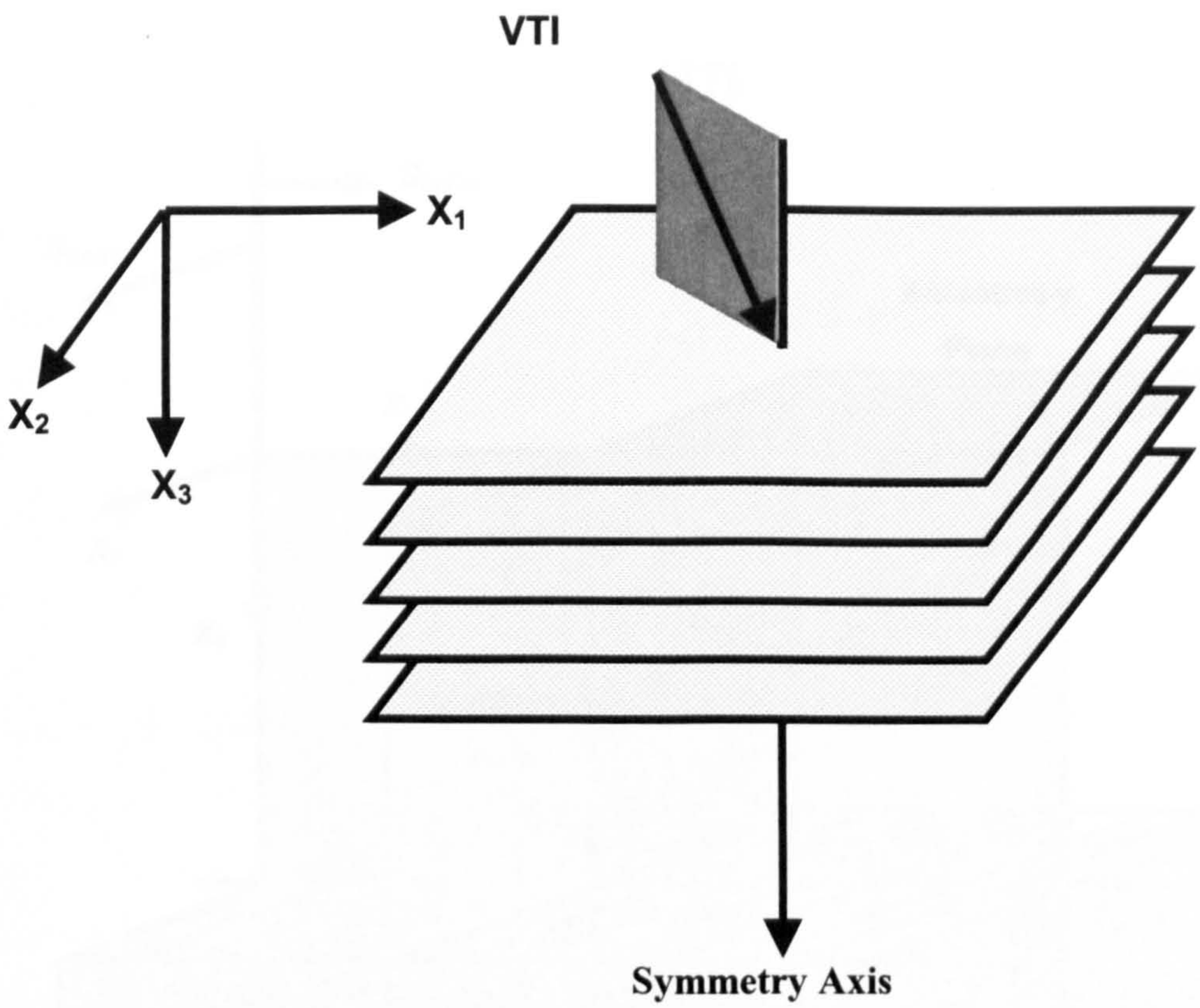

Figure 2.6: Layered sediments like shale form a VTI medium. The vertical axis x_3 is the symmetry axis, and plane $<x_1, x_2>$ is the isotropic symmetry plane, hence in a VTI medium there are no azimuthal variations. Velocity variations are observable in planes $<x_2, x_3>$ and $<x_1, x_3>$, so velocity variations with depth can be studied.

Stress, vertically aligned fractures and vertically tilted beds are known to form an HTI medium (horizontal transverse isotropy). For an HTI medium (Figure 2.7), the stiffness tensor C_{IJ} can be written in the form:

$$C_{IJ} = \begin{bmatrix} C_{11} & C_{13} & C_{13} & 0 & 0 & 0 \\ C_{13} & C_{33} & C_{33}-2C_{44} & 0 & 0 & 0 \\ C_{13} & C_{33}-2C_{44} & C_{33} & 0 & 0 & 0 \\ 0 & 0 & 0 & C_{44} & 0 & 0 \\ 0 & 0 & 0 & 0 & C_{66} & 0 \\ 0 & 0 & 0 & 0 & 0 & C_{66} \end{bmatrix} \tag{2.16}$$

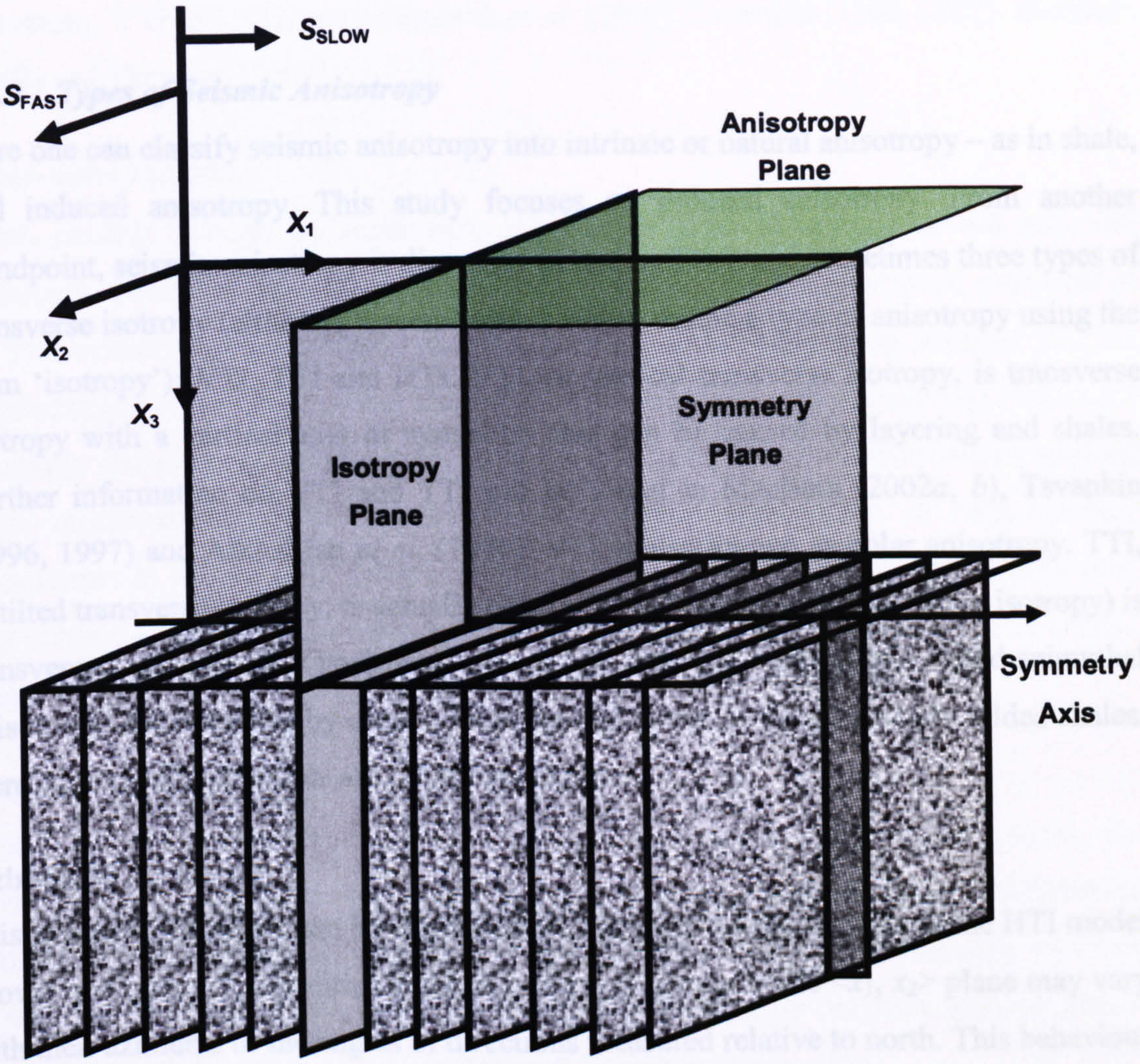

Figure 2.7: HTI medium. Aligned vertical fractures can give rise to an HTI medium. Azimuthal anisotropy can be detected in the azimuthal plane $<x_1, x_2>$.

Tsvankin (1997) and Rüger (1998) give relations to recover the HTI anisotropy parameters from the VTI ones:

$$\varepsilon_{\mathrm{HTI}} = -\frac{\varepsilon_{\mathrm{VTI}}}{1+2\varepsilon_{\mathrm{VTI}}} \tag{2.17}$$

$$\delta_{\mathrm{HTI}} = \frac{\delta_{\mathrm{VTI}} - 2\varepsilon_{\mathrm{VTI}}(1+\varepsilon_{\mathrm{VTI}}/f)}{(1+2\varepsilon_{\mathrm{VTI}})(1+2\varepsilon_{\mathrm{VTI}}/f)} \tag{2.18}$$

$$\gamma_{\mathrm{HTI}} = -\frac{\gamma_{\mathrm{VTI}}}{1+2\gamma_{\mathrm{VTI}}} \tag{2.19}$$

where f is a function of compressional-wave velocity V_{P} and shear-wave velocity, V_{S} as:

$$f = 1 - (V_S / V_P)^2 \tag{2.20}$$

2.4.2 Types of Seismic Anisotropy

Here one can classify seismic anisotropy into intrinsic or natural anisotropy – as in shale, and induced anisotropy. This study focuses on induced anisotropy. From another standpoint, seismic anisotropy is discussed in terms of two and sometimes three types of transverse isotropy (although it seems rather odd to define a type of anisotropy using the term 'isotropy'): VTI, TTI and HTI. VTI, or vertical transverse isotropy, is transverse isotropy with a vertical axis of symmetry that can be caused by layering and shales. Further information on VTI and TTI can be found in MacBeth (2002*a*, *b*), Tsvankin (1996, 1997) and Alkhalifah *et al.* (1996). VTI is also known as polar anisotropy. TTI, or tilted transverse isotropy, is actually tilted VTI. HTI (horizontal transverse isotropy) is transverse isotropy with a horizontal axis of symmetry. It is sometimes called azimuthal anisotropy, and is caused by cracks, fractures and stress, or even vertically folded shales. Here, a few useful concepts are briefly reviewed.

Azimuthal Anisotropy

Seismic-wave velocities can be dependent on azimuth. As can be seen in the HTI model shown in Figure 2.7, velocities measured in any direction in the $<x_1, x_2>$ plane may vary with their azimuths or the angles of directions measured relative to north. This behaviour of the azimuth dependence of seismic velocity is known as azimuthal anisotropy. Aligned vertical fractures (like those shown in Figure 2.7), directional horizontal stresses, vertically folded shales, and a combination of these factors, can cause azimuthal anisotropy. Other variations in, for example, reflection coefficient, amplitude, travel time and phase, can be observed as the results of velocity azimuthal anisotropy. For further reading on azimuthal anisotropy, see Lynn and Thomsen (1990), Lefeuvre (1993), Rüger and Tsvankin (1995), Rüger (1996, 1998), Li (1998), MacBeth (1999) and Olofsson *et al.* (2003).

Polar Anisotropy

Unlike azimuthal anisotropy, which is defined as the velocity variation in the horizontal plane ($<x_1, x_2>$ plane) as a function of the angle between the direction of wave propagation and the north, polar anisotropy is given by the velocity variation in the vertical plane (the $<x_1, x_3>$ plane and the $<x_2, x_3>$ plane) as shown in the VTI model in

Figure 2.6 as a function of ray angle from the vertical direction (x_3 axis). Polar velocity anisotropy can be caused by shales, thin beds and layering. For further reading on polar anisotropy, VTI and TTI, see Alkhalifah *et al.* (1996), Tsvankin (1996, 1997), MacBeth (2002) and Thomsen (2002).

Shear-wave Splitting

When passing through an anisotropic medium, a shear wave is polarized into two differently travelling waves S_1 and S_2, with S_1 propagating at a higher speed compared to S_2. This azimuthally anisotropic behaviour of shear-wave propagation is called splitting or birefringence, leading to a fast shear wave (S_1) and a slow shear wave (S_2). Figure 2.8 illustrates shear-wave birefringence. Crampin (1998) characterizes shear-wave splitting as 'a measurement monitoring the dynamic internal deformation of fluid-saturated microcracks in *in-situ* rock' for which the response of the rock mass can be predicted. (For further reading on this topic, see Liu *et al.* (1989), MacBeth and Crampin (1991), Crampin (2001), Winterstein *et al.* (2001) and Olofsson *et al.* (2003)).

Stress-induced anisotropy

If two horizontal stresses are equal and vertical stress is the prevailing stress, the medium is VTI, and polar velocity anisotropy is observed. In the case of differential horizontal stresses, the rock gives rise to an HTI medium and there is velocity variation in different azimuths, which is called azimuthal anisotropy. In the more general case of unequal stresses the stress-induced anisotropy will be orthorhombic.

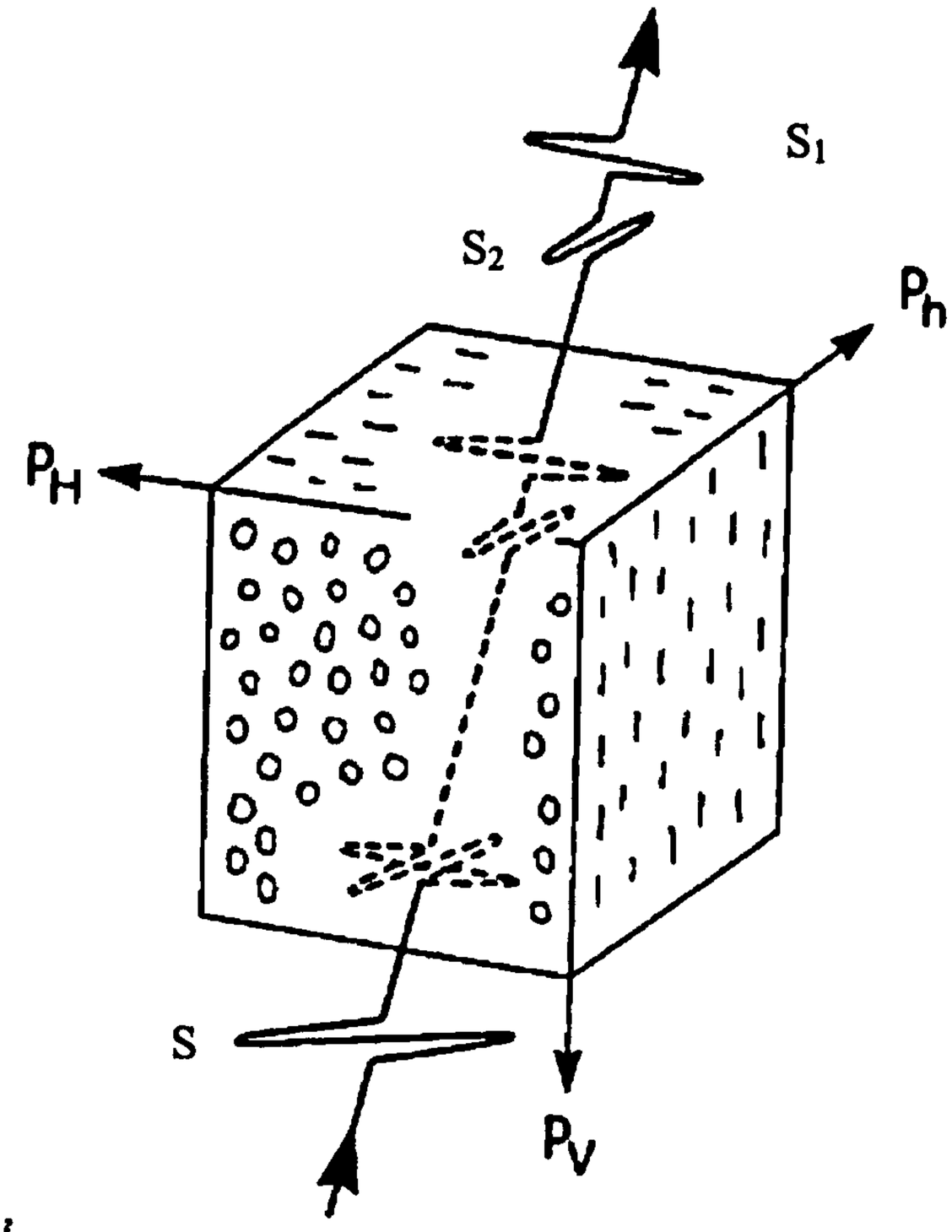

Figure 2.8: The shear wave (S), while propagating through an azimuthal anisotropic medium, resulting from vertically aligned cracks, is polarized into two components S_1 and S_2, travelling at different speeds ($S_1 > S_2$). P_V, P_H and P_h are the vertical, maximum, and minimum horizontal compressional stresses respectively (Liu et al., 1989).

2.4.3 Measurement of Stress-Induced Anisotropy

Several authors have undertaken research on stress-induced anisotropy. Nur and Simmons (1969), in their pioneering work, demonstrate through an experimental study how the velocities of the compressional waves and shear waves in Barre granite vary with increasing stress. However, similar observations date back to 1923, when Adams and Williamson attributed velocity variations with stress to the internal microcracks within rocks. In 1957, Tocher suggested that velocity increase with stress can lead to information on stress changes, and in 1960, Matsushima demonstrated that the elastic properties of some rocks vary with uniaxial stress, especially in the direction of applied stress. In another work Nur (1971) deliberately depicted measured and computed wave velocities as a function of stress and the direction of the applied stress. Lynn (1991) measured azimuthal anisotropy in down-hole shear-wave data from two different sites, and attributed it to possible stress-induced anisotropy caused by unequal horizontal stresses. Yin and Nur (1992) demonstrated that several rock types (granite, sandstone, shales and Ottawa sand) show stress-induced anisotropy and found it to be significant in

soft rocks. Based on Bruno and Winterstein (1994), the stress state has a controlling effect on the observed anisotropy.

Sayers and Kachanov (1995) expressed stress-induced anisotropy in terms of crack density tensors of the second and fourth ranks. After brittle rocks experience failure due to compression, coalescence of microcracks occurs, and rocks therefore exhibit anisotropy. Mavko *et al.* (1995) predicted stress-induced anisotropy by calculating the excess compliance of the rock. Dillen *et al.* (1999) concluded that the compressional- and shear-wave velocities exhibit the greatest sensitivity to the normal stresses in a triaxial loading. Horizontal differential stress is considered to be the source of anisotropy in studying azimuthal variations of compressional-wave AVOA, NMO and internal velocities (MacBeth and Lynn, 2001). Sayers (2002) attributed variations of the elastic-wave velocities in sandstones to discontinuities like grain boundaries and internal microcracks. MacBeth (2002) derived relations for tangential and normal compliances from the pressure dependence of sandstones, and approximated the rock elastic moduli via comprehensive laboratory measurements on the plugs from dozen of reservoirs.

Nur and Simmons (1969) performed four measurements on Barre granite to study the variations in acoustic-wave velocities with stress and angle at the following settings: uniaxial stress applied to the axis (one of the diameters of a 10 cm by 10 cm cylinder sample), compressional waves measured normal to the axis; shear waves propagating normal to the axis and polarized normal to the axis; shear waves propagating normal to the axis and polarized parallel to the axis; and shear waves propagating parallel to the axis. All velocities show an increase with uniaxial stress; however, the amount of the increase depends upon the angle between the direction of stress and the direction of wave propagation (and polarization in case of shear waves). When the acoustic waves propagate along or parallel to the stress direction, the maximum increase in velocity occurs. The minimum velocity increases is associated with the case where waves propagate perpendicular to the direction of uniaxial stress. Variations in wave velocities are shown in Figures 2.9, 2.10 and 2.11.

Down-hole field measurements at the Lawrence Livermore site (LLL), San Francisco Bay show considerable azimuthal anisotropy (Figure 2.12) (Redpath and Lee, 1986). Yin and Nur (1992) found SIA in rock types such as granite, sandstone, shales and Ottawa sand. They concluded that SIA is significant in soft rocks. Table 2.2 shows the maximum anisotropy in triaxial ($P_{xx} = P_{yy} = 1.72$ MPa and $P_{zz} = 1.72$–5.17 MPa) and

polyaxial (P_{xx} = 1.72 MPa, P_{yy} = 5.17 MPa and P_{zz} = 1.72–10.35 MPa) loadings. P_{xx}, P_{yy}, and P_{zz} are compressional pressures, for example, P_{xx} is compressional pressure in the direction of x and applied normal to the <y, z> plane.

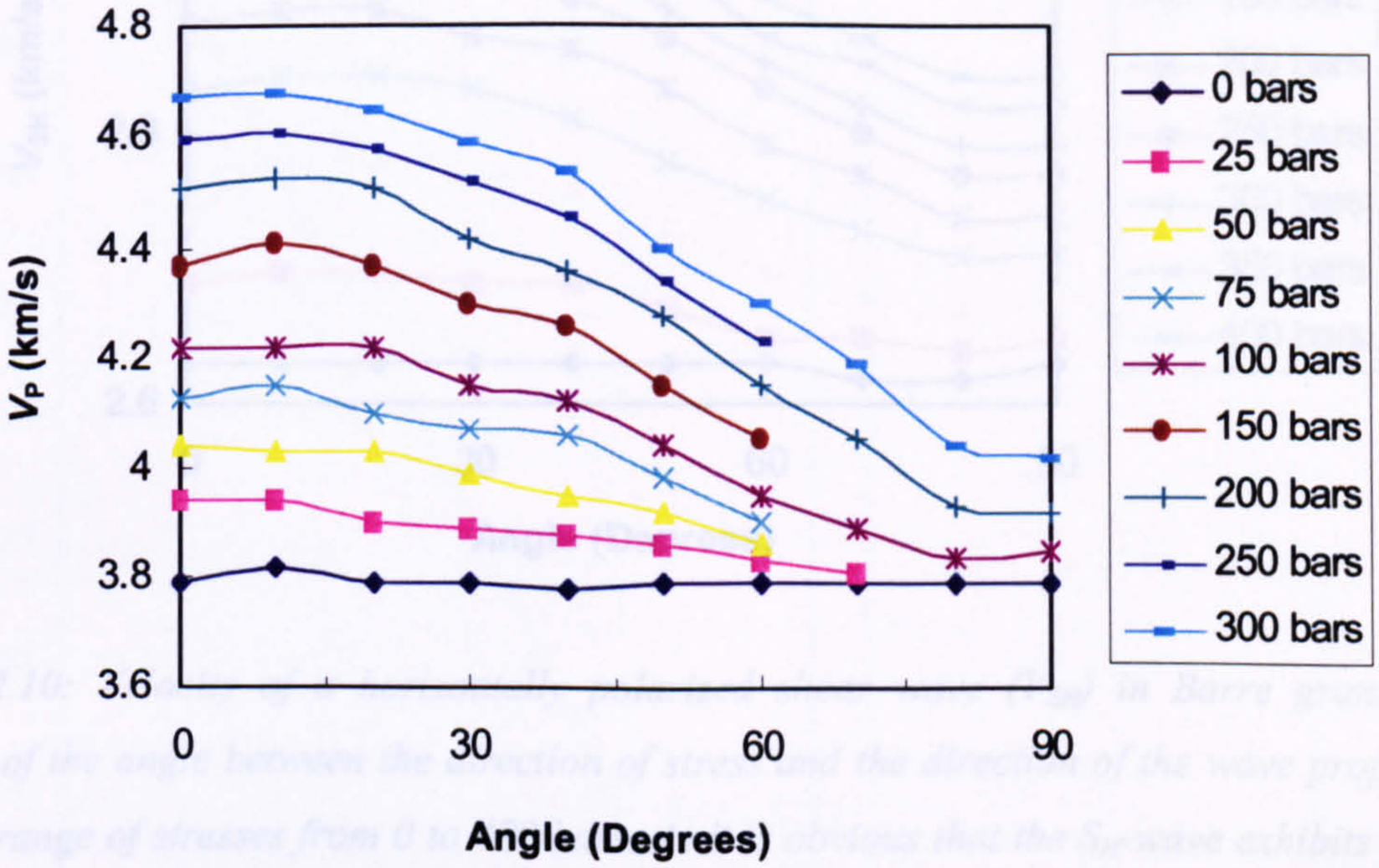

Figure 2.9: P-wave velocity (V_P) in Barre granite as a function of angle between the direction of stress and thedirection of the wave propagation under a range of stresses from 0 to 300 bars. The maximum velocity increase with stress occurs at small angles. The velocity anisotropy shows the lowest rate in the direction normal to the applied stress. Under an isotropic stress state (0 bar), the velocity is almost independent of direction (Nur and Simmons, 1969).

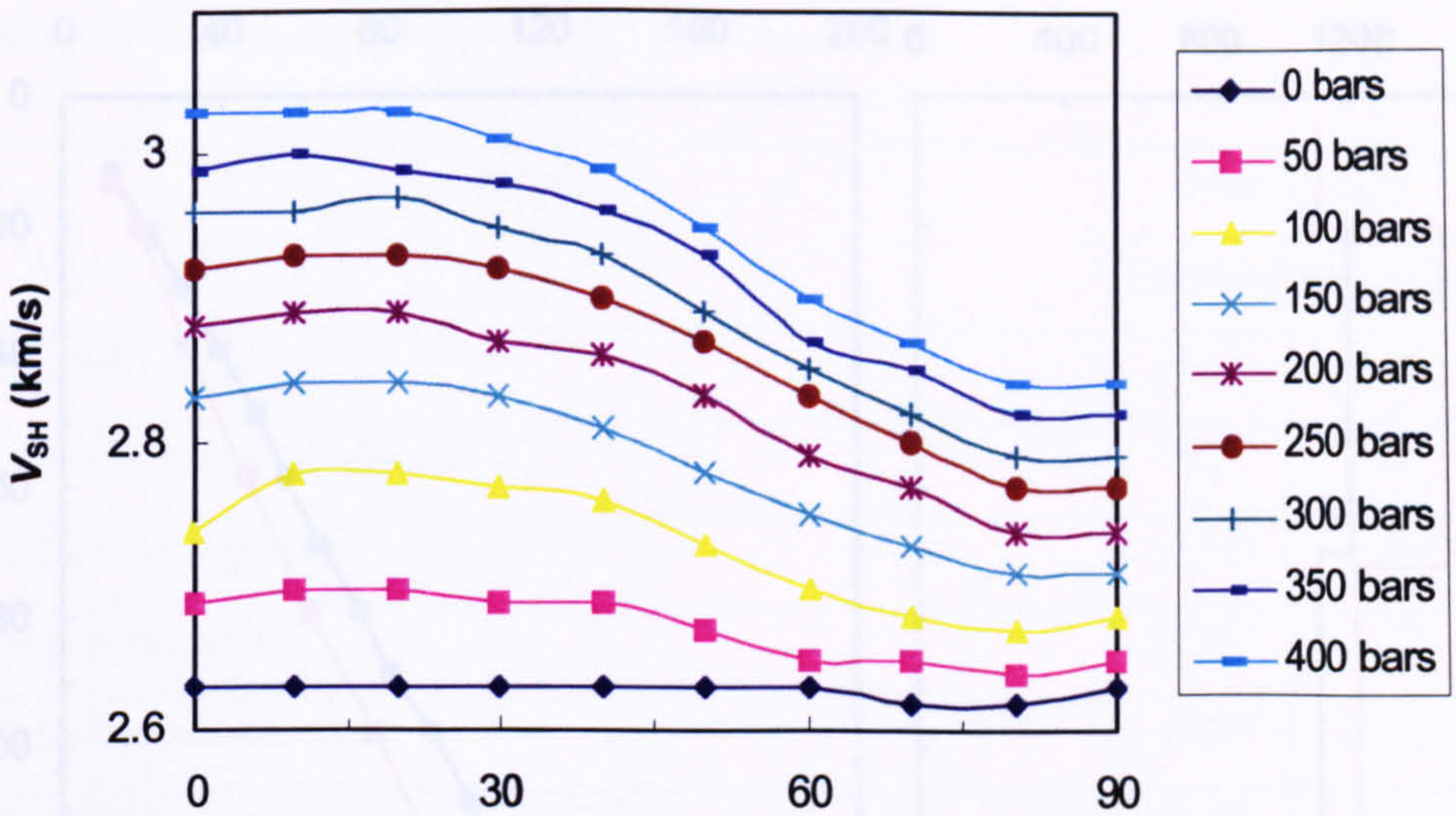

Figure 2.10: Velocity of a horizontally polarized shear wave (V_{SH}) in Barre granite, as a function of the angle between the direction of stress and the direction of the wave propagation, under a range of stresses from 0 to 400 bars. As it is obvious that the S_H-wave exhibits identical velocity anisotropy to the compressional wave, the velocity drop due to angle is not as high as is the case for the latter (Nur and Simmons, 1969).

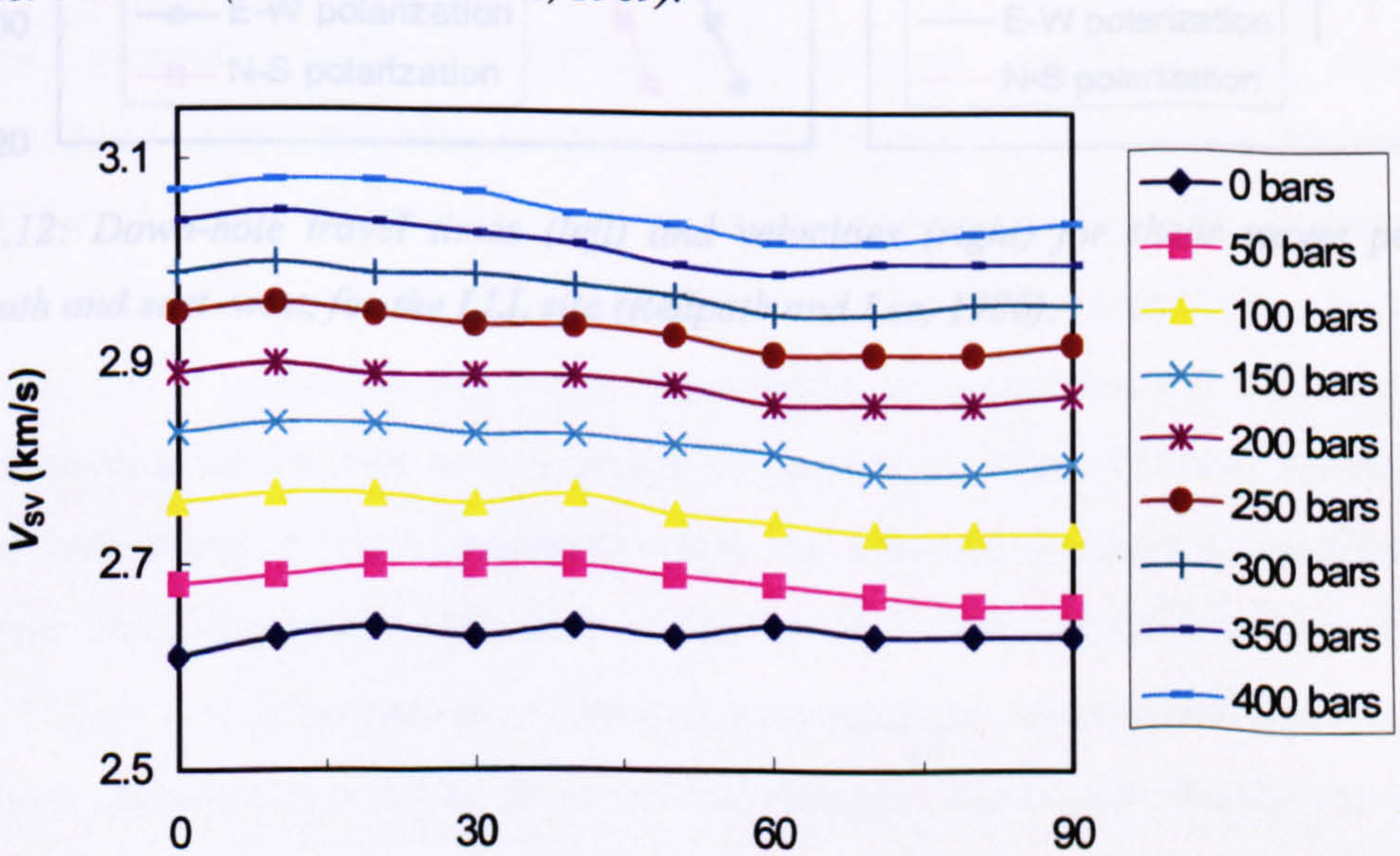

Figure 2.11: The velocity of a vertically polarized shear wave (V_{sv}) in Barre granite increases with applied stress, but its change with angle is not large compared to that seen in Figures 2.9 and 2.10 (Nur and Simmons, 1969).

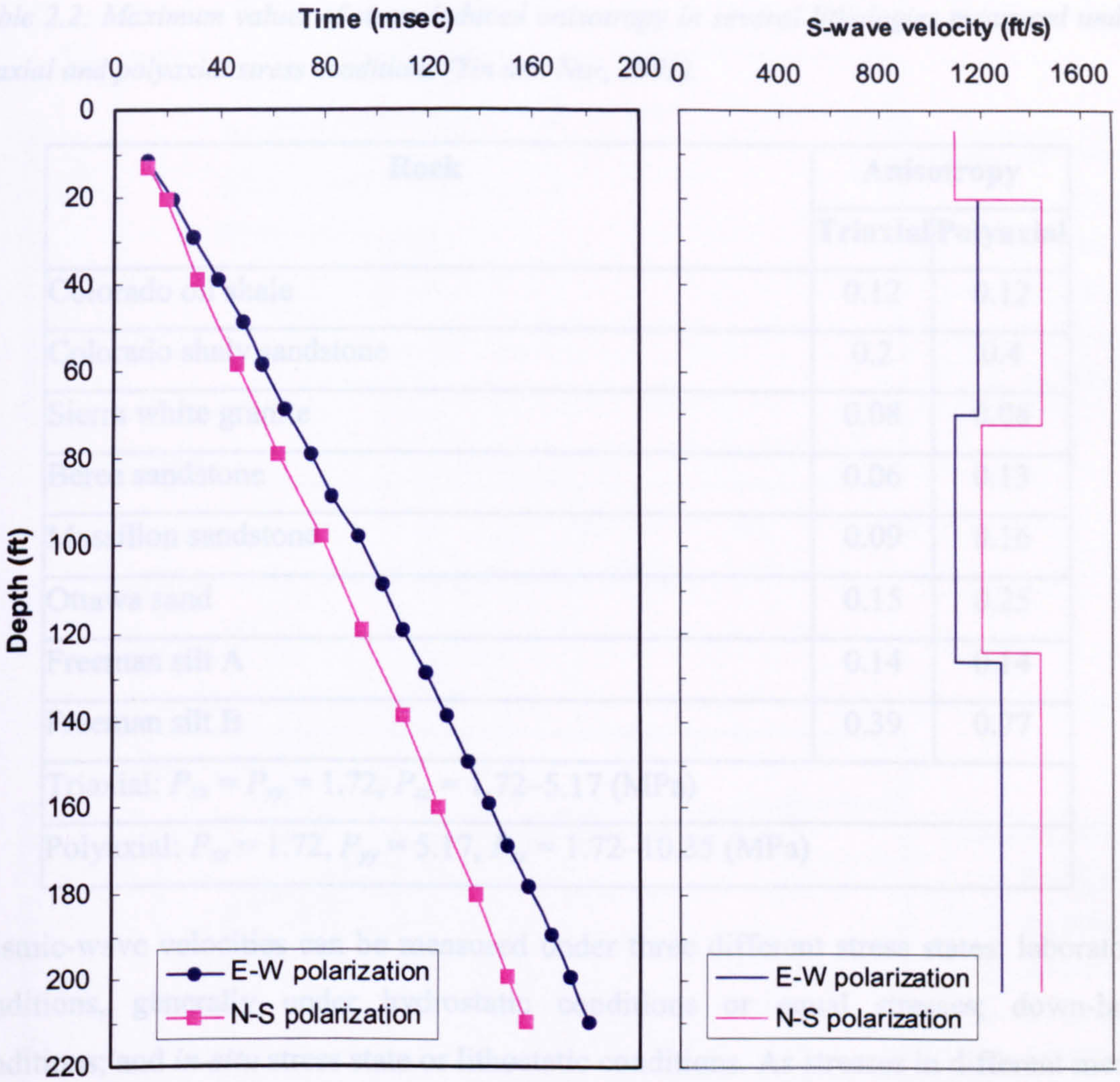

Figure 2.12: Down-hole travel times (left) and velocities (right) for shear waves polarized north–south and east–west, for the LLL site (Redpath and Lee, 1986).

Table 2.2: Maximum values of stress-induced anisotropy in several lithologies measured under triaxial and polyaxial stress conditions (Yin and Nur, 1992).

Rock	**Anisotropy**	
	Triaxial	**Polyaxial**
Colorado oil shale	0.12	0.12
Colorado shaly sandstone	0.2	0.4
Sierra white granite	0.08	0.08
Berea sandstone	0.06	0.13
Massillon sandstone	0.09	0.16
Ottawa sand	0.15	0.25
Freeman silt A	0.14	0.14
Freeman silt B	0.39	0.77
Triaxial: $P_{xx} = P_{yy} = 1.72$, $P_{zz} = 1.72–5.17$ (MPa)		
Polyaxial: $P_{xx} = 1.72$, $P_{yy} = 5.17$, $P_{zz} = 1.72–10.35$ (MPa)		

Seismic-wave velocities can be measured under three different stress states: laboratory conditions, generally under hydrostatic conditions or equal stresses; down-hole conditions; and *in-situ* stress state or lithostatic conditions. As stresses in different media can be different, they will influence seismic-wave velocities differently. Consequently, correlation of velocities will be difficult and some degree of discrepancy can occur. Ball and Batzle (1994) compared the stress dependence of compressional waves to shear waves in several sandstones with a range of porosities, with different results. They measured velocities in the laboratory close to realistic lithostatic conditions, by simplifying field conditions, but still within valid limits, which provided valuable insights. Figure 2.13 illustrates the measured velocities for Berea sandstone for a range of confining pressures at constant axial vertical stresses. The compressional wave shows an increase in velocity with vertical axial stress, and at the same time a small decrease with the lateral stress (minimum horizontal stress). However, at higher axial stress (above 30 MPa) the velocity increases with both axial and lateral stresses. On the other hand, the shear-wave velocity shows a monotonous (steady) increase with axial and lateral stresses.

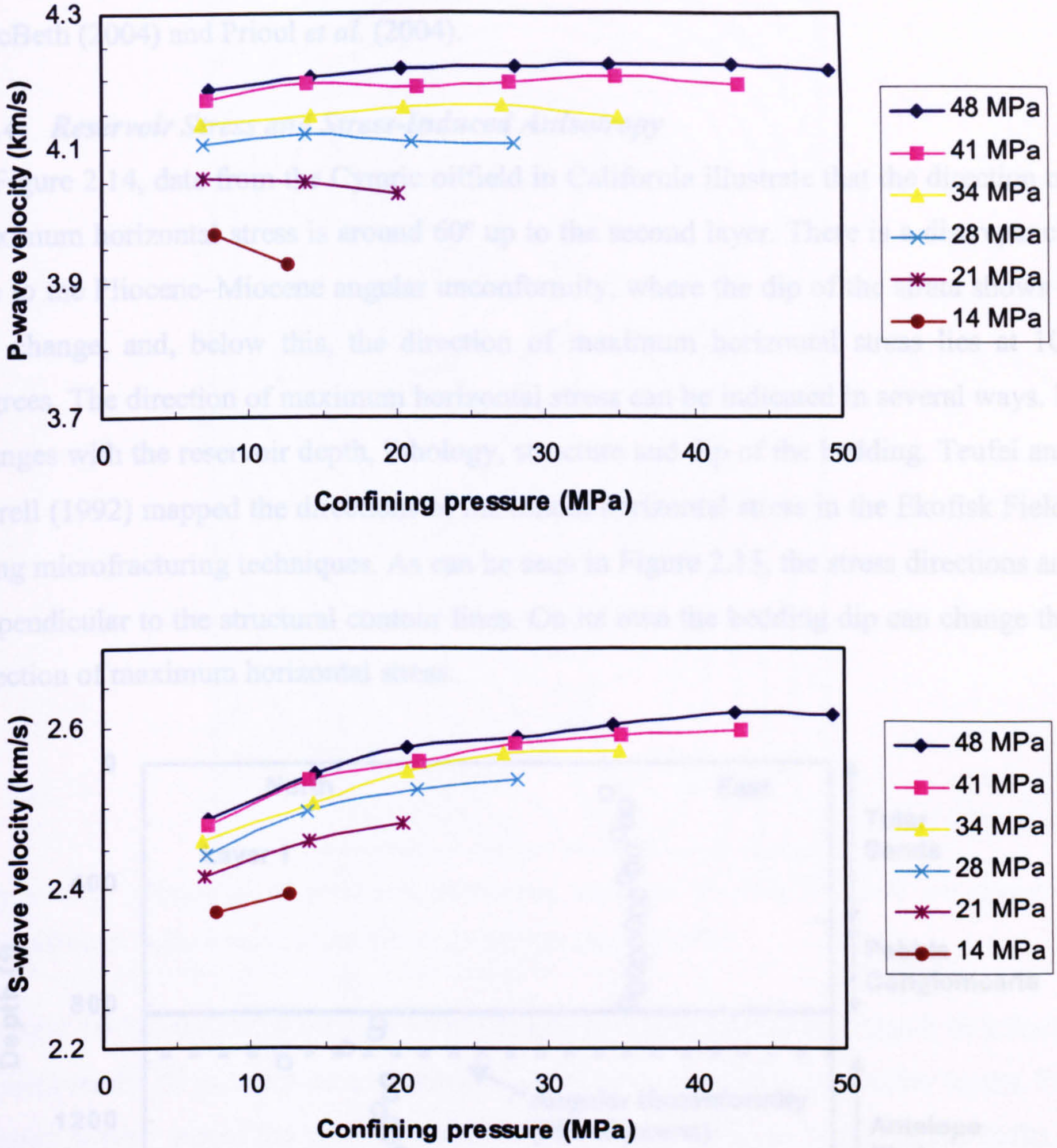

Figure 2.13: Variations in compressional-wave velocities (top) and shear-wave velocities (bottom) of Berea sandstone with vertical axial stress and confining pressure (lateral stress) (Ball and Batzle, 1994).

In Chapter 3, I will compare the variations in the velocities of the compressional and shear waves measured in my study, with the variations shown in Figure 2.13.

Other authors who have contributed to this issue include Lo *et al.* (1986), Sayers *et al.* (1990), Zamora and Poirier (1990), Sayers and Kachanov (1991, 1995), Schwartz *et al.* (1994), Mavko *et al.* (1995), Dvorkin *et al.* (1996), Holt *et al.* (1996), Johnson and Rasolofosaon (1996), Rasolofosaon (1998), Dillen *et al.* (1999), Fjaer and Holt (1999), Ohlson and MacBeth (1999), Hudson (2000), Nes *et al.* (2000), Kirstetter and MacBeth (2001), MacBeth and Lynn (2001), Gurevich (2002), Liu *et al.* (2002), Sarkar *et al.*

(2002), Sayers (2002), Shapiro and Kaselow (2002), Tod (2002), Wang (2002), MacBeth (2004) and Prioul *et al.* (2004).

2.4.4 Reservoir Stress and Stress-Induced Anisotropy

In Figure 2.14, data from the Cymric oilfield in California illustrate that the direction of maximum horizontal stress is around 60° up to the second layer. There is a discrepancy due to the Pliocene–Miocene angular unconformity, where the dip of the strata shows a 35° change, and, below this, the direction of maximum horizontal stress lies at 10° degrees. The direction of maximum horizontal stress can be indicated in several ways. It changes with the reservoir depth, lithology, structure and dip of the bedding. Teufel and Farrell (1992) mapped the directions of maximum horizontal stress in the Ekofisk Field, using microfracturing techniques. As can be seen in Figure 2.15, the stress directions are perpendicular to the structural contour lines. On its own the bedding dip can change the direction of maximum horizontal stress.

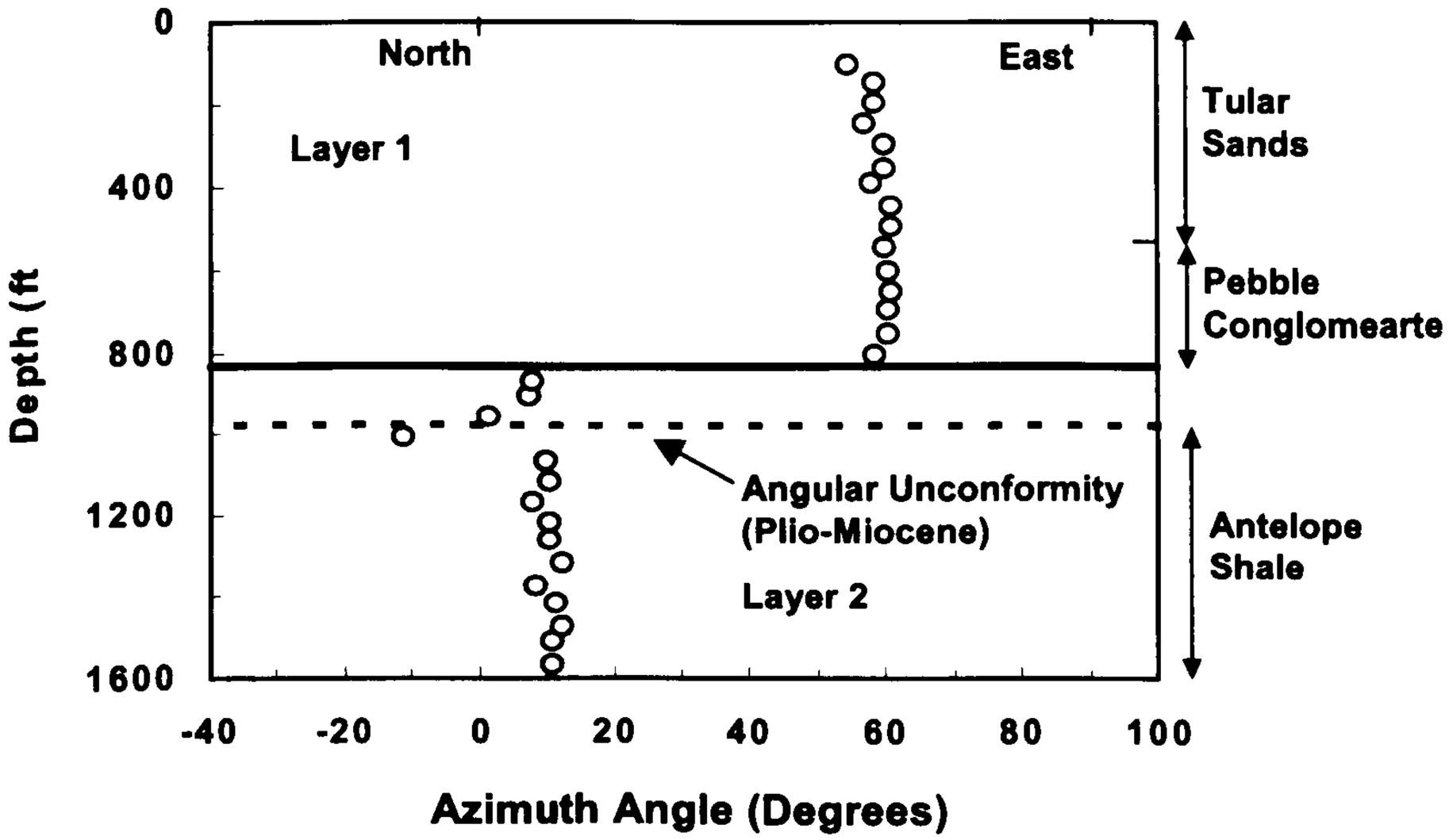

Figure 2.14: Polarization angles of the fast shear wave in the Cymric oilfield, California. The directions of maximum horizontal stress are believed to be along the observed polarization directions. The sudden change in the direction is due to an angular unconformity (Bruno and Winterstein, 1994).

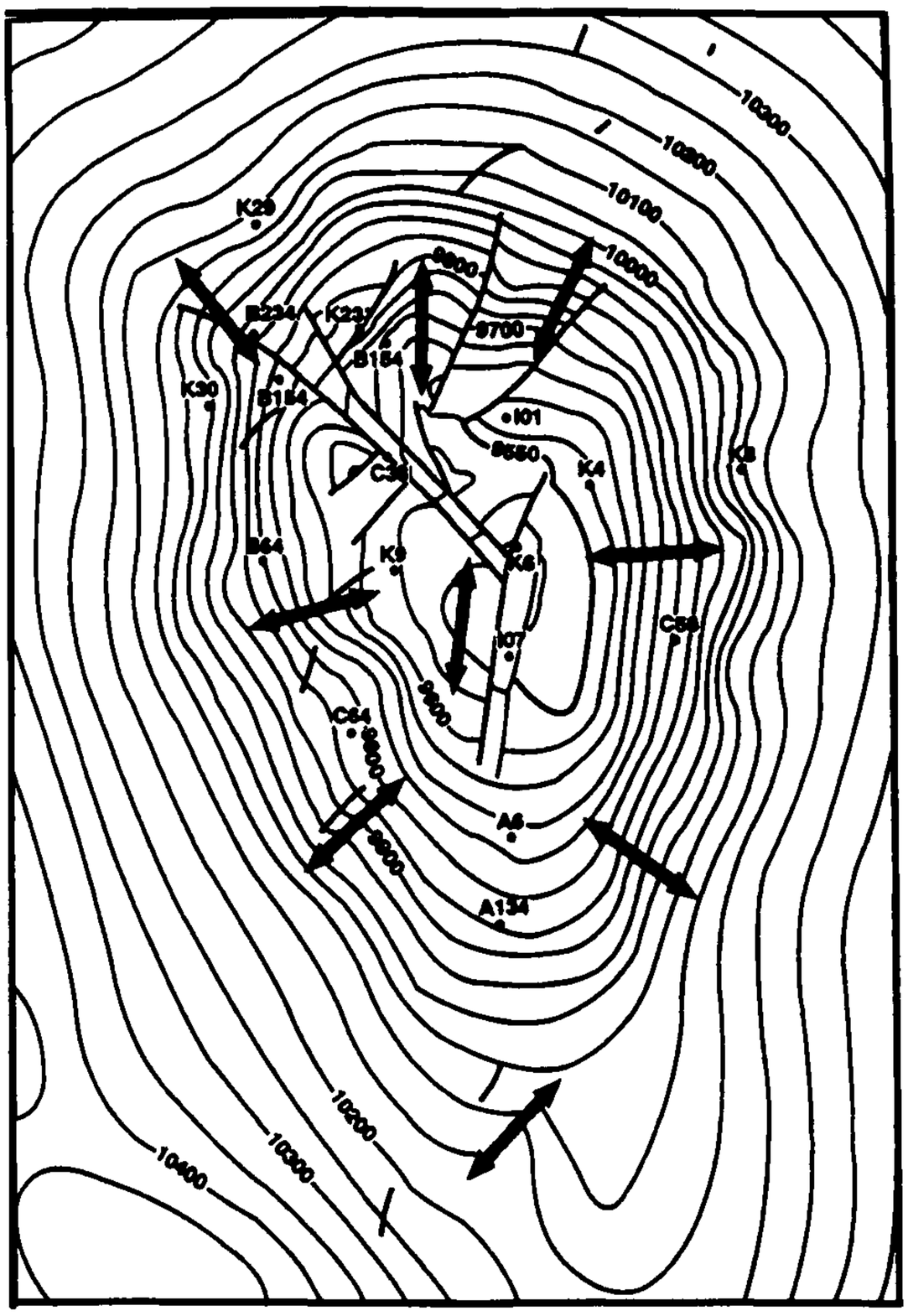

Figure 2.15: Directions of maximum horizontal stress in the Ekofisk Field are generally perpendicular to the structural contours (Teufel and Farrell, 1992).

Figure 2.16 illustrates the rotation of maximum horizontal stress with depth in a finite-element model of an anticline consisting of a stiff stratum between two softer layers. The rotation pattern across the crest of the anticline is quite different to that at the limbs of the structure. The degree of rotation of the maximum horizontal stress decreases with depth at the limbs, and increases across the crest of the anticline.

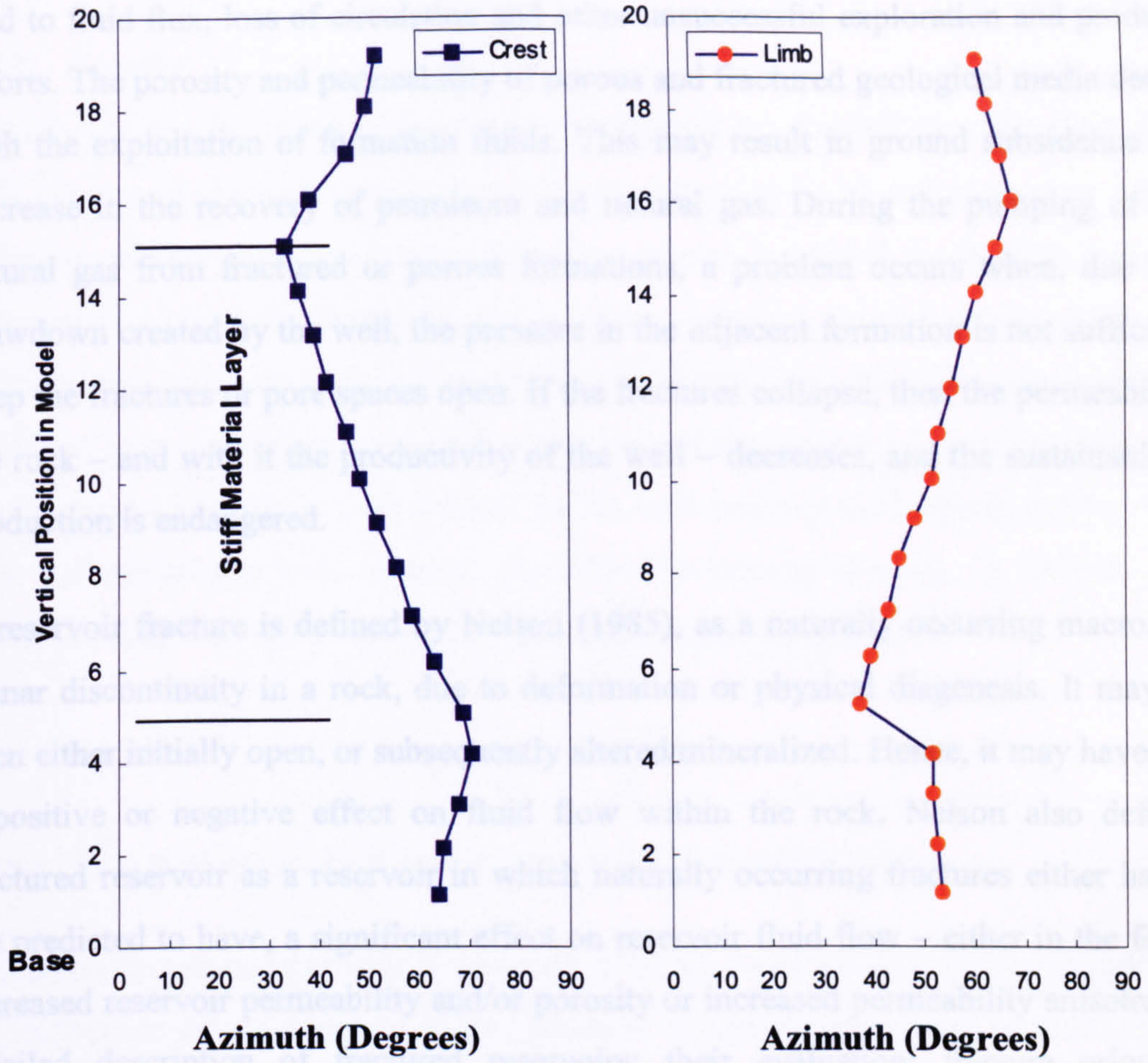

Figure 2.16: Rotation of principal stress direction in an anticline with a single stiff layer. The fold axis is at zero degrees. Thick lines indicate boundaries with softer material (Bruno and Winterstein, 1994).

2.5 Fractures and Fractured Reservoirs

Production and increasing recovery rate of the existing oil and gas fields have shown to attract arrested attention and new emphasis. Fractured reservoirs contain an enormous amount of oil and natural gas (Nelson, 1985). Fractures control *in situ* permeability; fluid storage and mobility; and rock strength; and thus the reservoir itself. Therefore, a clear insight into the subsurface fracture network will definitely promote optimization of well planning and production. Rock properties in a fractured reservoir indicate the amount of hydrocarbons and the convenience or inconvenience of production. For instance, porosity is a direct index for reflecting significance of volume of hydrocarbons, and permeability shows the ability of fluids to flow into a well. In addition to faults that act as conduits or barriers to fluids, joints, fractures, microfractures and cracks can all increase the permeability of the rocks. On the other hand, ignoring open fractures may

lead to fluid flux, loss of circulation and other unsuccessful exploration and production efforts. The porosity and permeability of porous and fractured geological media decrease with the exploitation of formation fluids. This may result in ground subsidence and a decrease in the recovery of petroleum and natural gas. During the pumping of oil or natural gas from fractured or porous formations, a problem occurs when, due to the drawdown created by the well, the pressure in the adjacent formation is not sufficient to keep the fractures or pore spaces open. If the fractures collapse, then the permeability of the rock – and with it the productivity of the well – decreases, and the sustainability of production is endangered.

A reservoir fracture is defined by Nelson (1985), as a naturally occurring macroscopic planar discontinuity in a rock, due to deformation or physical diagenesis. It may have been either initially open, or subsequently altered/mineralized. Hence, it may have either a positive or negative effect on fluid flow within the rock. Nelson also defines a fractured reservoir as a reservoir in which naturally occurring fractures either have, or are predicted to have, a significant effect on reservoir fluid flow – either in the form of increased reservoir permeability and/or porosity or increased permeability anisotropy. A detailed description of fractured reservoirs; their evaluation; fracture origin and morphology; generic and geological classifications can be found in Aguilera (1980), Nelson (1985) and Saidi (1987).

The mechanical properties of the host rock; its modes of origin; and subsurface diagenesis, all control the physical characters of fractures. A feature resulting from combination of these factors can either increase or decrease reservoir porosity and permeability. Despite the fact that fractures can occur on a large scale, in all rock formations, subsurface or outcrop, it is only when they are present with an adequate length or spacing that their positive or negative impact upon fluid flow emerges as being considerable. In order to evaluate this impact, one should focus on the fluid-flow properties of individual representative fractures and the number of fractures that run in a given direction in the studied reservoir volume. Hence, besides making the usual petrophysical measurements on the rock matrix, it is necessary to indicate the reservoir properties of the fracture network and their fluctuations with reservoir depletion and depth. The most effective petrophysical determinations are fracture porosity, fracture permeability, fluid saturation within the fractures, and the expected recovery factor of the fracture system (Nelson, 1985). Here some important reservoir rocks and fracture properties are reviewed in order to discuss two fracture theories in this chapter.

2.5.1 Porosity

Porosity (ϕ) or void space within a rock is obtained by dividing the void space by the bulk volume of the rock (Aguilera, 1980). Porosity can be classified as total primary, effective primary, and secondary. Primary porosity is related to the time when the sediment was originally deposited, and so it is an inherent, original characteristic of the rock. Factors such as grain arrangement and distribution, and also cementation and degree of interconnection among the voids, control the amount of the primary porosity. Total primary porosity can be defined as the total primary void spaces divided by the bulk volume of the rock, whereas the effective primary porosity is defined as the interconnected void spaces divided by the bulk volume of the rock.

$$\phi = \frac{V_{VS}}{V_B} = \frac{V_B - V_{SP}}{V_B} \tag{2.21}$$

where V_{VS} is void space, V_B is bulk volume and V_{SP} is sphere volume.

Secondary or induced porosity is assumed to be the result of geological processes after the deposition of sedimentary rocks. Solution, recrystallization and dolomitization in fractures and joints can cause secondary porosity.

2.5.2 Fracture Aperture

Fracture aperture is an important geometrical property of fractures that contributes directly to the fluid flow and productivity of a reservoir. A wide fracture or crack can often be at the same time taller, longer and more widely distributed. Figure 2.17 relates fracture aperture in millimetres to well productivity in barrels per day (bbd).

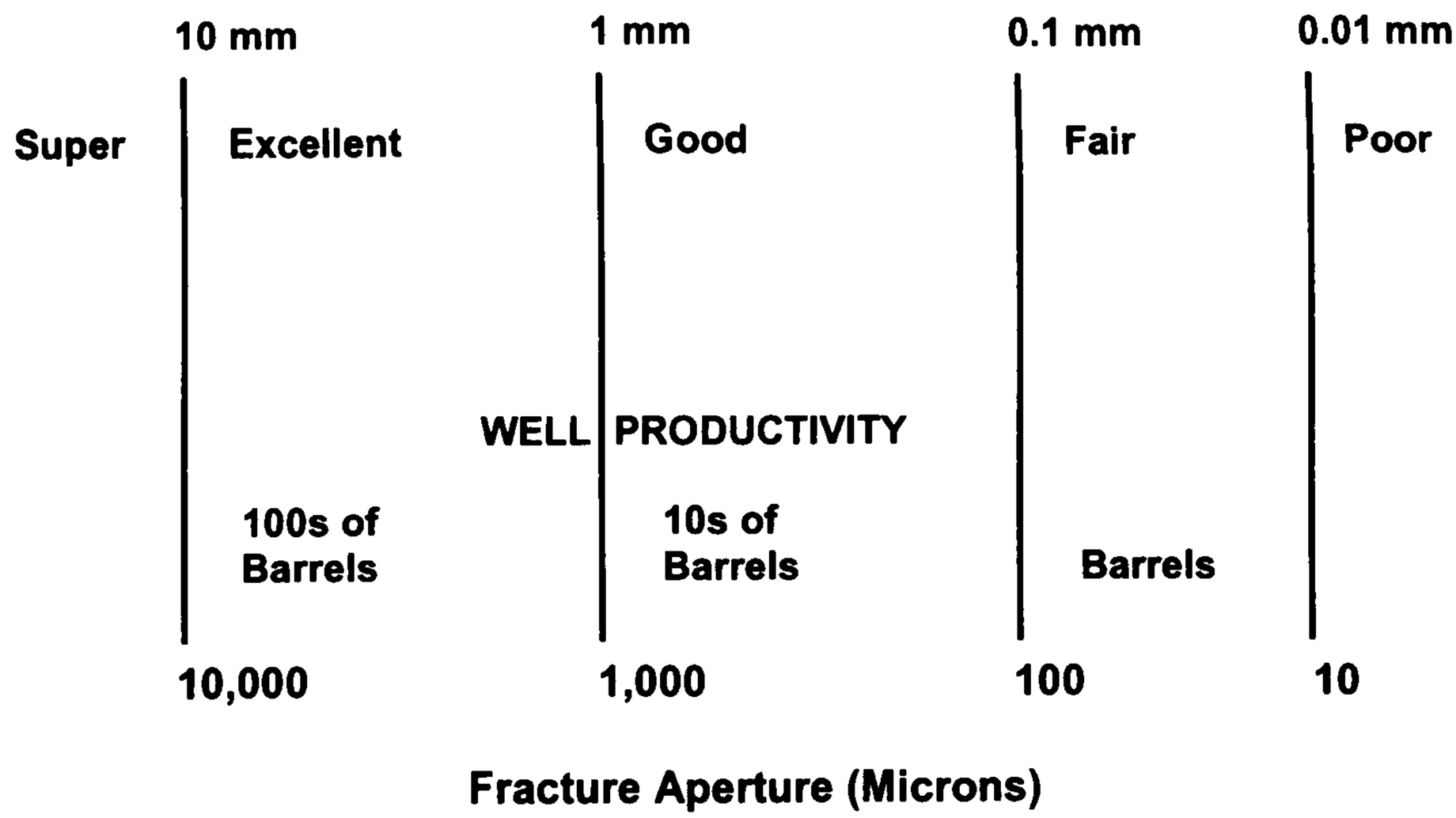

Figure 2.17: Correlation between fracture aperture in microns or millimetres with well productivity in barrels per day, in the Austin Chalk, Texas (Fett, 1991).

2.5.3 Fracture/Crack Aspect Ratio

Fracture or crack aspect ratio is defined as follows:

$$\alpha = \frac{c}{a} \tag{2.22}$$

where c is the crack width and a is the crack length, as shown in Figure 2.18. Aspect ratios can be in the range of 0.001 to 0.1 and relate the rock's mechanical integrity to its flow characteristics

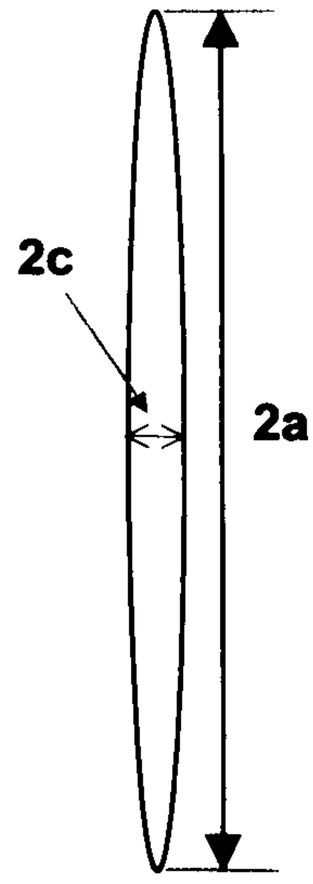

Figure 2.18: Side view of a crack, showing large and small dimensions in defining the crack aspect ratio.

2.5.4 Fracture (Crack) Density

Crack density (e) is another important factor which adds to our information on the structure of crack or fracture model and is written in the form of:

$$e = \frac{N}{V} a^3 \tag{2.23}$$

or:

$$e = \frac{3\phi_c}{4\pi\alpha} \tag{2.24}$$

where N is the number of cracks of radius a in a volume of V; ϕ_c is the total volume of the inclusions or crack porosity; and α is the crack aspect ratio.

2.6 Effective Medium and Fracture Theories

As discussed in the literature, the oil and gas industry is interested in investigating fluid-conducting reservoir fractures, therefore the next focus of attention is the mechanical behaviour of the reservoir rocks. On the other hand, most hydrocarbon reservoirs are encountered at several hundreds or a few thousand metres depth, where they are highly tectonized, cracked and fractured. Therefore, a rock's internal failures, defects and pore spaces control its mechanical response to external forces. In addition to pores and internal defects, the mineralogical and crystallographic properties of the rock and whether pore spaces are filled with fluids and/or interconnected also affect the rock behaviour expressed in terms of moduli. Here the geometry, distribution, density and intensity of these void spaces or cracks are of major importance. In order to make the study of cracked or fractured rocks possible, equivalently they are assumed as effective media that are meanwhile homogeneous and either embedded by pore spaces or inclusions (Hudson, 1980, 1981) or planes of weakness or defects (Schoenberg and Muir, 1989). After a discussion on the justifications for using the Hudson crack model (Hudson, 1980, 1981; Hudson *et al.*, 1996*b*, 1997) for fracture-induced anisotropy, I will explain how to use the framework of Schoenberg and Muir's theory combined by Hudson's crack model.

On the other hand, to connect crack models (*e.g.* Hudson, 1980) to fracture models (*e.g.* Schoenberg, 1999; Liu *et al.*, 2000) (Figure 2.19), it is necessary to discuss the evolution of fracture theories from crack theories. Cracks are perceived to be very small void- or fluid-filled spaces of oblate spheroid shape, distributed randomly as clusters making up conduits (fractures) for fluid flow. In comparison to the average seismic wavelength, in

the range of tens of metres at least, cracks are many orders of magnitude smaller, in the range of tenths of a millimetre to millimetres thick. Fractures, which are still small compared to the wavelength of passing seismic waves, can be thought of as planes of discontinuity or concentrations of cracks.

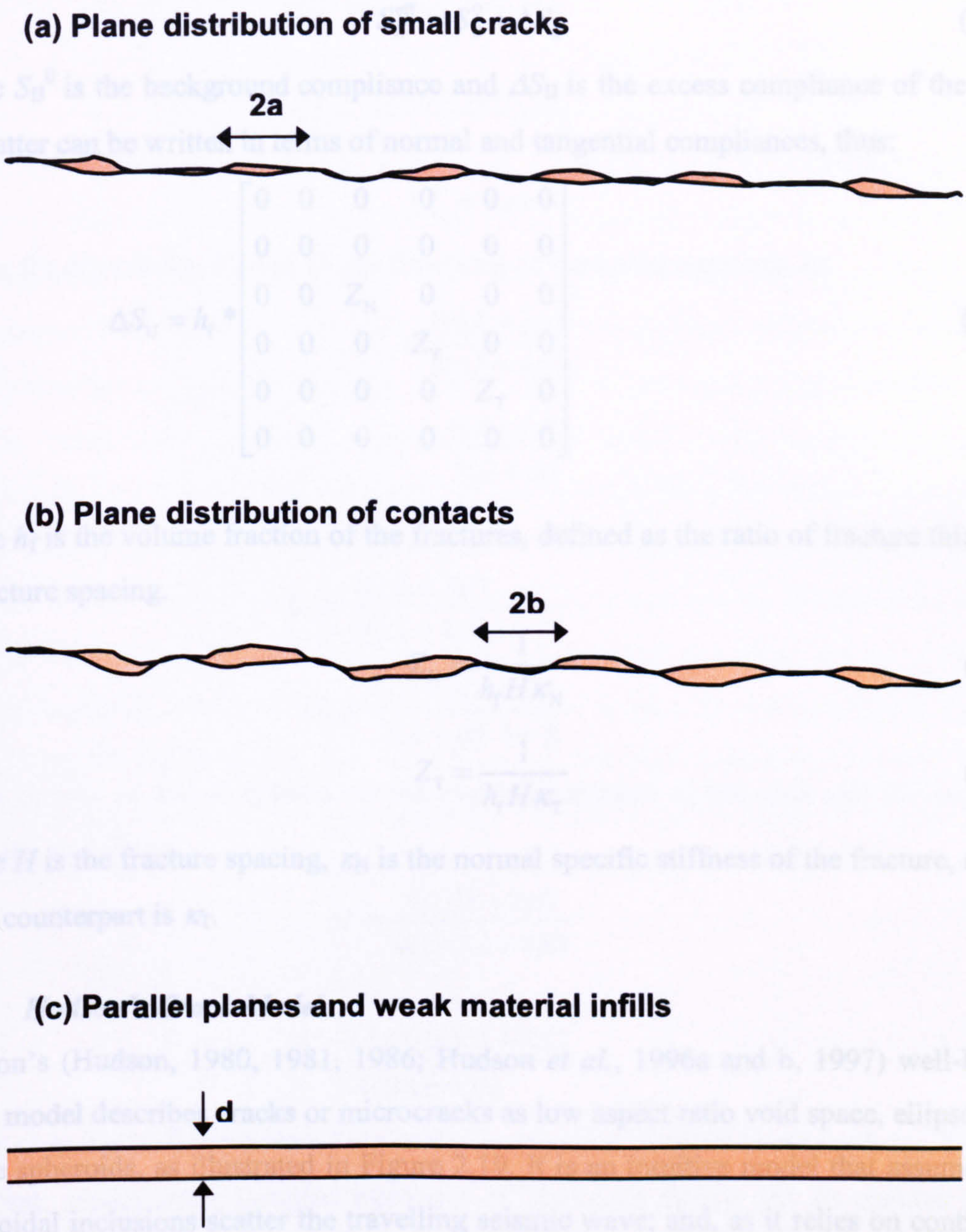

Figure 2.19: Crack and fracture models showing: (a) a plane distribution of small oblate voids (e.g. Hudson et al., 1996b), (b) a plane distribution of contacts (e.g. Hudson et al., 1997) and (c) parallel planes with weak solid infills (e.g. Schoenberg, 1980), (Liu et al., 2000).

2.6.1 Schoenberg and Muir

Schoenberg and Muir (1989) considered an accumulation of infinitely thin horizontal layers, each with a thickness much smaller than a seismic wavelet. They used matrix algebra and group theory to compute the response of an anisotropic, homogeneous

medium, perturbed by the heterogeneous distribution of thin layers, to a seismic wave in the long-wavelength limit. Sets of parallel fractures and aligned microcracks can be treated well using this. The theory gives the effective compliance of a medium, caused by a set of horizontal fractures, as:

$$S_{IJ}^{eff} = S_{IJ}^{0} + \Delta S_{IJ} \tag{2.25}$$

where $S_{IJ}{}^{0}$ is the background compliance and ΔS_{IJ} is the excess compliance of the rock. The latter can be written in terms of normal and tangential compliances, thus:

$$\Delta S_{IJ} = h_f * \begin{bmatrix} 0 & 0 & 0 & 0 & 0 & 0 \\ 0 & 0 & 0 & 0 & 0 & 0 \\ 0 & 0 & Z_N & 0 & 0 & 0 \\ 0 & 0 & 0 & Z_T & 0 & 0 \\ 0 & 0 & 0 & 0 & Z_T & 0 \\ 0 & 0 & 0 & 0 & 0 & 0 \end{bmatrix} \tag{2.26}$$

where h_f is the volume fraction of the fractures, defined as the ratio of fracture thickness to fracture spacing.

$$Z_N = \frac{1}{h_f H \kappa_N} \tag{2.27}$$

$$Z_T = \frac{1}{h_f H \kappa_T} \tag{2.28}$$

where H is the fracture spacing, κ_N is the normal specific stiffness of the fracture, and its shear counterpart is κ_T.

2.6.2 Hudson's Crack Model

Hudson's (Hudson, 1980, 1981, 1986; Hudson *et al.*, 1996a and b, 1997) well-known crack model describes cracks or microcracks as low aspect ratio void space, ellipsoids or oblate spheroids, as illustrated in Figure 2.19. It is an intuitive model that assumes that spheroidal inclusions scatter the travelling seismic wave; and, as it relies on continuous strain around the crack, it can also be interpreted as perturbed stiffness. The perturbed stiffness tensor reads:

$$C_{ijkl} = C_{ijkl}^{0} + C_{ijkl}^{1} + C_{ijkl}^{2} + ... \tag{2.29}$$

where $C_{ijkl}{}^{0}$ is the background stiffness; $C_{ijkl}{}^{1}$ is the first-order stiffness; and $C_{ijkl}{}^{2}$ is the second-order stiffness, all of which are affected by geometrical properties of the cracks, such as density, aspect ratio and orientation. The theory works well for one or more sets of aligned fractures, but its accuracy is limited to low aspect ratios and low crack

densities. For a VTI medium formed by horizontal cracks with their normal in the direction of x_3, non-zero elements of the first-order stiffness can be written as:

$$C_{11}^1 = -\frac{\lambda^2}{\mu} eU_3 \tag{2.30}$$

$$C_{33}^1 = -\frac{(\lambda+2\mu)^2}{\mu} eU_3 \tag{2.31}$$

$$C_{13}^1 = -\frac{\lambda(\lambda+2\mu)}{\mu} eU_3 \tag{2.32}$$

$$C_{44}^1 = -\mu e U_1 \tag{2.33}$$

where, for dry cracks, U_1 and U_3 are functions of the Lamé constants as:

$$U_1 = \frac{16(\lambda+2\mu)}{3(3\lambda+4\mu)} \tag{2.34}$$

$$U_3 = \frac{4(\lambda+2\mu)}{3(\lambda+\mu)} \tag{2.35}$$

For weak inclusions:

$$U_1 = \frac{16(\lambda+2\mu)}{3(3\lambda+4\mu)} \frac{1}{1+M} \tag{2.36}$$

$$U_3 = \frac{4(\lambda+2\mu)}{3(\lambda+\mu)} \frac{1}{1+K} \tag{2.37}$$

where factors M and K depend on the elastic properties of the rock and the inclusion material, as follows:

$$M = \frac{4\mu'(\lambda+2\mu)}{\pi\alpha\mu(3\lambda+4\mu)} \tag{2.38}$$

$$K = \frac{[\kappa'+(4/3)\mu'](\lambda+2\mu)}{\pi\alpha\mu(\lambda+\mu)} \tag{2.39}$$

where κ' is the bulk modulus of the inclusion material, μ' is its shear modulus, and α is the crack aspect ratio. Detailed treatment of Hudson's theory and its updates can be found in Hudson (1980, 1981, 1986), Hudson *et al.* (1996a and b, 1997, 2000), Liu *et al.* (2000), Hall (2000), Pointer (2000) and MacBeth (2002).

2.7 Summary

Several aspects of the significance of stresses in oil and gas reservoirs have been discussed in two sections covering reservoir stress-sensitivity and stress orientation in reservoirs. The types of stress, and the stress states that cause the different faulting systems, have also been explained. Shear waves demonstrate the ability to indicate the direction of maximum horizontal stress through their polarization. Several methods for stress characterization have been listed and a brief history of anisotropy has been presented, along with its definition and the ways in which it differs from heterogeneity. The important types of anisotropy have also been introduced. In reviewing past measurements of stress-induced anisotropy, several significant published results have been presented in order to give an insight into the practicality and potential of the subject, based upon laboratory measurements, of which a few examples have been reproduced. The basis of stress-induced anisotropy has been illustrated. To achieve a proper insight into the implications of stresses for seismic-wave velocity, one ought to consider *in situ* stresses in their realistic state, a state that can be simulated by triaxial loading. Furthermore, as the velocities of compressional and shear waves exhibit the greatest sensitivity to normal stresses, in Chapter 3 a method will be adopted to tackle the problem in the most practical way. Fracture, fractured reservoirs, effective media, and fracture theories have been covered to the required extent, in order to prepare a basis for the calculation of fracture-induced anisotropy in Chapter 4.

Chapter 3

Calculation of Stress-Induced Anisotropy in Sandstones

3.1 Introduction

In this chapter the basis of the calculation of stress-induced seismic anisotropy is presented. The focus in particular is on TI (VTI and HTI) media, and the computation of anisotropy parameters for a region which exhibits a strike-slip faulting system where the maximum horizontal stress is the prevailing stress. Use is also made of laboratory data from previously published work – data which provide estimates for excess compliances as a function of applied isotropic stress for saturated and dry Palaeocene and Rotliegend sandstone samples. The outcome of this work is a range of Thomsen's parameters with a dependence on the differential stress and background isotropic stress. Finally, convenient approximations to this stress dependence are presented.

3.2 Anisotropy Parameterization – Dry-Frame Sand

My workflow for this calculation is displayed in Figure 3.1. In geographical areas for which the prevailing stress at depth in the reservoir is the maximum horizontal stress σ_H, azimuthally dependent seismic properties can be created by unequal loading of the rock frame. Although the most common triaxial compressive stress regime that might arise in this situation is $\sigma_H > \sigma_V > \sigma_h$ (leading to the generation of strike-slip faults), for simplicity of calculation, I will assume the condition $\sigma_H > \sigma_V \approx \sigma_h$ in order to make the studied medium HTI, as the key assumption of strike-slip faulting system implies that

medium is orthorhombic. Such an arrangement is not as artificial as one might think, and it has been observed in many cases – for example in the Visund Field in the Norwegian Basin (Wiprut and Zoback, 2000). Obviously this cannot be the only possibility to start with for calculation of stress-induced anisotropy and it is thus adopted to later facilitate the comparison with HTI medium caused by vertically aligned fractures. The effects of this particular stress state are equivalent to an isotropic loading component σ_0 (essentially the lithostatic overburden stress minus reservoir fluid pressure), combined with a single uniaxial compression σ_U directed along the x_1 axis, so that $\sigma_H = \sigma_U + \sigma_0$, $\sigma_h = \sigma_0$ and $\sigma_V = \sigma_0$. Figure 3.2 illustrates such a stress state.

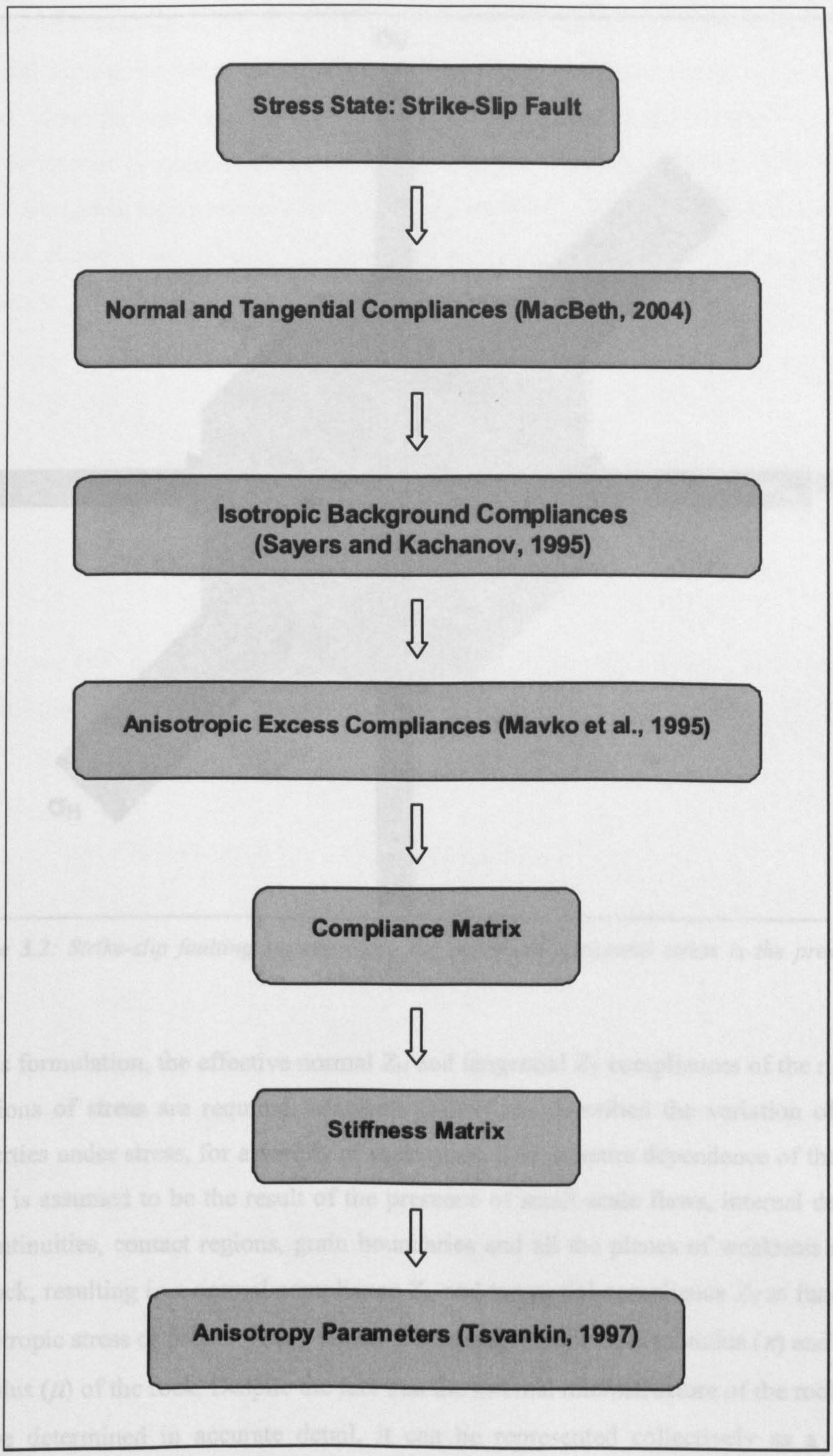

Figure 3.1: Workflow to parameterize stress-induced anisotropy.

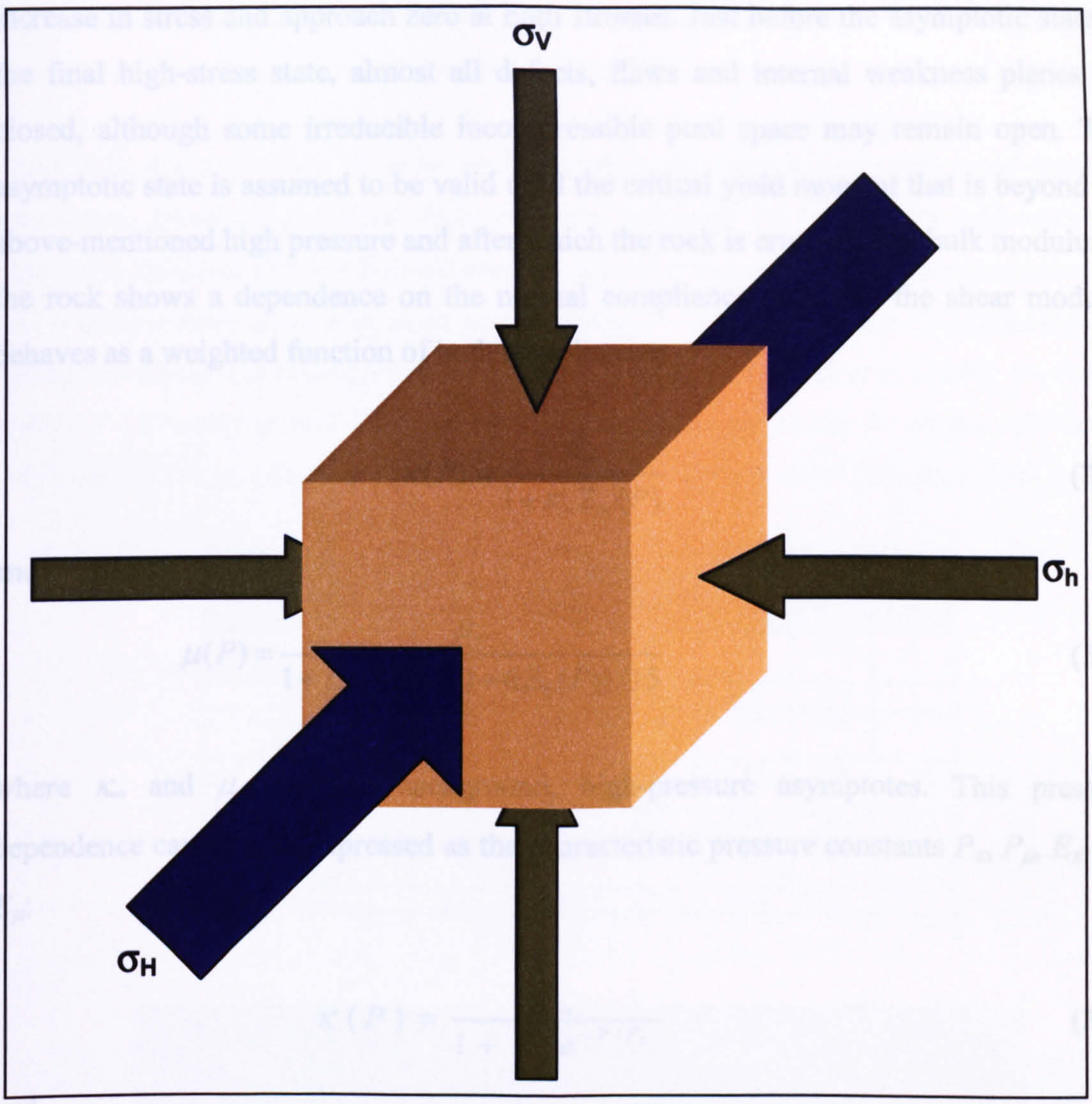

Figure 3.2: Strike-slip faulting system where the maximum horizontal stress is the prevailing stress.

In this formulation, the effective normal Z_N and tangential Z_T compliances of the rock as functions of stress are required. MacBeth (2004) has described the variation of rock properties under stress, for a variety of rock types. The pressure dependence of the rock frame is assumed to be the result of the presence of small-scale flaws, internal defects, discontinuities, contact regions, grain boundaries and all the planes of weakness inside the rock, resulting in a normal compliance Z_N and tangential compliance Z_T as functions of isotropic stress or pressure (σ_0), which then appears in the bulk modulus (κ) and shear modulus (μ) of the rock. Despite the fact that the internal microstructure of the rock may not be determined in accurate detail, it can be represented collectively as a single pseudo-function of pressure to a satisfactory degree. Thus, in its intact form the rock is assumed to be a homogeneous isotropic elastic medium containing a random distribution of internal flaws which vary as a function of isotropic stress, and which decrease with an

increase in stress and approach zero at high stresses. Just before the asymptotic state of the final high-stress state, almost all defects, flaws and internal weakness planes are closed, although some irreducible incompressible pore space may remain open. This asymptotic state is assumed to be valid until the critical yield moment that is beyond the above-mentioned high pressure and after which the rock is crushed. The bulk modulus of the rock shows a dependence on the normal compliance only, but the shear modulus behaves as a weighted function of both compliances:

$$\kappa(P) = \frac{\kappa_\infty}{1+\kappa_\infty Z_N(P)} \tag{3.1}$$

and

$$\mu(P) = \frac{\mu_\infty}{1+\mu_\infty (4Z_N(P)+6Z_T(P))/15} \tag{3.2}$$

where κ_∞ and μ_∞ are the background, high-pressure asymptotes. This pressure dependence can also be expressed as the characteristic pressure constants P_κ, P_μ, E_κ and E_μ:

$$\kappa(P) = \frac{\kappa_\infty}{1 + E_\kappa e^{-P/P_\kappa}} \tag{3.3}$$

and

$$\mu(P) = \frac{\mu_\infty}{1 + E_\mu e^{-P/P_\mu}} \tag{3.4}$$

These pressure constants represent the asymptotic state at which the rock is observed to be relatively insensitive to pressure change. Stress-sensitivity parameters S_κ and S_μ can be expressed as functions of these constants in the form of:

$$S_\kappa = \frac{\kappa_\infty - \kappa(0)}{\kappa_\infty} = \frac{E_\kappa}{1+E_\kappa} \tag{3.5}$$

and

$$S_\mu = \frac{\mu_\infty - \mu(0)}{\mu_\infty} = \frac{E_\mu}{1+E_\mu} \tag{3.6}$$

A database consisting of 179 sets has been analysed previously and the pressure-dependence relations have been fitted. Tables 3.1 and 3.2 give the elastic properties and the pressure sensitivity of the rocks being studied. An example of the pressure

dependence of Lochaline sandstone is illustrated in Figure 3.3, depicting the dependence for three different porosity levels: 5, 18.9 and 36.2%.

Table 3.1: Average values of some rock properties for several outcropping and reservoir sandstones, based on published data and data generated by Heriot-Watt University and elsewhere. Velocities (VP and VS) and densities (ρ) are zero-pressure values, core porosity is Φ, and N is the number of samples. Data originate from: 1 – Tao et al. (1995); 2 – Kirstetter et al. (2000); 3 – Cheng and Toksöz (1979); 4 – Winkler (1983); 5 – Khaksar et al. (1999); 6 – Freund (1992); 7 – Courtesy of Shell UK Expro; 8 – Courtesy of Enterprise Oil; 9 – Gregory (1976); 10 – Courtesy of Michael King, Imperial College; and 11 – Courtesy of BP (MacBeth, 2004).

OUTCROP SANDSTONES - GEOLOGY	VP (km/s)	VS (km/s)	ρ (g/cc)	VP/VS	Φ(%)	N
Unconsolidated Lochaline[1,2]	3.67	2.22	2.17	1.65	18.0	3
Molasse[1]	2.11	1.41	2.66	1.50	25.9	1
Disaggregated Lochaline[1,2]	0.97	0.64	1.64	1.51	37.1	3
Berea[1,3,4]	3.25	2.10	2.44	1.54	17.8	4
Clashach[1]	3.92	2.58	2.69	1.52	17.0	1
Navajo[3]	3.47	2.28	2.22	1.52	16.4	1
Cemented Lochaline[1,2]	4.88	2.77	2.52	1.76	5.0	3
Boise[3]	3.15	1.92	1.99	1.64	25.0	1

RECOVERED RESERVOIR ROCKS - GEOLOGY/ FORMATION (FIELD)	VP (km/s)	VS (km/s)	ρ (g/cc)	VP/VS	Φ(%)	N
Forties[8] (Nelson), Facies A	1.82	1.13	2.00	1.61	25.4	7
Paleocene (West of Shetlands)[11]	2.24	1.35	1.91	1.66	27.1	37
Miocene, (Gulf Coast)[9]	2.46	1.84	1.99	1.34	21.7	1
Rotliegend (southern North Sea)[7], Facies A	2.28	1.51	2.08	1.51	23.6	11
Rotliegend (southern North Sea)[7], Facies B	2.71	1.67	2.27	1.62	15.8	12
Forties[8] (Nelson), Facies B	3.32	2.05	2.31	1.62	13.0	1
Cooper Basin[5], Facies A	2.69	1.74	2.26	1.55	13.2	13
Rotliegend (southern North Sea)[7], Facies C	2.86	1.66	1.64	1.72	10.9	5
Rotliegend (Germany)[6], Facies A	3.23	2.33	2.43	1.38	9.5	31
Cooper Basin[5], Facies B	3.81	2.47	2.47	1.54	5.5	10
Rotliegend (Germany)[6], Facies B	3.65	2.58	2.63	1.41	3.4	24
(North Sea)[10]	3.43	2.42	2.41	1.41	7.4	10

Table 3.2: Average values of pressure-sensitivity properties for the sets of outcrop (top) and reservoir sandstones (bottom) detailed in Table 3.1. The tabulated values are determined by least-squares line fits or averages within each particular group. Additional italicized values in rows correspond to refits using only data points at confining pressures greater than the estimated in situ effective stress (20 MPa, apart from the deeper Freund results when 75 MPa is used). The second row in the WoS results corresponds to a subset of the larger database, while the bottom row is the same subset, but with the refits. No second row entry means there are insufficient points for a stable fit (MacBeth, 2004).

OUTCROP SANDSTONES - GEOLOGY	Φ(%) (ΦMIN– ΦMAX)	Sκ	Sμ	Sη	Pκ MPa	Pμ MPa	κinf GPa	μinf GPa
Unconsolidated Lochaline[1,2]	18.0 (17-19)	0.57	0.59	+0.02	6.14	7.75	13.89	16.85
Molasse[1]	25.9 (26-26)	0.66	0.57	-0.08	10.01	13.23	14.20	12.35
Disaggregated Lochaline[1,2]	37.1 (36-38)	0.79	0.75	-0.07	14.85	15.20	3.05	2.70
Berea [1,3,4]	17.8 (16-22)	0.38	0.38	+0.05	11.91	8.16	18.27	17.43
Clashach[1]	17.0 (17-17)	0.24	0.22	-0.01	9.22	10.75	22.77	23.03
Navajo[3]	16.4 (16-16)	0.39	0.33	-0.04	22.31	18.20	18.76	17.28
Cemented Lochaline[1,2]	5.0 (5-5)	0.07	0.39	+0.17	4.49	6.94	36.79	31.68
Boise[3]	25.0 (25-25)	0.22	0.19	-0.01	27.45	15.17	12.72	9.07

RECOVERED RESERVOIR ROCKS - GEOLOGY/ FORMATION (FIELD)	Φ(%) (ΦMIN– ΦMAX)	Sκ	Sμ	Sη	Pκ MPa	Pμ MPa	κinf GPa	μinf GPa
Forties[8] (Nelson), Facies A	25.4 (24-26)	0.65 *0.57*	0.67 *0.41*	+0.04 *-0.12*	7.12 *23.99*	6.78 *13.89*	9.15 *10.71*	7.75 *7.98*
Paleocene (West of Shetlands)[11]	27.1 (17-36)	0.50 *0.53* *0.46*	0.55 *0.52* *0.41*	+0.03 *-0.06* *-0.05*	6.32 *5.62* *44.62*	7.23 *7.97* *22.37*	9.94 *12.85* *14.34*	7.75 *11.06* *11.80*
Miocene, (Gulf Coast)[9]	21.7 (22-22)	0.75 *0.57*	0.53 *0.55*	-0.29 *-0.02*	9.55 *17.63*	23.24 *19.42*	12.40 *13.12*	14.30 *13.90*
Rotliegend (southern North Sea)[7], Facies A	23.6 (20-28)	0.64 ---	0.57 ---	-0.05 ---	9.82 ---	13.54 ---	12.41 ---	10.99 ---
Rotliegend (southern North Sea)[7], Facies B	15.8 (11-19)	0.60 *0.62*	0.55 *0.42*	-0.03 *-0.08*	9.99 *15.75*	11.61 *56.47*	20.50 *22.39*	14.03 *17.48*
Forties[8] (Nelson), Facies B	13.0 (13-13)	0.58 *0.59*	0.50 *0.61*	-0.05 *0.01*	9.93 *9.89*	13.05 *9.56*	29.86 *29.88*	19.33 *19.02*
Cooper Basin[5], Facies A	13.2 (11-17)	0.61 *0.61*	0.63 *0.64*	-0.00 *0.01*	15.08 *15.00*	11.53 *11.30*	18.63 *18.43*	18.44 *18.26*
Rotliegend (southern North Sea)[7], Facies C	10.9 (8-11)	0.56 *0.56*	0.61 *0.46*	0.03 *-0.02*	22.12 *22.75*	10.98 *16.47*	15.93 *19.88*	11.45 *14.30*
Rotliegend (Germany)[6], Facies A	9.5 (6-15)	0.69 *0.66*	0.43 *0.54*	-0.23 *-0.07*	24.28 *124.71*	36.00 *105.57*	24.83 *24.97*	23.19 *15.81*
Cooper Basin[5], Facies B	5.5 (4-10)	0.41 *0.42*	0.45 *0.45*	+0.01 *0.01*	17.74 *17.72*	17.67 *17.62*	26.76 *26.24*	27.29 *24.71*
Rotliegend (Germany)[6], Facies B	3.4 (1-5)	0.66 *0.41*	0.41 *0.24*	-0.22 *-0.10*	29.02 *67.48*	37.56 *97.97*	34.40 *35.65*	29.77 *30.98*
North Sea[10]	7.4 (5-10)	0.59 --	0.40 --	-0.16 --	25.33 --	27.45 --	22.93 --	23.60 --

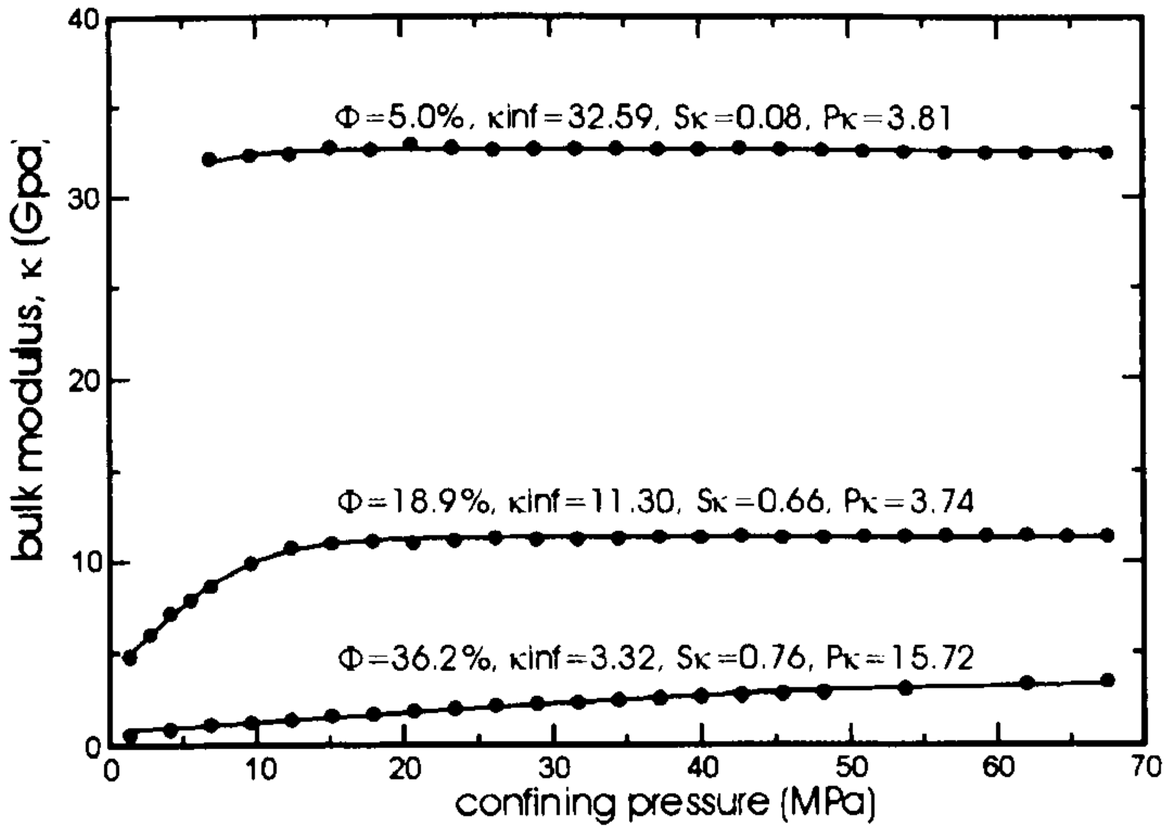

Figure 3.3: An example of the pressure dependence for different physical states of the same outcrop rock. The Lochaline is a Cretaceous shallow-marine sandstone. It is very well sorted, with almost a single grain size, and it is exceptionally clean (99.6% silica). The samples here represent three conditions: well-cemented, extracted from hard lenses of rock containing post-depositional silica cement (5% porosity); unconsolidated – common in most of the outcrop (18.9% porosity); and manually disaggregated, and then reassembled to provide a sand pack (36.2% porosity). The stress-sensitivity parameters follow predictable trends from the stronger to the less-consolidated material (MacBeth, 2004).

The application of differential stress leads to opening or closing of discontinuities in the sandstone, resulting in anisotropy. Given the elastic compliance tensor S_{ijkl}, the anisotropy can be written in the form (as in Sayers and Kachanov, 1991, 1995 – Appendix 3):

$$S_{ijkl} = S^0_{ijkl} + \Delta S_{ijkl} \tag{3.7}$$

where S_{ijkl}^{0} is the background compliance and ΔS_{ijkl} is the excess compliance of the rock.

As mentioned, the weaknesses in the rock are collectively evaluated by a single set of pressure-dependent normal and tangential bulk compliances $Z_N(P)$ and $Z_T(P)$ given above, which lead to the following expression for bulk and shear moduli; Equations (3.1) and (3.2) are inputted in order to compute the background compliances of the rock. Here, I will define an exponential dependence for these compliances in the form of following empirical relations:

$$Z_N(P) = ae^{-P/P\kappa} \tag{3.8}$$

and

$$Z_T(P) = a'e^{-P/P\kappa} + b'e^{-P/P_\mu} \tag{3.9}$$

where a, a' and b' are combinations of stress-sensitivity parameters determined by fitting Equations (3.1) and (3.2) to the measured laboratory data. Therefore the other Lamé parameter, λ, is computed from the bulk and shear moduli as a function of pressure:

$$\lambda(P) = \kappa(P) - 2\mu(P)/3 \tag{3.10}$$

The rock background compliances can be obtained as follows:

$$S_{11}^0 = S_{22}^0 = S_{33}^0 = \frac{\lambda + \mu}{\mu(3\lambda + 2\mu)} \tag{3.11}$$

$$S_{12}^0 = S_{13}^0 = S_{23}^0 = -\frac{\lambda}{2\mu(3\lambda + 2\mu)} \tag{3.12}$$

and

$$S_{44}^0 = S_{55}^0 = S_{66}^0 = \frac{1}{\mu} \tag{3.13}$$

Now the recipe of Mavko *et al.* (1995) is used to calculate the excess compliances of the rock (ΔS_{ijkl}). Their methodology for calculating the excess compliances of the rock is relatively independent on any assumed crack geometry and without any limitations to low crack density. This requires the excess compliance $\Delta S_{ijkl}(\sigma_0, \sigma_U)$ to be inputted into their formulae for each particular loading combination of σ_0 and σ_U. The numerical calculation of $\Delta S_{ijkl}(\sigma_0, \sigma_U)$ is performed using knowledge of the response of the excess normal and tangential compliances to isotropic loading.

$$\Delta S_{33} = 2\pi \int_0^{\frac{\pi}{2}} [Z_N(\sigma_U + \sigma_0) - 4Z_T(\sigma_U + \sigma_0)] \cos^4\theta \sin\theta d\theta$$

$$+2\pi \int_0^{\frac{\pi}{2}} 4Z_T(\sigma_U + \sigma_0) \cos^2\theta \sin\theta d\theta$$

$$\Delta S_{11} = 2\pi \int_0^{\frac{\pi}{2}} \frac{3}{8} [Z_N(\sigma_U + \sigma_0) - 4Z_T(\sigma_U + \sigma_0)] \sin^4\theta \sin\theta d\theta$$

$$+2\pi \int_0^{\frac{\pi}{2}} 2Z_T(\sigma_U + \sigma_0) \sin^2\theta \sin\theta d\theta$$

$$\Delta S_{13} = 2\pi \int_0^{\frac{\pi}{2}} \frac{1}{2} [Z_N(\sigma_U + \sigma_0) - 4Z_T(\sigma_U + \sigma_0)] \sin^2\theta \cos^2\theta \sin\theta d\theta$$

$$\Delta S_{44} = 2\pi \int_0^{\frac{\pi}{2}} \frac{1}{2} [Z_N(\sigma_U + \sigma_0) - 4Z_T(\sigma_U + \sigma_0)] \sin^2\theta \cos^2\theta \sin\theta d\theta$$

$$+2\pi \int_0^{\frac{\pi}{2}} \frac{1}{2} Z_T(\sigma_U + \sigma_0) \sin^2\theta \sin\theta d\theta + 2\pi \int_0^{\frac{\pi}{2}} Z_T(\sigma_U + \sigma_0) \cos^2\theta \sin\theta d\theta$$

$$\Delta S_{66} = 2\pi \int_0^{\frac{\pi}{2}} \frac{1}{8} [Z_N(\sigma_U + \sigma_0) - 4Z_T(\sigma_U + \sigma_0)] \sin^4\theta \sin\theta d\theta$$

$$+2\pi \int_0^{\frac{\pi}{2}} Z_T(\sigma_U + \sigma_0) \sin^2\theta \sin\theta d\theta \qquad (3.14)$$

where θ is the angle between direction of wave propagation and the applied stress.

Hence the five independent elements ΔS_{11}, ΔS_{33}, ΔS_{13}, ΔS_{44} and ΔS_{66} are determined. Now, using Equation (3.7), the total compliance of the rock can be found. The total compliance of the rock can be illustrated by the following matrix:

$$S_{IJ} = \begin{bmatrix} S_{11} & S_{12} & S_{13} & 0 & 0 & 0 \\ S_{12} & S_{11} & S_{13} & 0 & 0 & 0 \\ S_{13} & S_{13} & S_{33} & 0 & 0 & 0 \\ 0 & 0 & 0 & S_{44} & 0 & 0 \\ 0 & 0 & 0 & 0 & S_{44} & 0 \\ 0 & 0 & 0 & 0 & 0 & S_{66} \end{bmatrix} \qquad (3.15)$$

The stiffness matrix is then recovered by inverting the compliance matrix:

$$C_{IJ} = \begin{bmatrix} \frac{\begin{vmatrix} S_{22} & S_{23} \\ S_{32} & S_{33} \end{vmatrix}}{|D|} & -\frac{\begin{vmatrix} S_{21} & S_{23} \\ S_{31} & S_{33} \end{vmatrix}}{|D|} & \frac{\begin{vmatrix} S_{21} & S_{22} \\ S_{31} & S_{32} \end{vmatrix}}{|D|} & 0 & 0 & 0 \\ -\frac{\begin{vmatrix} S_{12} & S_{13} \\ S_{32} & S_{33} \end{vmatrix}}{|D|} & \frac{\begin{vmatrix} S_{11} & S_{13} \\ S_{31} & S_{33} \end{vmatrix}}{|D|} & -\frac{\begin{vmatrix} S_{11} & S_{12} \\ S_{31} & S_{32} \end{vmatrix}}{|D|} & 0 & 0 & 0 \\ \frac{\begin{vmatrix} S_{12} & S_{13} \\ S_{22} & S_{23} \end{vmatrix}}{|D|} & -\frac{\begin{vmatrix} S_{11} & S_{13} \\ S_{21} & S_{23} \end{vmatrix}}{|D|} & \frac{\begin{vmatrix} S_{11} & S_{12} \\ S_{21} & S_{22} \end{vmatrix}}{|D|} & 0 & 0 & 0 \\ 0 & 0 & 0 & \frac{1}{S_{44}} & 0 & 0 \\ 0 & 0 & 0 & 0 & \frac{1}{S_{44}} & 0 \\ 0 & 0 & 0 & 0 & 0 & \frac{1}{S_{66}} \end{bmatrix} \tag{3.16}$$

where:

$$D = S_{11}(S_{22}S_{33} - S_{32}S_{23}) - S_{12}(S_{21}S_{33} - S_{31}S_{23}) + S_{13}(S_{21}S_{32} - S_{31}S_{22}) \tag{3.17}$$

After finding $C^{Dry}{}_{ijkl}$ the resultant HTI anisotropy is parameterized in the usual way with the Tsvankin (1997) Thomsen-like parameters (Equations 2.3, 2.4 and 2.5) and Rüger (1998) (Equations 2.7, 2.8 and 2.9).

Palaeocene sandstones from the Nelson Field of the North Sea and the Rotliegend Formation of the Southern Gas Basin are chosen for computing stress-induced anisotropy (MacBeth, 2004). The pressure-dependent anisotropy parameters of the dry-frame Nelson sandstone and Rotliegend sandstone are shown in Figure 3.4. Dry-frame stress-sensitive Palaeocene sandstone exhibits a medium to large velocity anisotropy, with maximum absolute values of ε = 7%, δ = 16% and γ = 7%. Highly compressible (0.10 GPa^{-1}) and porous (25%) Nelson sand complies fairly easily with the applied stress. The response of the tight, consolidated and less porous (10%) Permian Southern Gas Basin Rotliegend sand is less stress-sensitive when subjected to an identical range of excess uniaxial stress due to its lack of compressibility (0.05 GPa^{-1}), and hence it generates a lower anisotropy. In the Rotliegend case, the maximum absolute values of stress-induced anisotropy are ε = 1%, δ = 2% and γ = 3%. The relatively larger magnitude of δ compared to ε may be interpreted as being due to the assumption that the maximum horizontal stress is the prevailing stress. Such an effect seems to be cancelled

out in γ, due to subtraction of one shear element of stiffness from the other ($C_{66} - C_{55}$), leading to a small range of variation.

In Chapter 2 it was shown that Ball and Batzle (1994) investigated the stress dependence of compressional- and shear-wave velocity (V_P and V_S) on constant lithostatic stress states and various confining pressures in several sandstones with a range of porosities, and that they found different results. As a test of our theoretical predictions, a comparison is made with the results of Ball and Batzle's (1994) study. For the purposes of this study, the predictions made using the Nelson sandstone parameters are chosen as the closest to the Berea sandstones used in their study. Figure 3.5 shows variations of V_P and V_S for Nelson sandstone with excess uniaxial stress. Both V_P and V_S increase with vertical stress and excess uniaxial stress in the direction of maximum horizontal stress.

Ball and Batzle's (1994) results for Berea sandstone (Figure 2.13) show a nearly horizontal trend of increase with confining pressure, especially at large vertical stresses. V_P increases with vertical axial stress and, at the same time, decreases to a smaller extent with the lateral stress (minimum horizontal stress). However, at higher axial stress (above 30 MPa) the velocity increases with both axial and lateral stresses. With a slight difference, V_S displays a monotonous increase with axial and lateral stresses.

Nelson sandstone (Figure 3.5) subjected to a varying uniaxial stress due to maximum horizontal stress at a constant axial vertical stress, exhibits increasing velocity. The trend is close to linear at 30 MPa vertical stress, but at the rest of the constant vertical stress levels, it is exponentially increasing, in contrast to the almost flat case of the Berea sandstone (Figure 2.13). About the maximum excess uniaxial stress, both compressional- and shear-waves velocities are converging for all vertical stress levels. This might derive from the fact that maximum horizontal stress obviously has the largest impact on the velocities measured along the direction of stress application.

In Figure 3.5 the trend of velocity variations of the Nelson sandstone is more or less similar to that of Berea sandstone (Figure 2.13). For the Nelson sand, the results for dependence on pressure are in agreement with those of the Berea sandstone, in spite of the fact that these studies have been conducted under various stress settings. Ball and Batzle (1994) conducted their measurements at a range of confining pressures and at constant levels of vertical stress all corresponding to the reservoir-specific stress states, depth, density, *etc.*, and the Nelson sandstone is studied under varying maximum

horizontal stress at constant vertical stresses related to realistic reservoir stress conditions, depth and other rock properties.

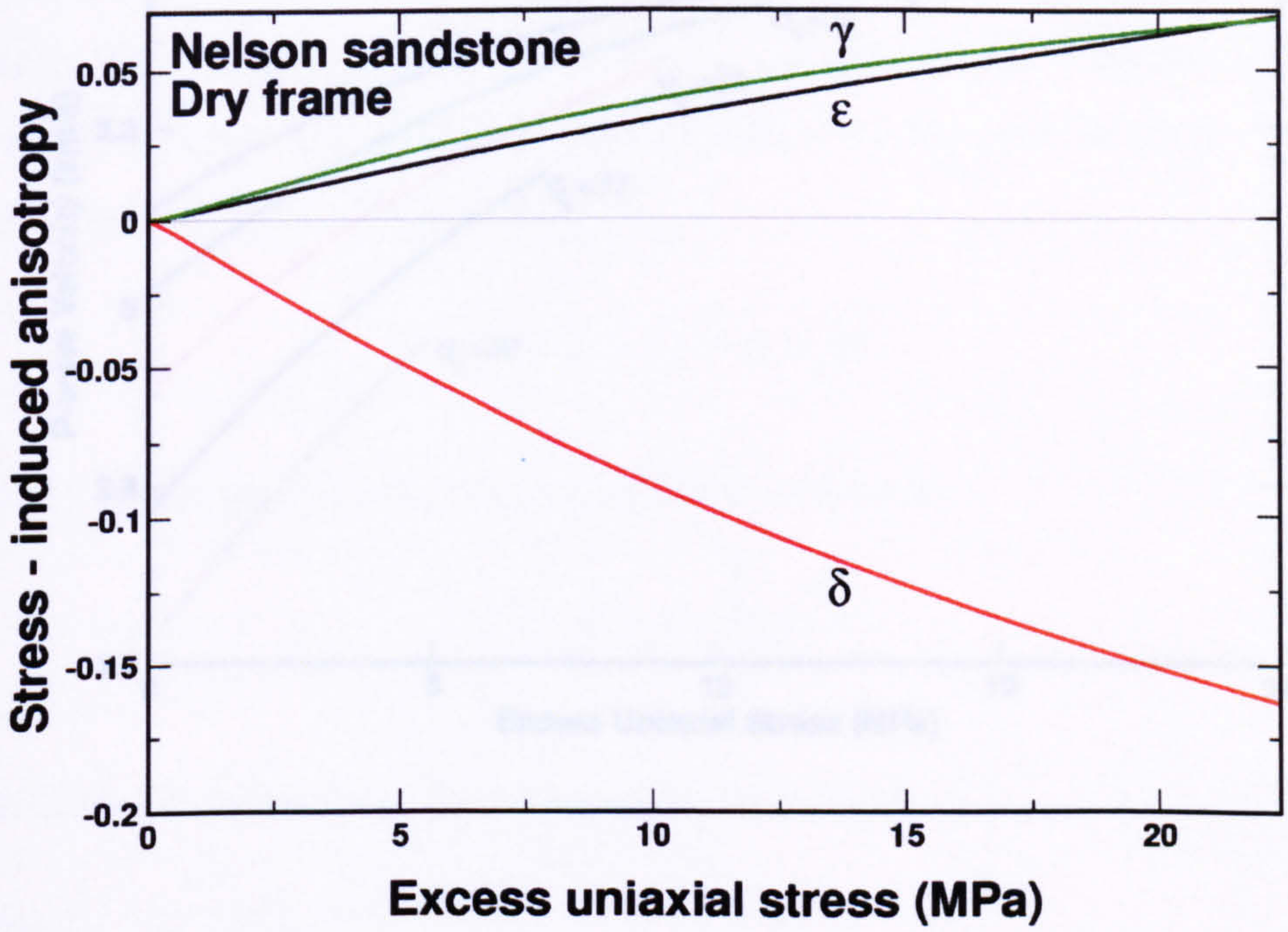

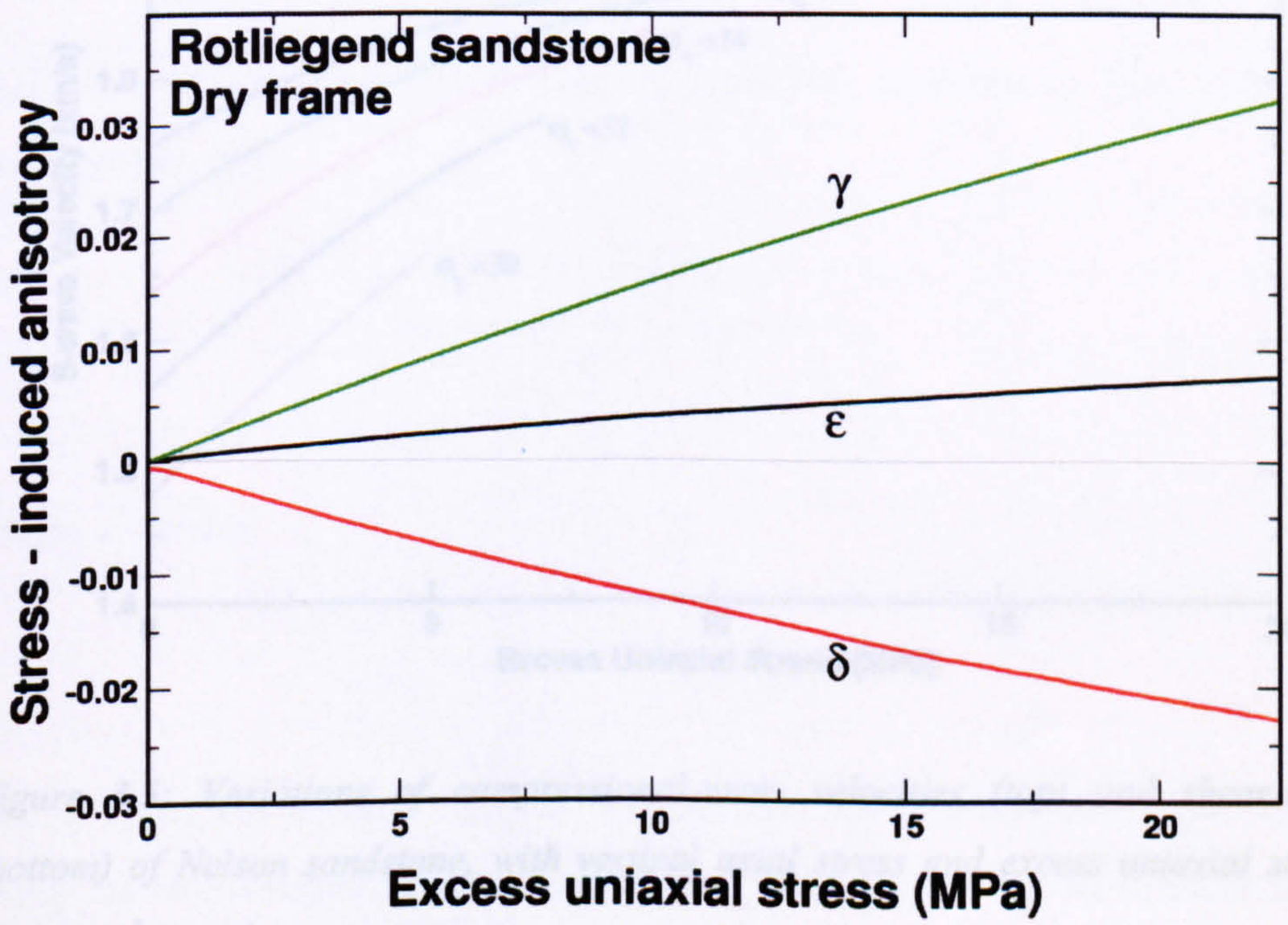

Figure 3.4: Dry-frame stress-induced anisotropy (ε, δ and γ) in Nelson sandstone (top), and Rotliegend sandstone (bottom).

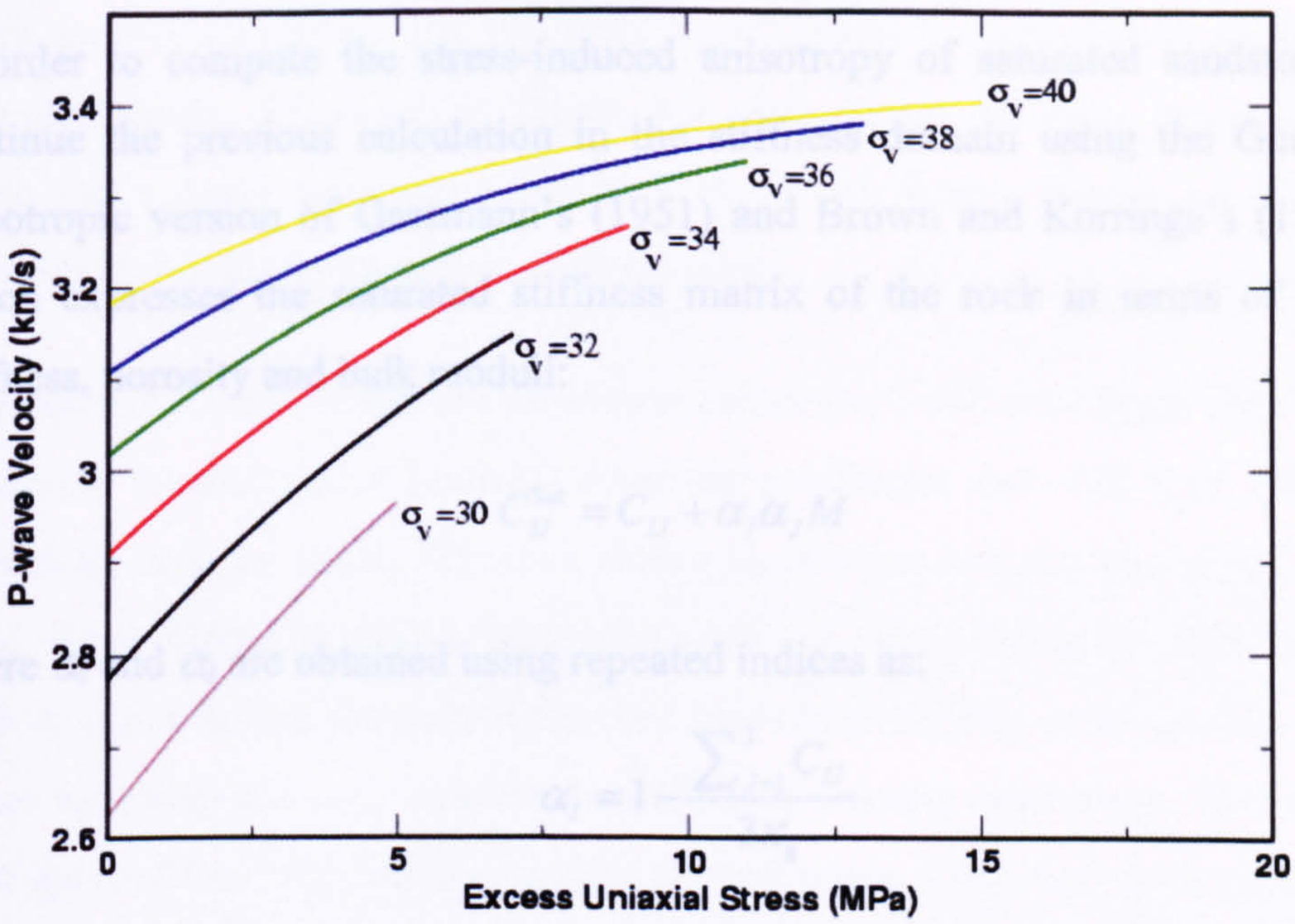

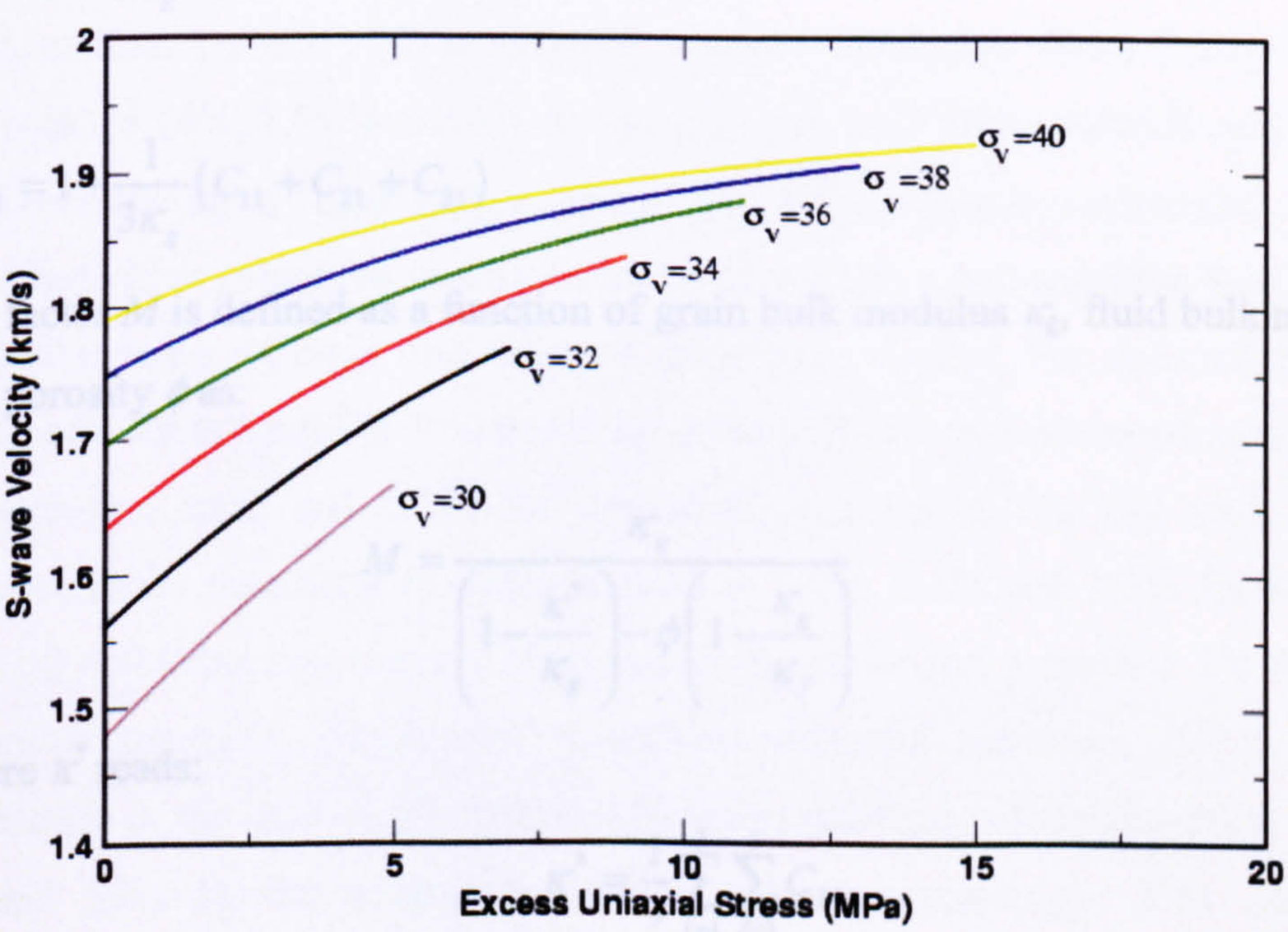

Figure 3.5: Variations of compressional-wave velocities (top) and shear-wave velocities (bottom) of Nelson sandstone, with vertical axial stress and excess uniaxial stress (maximum horizontal stress).

3.3 The Effect of Saturation

In order to compute the stress-induced anisotropy of saturated sandstones, one can continue the previous calculation in the stiffness domain using the Gurevich (2002) anisotropic version of Gassmann's (1951) and Brown and Korringa's (1975) relation, which expresses the saturated stiffness matrix of the rock in terms of its dry-frame stiffness, porosity and bulk moduli:

$$C_{IJ}^{\text{Sat}} = C_{IJ} + \alpha_I \alpha_J M \tag{3.18}$$

where α_I and α_J are obtained using repeated indices as:

$$\alpha_I = 1 - \frac{\sum_{J=1}^{3} C_{IJ}}{3\kappa_g} \tag{3.19}$$

for example, when $I = 1$, α_I and α_J are in the form of:

$$\alpha_{I=1} = 1 - \frac{1}{3\kappa_g}(C_{11} + C_{12} + C_{13})$$

and

$$\alpha_{J=1} = 1 - \frac{1}{3\kappa_g}(C_{11} + C_{21} + C_{31})$$

and factor M is defined as a function of grain bulk modulus κ_g, fluid bulk modulus κ_f, κ^* and porosity ϕ as:

$$M = \frac{\kappa_g}{\left(1 - \frac{\kappa^*}{\kappa_g}\right) - \phi\left(1 - \frac{\kappa_g}{\kappa_f}\right)} \tag{3.20}$$

where κ^* reads:

$$\kappa^* = \frac{1}{9}\sum_{I=1}^{3}\sum_{J=1}^{3} C_{IJ} \tag{3.21}$$

So, by using the values in Tables 3.1 and 3.2, the effect of saturation can be computed using the stress-sensitive saturated stiffness elements of the sandstones in this study. A workflow for computing stress-induced anisotropy parameters of fluid-saturated sands is shown in Figure 3.6. Figure 3.7 gives the results for the stress-induced anisotropy parameters of Nelson and Rotliegend sandstones when they are saturated with gas. The

utilized values for bulk moduli of gas, oil, brine and the mineral grain (quartz) are 0.15, 1.193, 2.7 and 37 GP respectively. The anisotropy parameters ε and δ are observed to decrease with saturation, but γ is unchanged due to its insensitivity to fluids. The oil-saturated results are shown in Figure 3.8; they depict the same increasing trend with stress and a lower anisotropy compared to the dry frame. Figure 3.9 also follows the same route, but for brine-saturated sandstones.

To understand what difference saturation can make, I will start again with the dry-frame sandstone located under realistic reservoir conditions and will then subject it to an increasing uniaxial stress. The rock shows an obvious velocity anisotropy increase with axial stress. Once the rock is saturated with gas, oil or brine, the increase in the fluid bulk modulus makes the rock stiffer and less compressible; consequently, under similar stress variations the rock exhibits less induced velocity anisotropy. This is because the void spaces filled with fluids resist the applied stress. The whole rock resists the applied stress in all directions and hence reduces the overall impact of the differential stress on the induced anisotropy. In the Nelson sandstone, the maximum value of ε decreases from 7% for the dry frame to 6% for gas saturation; however, in the oil-saturated case it changes from 2.5% to 1.5% when oil is replaced with brine. The δ change is 16% for the dry rock, to 14%, 7.5% and 5.5% for the gas-, oil- and brine-saturated cases respectively. The corresponding value of γ is about 7%, which remains unchanged – as might be expected. Such variations in anisotropy occur for less stress-sensitive Rotliegend sand at a smaller scale – nearly one order of magnitude weaker. For instance, the maximum value of ε for dry sand is 1%, which drops to 0.5% for gas-saturated rock; 0.2% for the oil-saturated case; and 0.1% for saturation with brine. The dry rock produces 2% anisotropy for parameter δ, which shrinks to 1.5%, 0.5% and 0.3% for saturation with gas, oil and brine respectively. The anisotropy parameter γ reaches 3% for all dry and saturated cases. In conclusion, it appears that the saturation effect is significant especially in the case of oil-saturated Nelson sandstone, which illustrates a decrease of around 50% in the magnitude of the velocity anisotropy. This emphasizes the importance of this effect in studies where reservoir changes in pressure and saturation are occurring.

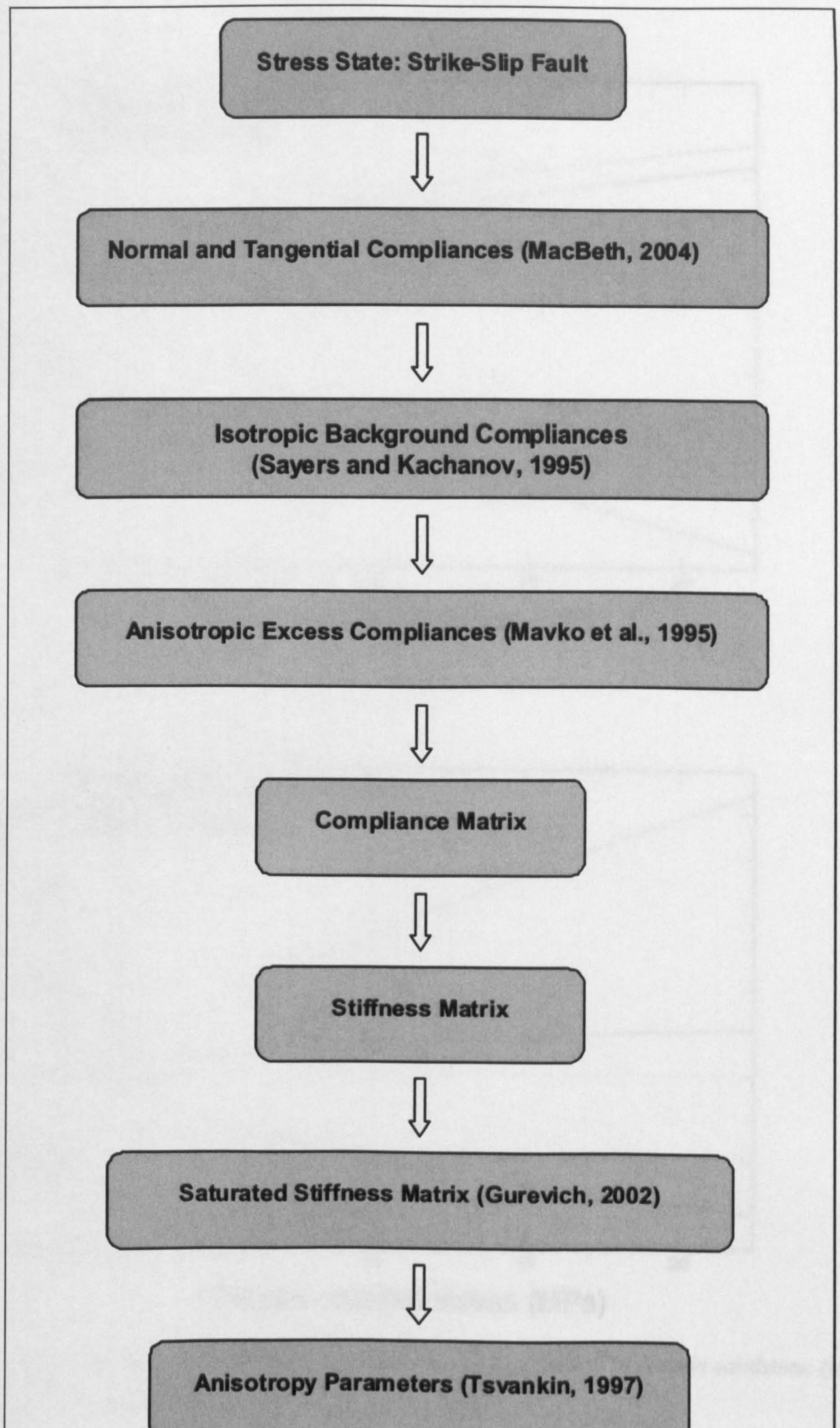

Figure 3.6: Workflow to involve the effect of fluid saturation on stress-induced anisotropy.

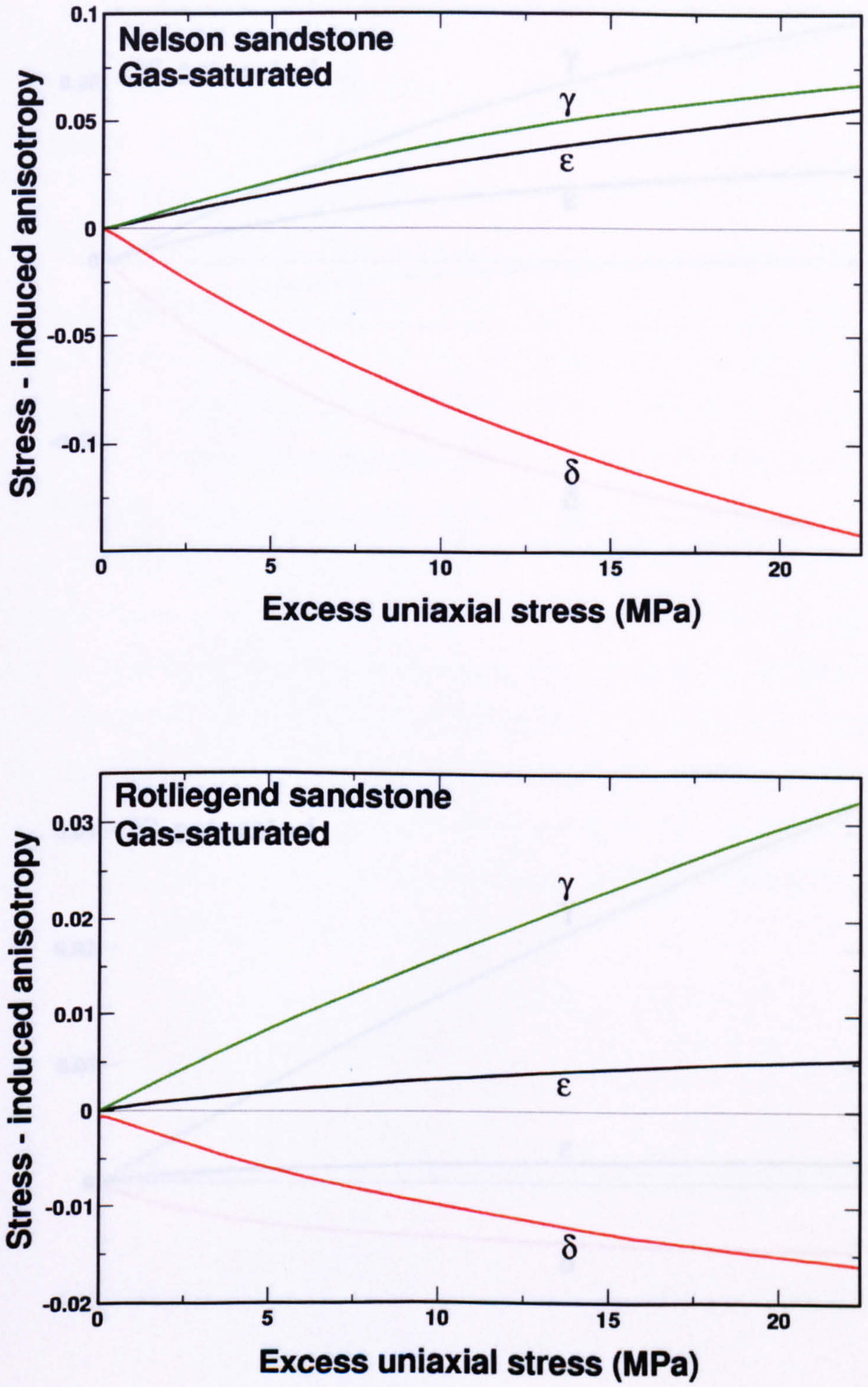

Figure 3.7: Gas-saturated: stress-induced anisotropy (ε, δ and γ) in Nelson sandstone (top) and Rotliegend sandstone (bottom).

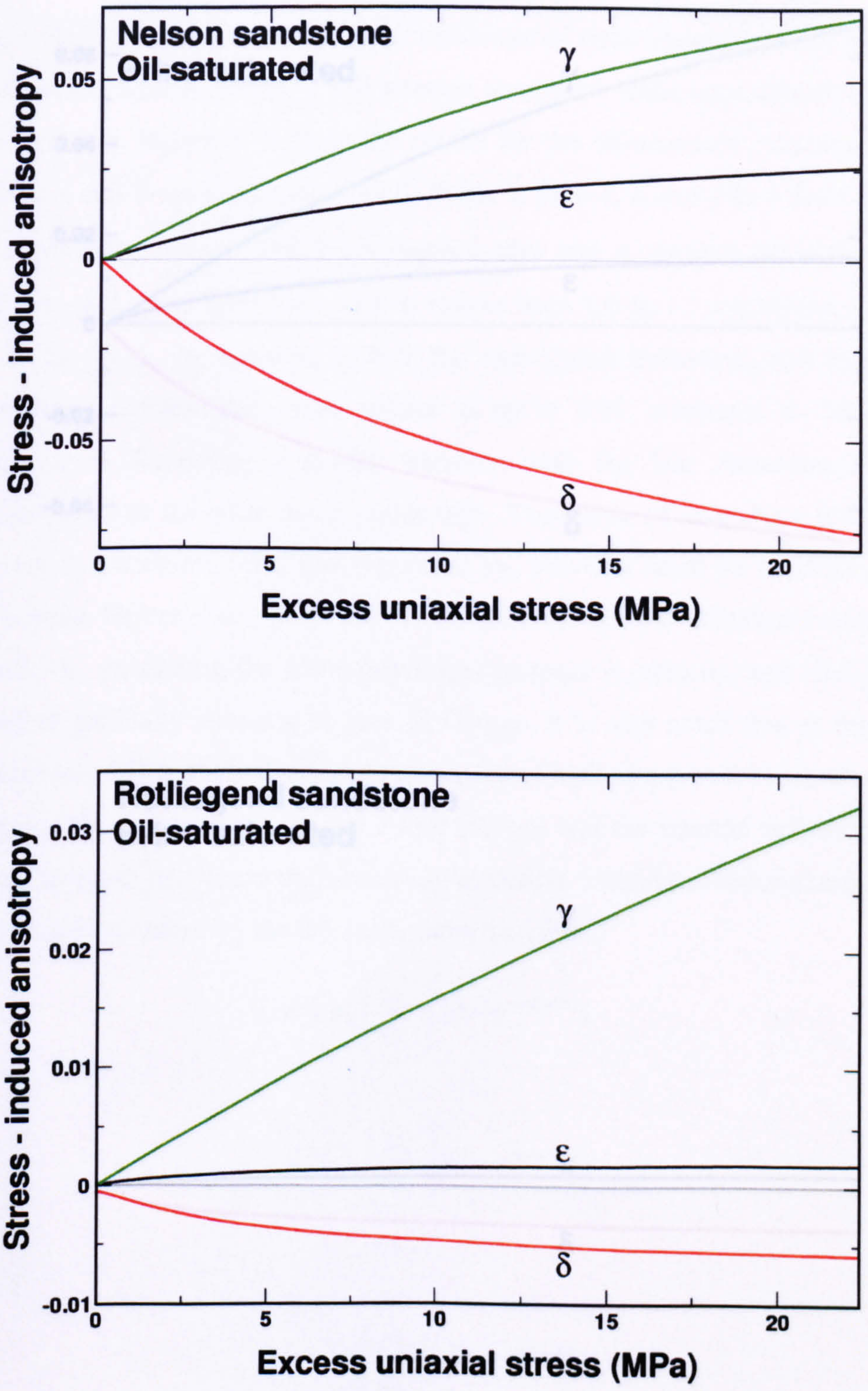

Figure 3.8: Oil-saturated: stress-induced anisotropy (ε, δ and γ) in Nelson sandstone (top) and Rotliegend sandstone (bottom).

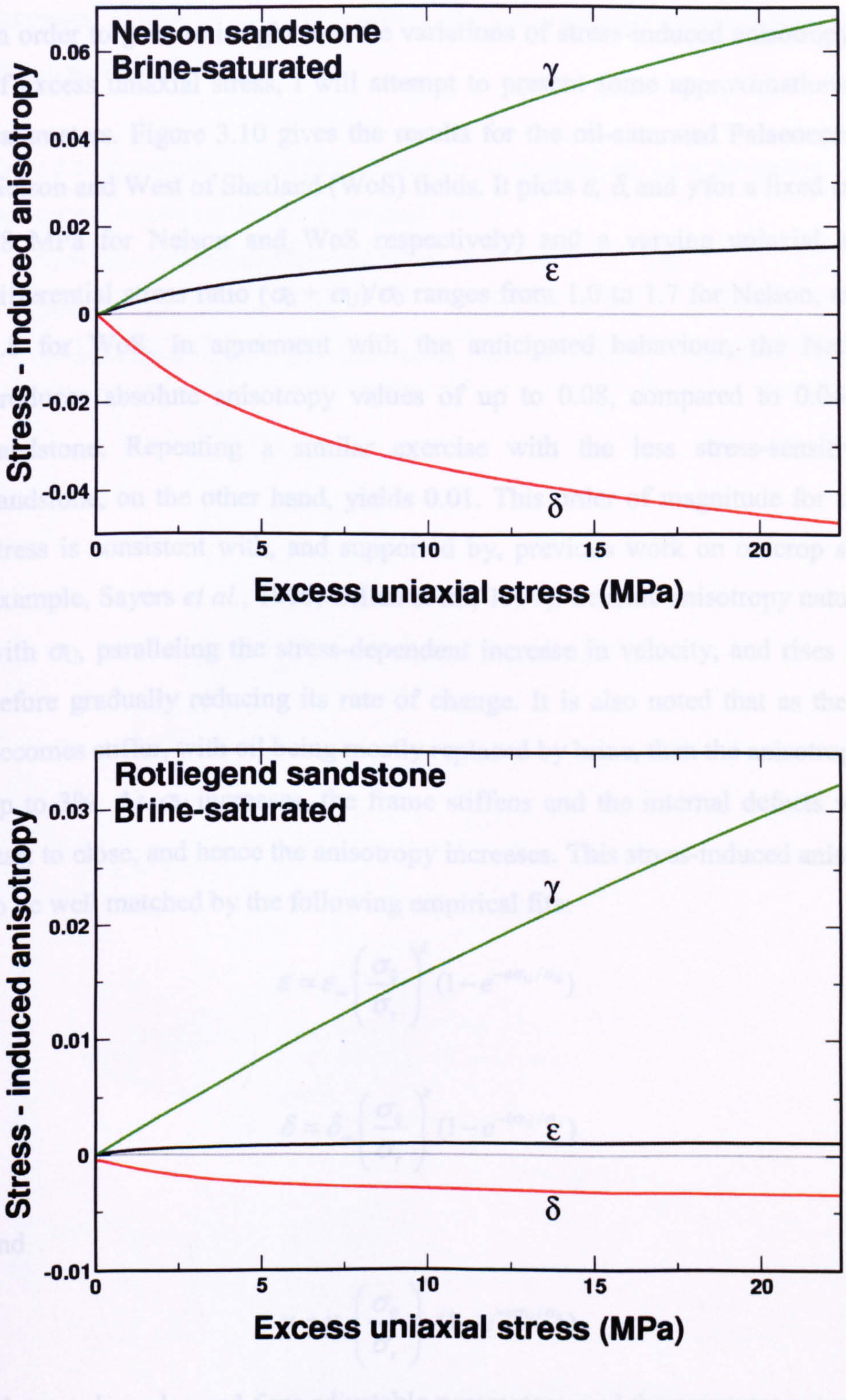

Figure 3.9: Brine-saturated: stress-induced anisotropy (ε, δ and γ) in Nelson sandstone (top) and Rotliegend sandstone (bottom).

3.4 Stress-Induced Anisotropy Approximations

In order to gain an insight into the variations of stress-induced anisotropy as a function of excess uniaxial stress, I will attempt to present some approximations to anisotropy parameters. Figure 3.10 gives the results for the oil-saturated Palaeocene sands of the Nelson and West of Shetland (WoS) fields. It plots ε, δ, and γ for a fixed σ_0 (33 MPa and 28 MPa for Nelson and WoS respectively) and a varying uniaxial stress σ_U. The differential stress ratio $(\sigma_0 + \sigma_U)/\sigma_0$ ranges from 1.0 to 1.7 for Nelson, and from 1.0 to 1.8 for WoS. In agreement with the anticipated behaviour, the Nelson sandstone produces absolute anisotropy values of up to 0.08, compared to 0.04 for the WoS sandstone. Repeating a similar exercise with the less stress-sensitive Rotliegend sandstone, on the other hand, yields 0.01. This order of magnitude for the response to stress is consistent with, and supported by, previous work on outcrop sandstones (for example, Sayers *et al.*, 1990; Dillen *et al.*, 1999). Seismic anisotropy naturally increases with σ_U, paralleling the stress-dependent increase in velocity, and rises steeply at first before gradually reducing its rate of change. It is also noted that as the fluid saturant becomes stiffer, with oil being mostly replaced by brine, then the anisotropy also falls by up to 3%. As σ_U increases, the frame stiffens and the internal defects within the rock start to close, and hence the anisotropy increases. This stress-induced anisotropy appears to be well matched by the following empirical fits:

$$\varepsilon = \varepsilon_\infty \left(\frac{\sigma_0}{\sigma_r} \right)^d (1 - e^{-a\sigma_U/\sigma_0}) \tag{3.22}$$

$$\delta = \delta_\infty \left(\frac{\sigma_0}{\sigma_r} \right)^e (1 - e^{-b\sigma_U/\sigma_0}) \tag{3.23}$$

and

$$\gamma = \gamma_\infty \left(\frac{\sigma_0}{\sigma_r} \right)^f (1 - e^{-c\sigma_U/\sigma_0}) \tag{3.24}$$

where *a*, *b*, *c*, *d*, *e* and *f* are adjustable parameters, and the asymptotes are the maximum attainable anisotropy at some reference isotropic loading σ_r. As can be seen from the similarity of the obtained relations, one may summarize them in a more contracted form such as $\mathrm{SIA}(\sigma_U) = a(b - \exp(-c\sigma_U))$, which expresses the anisotropy induced by excess uniaxial stress as an exponential function of the applied stress. The relation is useful

because it can provide a quick and direct understanding of stress-induced anisotropy varying with excess uniaxial stress. For example, for anisotropy parameter ε when expressed as $\varepsilon(\sigma_U) = a(b - \exp(-c\sigma_U))$, the approximation coefficients can be derived as shown in Table 3.3.

Table 3.3: Approximation coefficients derived from fitting anisotrpy parameter ε to the proposed exponential function of the excess uniaxial stress.

Approximation coefficients for *ε*	***a***	***b***	***c***
Oil-saturated Nelson sand	0.029175768	1.0126075	0.088475853
Oil-saturated West of Shetland sand	0.014231627	1.0308167	0.11237459

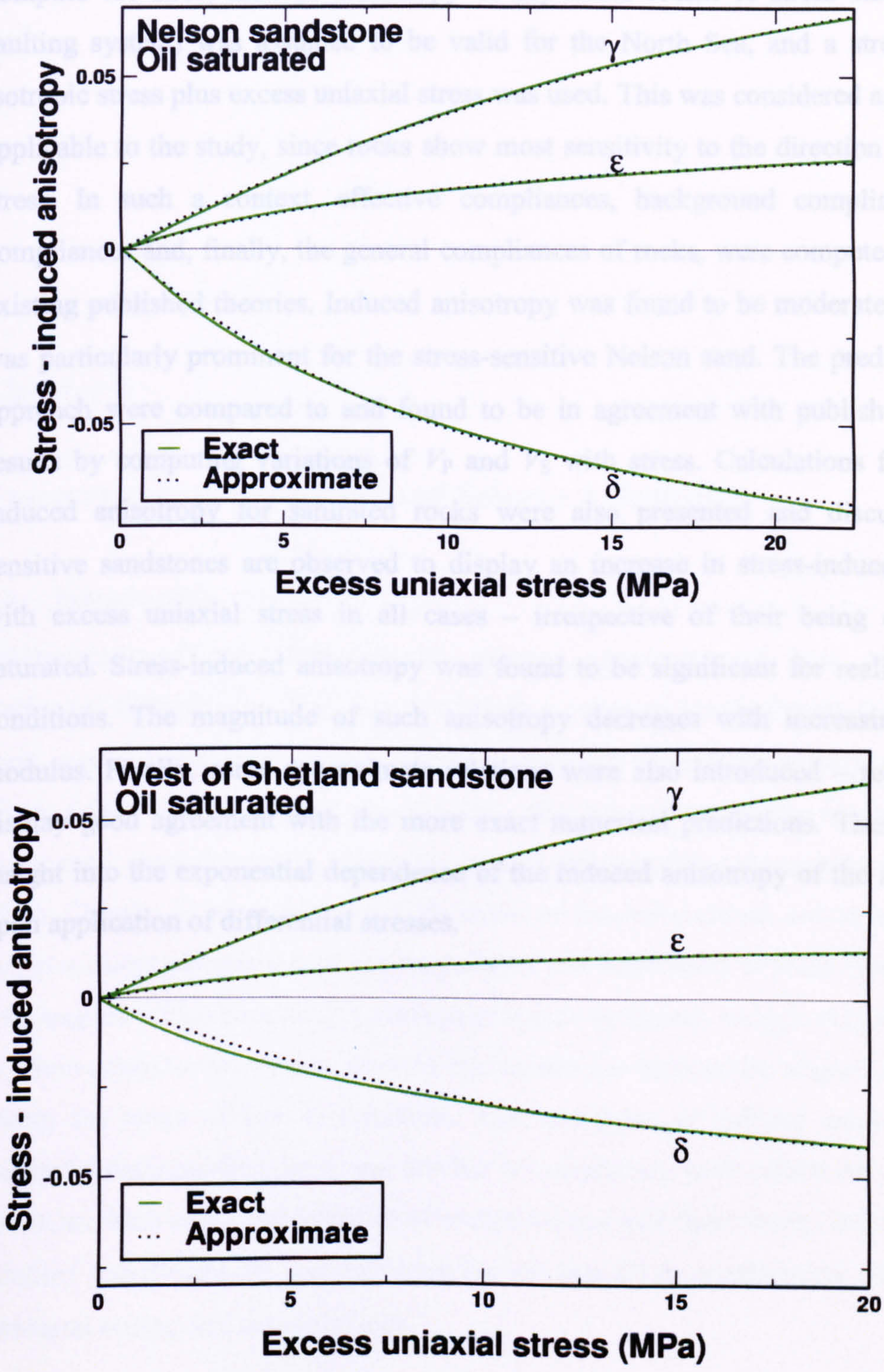

Figure 3.10: Exact compared to approximate anisotropy parameters (ε, δ and γ) in oil-saturated cases of Nelson sandstone (top) and West of Shetland sandstone (bottom).

3.5 Summary

As the first step in my study of stress-induced anisotropy, I presented a workflow to compute the stress-induced anisotropy of dry-frame rocks. A stress state (strike-slip faulting system) was assumed to be valid for the North Sea, and a stress setting of isotropic stress plus excess uniaxial stress was used. This was considered as realistic and applicable to the study, since rocks show most sensitivity to the direction of prevailing stress. In such a context, effective compliances, background compliances, excess compliances and, finally, the general compliances of rocks, were computed by utilizing existing published theories. Induced anisotropy was found to be moderate to large, and was particularly prominent for the stress-sensitive Nelson sand. The predictions of my approach were compared to and found to be in agreement with published laboratory results by computing variations of V_P and V_S with stress. Calculations for the stress-induced anisotropy for saturated rocks were also presented and discussed. Stress-sensitive sandstones are observed to display an increase in stress-induced anisotropy with excess uniaxial stress in all cases – irrespective of their being dry frame or saturated. Stress-induced anisotropy was found to be significant for realistic reservoir conditions. The magnitude of such anisotropy decreases with increasing fluid bulk modulus. Finally, some approximate relations were also introduced – relations which display good agreement with the more exact numerical predictions. These provide an insight into the exponential dependence of the induced anisotropy of the saturated rock upon application of differential stresses.

Chapter 4

Fracture versus Stress-Induced Seismic Anisotropy

4.1 Introduction

Fracture-induced and stress-induced seismic anisotropy are here compared and contrasted theoretically. This then leads into a series of practical tests that help to tell them apart. A summary of the current knowledge of fracture-induced anisotropy is given, followed by a section on modelling this induced anisotropy in the Nelson and Rotliegend sand reservoirs. Then the results of modelling stress-induced anisotropy (from Chapter 3) are compared with those of fracture-induced anisotropy. This step includes direct comparison of the magnitudes and behaviours of these types of induced anisotropies, which reveals that stress may induce moderate- to high-velocity anisotropy in stress-sensitive reservoirs, whereas the anisotropy induced by aligned fractures falls within the range of low to moderate. The two types of induced anisotropy can be indirectly distinguished from one another by comparing their effects on some seismic attributes, such as the reflectivities of compressional and shear waves; and P-wave AVO gradient (coefficient B) and curvature (coefficient C) in combination with the fields' structural setting and stress regimes.

4.2 Fracture-Induced Anisotropy (FIA)

A set of aligned vertical fractures is assumed to be inserted in an otherwise isotropic rock mass, comprising an HTI medium – a medium with transverse isotropy with a

horizontal axis of symmetry, causing azimuthal anisotropy. The first-order approximation of Hudson's model also represents anisotropy values in terms of some geometrical aspects of fractures (cracks) (as in Li, 1998). The parameters of fracture-induced anisotropy read:

$$\varepsilon \approx 2e(1-\frac{V_S^2}{V_P^2})U_{33} \tag{4.1}$$

$$\delta \approx 2e(U_{33}-\frac{V_S^2}{V_P^2}U_{11}) \tag{4.2}$$

$$\gamma \approx \frac{1}{2}eU_{11} \tag{4.3}$$

where crack density is defined as a function of crack porosity and aspect ratio, as follows:

$$e=\frac{3\phi_c}{4\pi\alpha} \tag{4.4}$$

and the U_{11} and U_{33} functions can be defined in terms of seismic velocities of isotropic background and fluid velocity V_f:

$$U_{11}=\frac{16V_P^2}{3(3V_P^2-2V_S^2)} \tag{4.5}$$

for dry rock:

$$U_{33}=\frac{4V_P^2}{3(V_P^2-V_S^2)} \tag{4.6}$$

and for saturated rock:

$$U_{33}=\frac{4V_S^2}{3V_f^2}\pi\alpha \tag{4.7}$$

An alternative is Schoenberg-Muir's slip-interface theory, where the rock compliances can be written as the sum of background isotropic compliance and excess compliance, in terms of rock elastic properties as follows:

$$S=\begin{bmatrix} \frac{\lambda+\mu}{\mu(3\lambda+2\mu)}+Z_N^f & -\frac{\lambda}{2\mu(3\lambda+2\mu)} & -\frac{\lambda}{2\mu(3\lambda+2\mu)} & 0 & 0 & 0 \\ -\frac{\lambda}{2\mu(3\lambda+2\mu)} & \frac{\lambda+\mu}{\mu(3\lambda+2\mu)} & -\frac{\lambda}{2\mu(3\lambda+2\mu)} & 0 & 0 & 0 \\ -\frac{\lambda}{2\mu(3\lambda+2\mu)} & -\frac{\lambda}{2\mu(3\lambda+2\mu)} & \frac{\lambda+\mu}{\mu(3\lambda+2\mu)} & 0 & 0 & 0 \\ 0 & 0 & 0 & \frac{1}{\mu} & 0 & 0 \\ 0 & 0 & 0 & 0 & \frac{1}{\mu}+Z_T^f & 0 \\ 0 & 0 & 0 & 0 & 0 & \frac{1}{\mu}+Z_T^f \end{bmatrix} \tag{4.8}$$

As in Liu *et al.* (2001) and MacBeth (2004), the Thomsen's anisotropy parameters read:

$$\varepsilon=\frac{-2\eta_{Dry}(1-\eta_{Dry})}{\frac{1}{(\lambda+\mu)Z_N^f}+1} \tag{4.9}$$

$$\delta=-2\eta_{Dry}\left[\frac{1-2\eta_{Dry}}{\frac{1}{(\lambda+\mu)Z_N^f}+1}+\frac{1}{\frac{1}{\mu Z_T^f}+1}\right] \tag{4.10}$$

and

$$\gamma=-\frac{1}{2(\frac{1}{\mu Z_T^f}+1)} \tag{4.11}$$

where η_{Dry} is expressed in terms of V_P and V_S, which are matrix P- and S-wave velocities respectively:

$$\eta_{Dry}=\frac{V_S^2}{V_P^2} \tag{4.12}$$

To find these parameters for the realistic conditions of the reservoir rocks, following MacBeth (2002), alternatively, the elastic stiffness matrix of a fractured rock when saturated by fluids can be written in terms of two dimensionless scalar parameters e_N and e_T, representing measures of the overall crack compliance of the fractured rock as functions of the crack porosity and response factors b_N and b_T.

For a gas:

$$e_{\mathrm{N}} = \frac{\phi_c b_{\mathrm{N}}^{\mathrm{gas}}}{\eta_{\mathrm{N}} b_{\mathrm{N}}^{\mathrm{gas}} + 1 - \frac{3}{4} A_0^{3/2}} \tag{4.13}$$

and:

$$e_{\mathrm{T}} = \frac{\phi_c b_{\mathrm{T}}^{\mathrm{gas}}}{\eta_{\mathrm{T}} b_{\mathrm{T}}^{\mathrm{gas}} + 1 - \frac{3}{4} A_0^{3/2}} \tag{4.14}$$

Fractures can, for most practical purposes, be represented by the macroscopic fracture compliances $Z^{\mathrm{f}}_{\mathrm{N}}$ and $Z^{\mathrm{f}}_{\mathrm{T}}$ introduced by Schoenberg (1980). These differ from the bulk compliances, as they are defined as averages along a fracture plane. They are not considered to be stress-dependent in the current work, and can also be verified from the following relations:

$$e_{\mathrm{N}} = \frac{(\lambda + 2\mu) Z^{\mathrm{f}}_{\mathrm{N}}}{1 + (\lambda + 2\mu) Z^{\mathrm{f}}_{\mathrm{N}}} \tag{4.15}$$

and:

$$e_{\mathrm{T}} = \frac{\mu Z^{\mathrm{f}}_{\mathrm{T}}}{1 + \mu Z^{\mathrm{f}}_{\mathrm{T}}} \tag{4.16}$$

For the purposes of my work, I will use the Schoenberg approach and 'insert' the fractures into the Nelson and Rotliegend sandstones of the previous example, assuming weak anisotropy:

$$Z^{\mathrm{f}}_{\mathrm{N}} \cong \frac{\phi}{(\lambda + 2\mu)\pi\alpha\eta_{Sat}(1 - \eta_{Sat})} \tag{4.17}$$

and

$$Z^{\mathrm{f}}_{\mathrm{T}} \cong \frac{4\varphi}{\mu\pi\alpha\eta_{Sat}(3 - 2\eta_{Sat})} \tag{4.18}$$

where η_{Sat} can be expressed as η_f *or* η_g in terms of fluid and matrix densities and velocities.

$$\eta_{\mathrm{f}} = \rho_{\mathrm{f}} V^2_{\mathrm{Pf}} / \rho V^2_{\mathrm{P}} \tag{4.19}$$

and for gas it reads as:

$$\eta_{\mathrm{g}} = V^2_{\mathrm{S}} / V^2_{\mathrm{P}} \tag{4.20}$$

where V_P and V_S are matrix P- and S-wave velocities respectively; and V_{Pf} denotes the P-wave velocity of the fluid.

Inserting these compliances into the equations of Schoenberg and Sayers (1995) evaluates the HTI anisotropy for aligned vertical fractures. Moreover, fluid exchange between the fractures and the matrix at seismic frequencies is considered by making use of Cardona (2002):

$$Z_N^{Sat} = \frac{Z_N^f (1 - \frac{\kappa_f}{\kappa_g})}{1 - \frac{\kappa_f}{\kappa_g} + \frac{\kappa_f}{\phi_c} Z_N^f} \tag{4.21}$$

This relation is used here for fluid substitution, for ease of use with the compliance-based terms. These terms reduce Z^f_N, but leave Z^f_T untouched. Again, the fluid is a gas, live oil and brine. Following MacBeth (2002), alternatively, the elastic stiffness matrix of a fractured rock can be found, and can be inputted into the following relations to compute the fracture-induced anisotropy.

$$\varepsilon = \frac{-2\eta_{Sat}(1-\eta_{Sat})}{\frac{1}{(\lambda+\mu)Z_N^{Sat}} + 1} \tag{4.22}$$

$$\delta = -2\eta_{Sat}\left[\frac{1-2\eta_{Sat}}{\frac{1}{(\lambda+\mu)Z_N^{Sat}}+1} + \frac{1}{\frac{1}{\mu Z_T^{Sat}}+1}\right] \tag{4.23}$$

and

$$\gamma = -\frac{1}{2(\frac{1}{\mu Z_T^{Sat}} + 1)} \tag{4.24}$$

4.3 Calculating the Fracture-Induced Anisotropy

In this section I will compute the fracture-induced anisotropy of the Nelson and Rotliegend sandstones and compare it with the results achieved from stress-induced anisotropy of the same reservoirs. Fracture-induced anisotropy is parameterized following the methodology presented in the preceding sections. Both reservoir-rock properties are derived from Tables 3.1 and 3.2. A maximum of 1.5% fracture (crack)

porosity is assumed in both reservoirs in order to determine the fracture-induced anisotropy. A similar faulting system (strike-slip) is adopted in computing stress-induced anisotropy, utilizing a corresponding pressure regime in each reservoir. The results are again evaluated numerically and compared directly with the stress-induced anisotropy. Figures 4.1–4.3 show fracture-induced anisotropy for Nelson sand and Rotliegend sand, for gas-, oil- and brine-saturated cases. They are plotted with the fracture porosity scaled to the maximum expected value (1.5%) in the subsurface. Thomsen parameters are again evaluated. Unlike the stress-induced anisotropy, the fast velocity direction is now parallel to the fracture strike (and hence perpendicular to the symmetry axis).

Based on these results, the fracture-induced anisotropy behaves almost linearly with fracture porosity. The anisotropies are generally much smaller than those predicted by the stress-induced anisotropy, and this reduces further when a stiff saturating fluid is present. Anisotropy is higher when the contrast between the fracture and matrix stiffness is highest, and thus the Rotliegend sands give a higher fracture-induced anisotropy than the Nelson sands. However it appears that ε and δ do have different behaviours than for stress-induced anisotropy, which could be possible distinguishing parameters.

Figure 4.1 illustrates the ranges of fracture-induced anisotropy for Nelson sandstone (top) and Rotliegend sandstone (bottom). Here, both reservoir rocks are assumed to be gas-saturated. Rotliegend sands exhibit a high anisotropy (28%), and the Nelson sands reach a maximum value of 17%. Note that the latter is not realistic as, in practice, it is actually an oil-sand, and the gas-saturated example is used here merely as a reference.

The anisotropy parameter ε of realistic gas-saturated Rotliegend sandstone increases almost linearly with fracture porosity from zero to approximately –20% Variation of shear-wave anisotropy (γ) is exponential and equates to 28%; unlike ε and γ, δ displays exponential changes with fracture porosity up to the middle of the curve. It is 8% when the porosity is 0.75%, and it shows little increase (it virtually plateaus) afterwards to the ultimate value of 11% for 1.5% fracture porosity.

When our sandstones are saturated with oil, this further decreases the normal compliance (Z_N). The sands exhibit small and, at the same time, linear, fracture-induced anisotropies versus fracture porosity (Figure 4.2). Oil-saturated Nelson sandstone (shown in the upper part of Figure 4.2) cannot produce more than 3.5% anisotropy (ε = –2%, γ = –3.5% and δ = 3%). In the lower part of this figure, oil-saturated Rotliegend sand displays

linear trends for all anisotropy parameters, and meanwhile medium to small magnitudes. The next figure (Figure 4.3 – brine-saturated sands) supports the linearity of the variation in anisotropy with increase in fracture porosity in this modelling, depicting less than 2% for Nelson sand and 4% for Rotliegend sand.

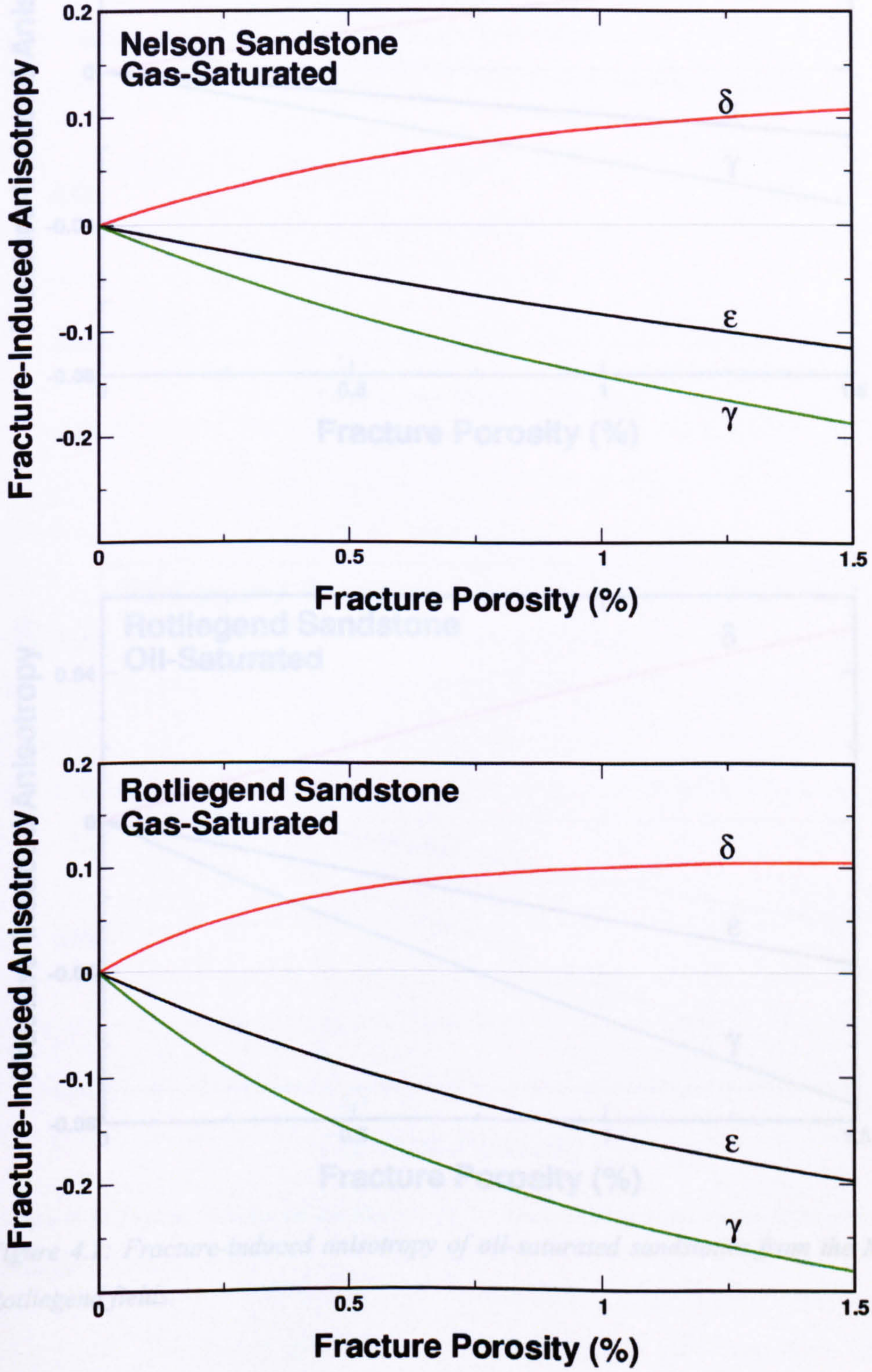

Figure 4.1: Fracture-induced anisotropy of gas-saturated sandstones from the Nelson and the Rotliegend fields.

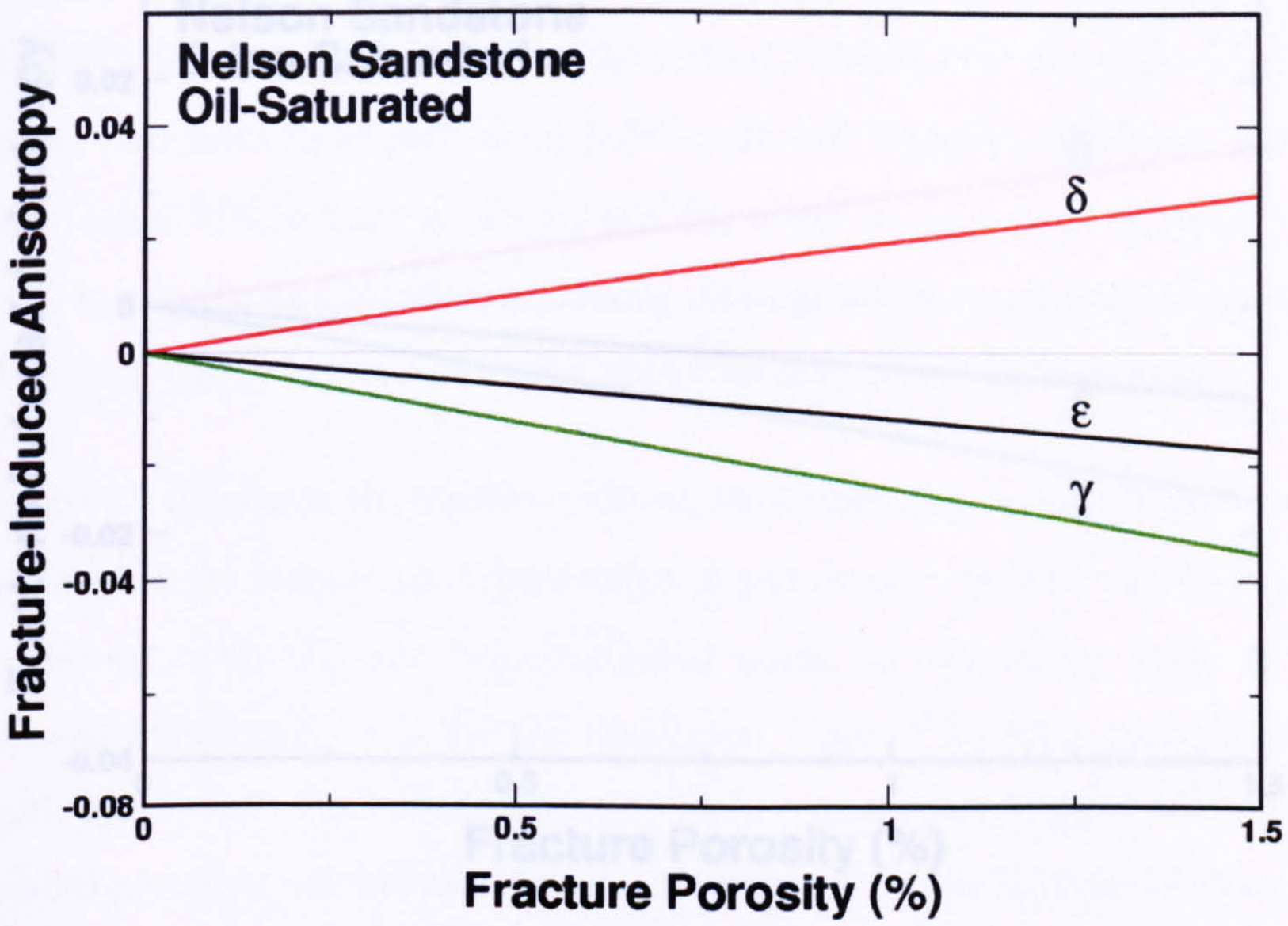

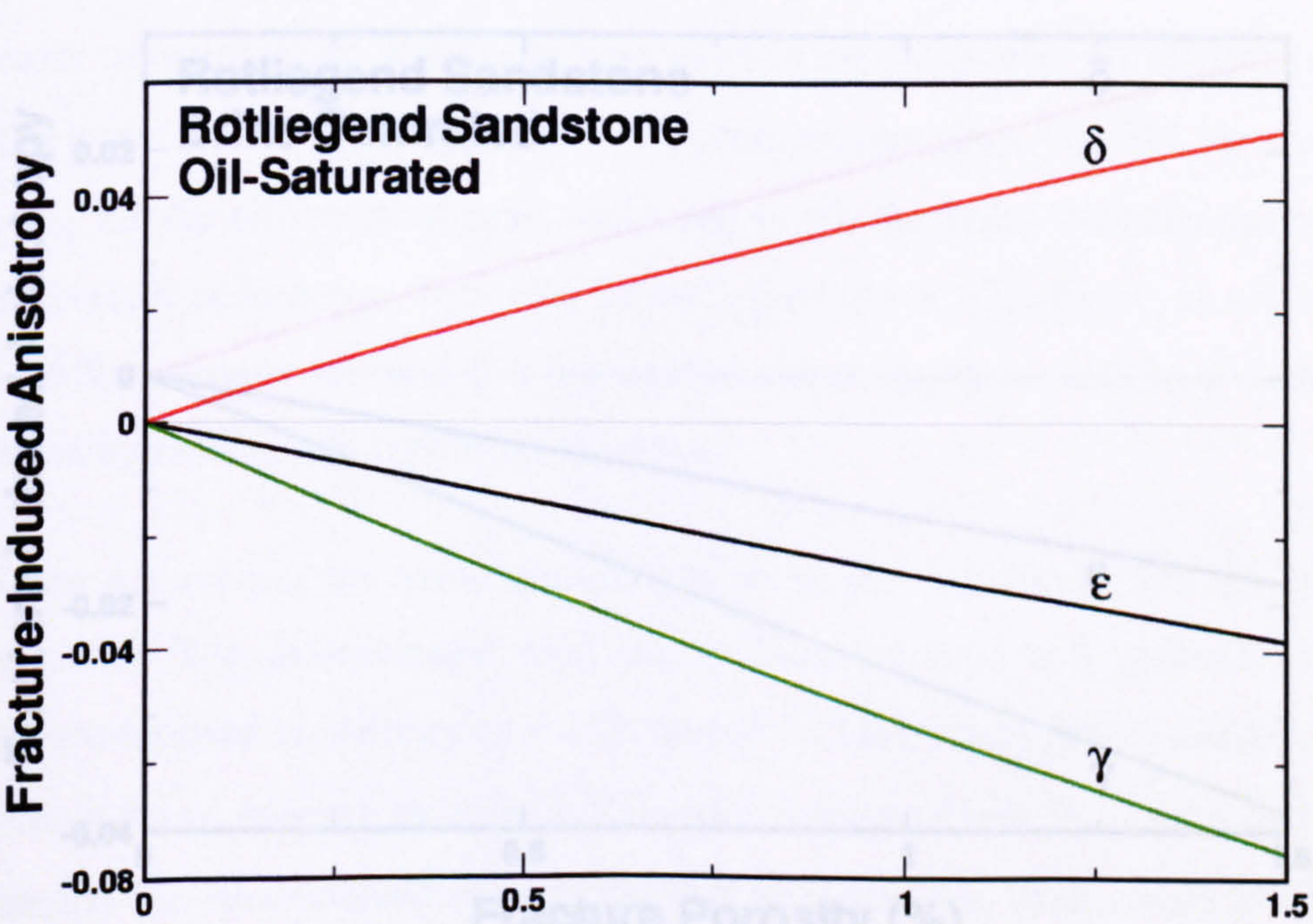

Figure 4.2: Fracture-induced anisotropy of oil-saturated sandstones from the Nelson and the Rotliegend fields.

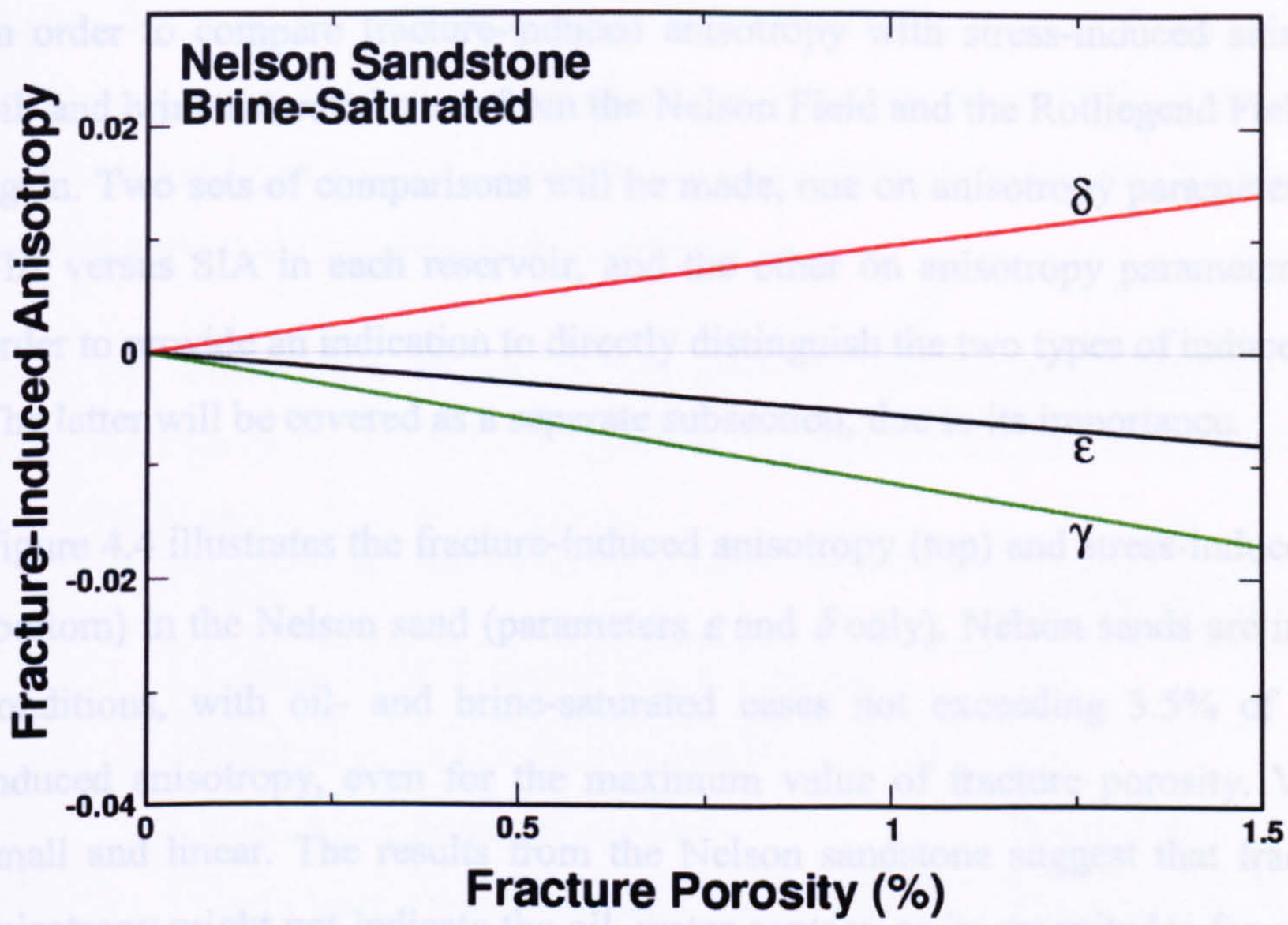

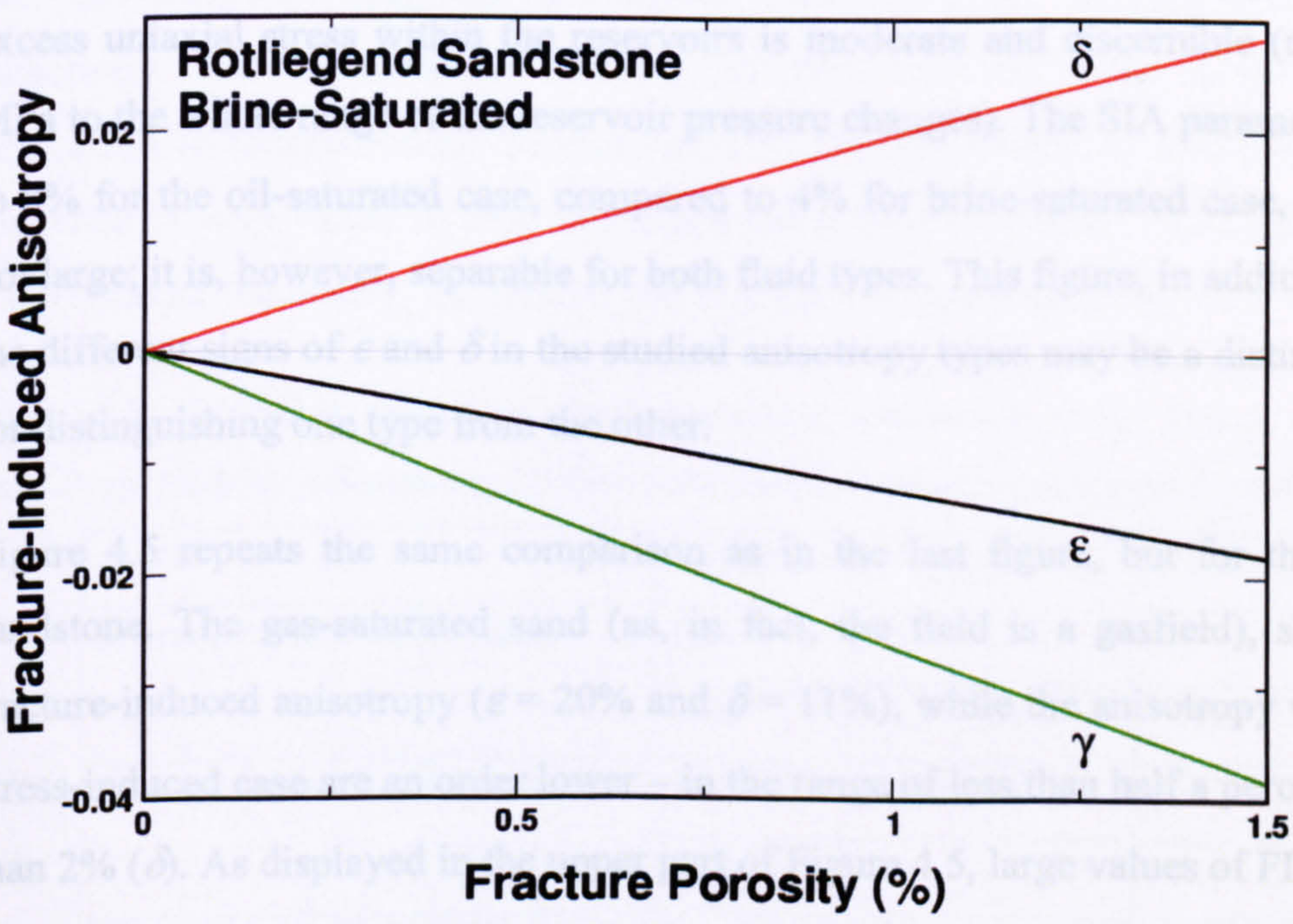

Figure 4.3: Fracture-induced anisotropy of brine-saturated sandstones from the Nelson and the Rotliegend fields.

4.4 Distinguishing FIA from SIA

4.4.1 Direct Indication through Magnitude

In order to compare fracture-induced anisotropy with stress-induced anisotropy, gas-, oil- and brine-saturated cases from the Nelson Field and the Rotliegend Field are utilized again. Two sets of comparisons will be made, one on anisotropy parameters ε and δ for FIA versus SIA in each reservoir, and the other on anisotropy parameters δ and γ, in order to provide an indication to directly distinguish the two types of induced anisotropy. The latter will be covered as a separate subsection, due to its importance.

Figure 4.4 illustrates the fracture-induced anisotropy (top) and stress-induced anisotropy (bottom) in the Nelson sand (parameters ε and δ only). Nelson sands are in the realistic conditions, with oil- and brine-saturated cases not exceeding 3.5% of the fracture-induced anisotropy, even for the maximum value of fracture porosity. Variations are small and linear. The results from the Nelson sandstone suggest that fracture-induced anisotropy might not indicate the oil–water contact, as its magnitudes for oil- and brine-saturated rocks are insignificant and close to one another. Unlike the case of fracture-induced anisotropy, the stress-induced anisotropy observed in the general range of excess uniaxial stress within the reservoirs is moderate and discernible (at and after 2 MPa to the whole range of the reservoir pressure changes). The SIA parameter δ equates to 8% for the oil-saturated case, compared to 4% for brine-saturated case, although ε is not large; it is, however, separable for both fluid types. This figure, in addition, hints that the different signs of ε and δ in the studied anisotropy types may be a distinctive feature for distinguishing one type from the other.

Figure 4.5 repeats the same comparison as in the last figure, but for the Rotliegend sandstone. The gas-saturated sand (as, in fact, the field is a gasfield), shows a large fracture-induced anisotropy ($\varepsilon = 20\%$ and $\delta = 11\%$), while the anisotropy values for the stress-induced case are an order lower – in the range of less than half a percent (ε) to less than 2% (δ). As displayed in the upper part of Figure 4.5, large values of FIA parameters ε (3–20%) and δ (3.5–11%), and also big differences between the gas-saturated Rotliegend sand ($\varepsilon = 20\%$ and $\delta = 11\%$) in comparison with the rock while saturated with brine ($\varepsilon = 3\%$ and $\delta = 3.5\%$), are promising for distinguishing gas from water saturations. The lower part of Figure 4.5 indicates that both brine-saturated (SIA parameters $\varepsilon \cong 0$ and δ less than 0.5%), and gas-saturated Rotliegend sand (SIA parameters $\varepsilon = 0.5\%$ and $\delta = 1.5\%$) are almost stress-insensitive. As in MacBeth and

Lynn (2001), these sands represent two end-members: the Neslon sand is more affected by the unequal horizontal stresses, and the Rotliegend sand shows the presence of aligned fractures, although, in reality, the *in situ* conditions of each reservoir lie between the two extremes. Table 4.1 summarizes the observed induced anisotropies presented by MacBeth and Lynn (2001) – demonstrating that each reservoir may register one type of induced anisotropy or a combination of both.

Table 4.1: Observation of one or two types of induced anisotropies in four different fields.(MacBeth and Lynn, 2001), 1. Lynn et al. (1999a); 2. Lynn et al. (1999b), 3. Grimm et al. (1999) and 4. Lynn et al. (1999c).

Field	**Anisotropy type**
Rulison Field, Piceance Basin, Colorado[1]	SIA
Bluebell Altamont Field, Uinta Basin, Utah[2]	FIA
Wind River Basin, Wyoming[3]	FIA and SIA
Gulf Coast, Onshore South Central Texas[4]	FIA and SIA

The compressible and compliant reservoir Nelson shows higher SIA and little FIA, but the less-compliant reservoir Rotliegend displays large fracture-induced velocity anisotropy. The maximum anisotropy parameters observed in the comparison of FIA versus SIA in Nelson and Rotliegend sands have been tabulated in Table 4.2, illustrating moderate to large values of SIA for Nelson and a large magnitude of FIA for Rotliegend – the stronger the matrix, the smaller the SIA and the larger the FIA.

Table 4.2: Maximum values of fracture-induced anisotropy (FIA) versus stress-induced anisotropy (SIA) for oil-saturated Nelson sand and gas-saturated Rotliegend sand.

Rock	**Anisotropy type**	**ε (%)**	**δ (%)**	**γ (%)**
Oil-saturated Nelson sand	FIA	–2	3	–3.5
	SIA	2.5	–7.5	7.4
Gas-saturated Rotliegend sand	FIA	–20	11	–28
	SIA	0.5	–1.6	3.3

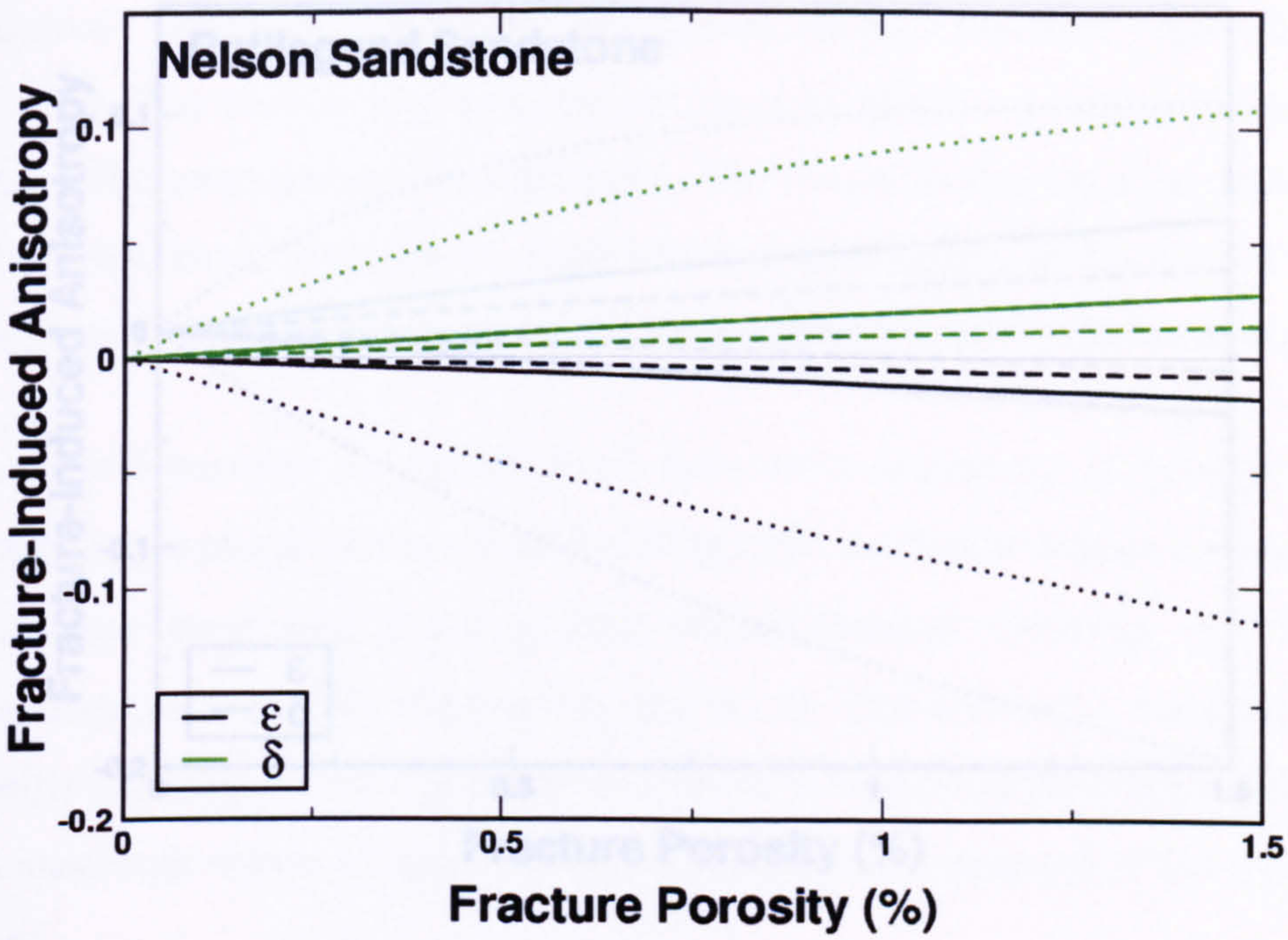

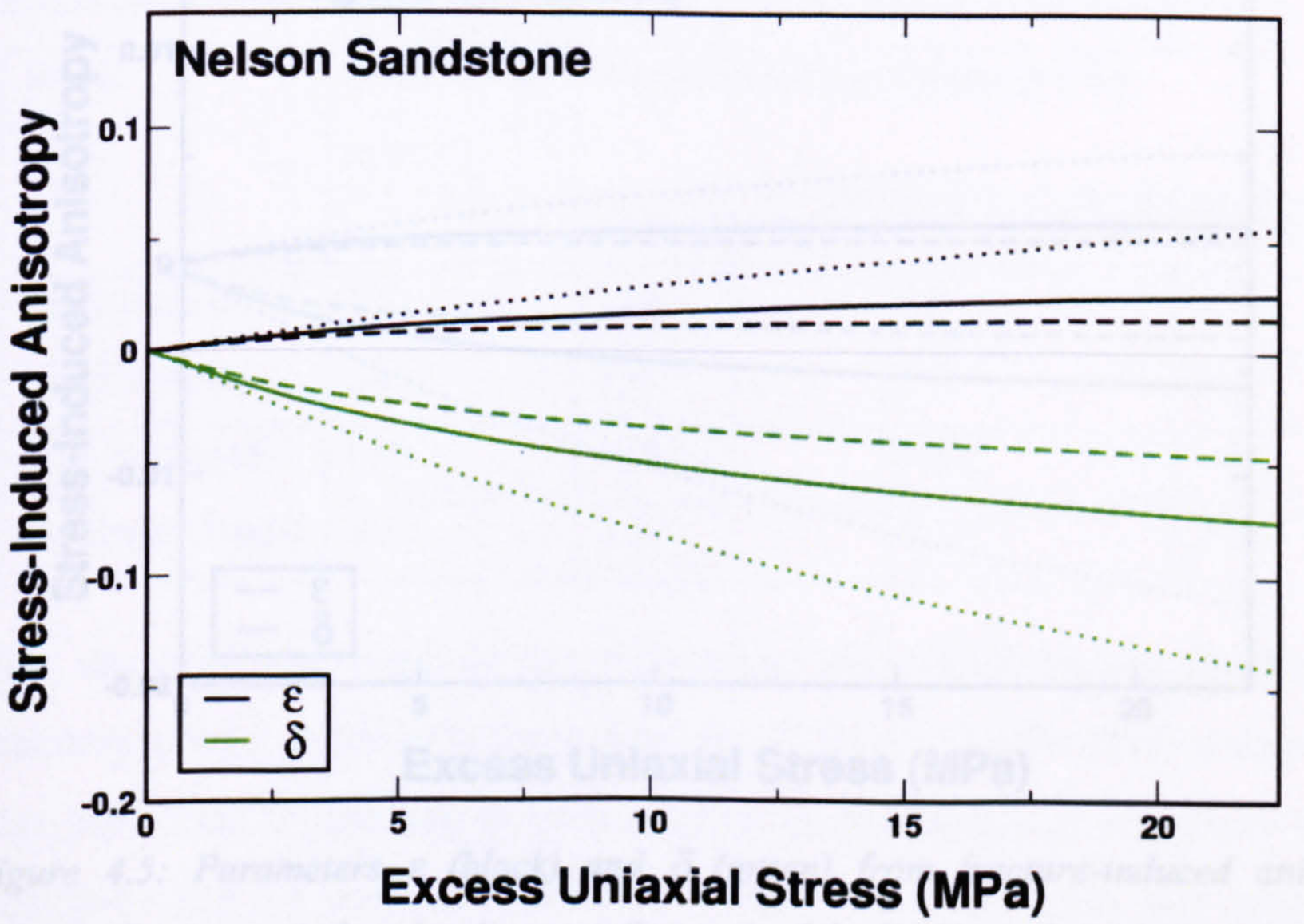

Figure 4.4: Parameters ε (black) and δ (green) from fracture-induced anisotropy (top), compared to stress-induced anisotropy (bottom) of the Nelson sandstone saturated with gas (dotted line), oil (solid line) and brine (dashed line), show that stress-sensitive Nelson exhibits a larger stress-induced anisotropy.

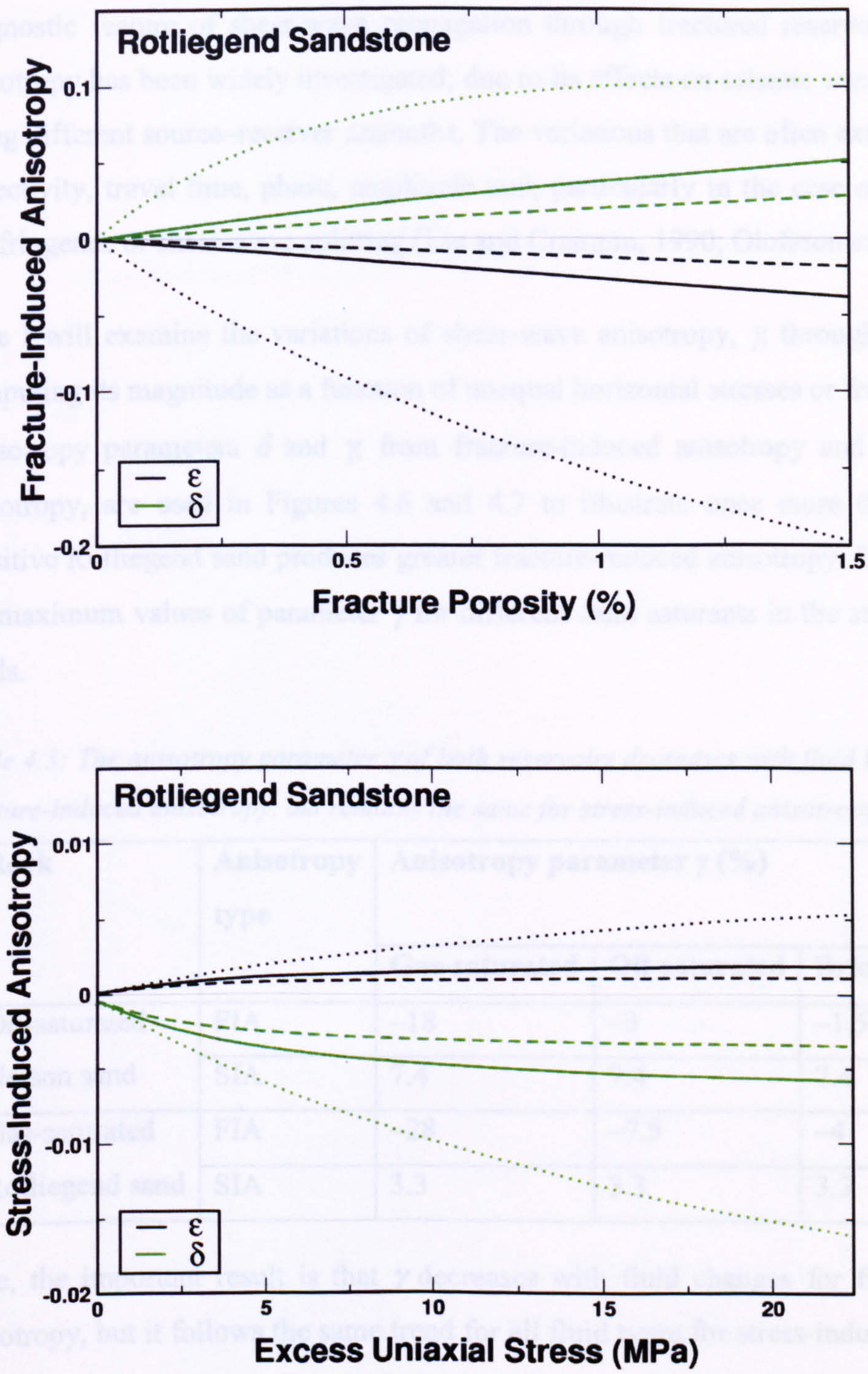

Figure 4.5: Parameters ε (black) and δ (green) from fracture-induced anisotropy (top), compared to stress-induced anisotropy (bottom) of the Rotliegend sandstone saturated with gas (dotted line), oil (solid line) and brine (dashed line), show that stress-insensitive Rotliegend exhibits higher fracture-induced anisotropy.

4.4.2 Shear-Wave Velocity Anisotropy as a Possible Indicator

There are a number of papers in the literature that characterize shear-wave splitting as a diagnostic feature of shear-wave propagation through fractured reservoirs. Azimuthal anisotropy has been widely investigated, due to its effects on seismic waves propagating along different source–receiver azimuths. The variations that are often examined include reflectivity, travel time, phase, amplitude and, particularly in the case of shear waves, birefringence or shear-wave splitting (Liu and Crampin, 1990; Olofsson *et al.*, 2003).

Here I will examine the variations of shear-wave anisotropy, γ, through usual way of computing its magnitude as a function of unequal horizontal stresses or fracture porosity. Anisotropy parameters δ and γ, from fracture-induced anisotropy and stress-induced anisotropy, are used in Figures 4.6 and 4.7 to illustrate once more that less stress-sensitive Rotliegend sand produces greater fracture-induced anisotropy. Table 4.3 shows the maximum values of parameter γ for different fluid saturants in the studied reservoir sands.

Table 4.3: The anisotropy parameter γ of both reservoirs decreases with fluid bulk modulus for fracture-induced anisotropy, but remains the same for stress-induced anisotropy.

Rock	**Anisotropy type**	**Anisotropy parameter γ (%)**		
		Gas-saturated	**Oil-saturated**	**Brine-saturated**
Oil-saturated Nelson sand	FIA	–18	–3	–1.5
	SIA	7.4	7.4	7.4
Gas-saturated Rotliegend sand	FIA	–28	–7.5	–4
	SIA	3.3	3.3	3.3

Here, the important result is that γ decreases with fluid changes for fracture-induced anisotropy, but it follows the same trend for all fluid types for stress-induced anisotropy. This behaviour is observed in both sandstones, meaning that γ or shear-wave velocity anisotropy can be used as a possible indicator to distinguish two types of induced anisotropies.

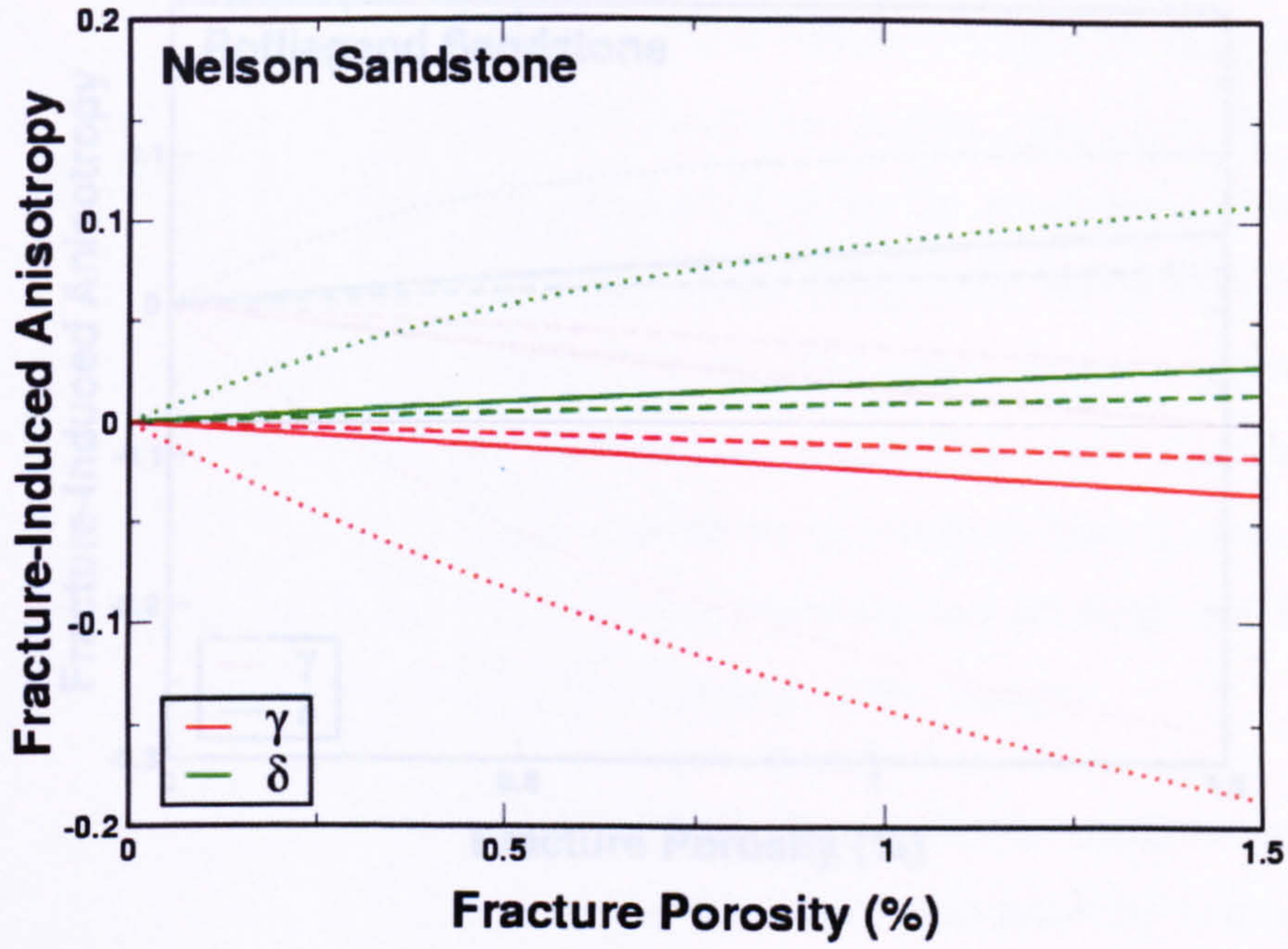

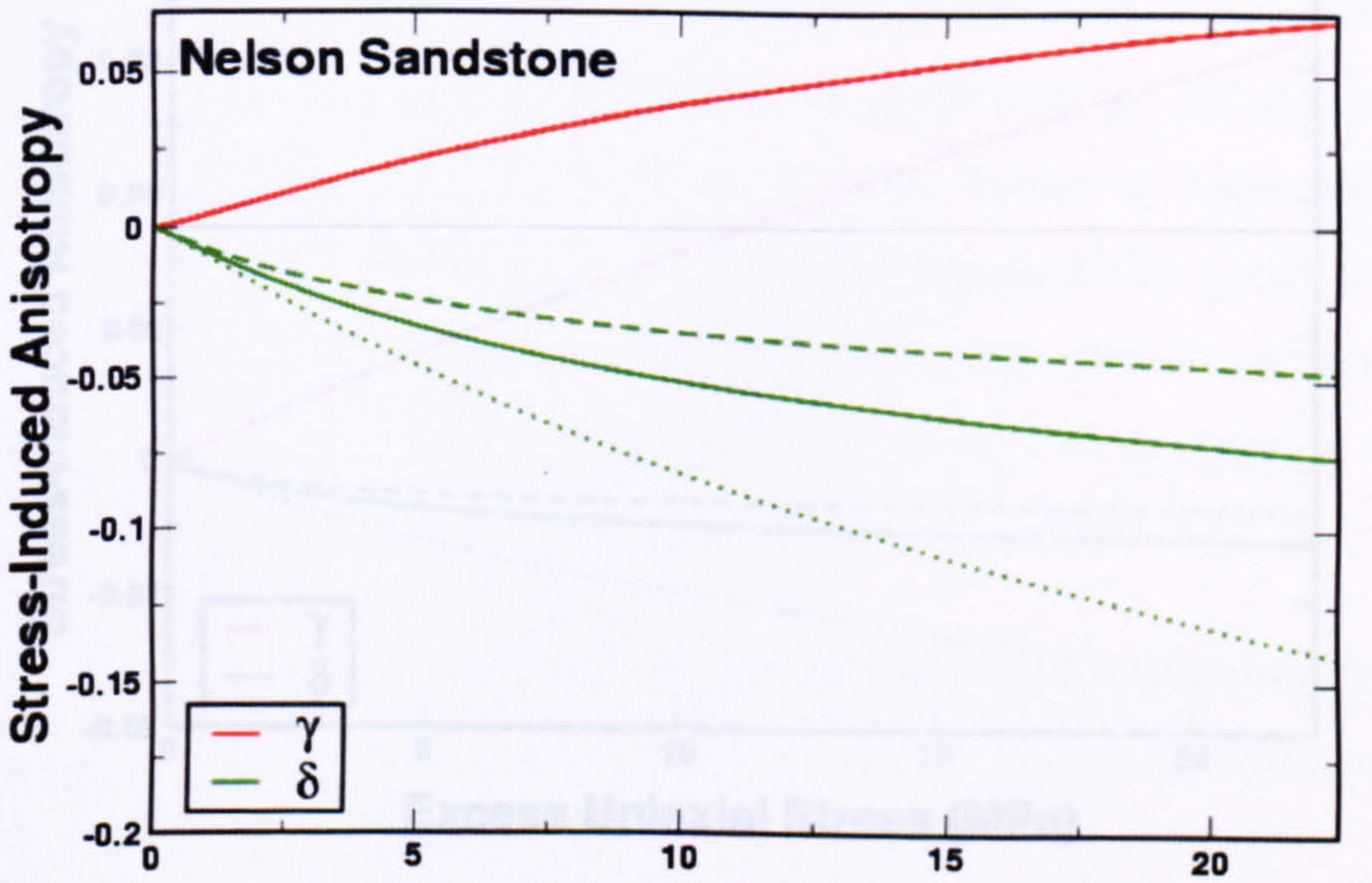

Figure 4.6: Parameters γ (red) and δ (green) from fracture-induced anisotropy (top) compared with stress-induced anisotropy (bottom) of the Nelson sandstone saturated with gas (dotted line), oil (solid line) and brine (dashed line), show that FIA γ decreases with fluid change but SIA γ is the same for all fluids.

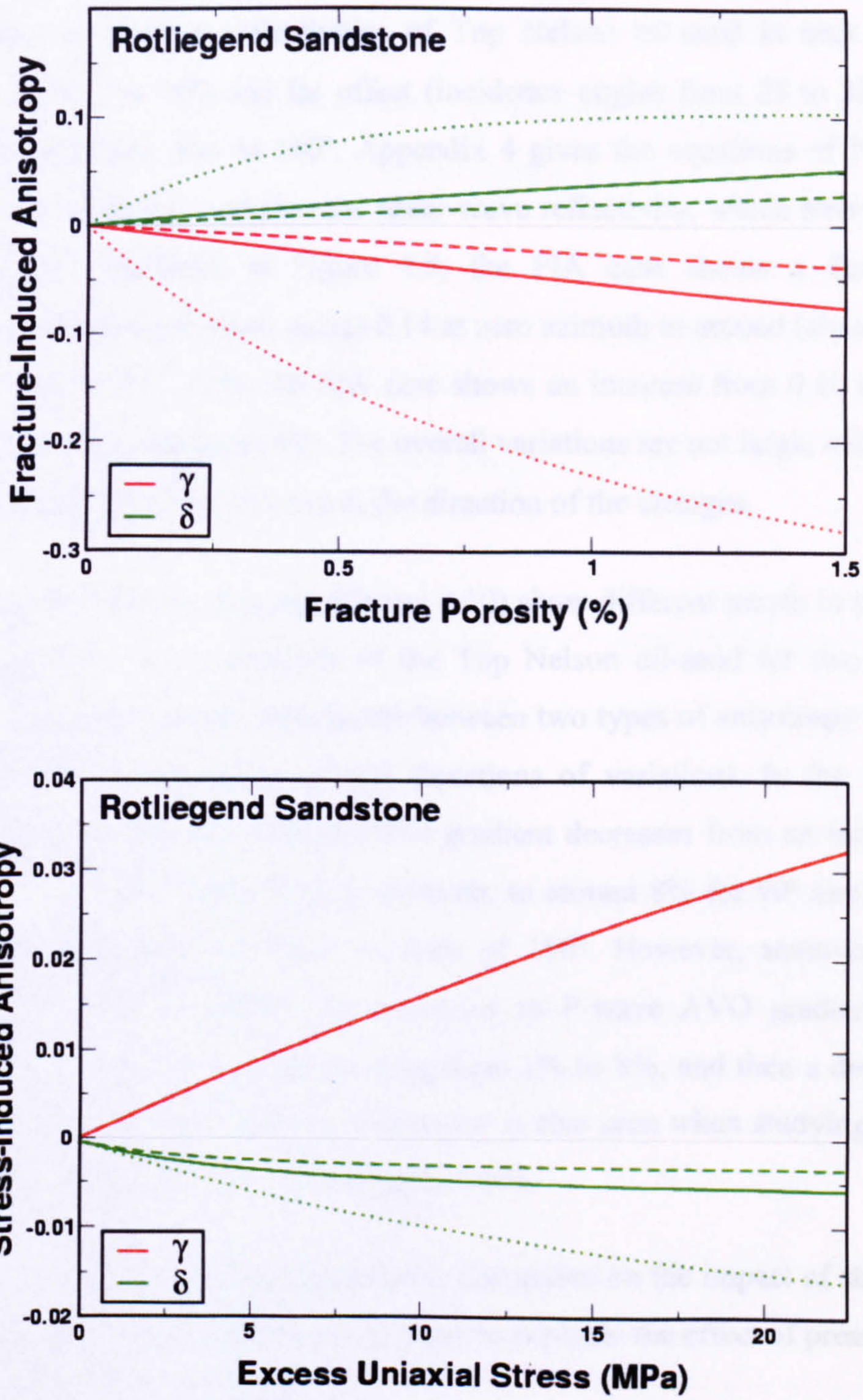

Figure 4.7: Parameters γ (red) and δ (green) from fracture-induced anisotropy (top) compared with stress-induced anisotropy (bottom) of the Rotliegend sandstone saturated with gas (dotted line), oil (solid line) and brine (dashed line), show that FIA γ decreases with fluid change but SIA γ is the same for all fluids.

4.4.3 Indirect Indication through Reflectivity, AVO and AVAZ

In this section, near-offset and far-offset compressional- and shear-wave reflectivities for varying azimuth in the Top Nelson oil-sand and Nelson oil–water contact are illustrated and compared. Compressional-wave AVO attributes such as gradient and curvature

(Appendix 4) of the corresponding scenarios are also discussed. Figure 4.8 (top – for fracture-induced anisotropy, and bottom – for stress-induced anisotropy) displays variations of P-wave reflectivities of Top Nelson oil-sand in near offset (incidence angles from 5 to 10°) and far offset (incidence angles from 25 to 30°), in an azimuth range of between zero to 180°. Appendix 4 gives the equations of P-wave reflectivity and AVO attributes, and also the shear-wave reflectivity, which have been used in this section. As displayed in Figure 4.8, the FIA case shows a decrease in P-wave reflectivity, from (absolute value) 0.14 at zero azimuth to around (absolute value) 0.13 at an azimuth of 90°, while the SIA case shows an increase from 0.10 at zero azimuth to around 0.12 at an azimuth 90°. The overall variations are not large, and therefore the two studied cases are only different in the direction of the changes.

The next two figures (Figures 4.9 and 4.10) show different trends in the fluctuations for AVO gradients and curvatures of the Top Nelson oil-sand for two anisotropy cases. These attributes can also distinguish between two types of anisotropy at the lower range of azimuth, with both values and directions of variations. In the study of fracture-induced anisotropy, the P-wave AVO gradient decreases from an initial absolute value of 13% for 0° of source–receiver azimuth, to around 8% for 90° azimuth and increases symmetrically to 13% for an azimuth of 180°. However, stress-induced anisotropy causes the rock to exhibit the variations in P-wave AVO gradient in the opposite direction, *i.e.* first an increase ranging from 1% to 8%, and then a decrease from 8% to 1% (Figure 4.9). Such differing behaviour is also seen when studying the P-wave AVO curvature of FIA and SIA cases (Figure 4.10).

Liu *et al.* (2002) gave a comprehensive discussion on the impact of stress and pore fluid on reflectivity, AVO and AVAZ in order to separate the effect of pressure and saturation by using converted wave data.

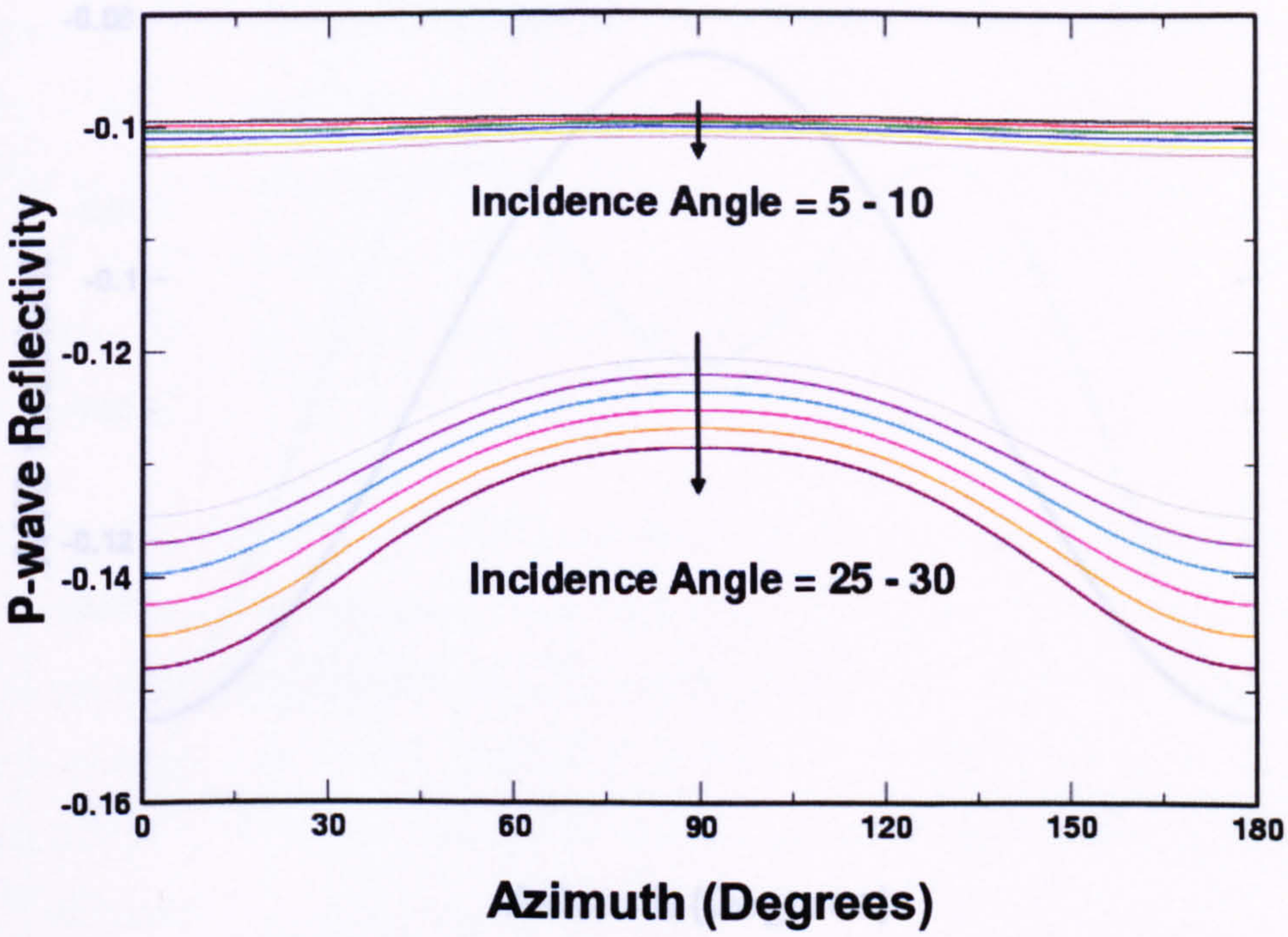

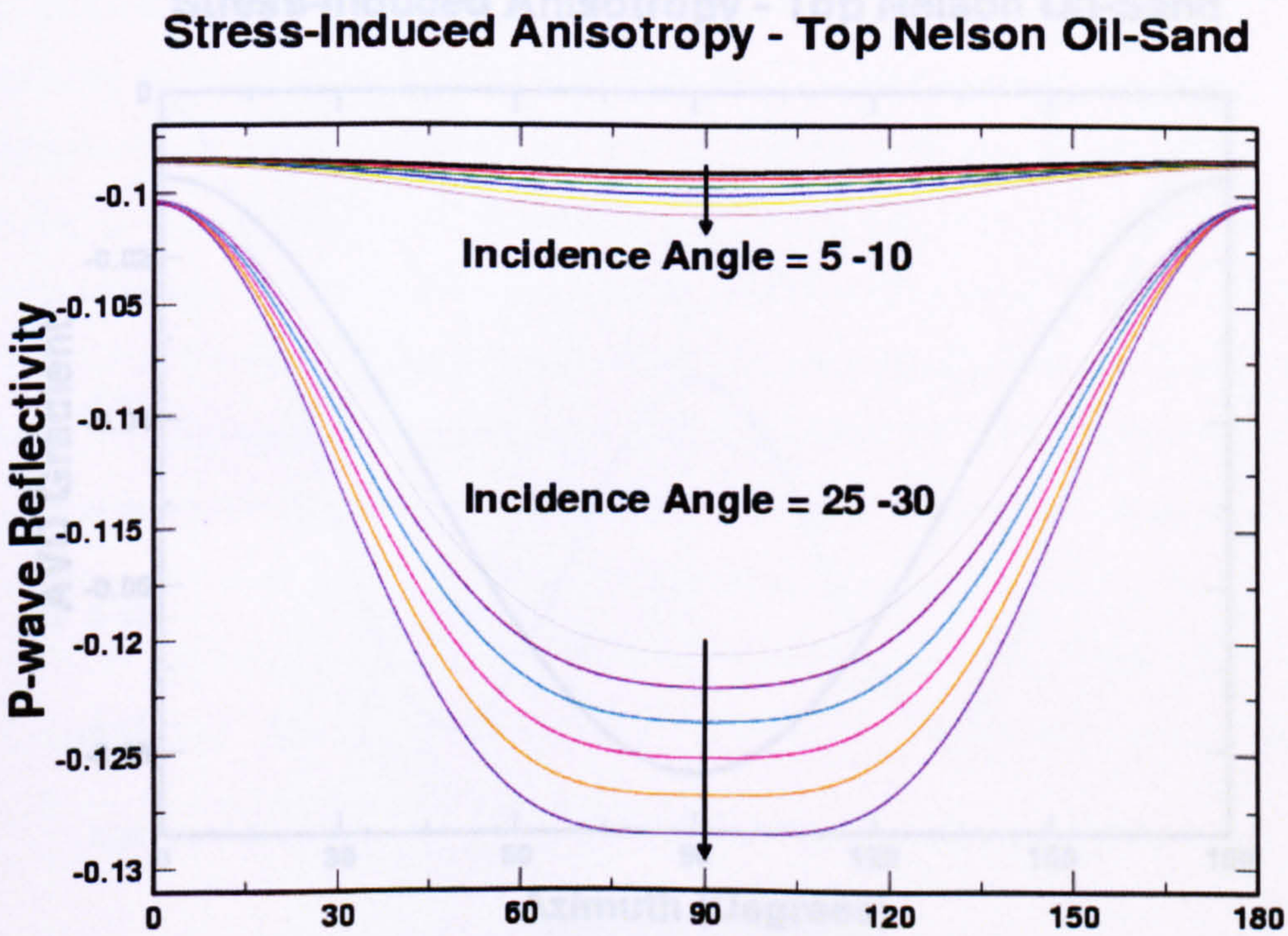

Figure 4.8: P-wave reflectivity of the Top Nelson oil-sand, using fracture-induced anisotropy (top), compared with stress-induced anisotropy (bottom).

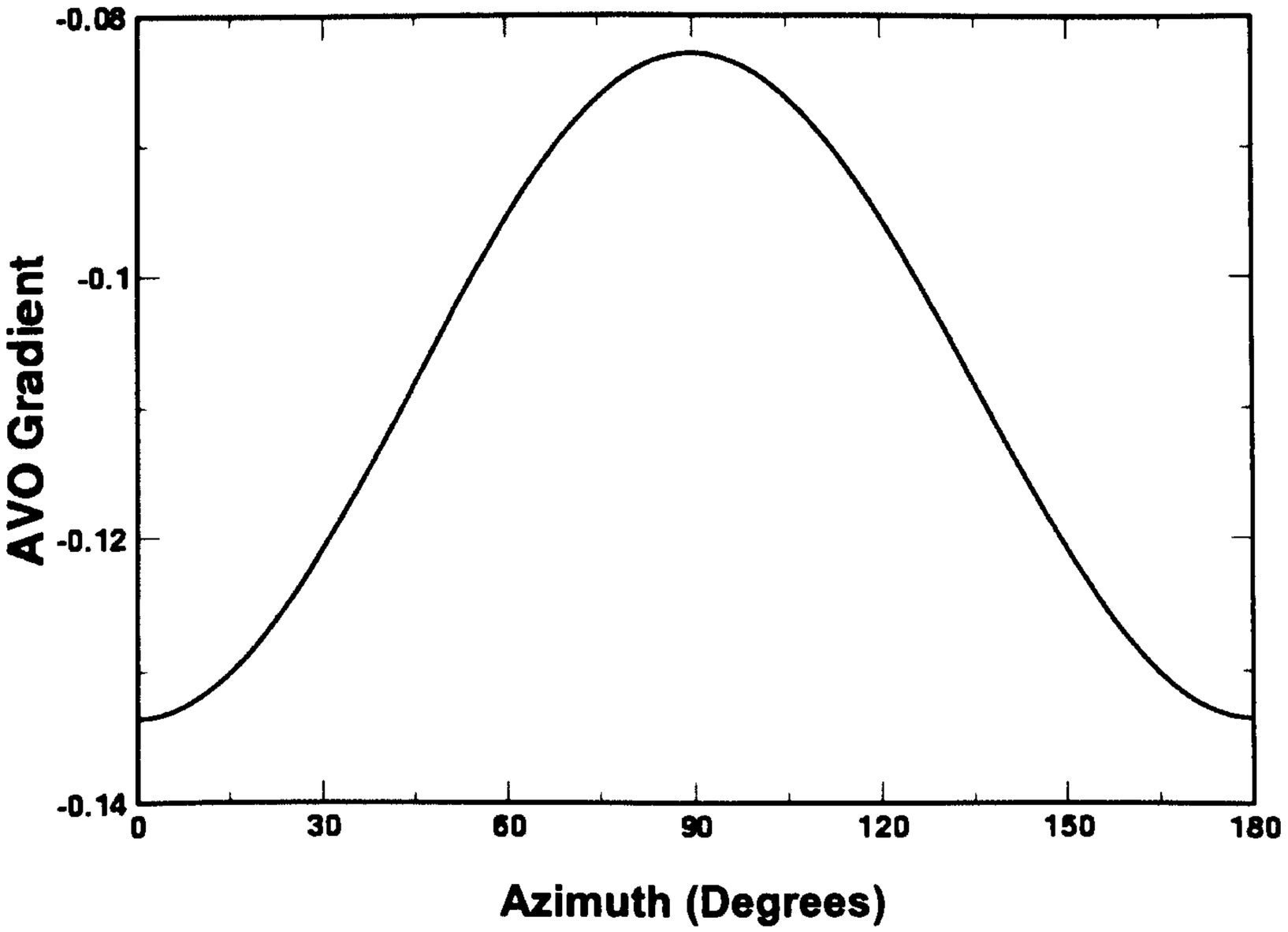

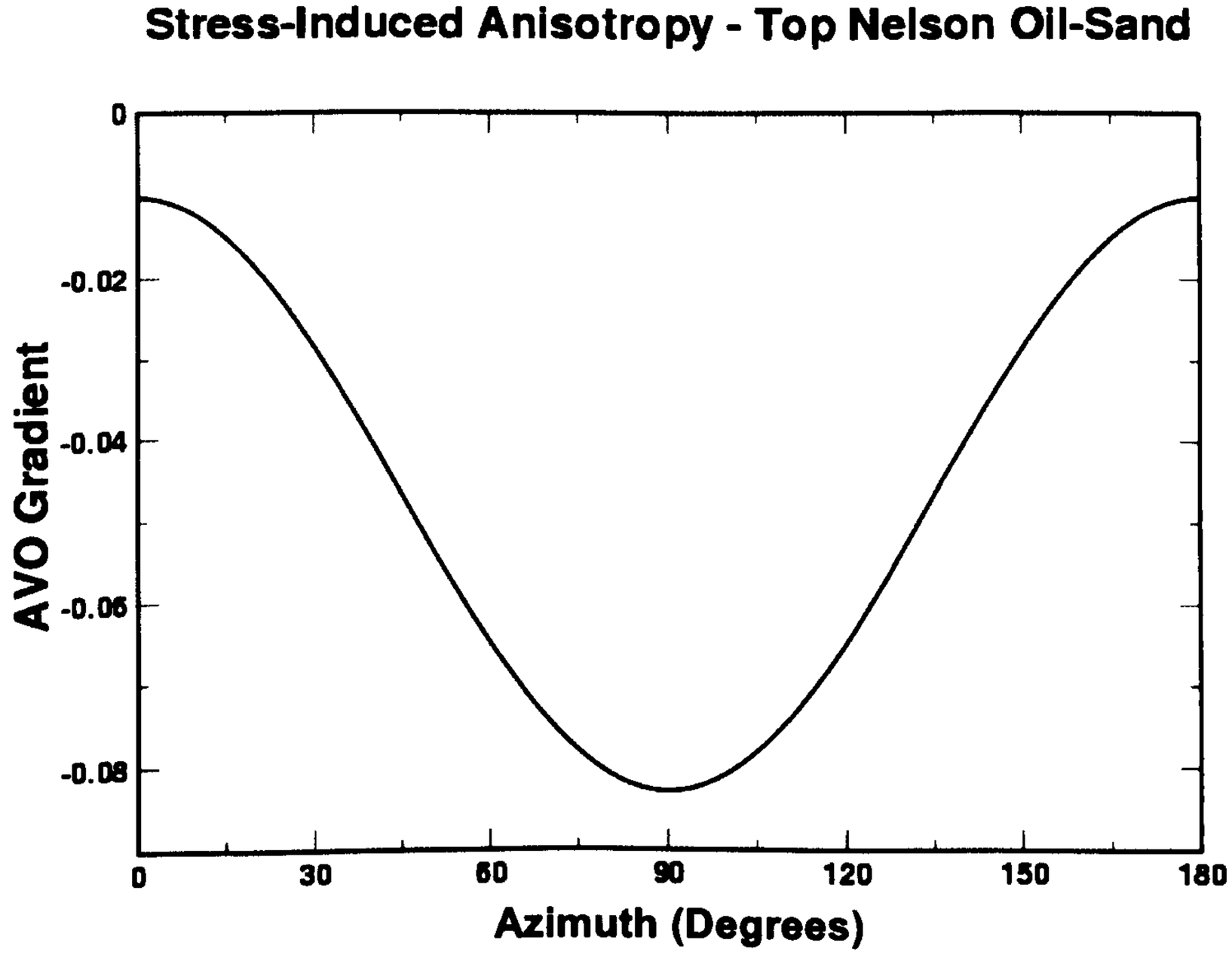

Figure 4.9: AVO gradient of the Top Nelson oil-sand, using fracture-induced anisotropy (top), compared with stress-induced anisotropy (bottom).

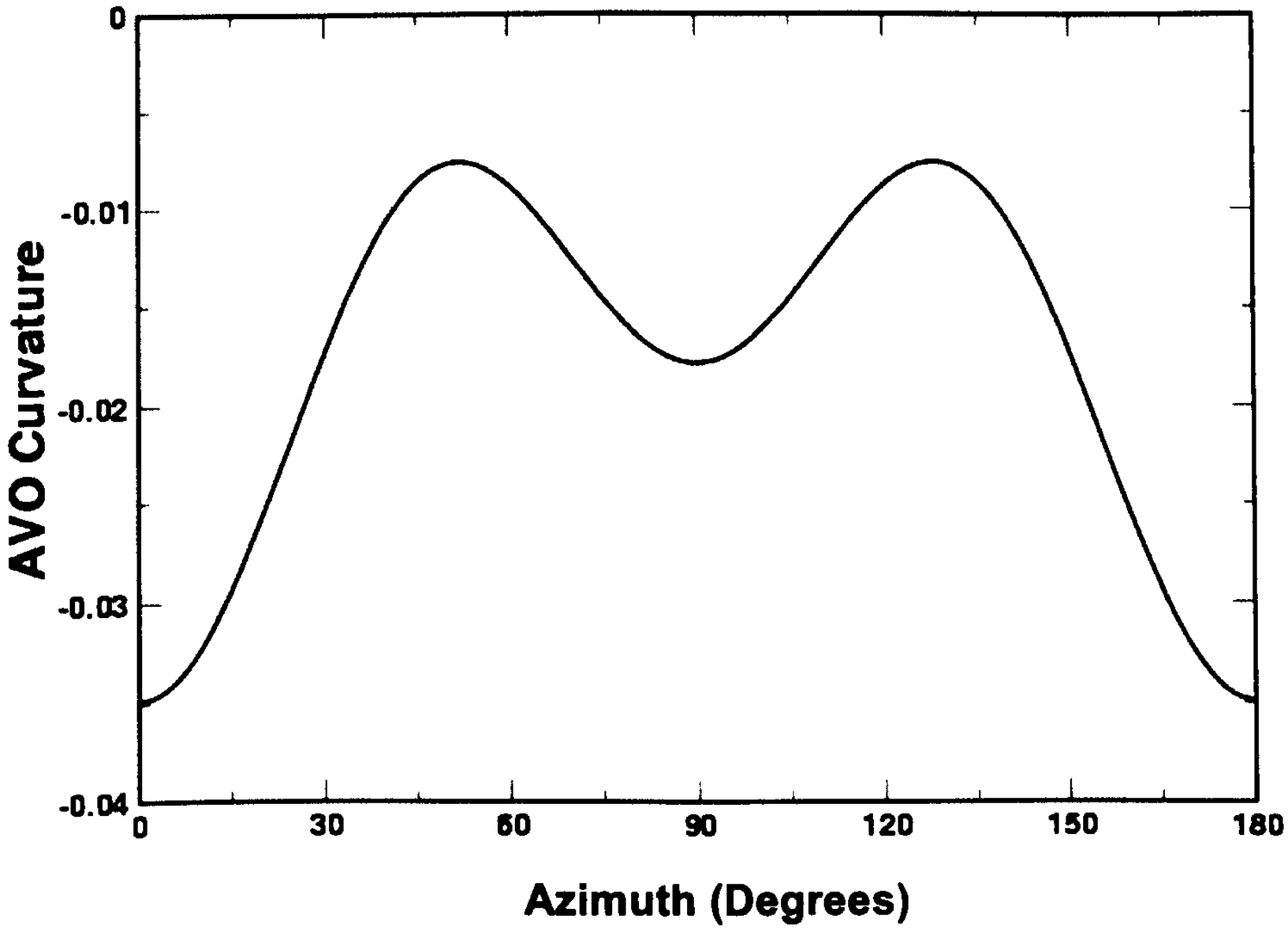

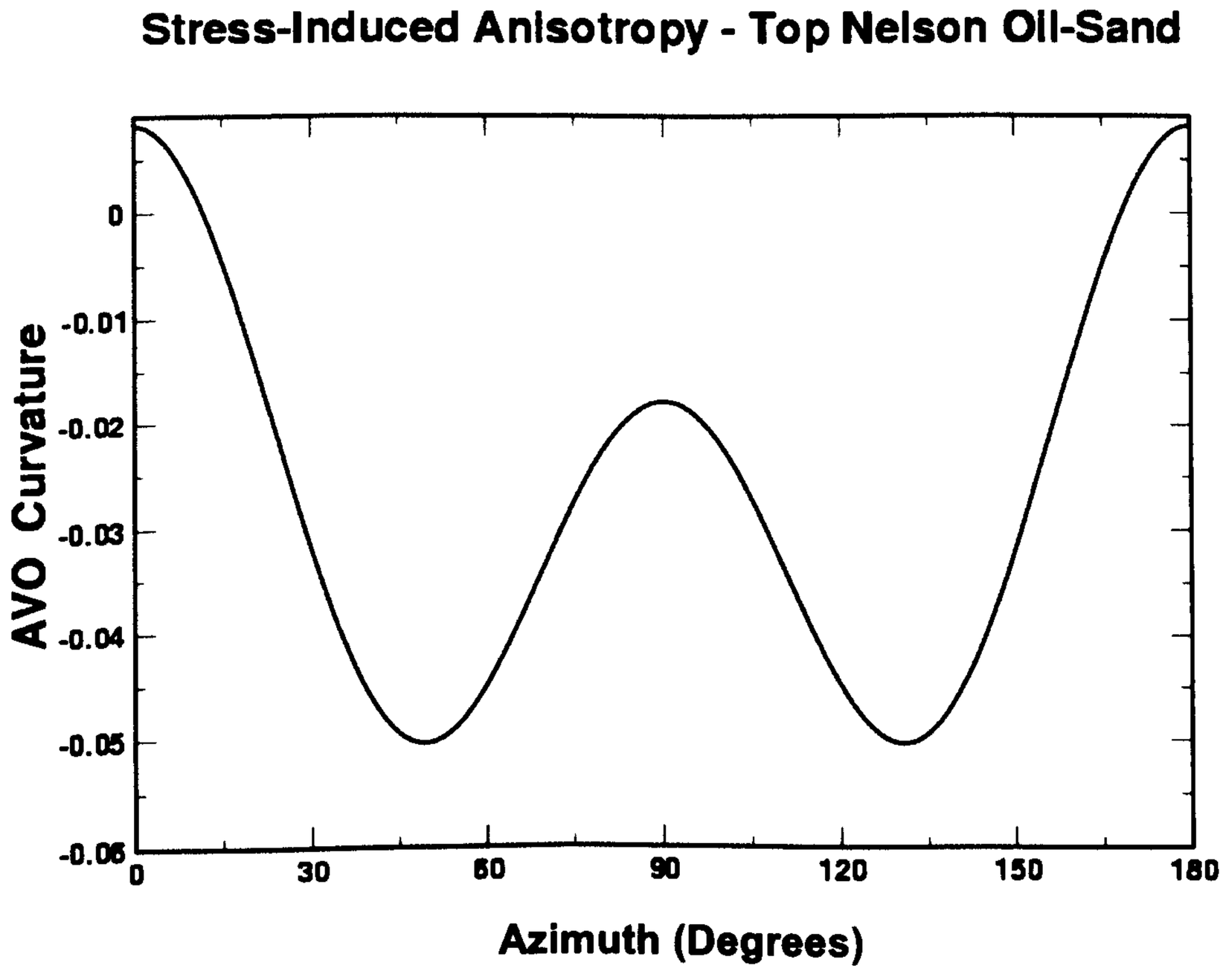

Figure 4.10: AVO curvature of Top Nelson oil-sand, using fracture-induced anisotropy (top), compared with stress-induced anisotropy (bottom).

P-wave reflectivity variations at the Nelson oil–water contact are studied in Figure 4.11. The overall variations look similar; however, an observable difference occurs at far-offset azimuths of zero to 30 degrees, where, in the case of stress-induced anisotropy, the reflectivity variations are more or less constant, while in the case of fracture-induced anisotropy they are declining. The AVO gradients of Nelson brine sand look similar and are in the same range for both cases of induced anisotropies. They are 0.013–0.047 for FIA and 0.013–0.042 for SIA, showing only a small difference at low azimuths only (Figure 4.12).

Figure 4.13 shows that the AVO curvatures of studied cases of Nelson brine sand have different directions and values of variation; are distinguishable at a lower azimuth range; and are still within a small range of zero to 2.5%. To be exact, in FIA they are 0.022 at zero azimuth, zero at 53°, and 0.0125 at 90°; and 0.0025 at zero azimuth, 0.025 at 53° and 0.0125 at 90°in SIA, noticeable extreme values are those corresponding to zero and 53° azimuths.

Shear-wave reflectivity variations with incidence angle for the top Nelson oil-sand and at Nelson oil–water contact, for the cases of fracture-induced anisotropy and stress-induced anisotropy, are illustrated in Figures 4.14 and 4.15. In both figures, the isotropic behaviours of the reflectivities are also plotted as a reference. For the top Nelson oil-sand, the fracture-induced anisotropy shows smaller shear-wave reflectivities, while stress-induced anisotropy displays higher reflectivities (Figure 4.14). Figure 4.15 (top) shows that for the fracture-induced anisotropy case, the shear-wave reflectivities deviate from the isotropic response, due to different values of γ for oil-sand and brine-sand, while the lower part of Figure 4.15 illustrates the exact trend of shear-wave reflectivity for stress-induced anisotropy and isotropic cases, because here the γ for both fluid types are of the same value. Hence, shear-wave velocity anisotropy, γ, appears to contribute to distinguishing the cause of induced anisotropy. Table 4.4 gives the observed reflectivities at zero and 20° incidence angles.

Table 4.4: Extreme values of shear-wave reflectivity variations for incidence angles of zero and 20° in FIA and SIA cases, as compared with the corresponding isotropic response.

Isotropic/Anisotropic	Top Nelson Oil-sand	Nelson Oil–Water Contact
Isotropic	(–0.027)–(–0.015)	(–0.0051)–(–0.0058)
FIA	(–0.027)–(–0.0175)	(–0.0051)–(–0.0046)
SIA	(–0.027)–(–0.011)	(–0.0051)–(–0.0058)

Recalling Thomsen's anisotropy parameters for a VTI medium:

$$\varepsilon = \frac{C_{11} - C_{33}}{2C_{33}} \tag{4.25}$$

$$\delta = \frac{(C_{13} + C_{55})^2 - (C_{33} - C_{55})^2}{2C_{33}(C_{33} - C_{55})} \tag{4.26}$$

$$\gamma = \frac{C_{66} - C_{55}}{2C_{55}} \tag{4.27}$$

and their counterparts for HTI media given by Rüger (1998):

$$\varepsilon_{\mathrm{HTI}} = -\frac{\varepsilon_{\mathrm{VTI}}}{1 + 2\varepsilon_{\mathrm{VTI}}} \tag{4.28}$$

$$\delta_{\mathrm{HTI}} = \frac{\delta_{\mathrm{VTI}} - 2\varepsilon_{\mathrm{VTI}}(1 + \varepsilon_{\mathrm{VTI}} / f)}{(1 + 2\varepsilon_{\mathrm{VTI}})(1 + 2\varepsilon_{\mathrm{VTI}} / f)} \tag{4.29}$$

$$\gamma_{\mathrm{HTI}} = -\frac{\gamma_{\mathrm{VTI}}}{1 + 2\gamma_{\mathrm{VTI}}} \tag{4.30}$$

where f is a function of compressional-wave velocity V_{P} and shear-wave velocity V_{S}, as:

$$f = 1 - (V_{\mathrm{S}} / V_{\mathrm{P}})^2 \tag{4.31}$$

compared to the anisotropy parameters of FIA; from Equations 4.22 to 4.24 presented by MacBeth (2004), we can see that these two types of induced anisotropies are different, but we cannot rely on such a level of contrast in order to distinguish one type from the other, and we should instead examine a number of seismic attributes, such as normal move-out, AVO gradient and curvature. The impacts of stress-induced anisotropy and fracture-induced anisotropy on some AVO attributes are illustrated in Figures 4.11 to 4.15.

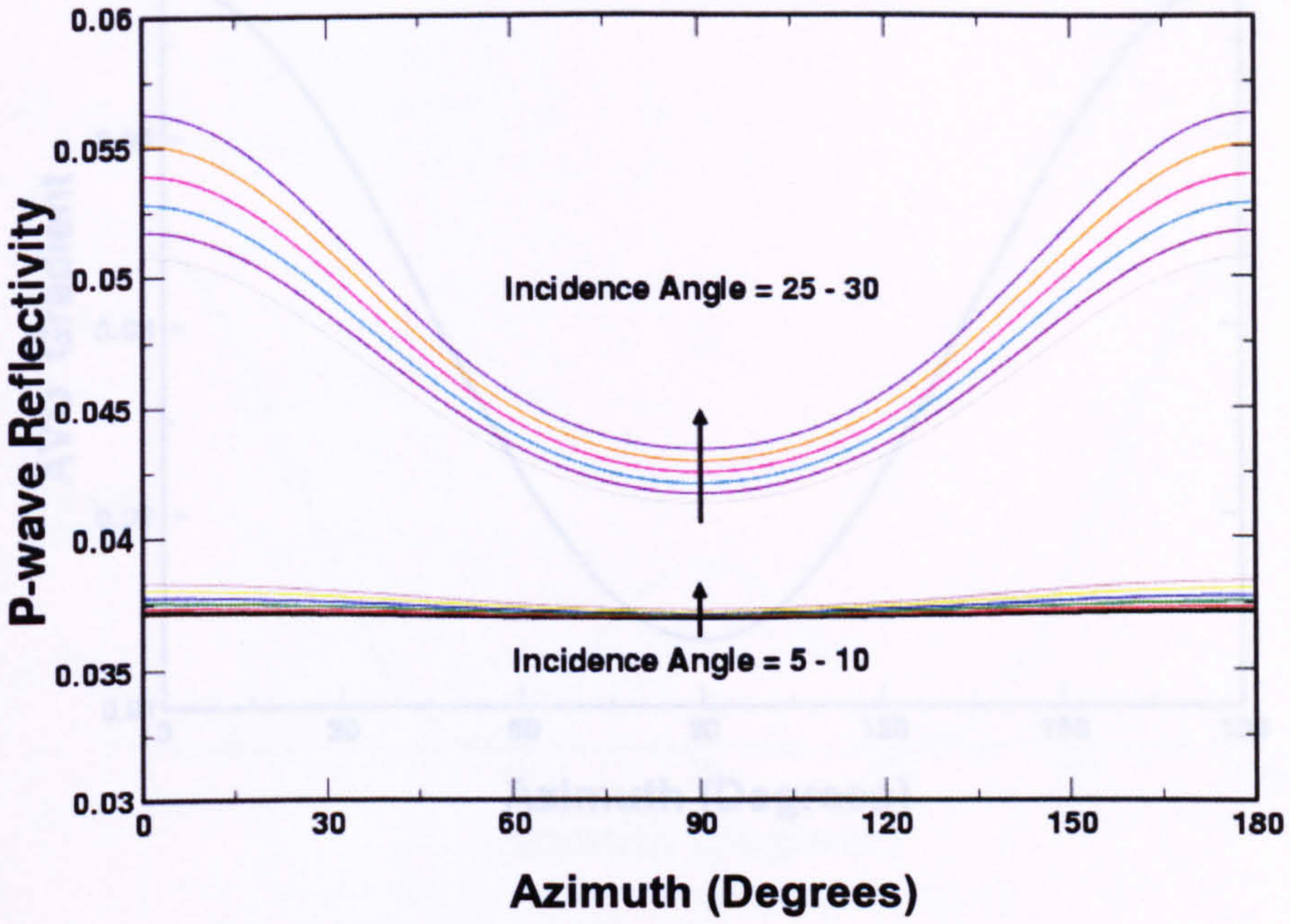

Figure 4.11: P-wave reflectivity of the Nelson oil–water contact, using fracture-induced anisotropy (top), compared with stress-induced anisotropy (bottom).

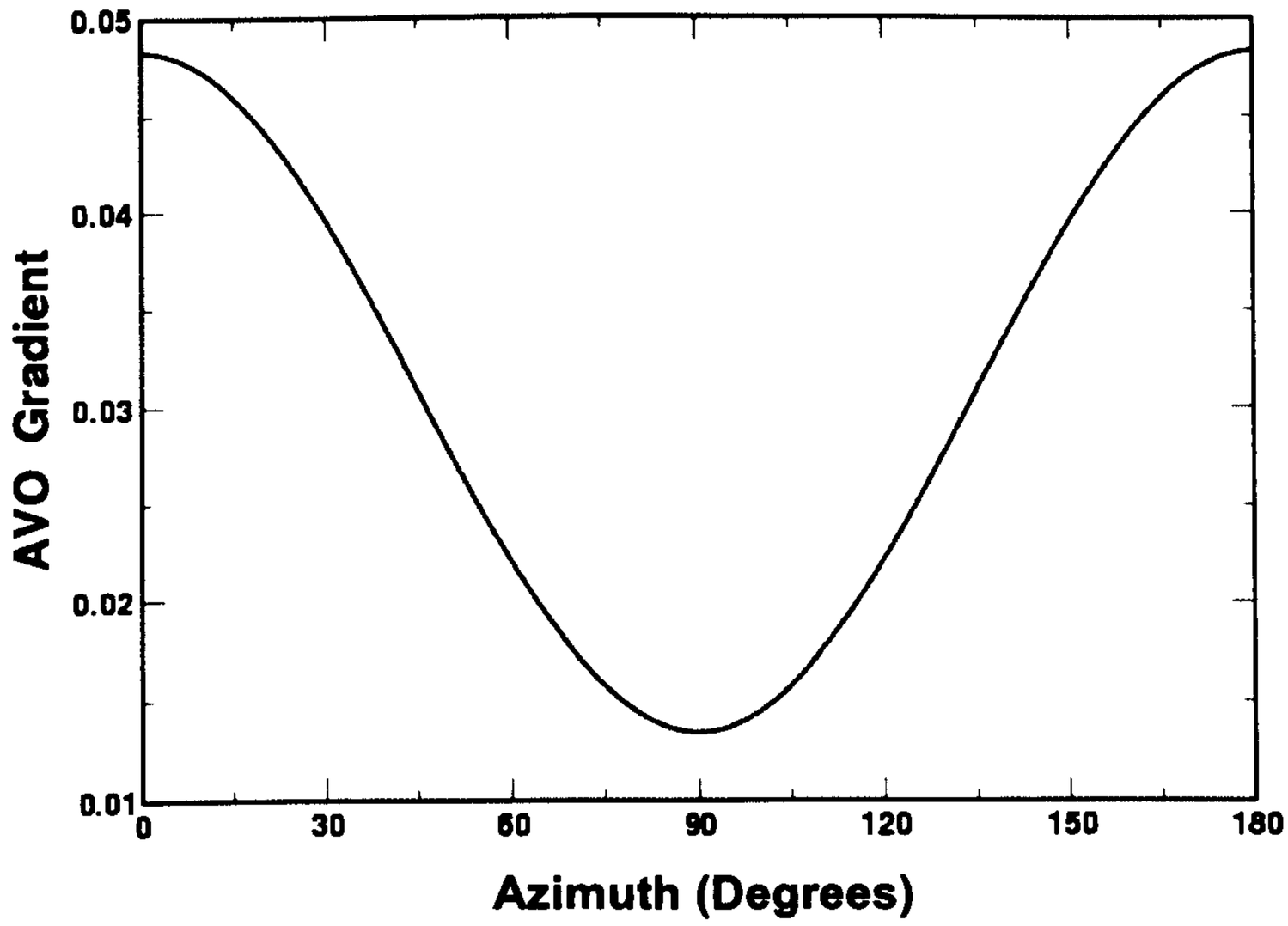

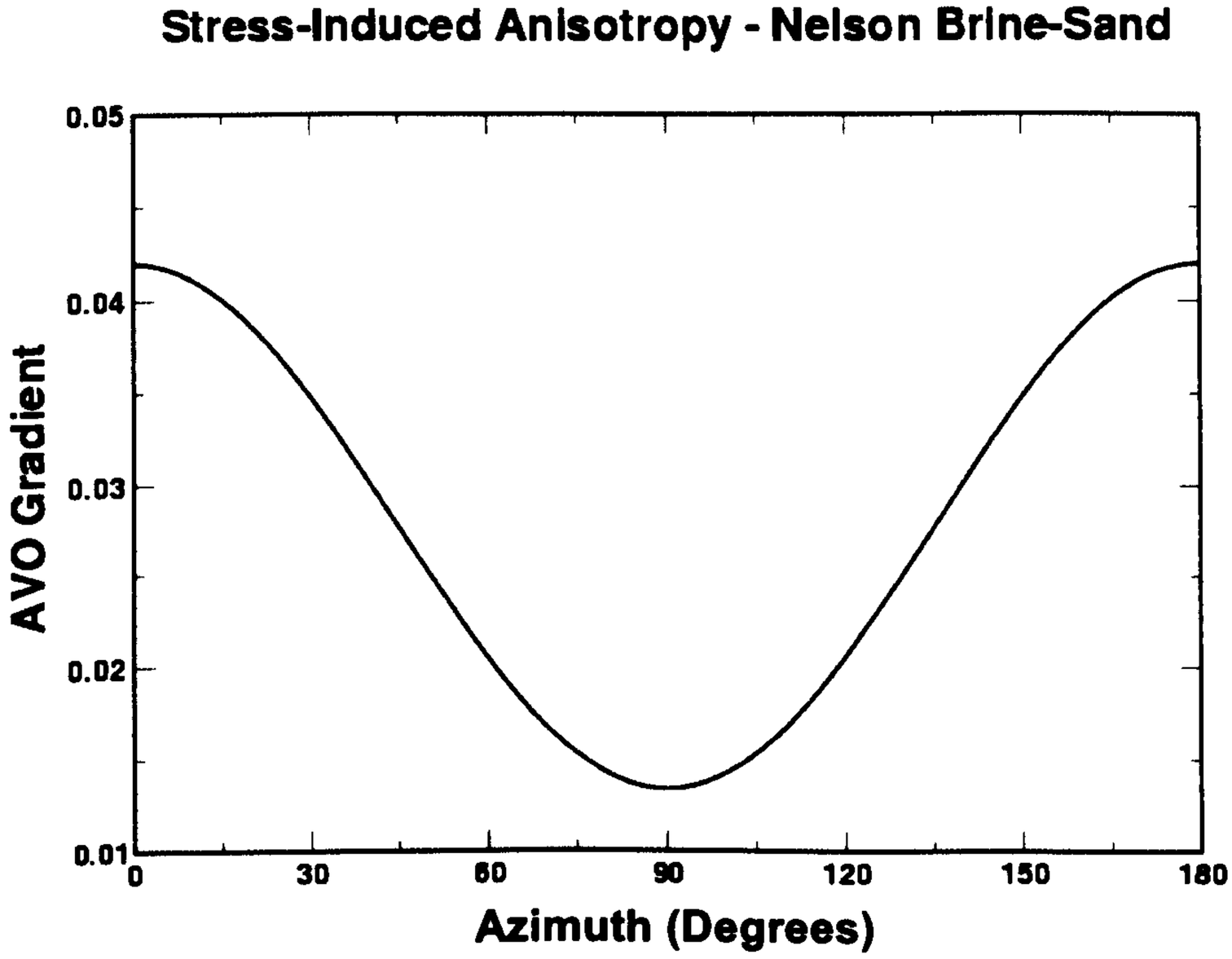

Figure 4.12: AVO gradient of Nelson oil–water contact, using fracture-induced anisotropy (top), compared with stress-induced anisotropy (bottom).

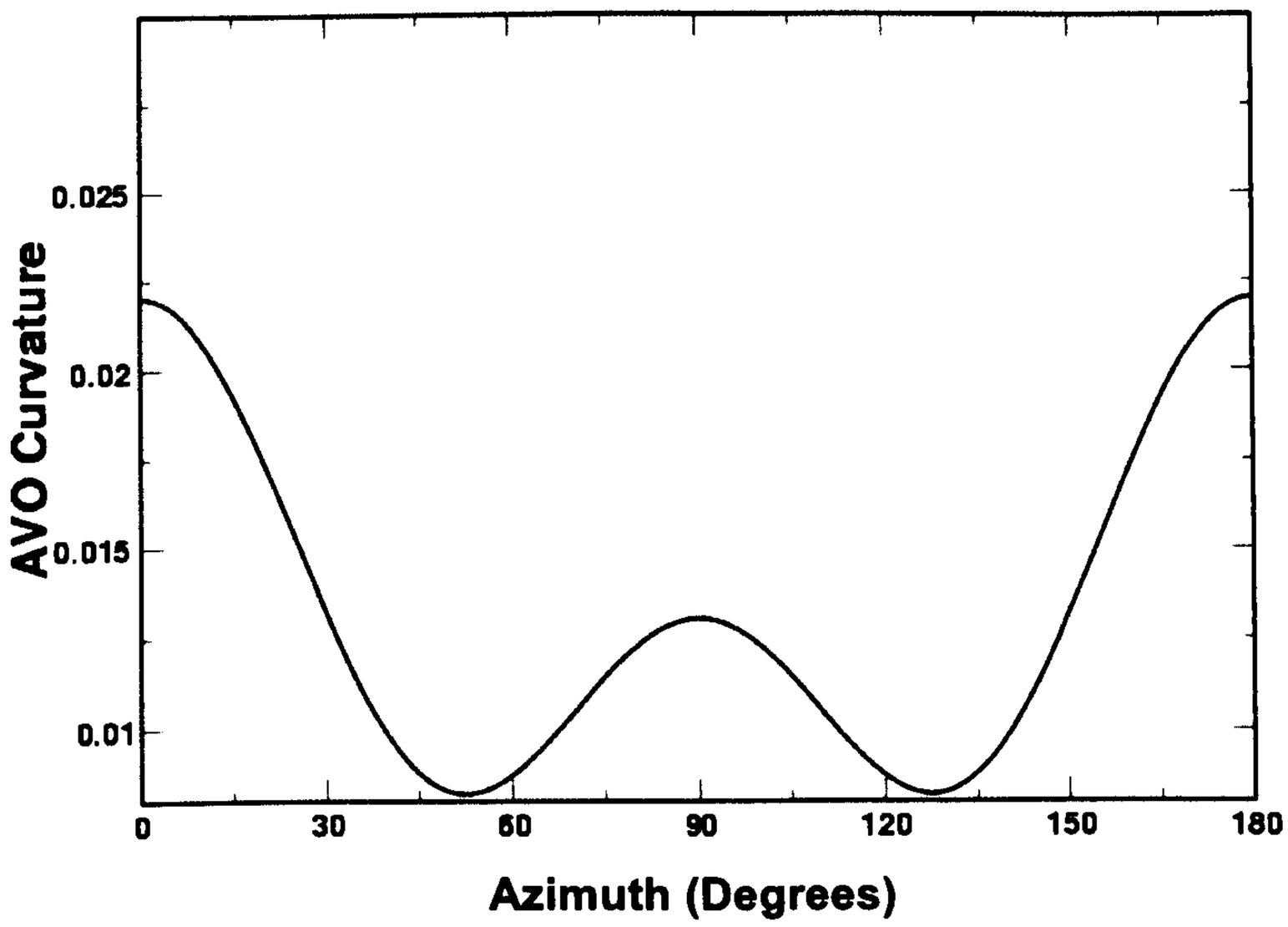

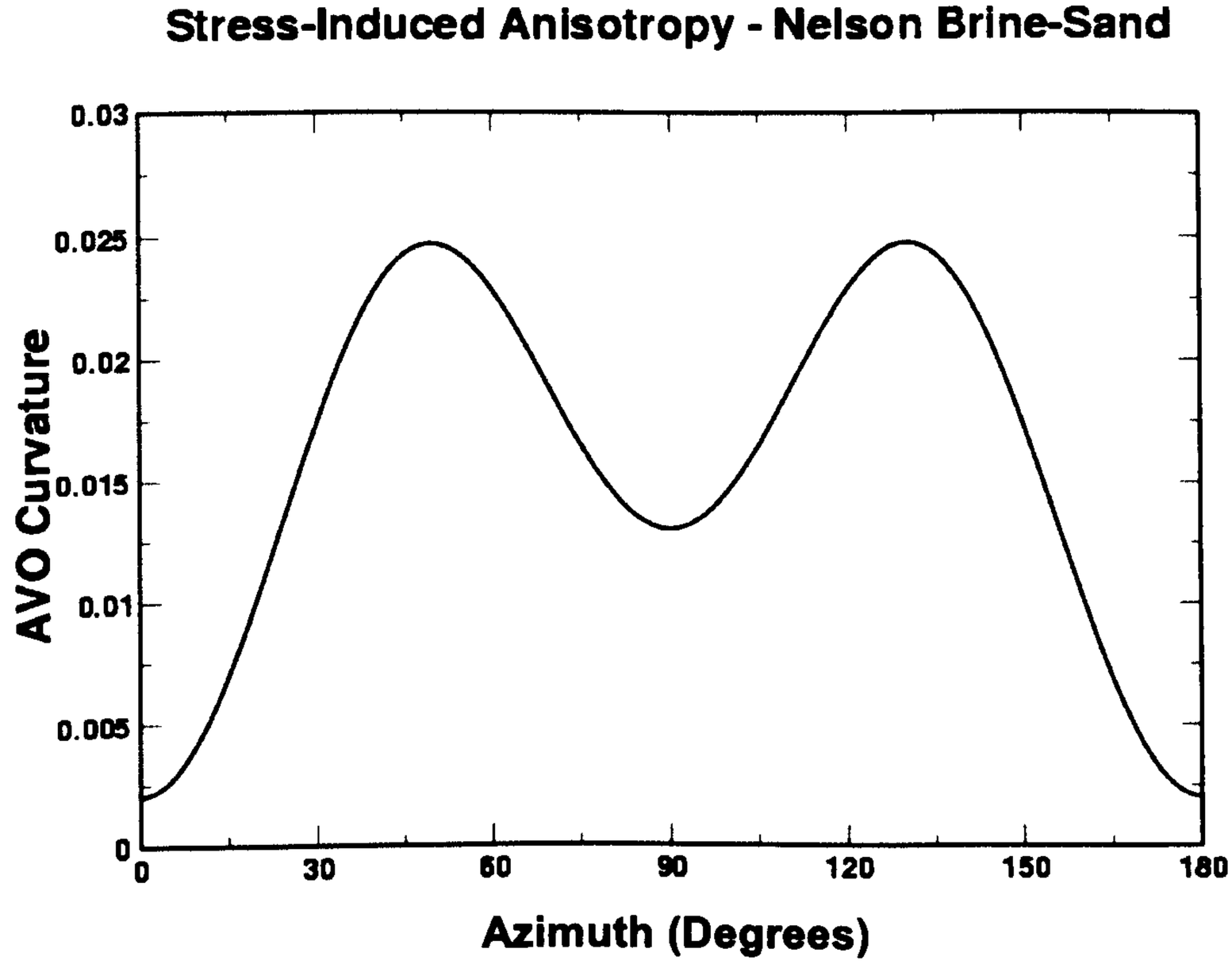

Figure 4.13: AVO curvature of the Nelson oil–water contact, using fracture-induced anisotropy (top), compared with stress-induced anisotropy (bottom).

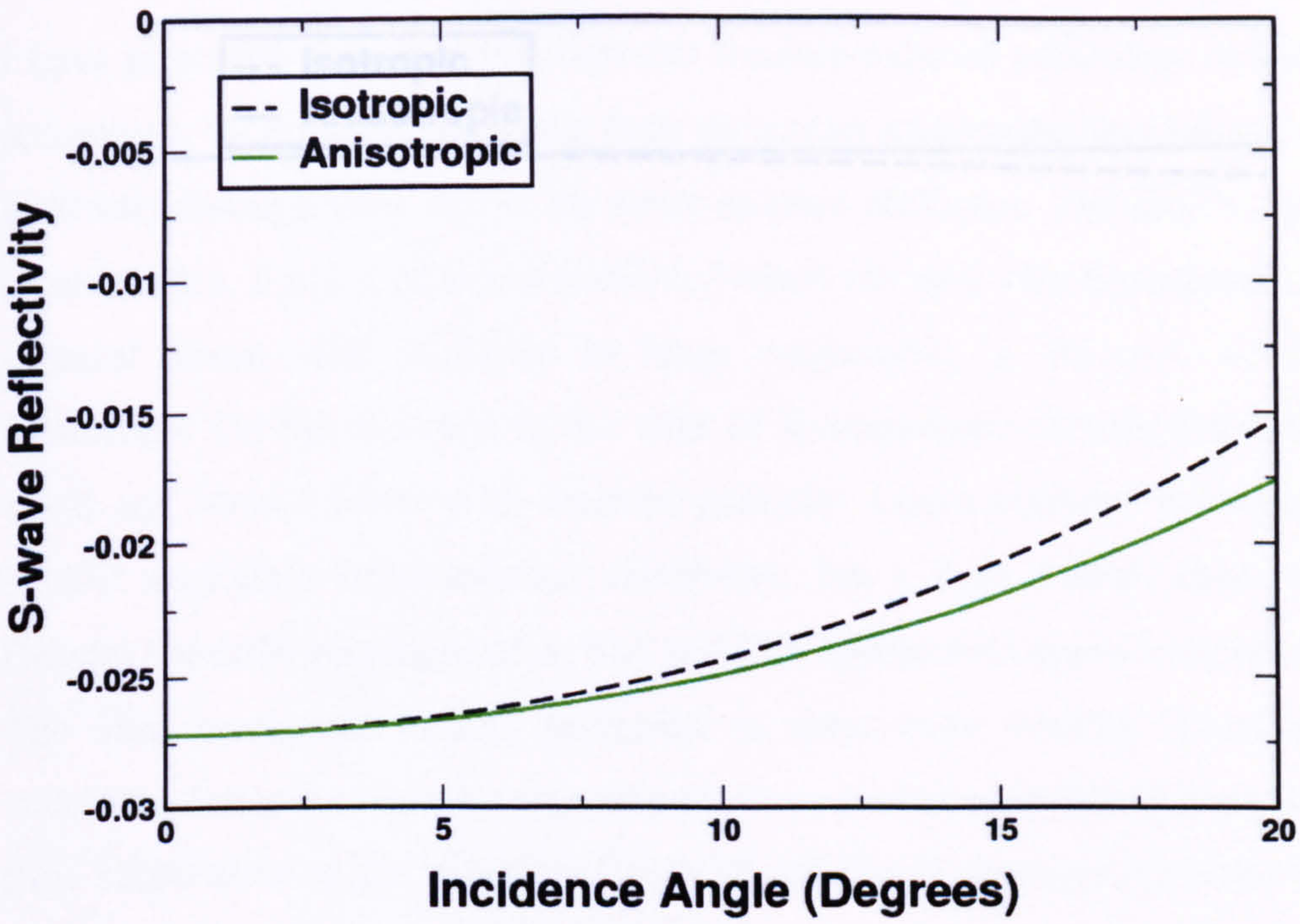

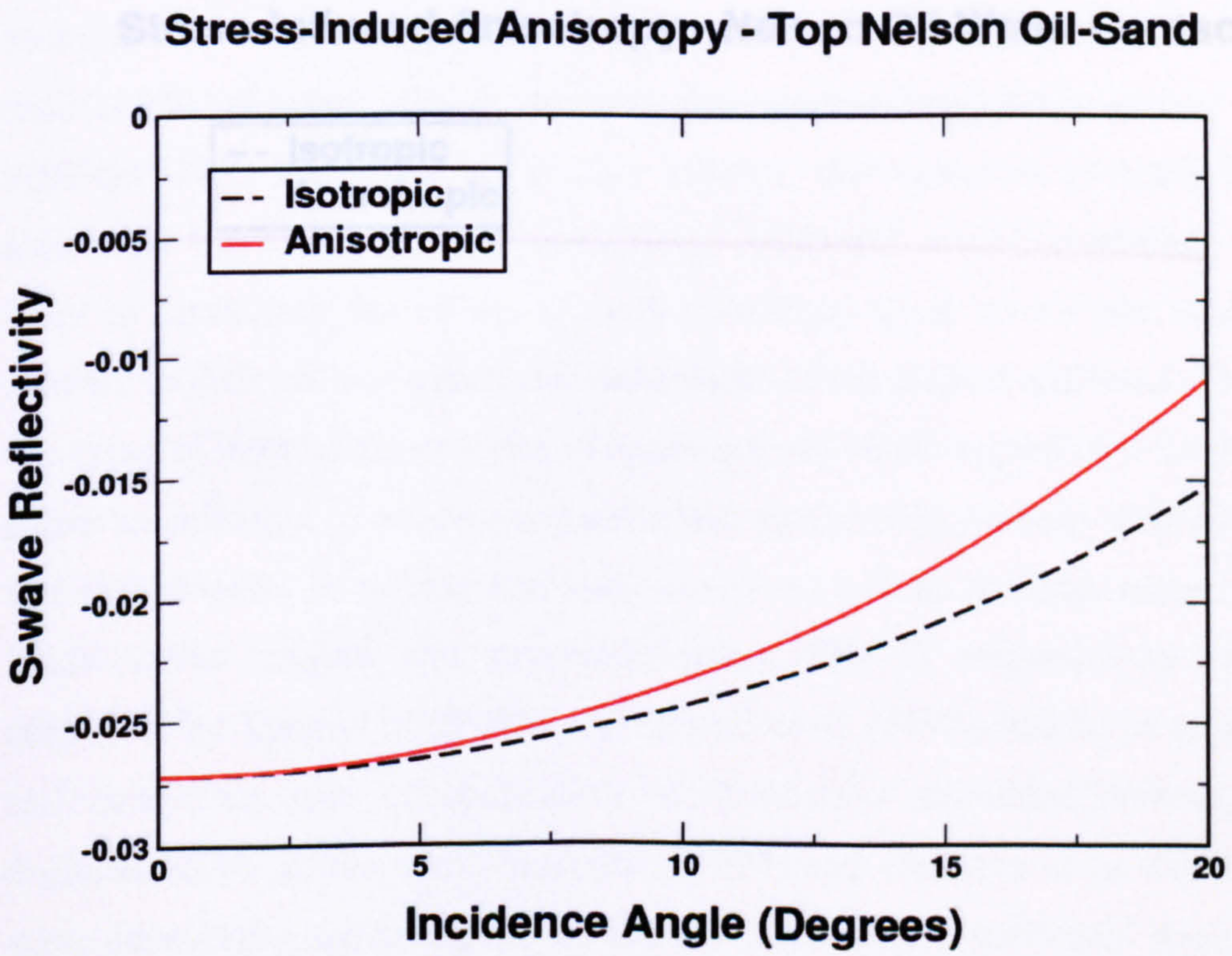

Figure 4.14: S-wave reflectivity of the Top Nelson oil-sand, using fracture-induced anisotropy (top), compared with stress-induced anisotropy (bottom).

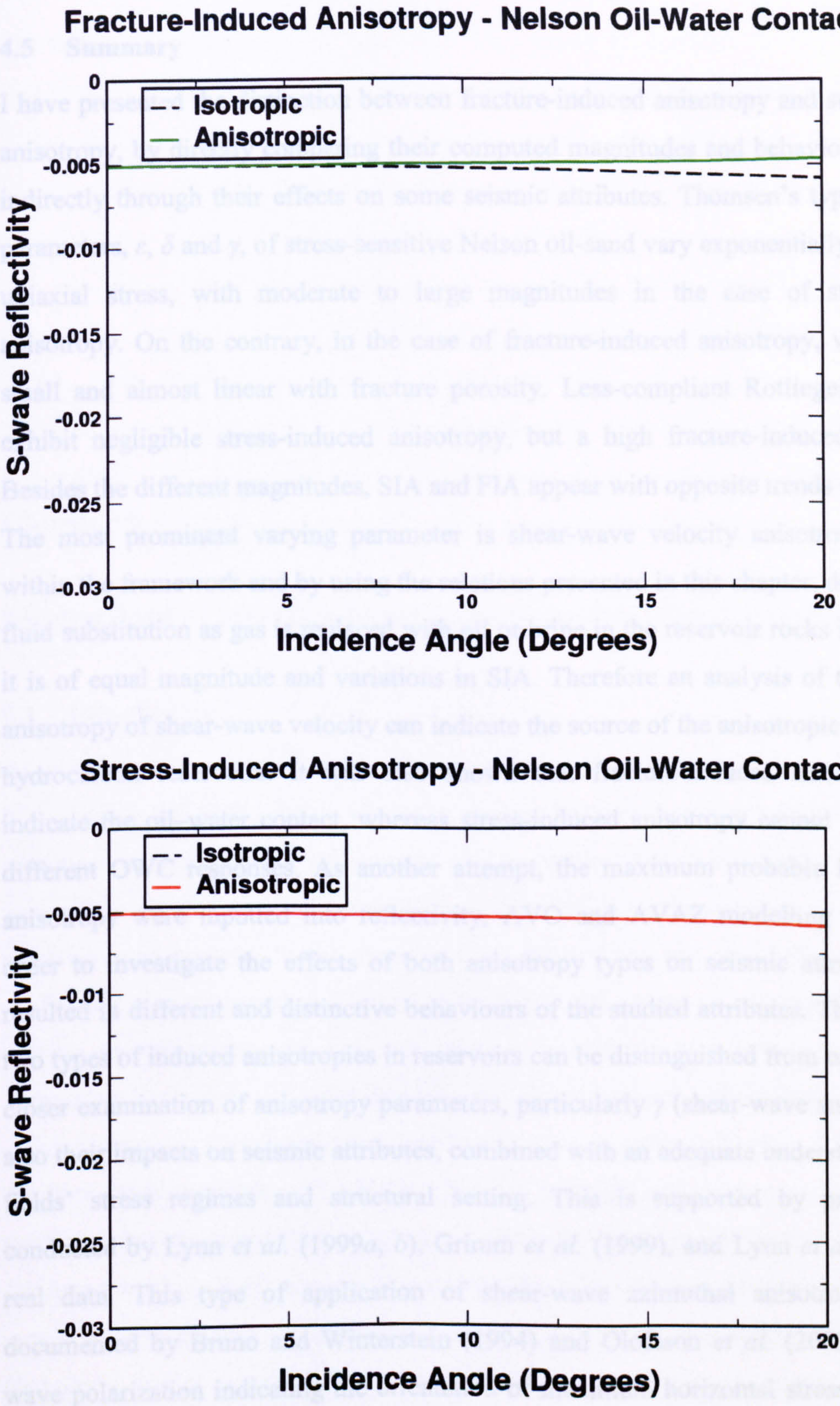

Figure 4.15: S-wave reflectivity of the Nelson oil–water contact, using fracture-induced anisotropy (top), compared with stress-induced anisotropy (bottom).

4.5 Summary

I have presented the distinction between fracture-induced anisotropy and stress-induced anisotropy, by directly comparing their computed magnitudes and behaviours, and also indirectly through their effects on some seismic attributes. Thomsen's type anisotropy parameters, ε, δ and γ, of stress-sensitive Nelson oil-sand vary exponentially with excess uniaxial stress, with moderate to large magnitudes in the case of stress-induced anisotropy. On the contrary, in the case of fracture-induced anisotropy, variations are small and almost linear with fracture porosity. Less-compliant Rotliegend gas-sands exhibit negligible stress-induced anisotropy, but a high fracture-induced anisotropy. Besides the different magnitudes, SIA and FIA appear with opposite trends of behaviour. The most prominent varying parameter is shear-wave velocity anisotropy, γ, which within the framework and by using the relations presented in this chapter, decreases with fluid substitution as gas is replaced with oil or brine in the reservoir rocks in FIA, while it is of equal magnitude and variations in SIA. Therefore an analysis of the azimuthal anisotropy of shear-wave velocity can indicate the source of the anisotropic behaviour of hydrocarbon reservoirs. It was also shown that fracture-induced anisotropy might indicate the oil–water contact, whereas stress-induced anisotropy cannot do so due to different OWC responses. As another attempt, the maximum probable FIA and SIA anisotropy were inputted into reflectivity, AVO and AVAZ modelling scenarios, in order to investigate the effects of both anisotropy types on seismic attributes, which resulted in different and distinctive behaviours of the studied attributes. Therefore these two types of induced anisotropies in reservoirs can be distinguished from one another by closer examination of anisotropy parameters, particularly γ (shear-wave anisotropy) and also their impacts on seismic attributes, combined with an adequate understanding of the fields' stress regimes and structural setting. This is supported by previous work conducted by Lynn *et al.* (1999*a*, *b*), Grimm *et al.* (1999), and Lynn *et al.* (1999*c*) on real data. This type of application of shear-wave azimuthal anisotropy has been documented by Bruno and Winterstein (1994) and Olofsson *et al.* (2003) through S-wave polarization indicating the orientation of maximum horizontal stress and fracture apertures.

Chapter 5

Implications of Stress-Induced Anisotropy for Time-Lapse Seismic

5.1 Introduction

As we saw in previous chapters, the stress-induced anisotropy may be important for investigating different seismic attributes, so here I intend to examine its influence on 4D signature. In Section 5.2 I will present a short review of time-lapse seismic monitoring as a tool to assist in reservoir management, although its applications are not restricted to reservoir management. In the same section, the success and credibility of time-lapse studies are also discussed and linked to the basic assumption of isotropy, which in turn creates an opportunity to link the topic to variations of seismic amplitude with parameters like offset – the distance between seismic source and receivers, and azimuth – the orientation of the source–receiver line relative to north. In Section 5.3 I will model the time–lapse response of the Nelson Field in isotropic and anisotropic scenarios. It is predicted that stress-induced anisotropy is likely to have a moderate to large impact on the interpretation of 4D seismic signatures. The effect is most obvious when base and repeat surveys are shot along different azimuths, but it can also be important in surveys shot along similar azimuths. The stress-induced anisotropy effects equate to a very large error in estimating pressure from the top reservoir event in the Palaeocene sands of the Nelson Field and an OWC movement uncertainty of 18 ft.

5.2 Time-Lapse Seismic and Assumption of Isotropy

Anisotropy of seismic-wave velocities has found recognition in the oil industry. However, it would be anomalous to have velocity isotropy in rock formations. In some reservoirs, the magnitude of the observed anisotropy is low, and consequently its contribution to seismic studies is considered to be negligible. On the contrary, in certain reservoirs the impact of velocity anisotropy is so huge that by only taking it into account can one avoid imaging problems, misties, vertical errors, *etc.* Detecting velocity anisotropy in rocks benefits virtually all of the key stages of a conventional seismic study: such as velocity analysis, normal move-out, dip move-out, stacking and time/depth migration. Many attribute analyses, such as amplitude variations with offset and azimuth, are also affected by velocity anisotropy, and hence the corresponding corrections will result in a remarkable improvement in the end product.

Many of the time-lapse examples to date (with the exception of the Colorado School of Mines' Reservoir Characterization Group) have worked without anisotropy. Among those who have not considered velocity anisotropy in their time-lapse studies are: Boyd-Gorst *et al.* (2001), Hansen *et al.* (2001), Davis *et al.* (2002), MacBeth *et al.* (2002) and McInally *et al.* (2003). But from those who have, I can mention the following: Duranti (2001) utilized shear-wave birefringence (splitting) and the corresponding azimuthal anisotropy in a time-lapse seismic study to map the dynamic changes resulting from CO_2 injection into porous and fractured dolomites of the Andres reservoir in the Vacuum Field, New Mexico, USA. Angerer *et al.* (2002) analysed two 4D, 3C onshore surveys of the same reservoir. Cabrera and Davis (2002) employed the 4D signature of shear-wave anisotropy for dynamic characterization of the San Andres carbonate reservoir.

First I will investigate AVO/AVAZ in the presence of azimuthal anisotropy induced by differential horizontal stresses illustrating how different the isotropic and anisotropic reflectivities will be. Next I will study the anticipated 4D signatures for two scenarios of isotropy and anisotropy of seismic-wave velocities. It is illustrated that, for a number of reservoirs, relying on the quantitative time-lapse results brought about by utilizing velocity isotropy is likely to carry a high risk of uncertainty. Anisotropic corrections in such circumstances resolve many intermediate ambiguities and enhance the final accuracy of time-lapse predictions.

Subtracting at least two 3D seismic surveys one from the other, the first one (the legacy or base survey) and the second one (the repeat or monitor survey) shot within several

years of reservoir activity, form a four-dimensional or time-lapse seismic analysis. The subject of study can be conventional seismic, VSP, converted mode waves, shear waves or varieties of seismic attributes. Further details on time-lapse seismic can be found in Jack (1998) and Tura and Lumley (1999).

Like other scientific techniques, time-lapse seismic is established upon some principles and assumptions. The more strict and realistic these are, the more reliable the time-lapse technique can be. Therefore, in order to increase the success rate and credibility of time-lapse studies, one should consider the assumptions upon which such studies are constructed. Among a few assumptions, I will discuss the isotropy of rock properties, and I will demonstrate a second scenario when this assumption is violated. In conventional seismic, where the compressional wave is our probe into the reservoir, the rock formations are assumed to behave isotropically, *i.e.* the propagated seismic wave travels with the same velocity in all directions. Time-lapse analyses will be close to complete once all corrections relating to velocity anisotropy are applied to the data.

After a brief introduction to the Nelson Field, its 4D signature with and without the isotropic assumption of seismic-wave velocities is investigated in adequate detail, revealing an error estimate while relying on the isotropic time-lapse technique which is currently common practice in the industry.

5.3 Modelling the Nelson 4D Response

5.3.1 The Reservoir Geology and Geophysics

The Nelson Field was discovered in 1988, following exploration activity for over two decades in the Central North Sea. The field is located 180 km east of Aberdeen. It lies under approximately 85 m of water in Blocks 22/11, 22/6a, 22/7 and 22/12a, in the vicinity of the Forties, Montrose and Arbroath Fields belonging to the same reservoir (Whyatt *et al.*, 1992. It is a Palaeocene anticline situated on the Forties–Montrose High. The Forties Sandstone Member containing this field belongs to the Sele Formation. Figure 5.1 shows a location map for the field. As Figure 5.1 illustrates, the Nelson Field is made up of four turbidite sand channels deposited at an approximate depth of 2195 m TVDSS (true vertical depth subsea). Production in this field started in 1994, at an initial rate of 60,000 barrels per day (according to the International Energy Agency Report of March 1994). The porosity of the reservoir rocks is around 23%, containing 270' of light

oil with 38° API. The permeability is in the range 50–1000 mD, and the reservoir temperature is about 107 °C.

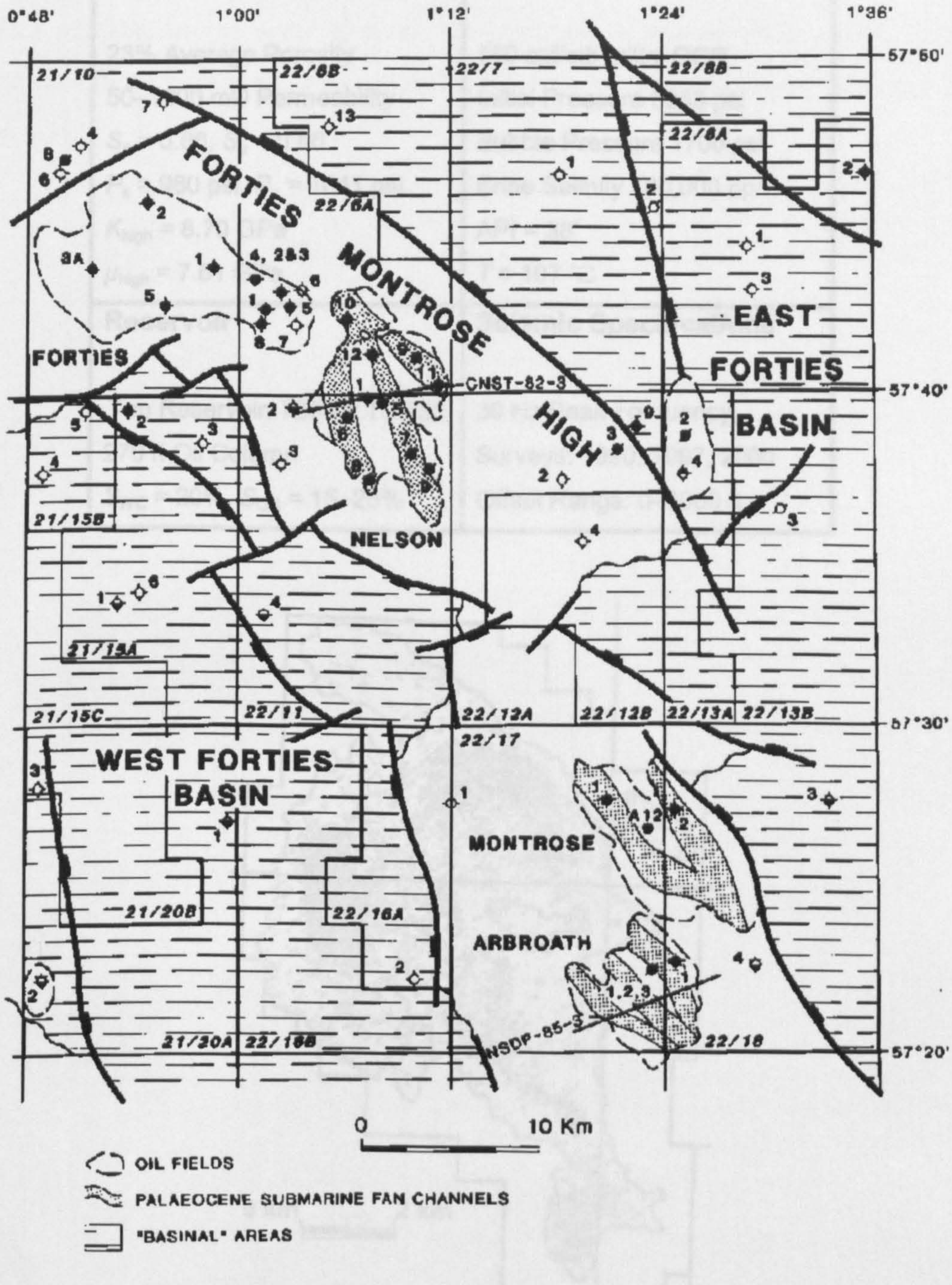

Figure 5.1: Location map of the Nelson Field (Whyatt et al., 1992).

The reservoir and fluid properties of the field are tabulated in Table 5.1. The first 3D survey was conducted in 1990, and a repeat survey was shot after three and a half years of production in 1997. Another 3D dataset was also acquired in the year 2000. The quality of seismic data is good, making Nelson a typical field for time-lapse studies. The first 3D seismic surveys were shot in the North Sea, and the first time-lapse studies were conducted in the Nelson Field. Figure 5.2 shows a 4D example from the field.

Table 5.1: Specifications of the Nelson Field, including reservoir-rock and fluid properties and seismic data vintages.

Forties Sandstone	**Fluids**
23% Average Porosity	550 scf/stb Initial GOR
50–1000 mD Permeability	Initial Pressure 3343 psi
S_κ = 0.66, S_μ = 0.66	Bubble Pressure 1700 psi
P_κ = 960 psi, P_μ = 1041 psi	Brine Salinity 100,000 ppm
K_{high} = 8.70 GPa	API = 38˚
μ_{high} = 7.61 GPa	T = 107 ˚C
Reservoir	**Seismic Specifications**
Top Reservoir: 7200 ft TVDSS	30 Hz Peak Frequency
270 ft Oil Column	Surveys: 1990, 1997, 2000
S_{WC} = 20%, S_{OR} = 15–25%	Offset Range: 0–8000 ft

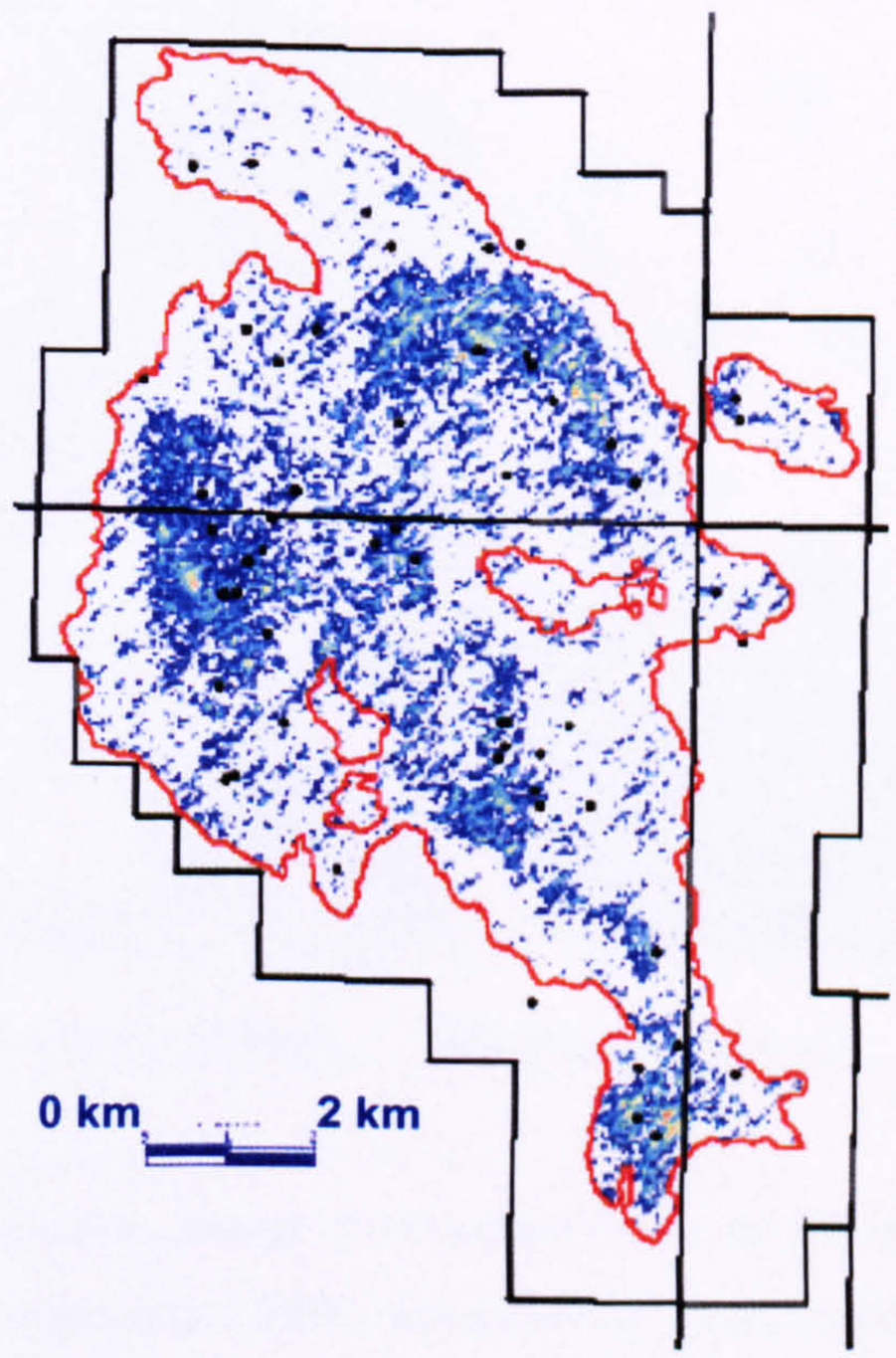

Figure 5.2: The Top Forties 4D response from far-offset stack results from 1990 to 1997 (MacBeth et al., 2002).

Boyd-Gorst *et al.* (2001) indicated that it is difficult to detect production changes due to water replacing oil, for P-wave impedance variations less than 4% -- implying limitations in estimating oil–water contact. MacBeth *et al.* (2002) emphasized that inter-

channel regions of the field filled with low net-to-gross sands reduce the resolution of the time-lapse signature. Here the fluid movement is not certain, and the predicted oil–water contact may be erroneous. The other problem that Nelson Field poses is the imperfect repeatability of some areas of the reservoir, which result in a high level of registration noise. The same type of noise is seen in the undershot peripheral zone (Figure 5.3).

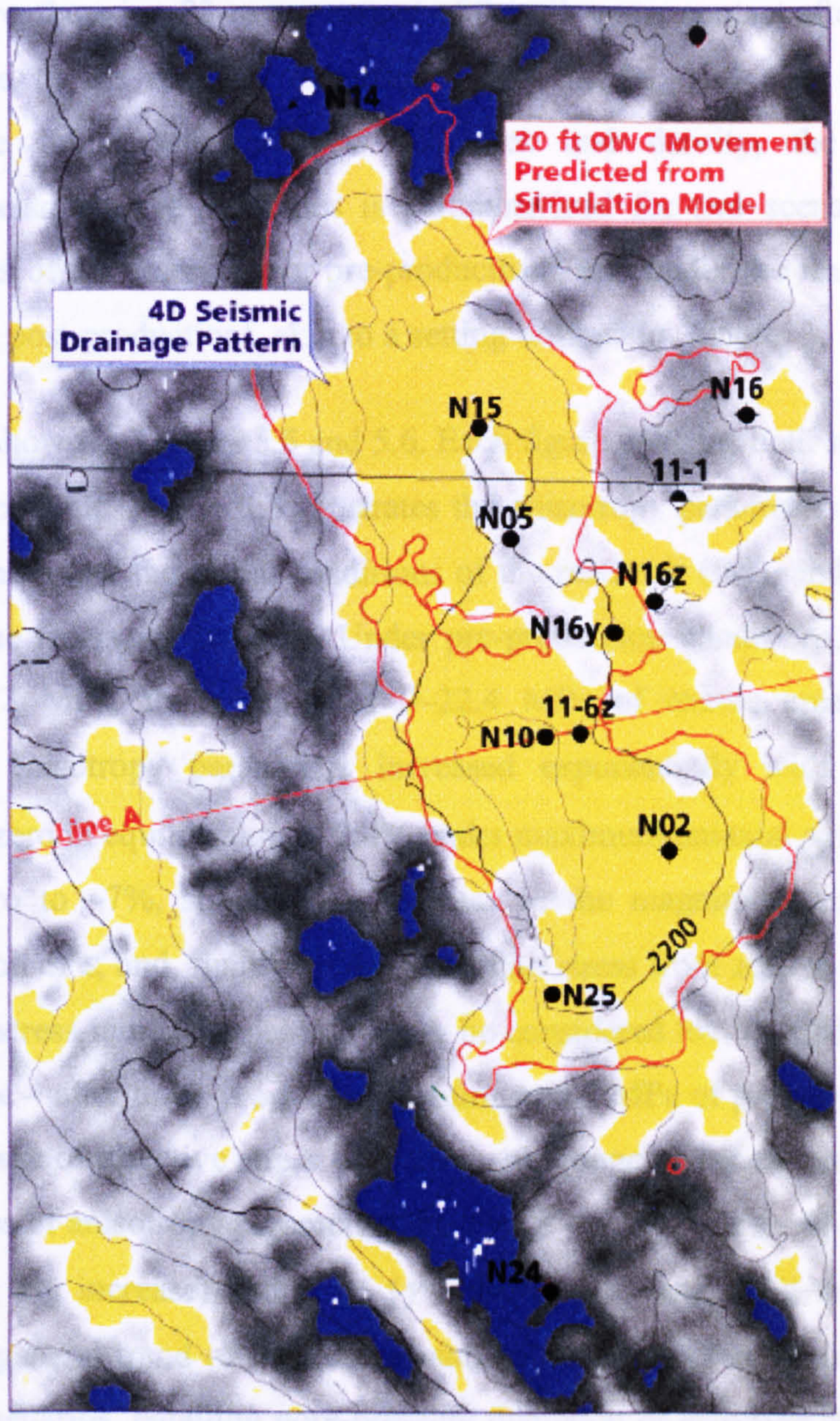

Figure 5.3: Maximum production change (yellow) indicated by far-offset difference data. The orange contour shows the anticipated OWC movement by flow simulation. The undershot area (to the west) is considered to be noisy (Boyd-Gorst et al., 2001).

5.3.2 Calculation of the Seismic Response

As mentioned in the previous section, the data acquired from the reservoir is of good quality, producing good AVO and 4D results; therefore, in this section I will try to investigate the isotropic AVO response of the reservoir, and also its anisotropic AVO and AVOAZ responses. In order to do this, the following model (Figure 5.4) is

considered. Inputting dry-frame rock properties into the Batzle and Wang (1992) relations, one can find those for the fluid-saturated rocks shown in Figure 5.4. As can be seen in the figure, there is a 23-m movement of the oil–water contact after three years of production. Due to the pressure depletion in the model, and also by using other parameters like initial saturated-rock velocities and density, the stress-induced anisotropy of seismic-wave velocities is parameterized for two scenarios: under the initial conditions of the reservoir (or pre-production), and under the final conditions of the reservoir (or post-production), akin to a setting utilized in Chapter 3.

The results are shown in Figures 5.5 and 5.6. Each figure contains both scenarios for one fluid type; for example, Figure 5.5 illustrates the anisotropy parameters of oil-saturated Nelson sandstone under the initial conditions of the reservoir (top), and under the final conditions of the reservoir (bottom). Under pre-production conditions, when the pore pressure was 23 MPa, for a range of 0–22.4 MPa of excess uniaxial stress, the magnitudes of anisotropy parameters increased exponentially with stress. Here ε increased from zero in equilibrium, to 2.4% under maximum uniaxial stress. Parameter δ varies from zero to –7%, showing an increase in the magnitude with stress in the opposite direction of ε, and, finally, γ increases with stress from zero to 6.8%. Although these ranges of stress-induced anisotropy may be considered low to medium, in the next part of the figure – after three years of production and 7 MPa of pore-pressure depletion and hence increase of effective stress – for the same range of excess uniaxial stress, the maximum values of anisotropy parameters are 3% (ε – showing a small increase), –11% (δ – showing a big increase) and 6.5% (γ – showing a very small and so negligible decrease). The general trend of increase of anisotropy parameters with excess uniaxial stress in both scenarios, entailing pore-pressure depletion or effective stress increase is, to a great degree, intuitively consistent with the increase in the saturated rock bulk modulus leading to an increase in seismic-wave velocities.

Based on the same circumstances, and again for a similar range of excess unaxial stress, brine-saturated Nelson sandstone under a pre-production scenario displays a higher (compared to the oil-saturated case) value for maximum ε (3%), a lower value for maximum δ(–5%) and an almost equal value for maximum γ(6.8%).

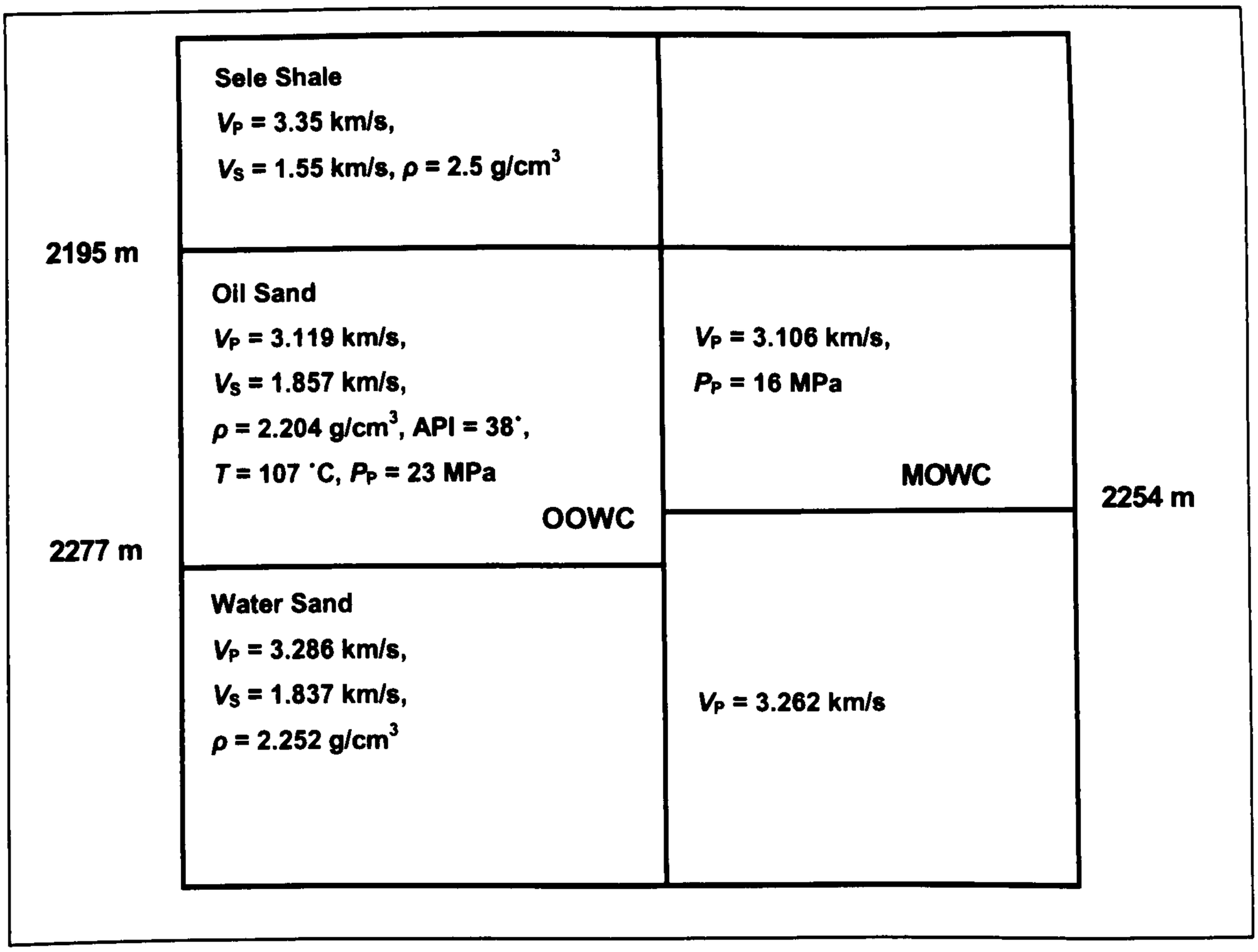

Figure 5.4: The Nelson reservoir model, comprising oil-sand and water-sand interfaces overlain by the Sele shale. The isotropic velocities of these saturated sandstones shown here are used to assign the background properties for the anisotropy calculation.

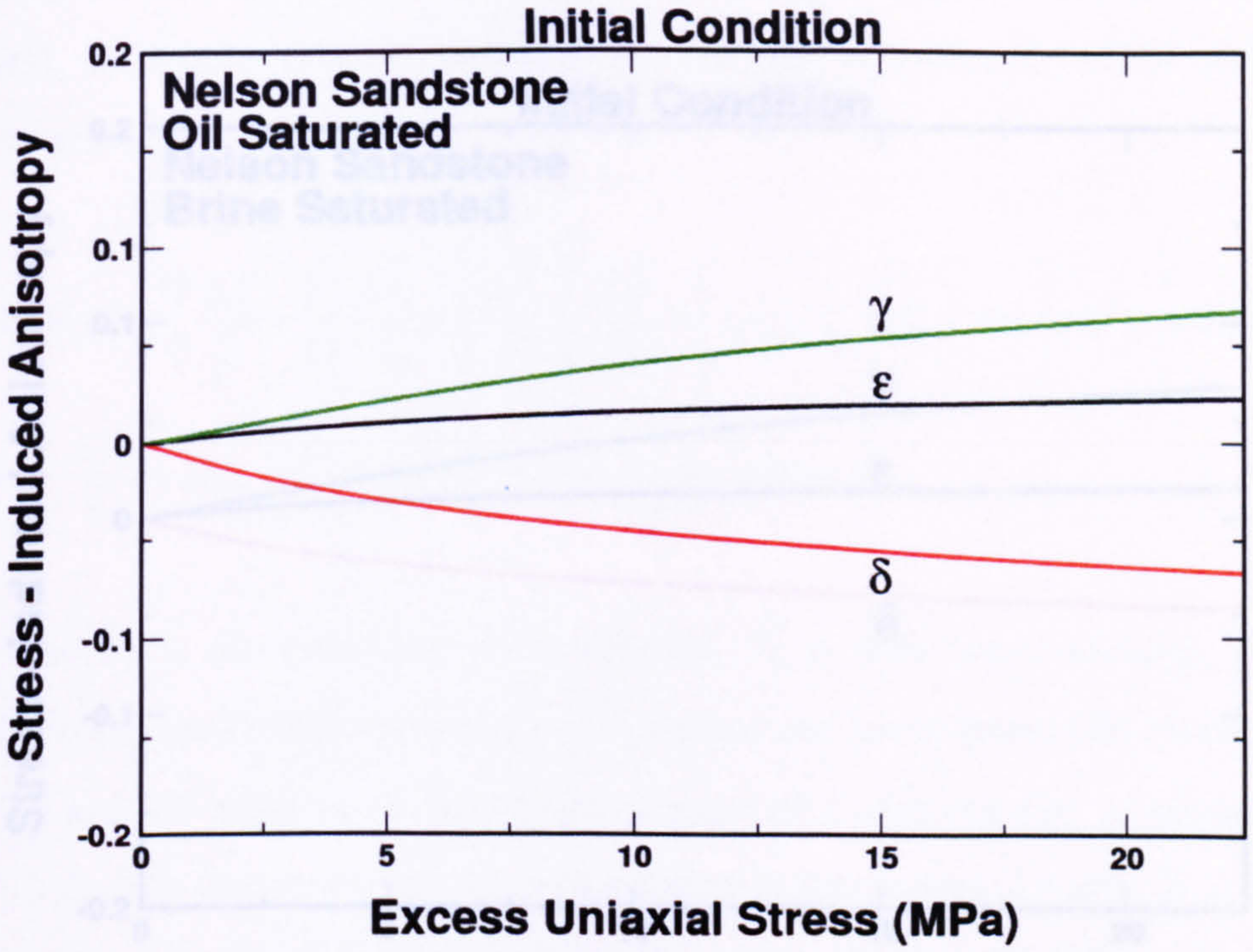

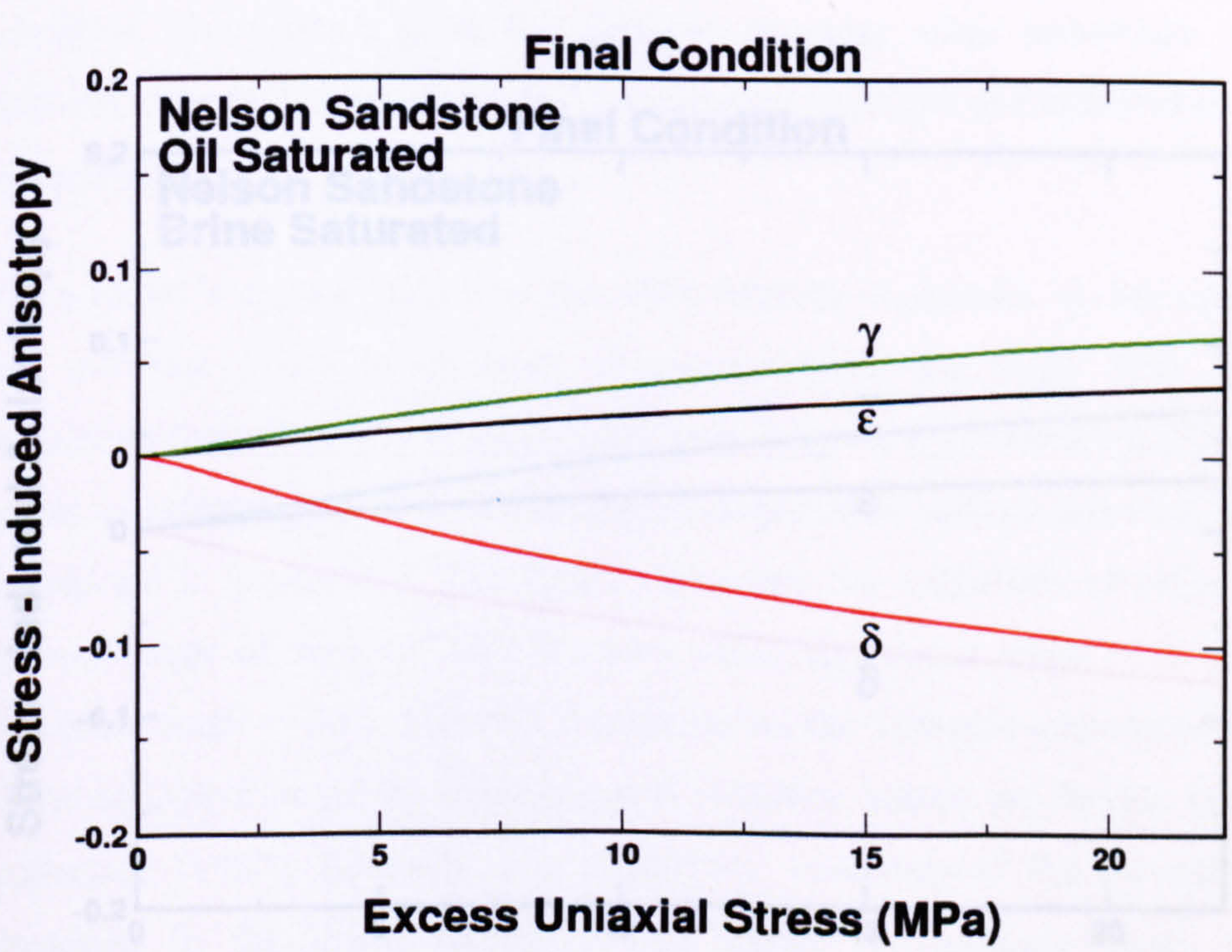

Figure 5.5: Stress-induced anisotropy of oil-saturated Nelson sandstone in 1990 (top) and 1997 (bottom). Due to pressure depletion, the anisotropy parameter δ shows a large increase. Variations of other parameters ε and γ are very small.

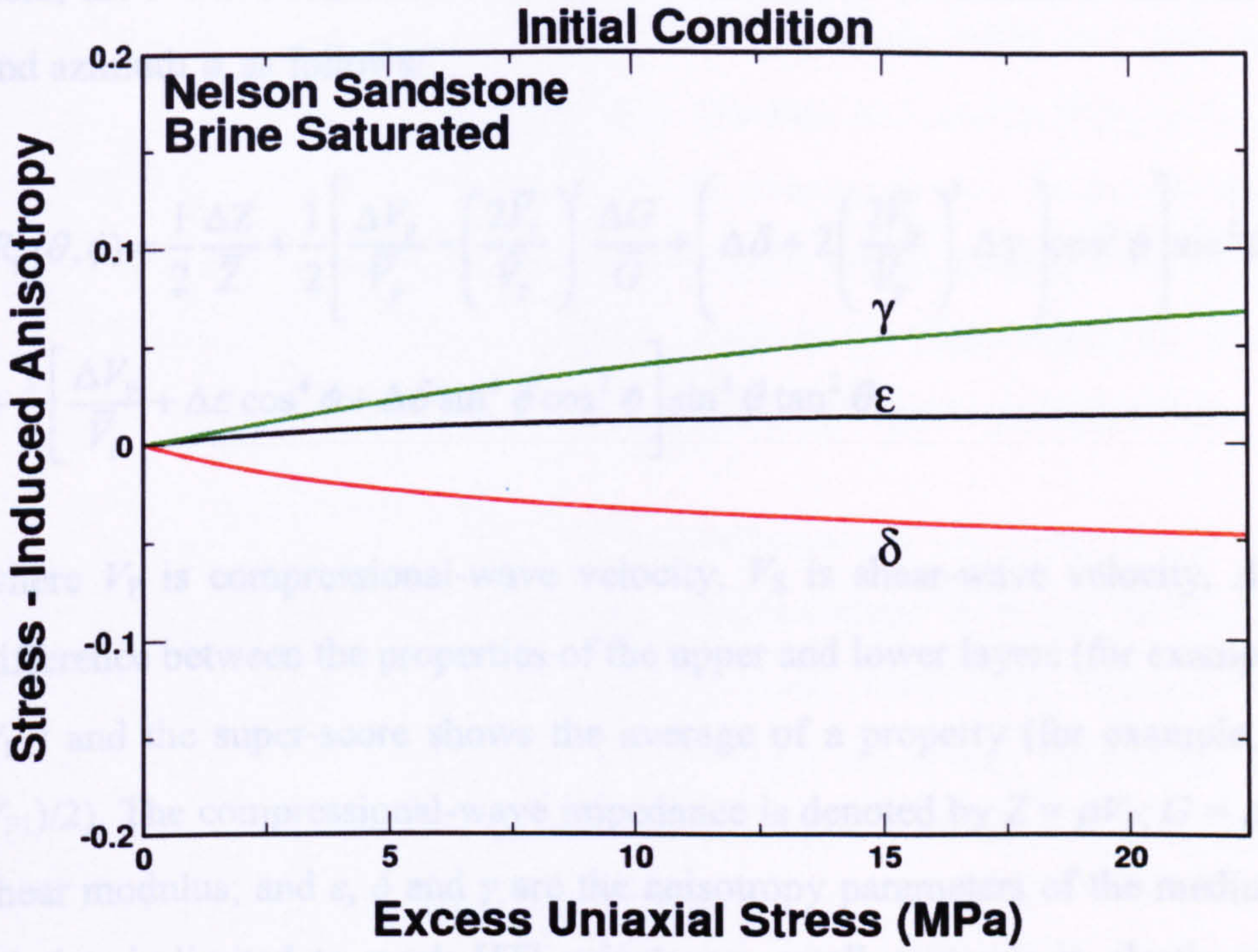

Figure 5.6: The same trend is seen in brine-saturated Nelson sandstone: ε and δ increase with effective stress.

When variation of azimuth is also taken into account, as seismic surveys can be shot in different azimuths or arbitrary azimuths other than the symmetry-axis direction of the field, the P-wave reflection coefficient is defined as a function of the incidence angle θ and azimuth ϕ, as follows:

$$R_{\mathrm{P}}(\theta,\phi)=\frac{1}{2}\frac{\Delta Z}{\bar{Z}}+\frac{1}{2}\left[\frac{\Delta V_{\mathrm{P}}}{\bar{V}_{\mathrm{P}}}-\left(\frac{2\bar{V}_{\mathrm{S}}}{\bar{V}_{\mathrm{P}}}\right)^2\frac{\Delta G}{\bar{G}}+\left(\Delta\delta+2\left(\frac{2\bar{V}_{\mathrm{S}}}{\bar{V}_{\mathrm{P}}}\right)^2\Delta\gamma\right)\cos^2\phi\right]\sin^2\theta$$
$$+\frac{1}{2}\left[\frac{\Delta V_{\mathrm{P}}}{\bar{V}_{\mathrm{P}}}+\Delta\varepsilon\cos^4\phi+\Delta\delta\sin^2\phi\cos^2\phi\right]\sin^2\theta\tan^2\theta \qquad (5.1)$$

where V_{P} is compressional-wave velocity, V_{S} is shear-wave velocity, Δ indicates the difference between the properties of the upper and lower layers (for example $\Delta V_{\mathrm{P}} = V_{\mathrm{P2}} - V_{\mathrm{P1}}$) and the super-score shows the average of a property (for example, $\bar{V}_{\mathrm{P}} = (V_{\mathrm{P2}} + V_{\mathrm{P1}})/2$). The compressional-wave impedance is denoted by $Z = \rho V_{\mathrm{P}}$; $G = \rho V_{\mathrm{S}}^2$ is vertical shear modulus; and ε, δ and γ are the anisotropy parameters of the medium. The above relation is limited to weak HTI anisotropy, small contrasts in elastic parameters and velocities. The relation gives the isotropic response when anisotropy parameters are assumed to be null. A more detailed treatment of isotropic and anisotropic AVO is given in Appendix 4.

Using Shuey's approximation to the AVO relation (Appendix 4), the reflectivity of the first interface (shale to oil-sand) is calculated for the years 1990 and 1997. For calculating the reflectivity in anisotropic case, Rüger's approximation (Equation 5.1) and values of anisotropy parameters computed in previous sections are used, and the results are plotted in Figure 5.7. The figure illustrates the variations of reflectivity with an azimuth range of zero to 180°, for near offset (incidence angle = 10°) and far offset (incidence angle = 30°). Figure 5.7 (top) shows the isotropic and anisotropic variations of the reflectivities of the shale/oil-sand interface before production (1990) and after production (1997). Similarly, the reflectivity variations of the oil–water contact are illustrated in the lower section of the figure. In isotropic cases, the computed reflectivities of each incidence angle (for instance 30°), are the same for the whole range of azimuths, while, in anisotropic cases, they vary with azimuth. The maximum differences between isotropic and anisotropic reflectivities are seen at an azimuth of zero. At an azimuth of 90°, the isotropic and anisotropic results are equal. The same pattern occurs for an incidence angle of 10°, but with less magnitude of variations.

In the next step, synthetic seismograms are generated by convolving reflectivity series with a 35 Hz zero-phase Ricker wavelet, at azimuths of zero and 90° for both cases in 1990 and 1997. For an azimuth of 0° there is a slight difference between isotropic and anisotropic AVAZ responses at the first interface in near-offset stack. In far-offset stack, the isotropic response is stronger than the anisotropic one. At the oil–water contact, for the far offset, the anisotropic case shows larger amplitude than the isotropic one (Figure 5.8). As the reflectivity at an azimuth of 90° in the anisotropic case is equal to that of isotropic case, the seismograms thus generated are identical (Figure 5.9).

Figure 5.10 compares the isotropic time-lapse results with those for the anisotropic case. Considering the first interface (shale/oil-sand) a slight 4D signal can be observed for far-offset stack, while time-lapse computed upon anisotropic assumptions produces an observable 4D signal in the middle-offset stack and a very good signal in the far-offset stack. The lower parts of Figure 5.10 and Figure 5.11 show the results of anisotropic time-lapse analysis for different azimuths.

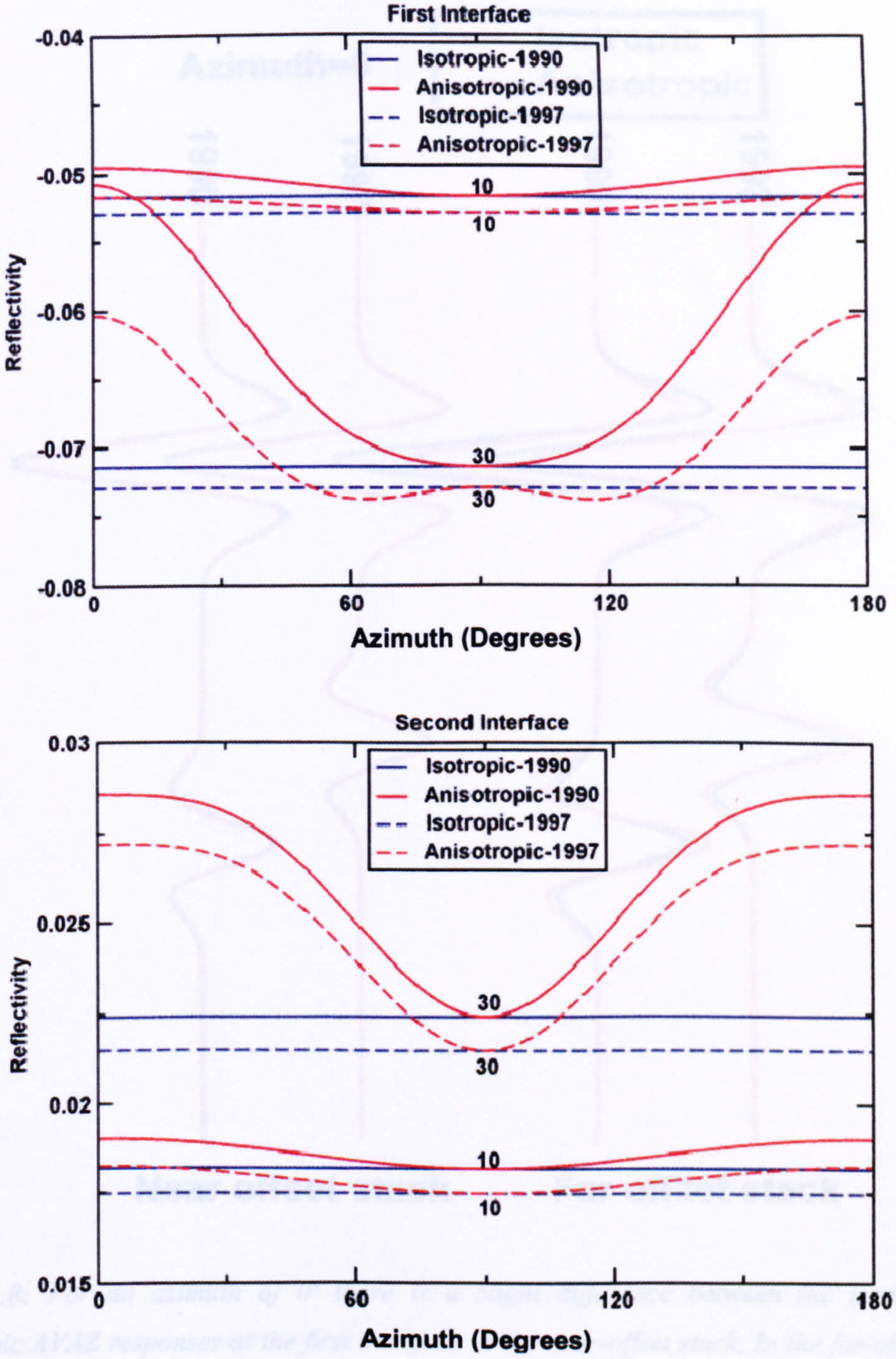

Figure 5.7: Variations in reflectivities for the first interface (shale/oil-sand) (top), and the second interface (oil-sand/water-sand) (bottom): isotropic versus anisotropic approaches in 1990 and 1997 for near offset (incidence angle = 10°) and far offset (incidence angle = 30°).

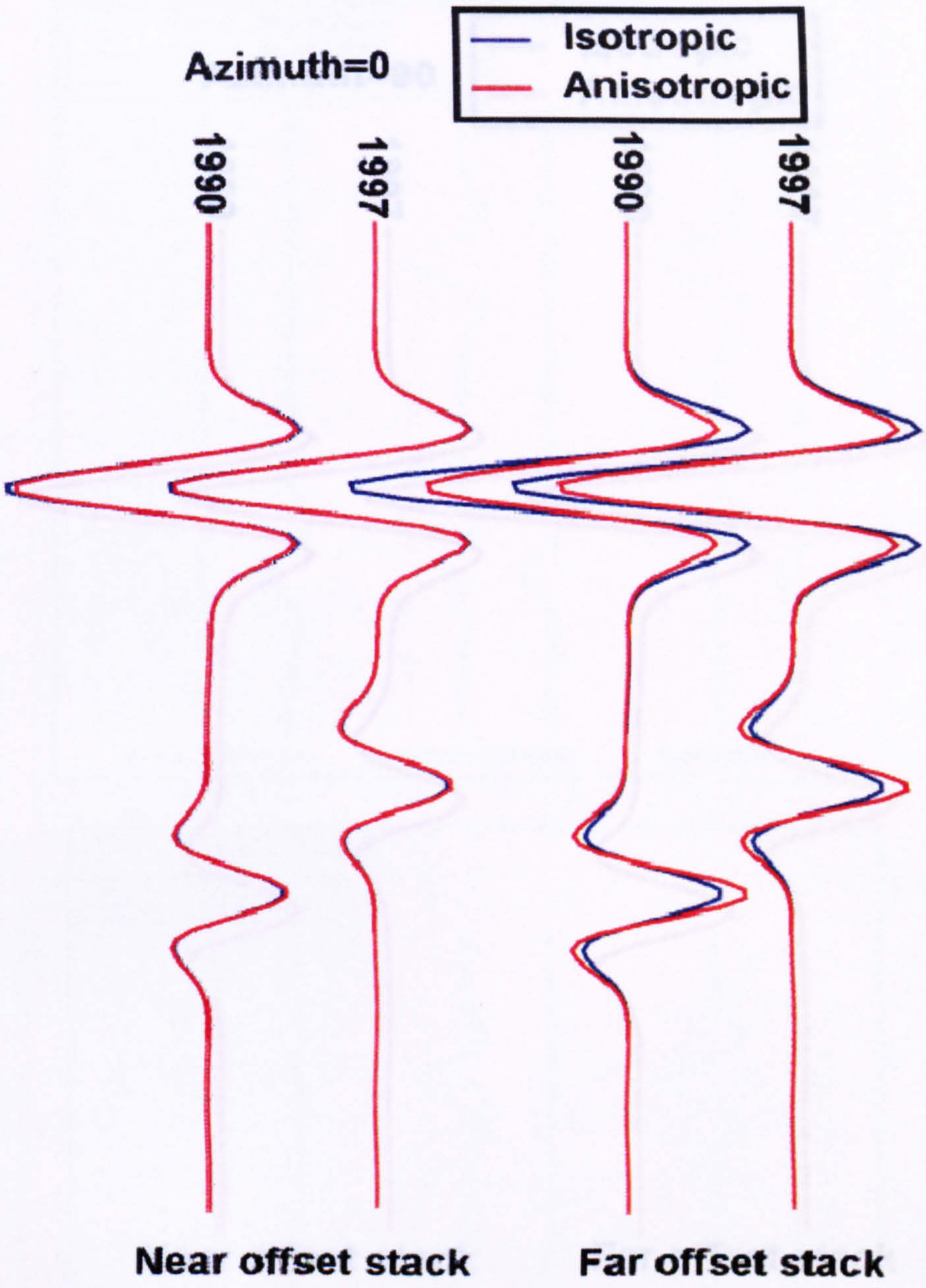

Figure 5.8: For an azimuth of 0° there is a slight difference between the isotropic and anisotropic AVAZ responses at the first interface in the near-offset stack. In the far-offset stack, the isotropic response is stronger than the ansiotropic one. At the oil–water contact, for the far offset, the anisotropic case shows a larger amplitude than the isotropic one.

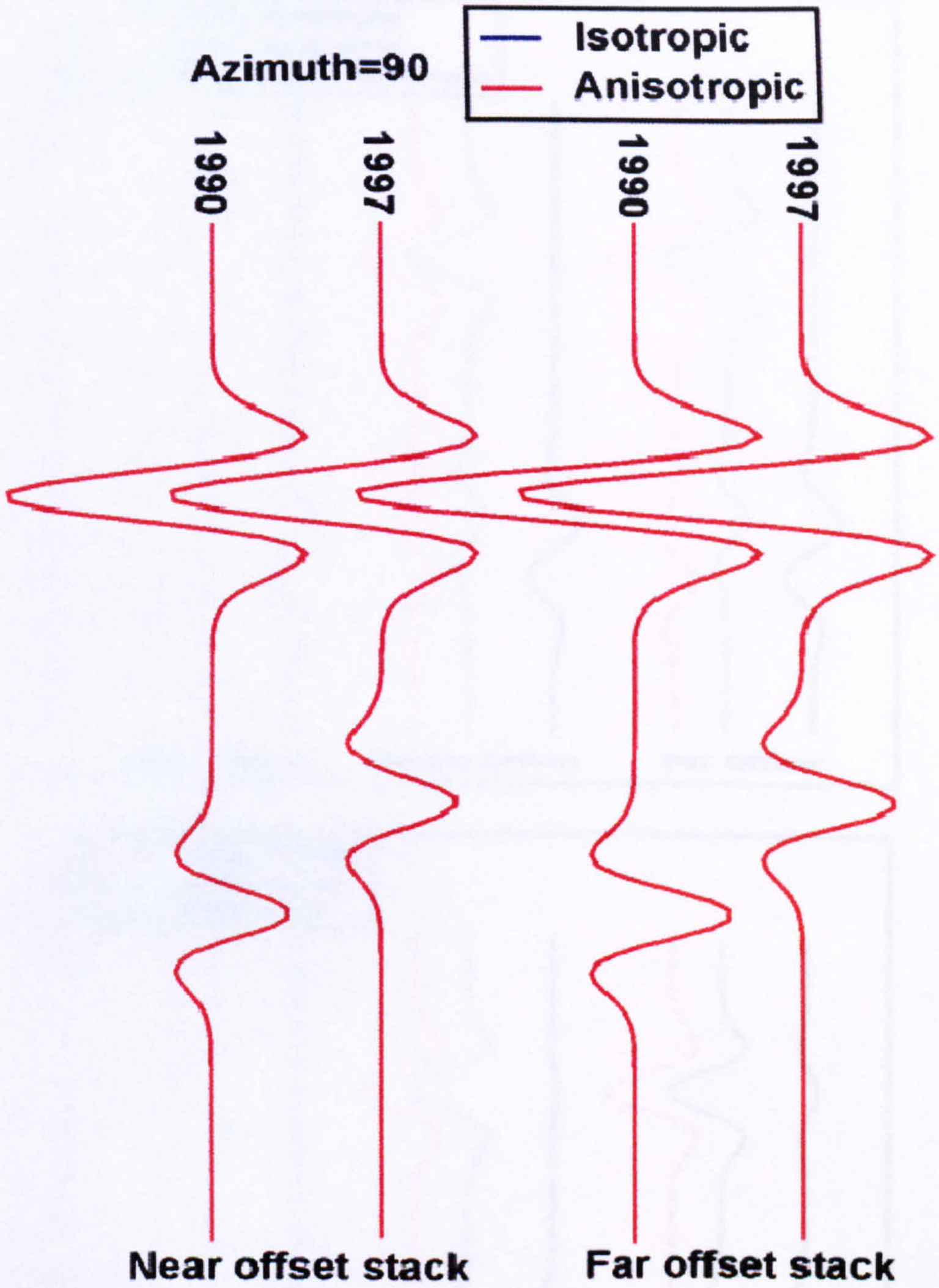

Figure 5.9: As the reflectivity for azimuth 90° in the anisotropic case is equal to that of the isotropic case, the seismograms generated are identical.

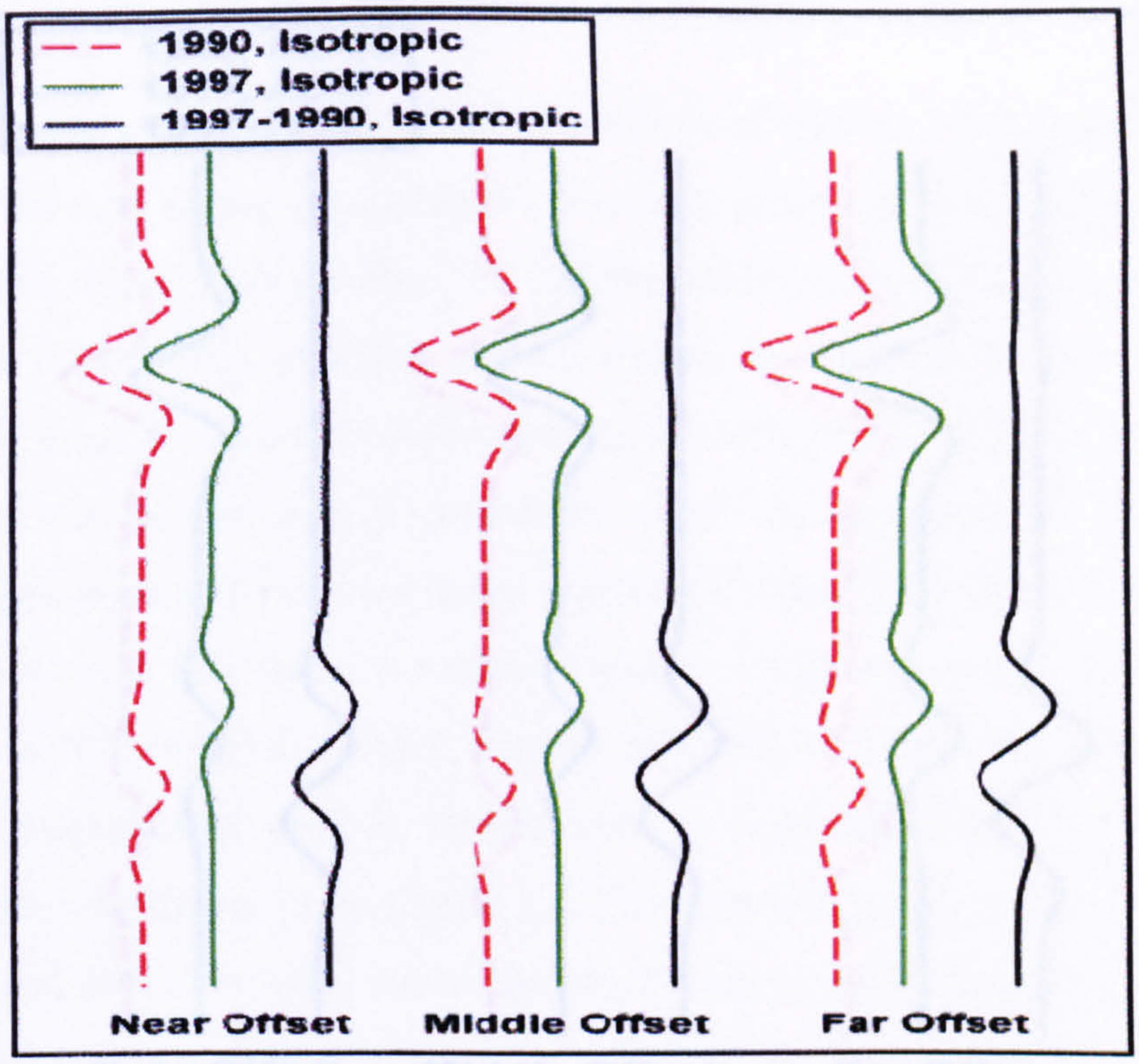

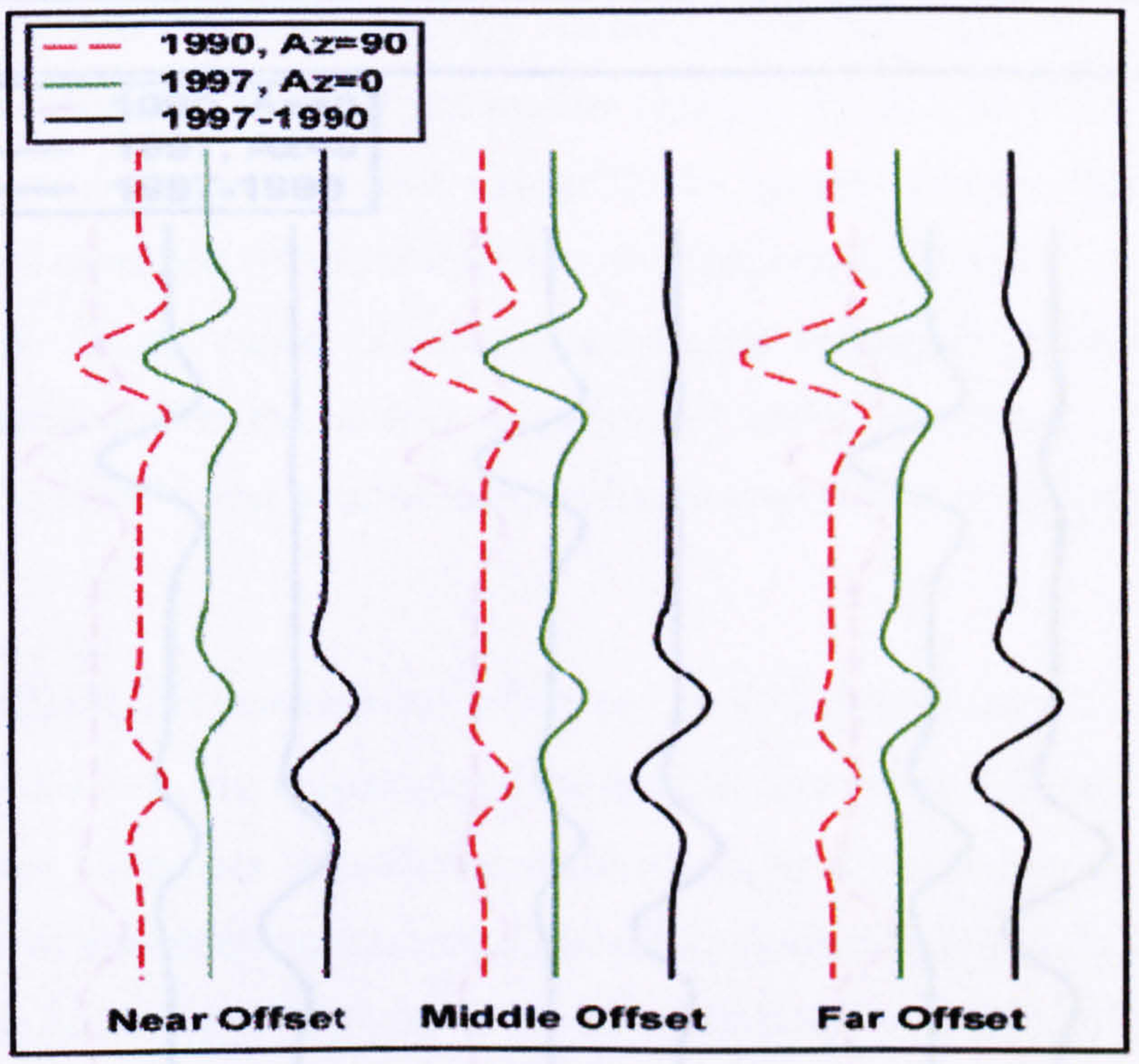

Figure 5.10: Results of isotropic (top) compared to anisotropic (bottom) scenarios. The 4D signal of the top reservoir is very good in far-offset stack and observable in the middle-offset stack of anisotropic case, but the isotropic case shows a weak signal in far-offset stack only.

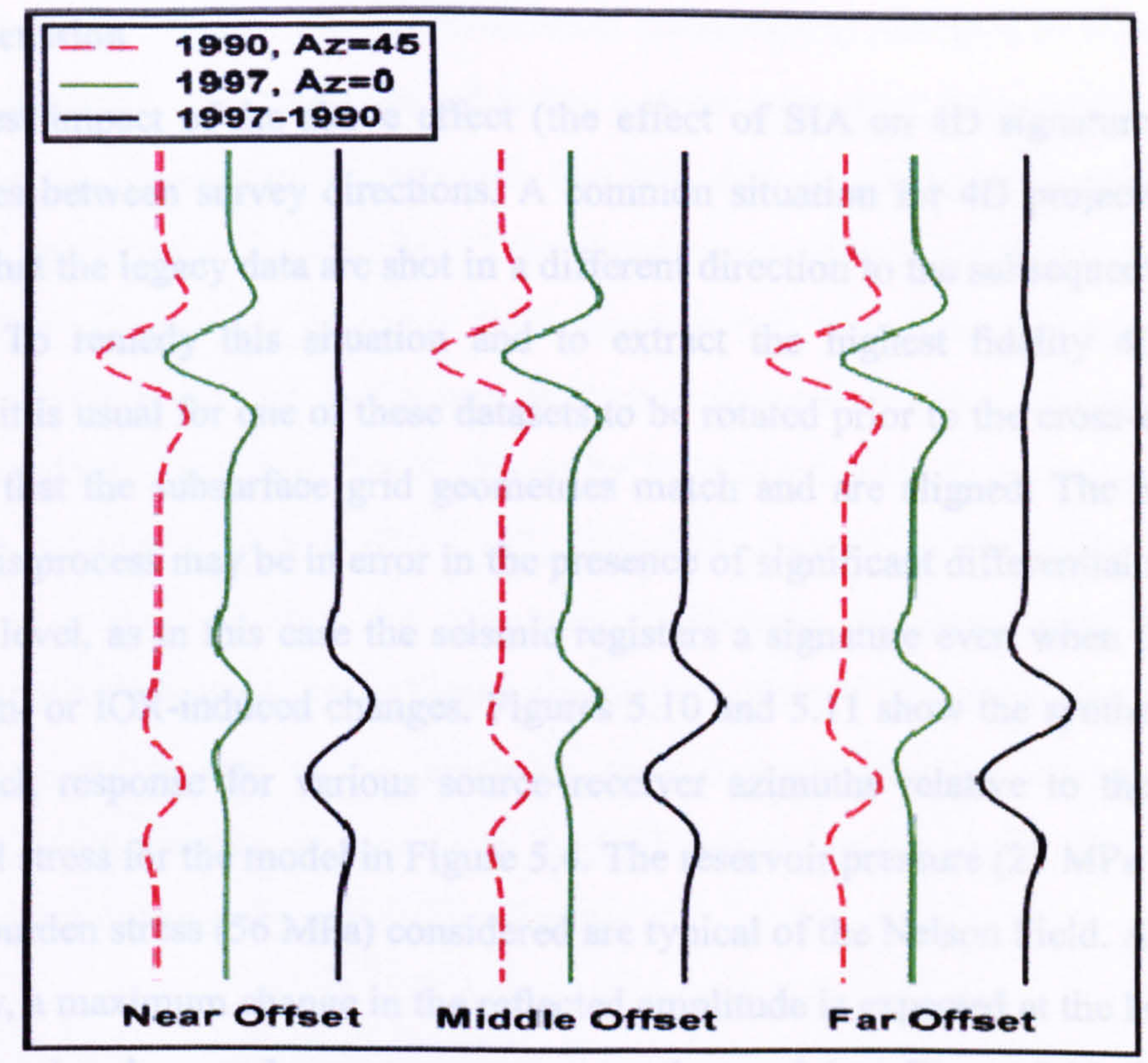

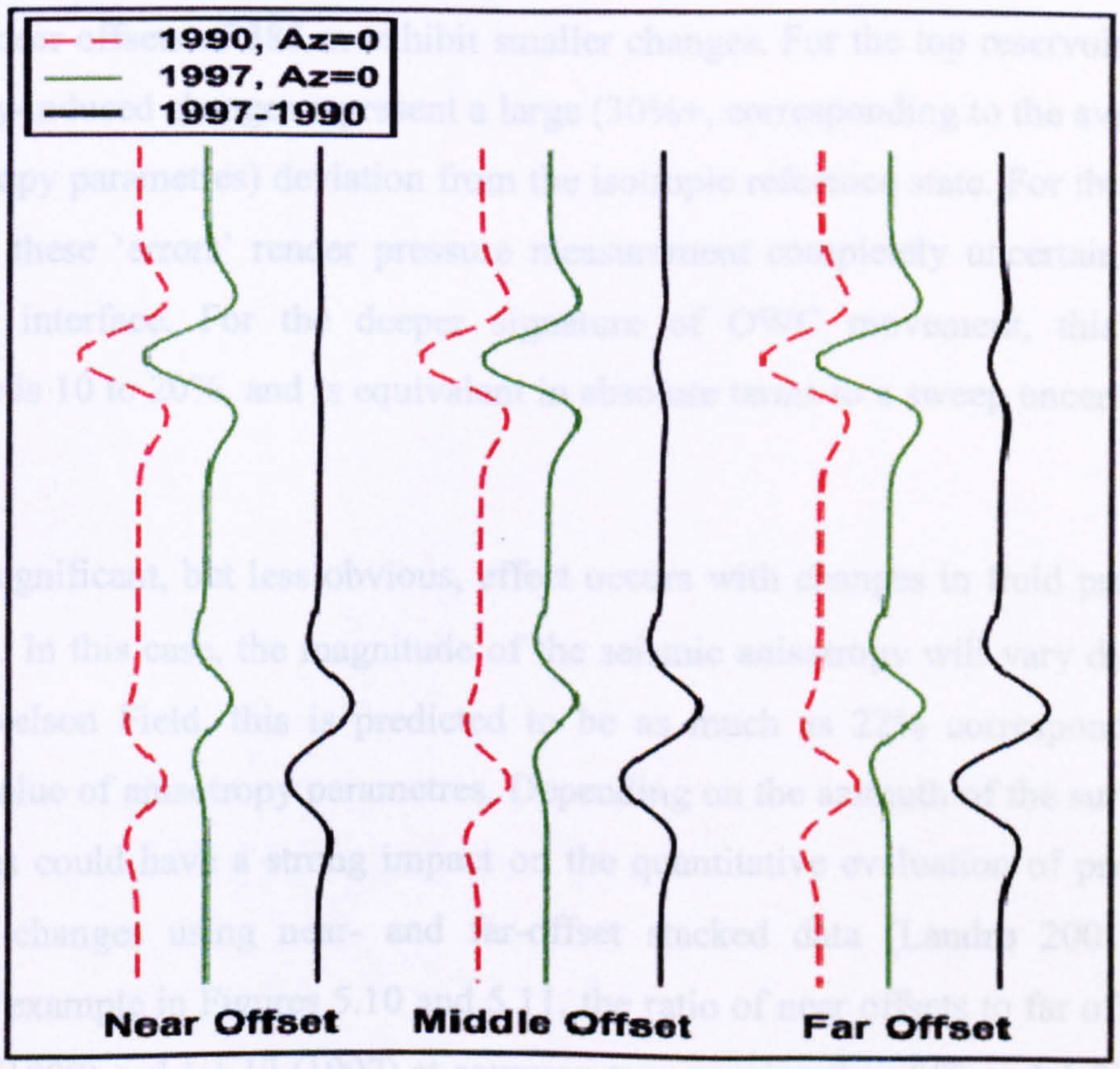

Figure 5.11: Different azimuths, producing varying 4D signature: comparison between azimuths 0/45 (top) and azimuth 0 (bottom).

5.4 Discussion

The largest impact of the above effect (the effect of SIA on 4D signature) is due to differences between survey directions. A common situation for 4D projects in mature fields is that the legacy data are shot in a different direction to the subsequently repeated datasets. To remedy this situation and to extract the highest fidelity 4D signature possible, it is usual for one of these datasets to be rotated prior to the cross-equalization stage, so that the subsurface grid geometries match and are aligned. The assumptions behind this process may be in error in the presence of significant differential stress at the reservoir level, as in this case the seismic registers a signature even when there are no production- or IOR-induced changes. Figures 5.10 and 5.11 show the synthetic limited-offset stack response for various source–receiver azimuths relative to the maximum horizontal stress for the model in Figure 5.4. The reservoir pressure (23 MPa to 16 MPa) and overburden stress (56 MPa) considered are typical of the Nelson Field. According to the theory, a maximum change in the reflected amplitude is expected at the largest offset (2052 m), when base and repeat surveys are orthogonal (see Figure 5.10 (bottom)). In contrast, near offsets of 385 m exhibit smaller changes. For the top reservoir event, the anisotropy-induced changes represent a large (30%+, corresponding to the average value of anisotropy parametres) deviation from the isotropic reference state. For this particular reservoir, these 'errors' render pressure measurement completely uncertain using this particular interface. For the deeper signature of OWC movement, this effect on amplitude is 10 to 20%, and is equivalent in absolute terms to a sweep uncertainty of 18 ft.

Another significant, but less obvious, effect occurs with changes in fluid pressure (and hence σ_0). In this case, the magnitude of the seismic anisotropy will vary dynamically. For the Nelson Field, this is predicted to be as much as 22% corresponding to the average value of anisotropy parametres. Depending on the azimuth of the surveys, these differences could have a strong impact on the quantitative evaluation of pressure- and saturation-changes using near- and far-offset stacked data (Landrø 2001). For the particular example in Figures 5.10 and 5.11, the ratio of near offsets to far offsets varies from 1:1 (1990) and 1:1.13 (1997) at common survey azimuths of 0°, to 1:1.2 (1990) and 1:1.5 (1997) when they are orthogonal to the x_1 direction.

Unequal horizontal stresses could produce considerable azimuthal anisotropy in sandstones. This is concluded from numerical calculations based on laboratory

measurements and theory. This stress-induced anisotropy is predicted to be moderate to large in magnitude, with reservoirs subject to a stress ratio σ_H/σ_h of up to 1.7, giving rise to as much as 8% anisotropy, although this will depend on the stress-sensitivity and hence the depositional environment. This phenomenon affects our desire to accurately evaluate the variations in reservoir fluid pressure and saturation. Seismic anisotropy therefore cannot, in general, be ignored, as it gives an error similar to that expected from the 4D signature -- an effect that is caused by fluid displacement or pressure depletion. The exact magnitude of this effect will, of course, depend on the stress state of the surrounding rocks, and thus the reflection coefficients calculated here for an HTI reservoir represent a rough upper limit estimate (in theory, if the overburden is subject to a σ_H orthogonal to that in the reservoir, then it could produce a larger error). If laboratory measurements are proven to overestimate stress sensitivity, then our results will have a proportionately reduced impact.

5.5 Summary

The reliability of time-lapse seismic was tested in the presence of velocity anisotropy in the reservoir formations. It is noted that virtually all of the conducted 4D analyses are based on an assumption of isotropic velocities. In order to enhance the success rate, and consequently the reliability of the time-lapse technique, velocity anisotropy is taken into account. To illustrate the difference which this approach will make, I have investigated the variations of seismic-wave amplitudes with offset in an isotropic medium, and those with offset and azimuth in an anisotropic medium. Both media were subjected to pore-pressure depletion due to oil production, and, in a similar setting to Chapter 3 (different horizontal stresses), the corresponding stress-induced anisotropies, reflectivities, AVO and AVAZ and 4D signatures were computed and compared. It was shown and concluded that the azimuthal anisotropy of seismic waves can have a huge effect on the time-lapse analysis. The study estimates an important uncertainty of OWC movement – caused by reservoir production changes. This uncertainty can be avoided by detecting azimuthal anisotropy in the reservoir rocks and then applying the corresponding corrections.

Chapter 6

Stress Fields and Resultant Seismic Response of Geomechanical Compaction

6.1 Introduction

In this chapter I will modify a zero-offset two-way travel-time method for estimating the geomechanical compaction of reservoirs, and will extend it to non-zero offset. Furthermore, I will include the impact of stress-induced velocity anisotropy on the method, and will demonstrate the resulting improvement to the estimation of compaction. In order to capture the importance of this issue, a brief overview is given of geomechanical deformation in hydrocarbon reservoirs and the types of the resulting rock deformations. An example of compaction is also analysed and modelled. Two main categories of problems have been documented in offshore reservoirs: sea-floor subsidence/compaction and sand production/well collapse. Compaction is known to occur in unconsolidated reservoir formations. A mechanism explains compaction as a product of a sequential process starting with major hydrocarbon extraction, hence causing a huge drop in fluid pressure that leads to the collapse of the reservoir rock matrix – a process that may decrease the reservoir thickness, porosity, permeability and ultimately lead to gradual compaction of the reservoir layers. Compaction can be devastating to a hydrocarbon field in many ways, and via many aspects. One positive impact of compaction on reservoir productivity has been documented when production is compaction drive, *i.e.* for a long time the overburden weight helps pump out the fluid. To a lesser extent, surface/sea-floor subsidence may occur as a result of compaction.

6.2 Importance of Geomechanical Issues to the Petroleum Industry

The mechanical behaviour of reservoir rocks causes various mishaps via deformation, including compaction, ground surface subsidence and sea-floor subsidence, *etc.*, which in turn may bring about various consequences, such as damage to urban and industrial installations, pipelines, *etc.*, on the ground; or, in the ocean: well failure, platform sinking and production loss (for example, production of liquefied chalk instead of oil in the Valhall Field of the North Sea). Well-documented examples of compaction around the world are: Belridge, California; Wilmington, California; Lake Maracaibo, Venezuela; Ekofisk and Valhall in the North Sea; Magnolia, Gulf of Mexico; and Groningen in The Netherlands. Reservoir-rock deformation is of great interest to reservoir management, because of many aspects, including economic forecasting, development planning and reservoir engineering. A likely deformation problem in a producing reservoir – either onshore or offshore – requires a new production strategy, cost assessment, and consideration of personnel safety, environmental hazards, damage to installations, estimation of compaction and subsidence, *etc.*

6.2.1 Deformation Caused by Pressure Change

In a producing reservoir, pore pressure declines and, as a result, effective stress rises; this effect is thus translated into a large displacement (especially if the reservoir formations are weak) which is generally vertical. Jones *et al.* (1992) discuss several other situations that are outcomes of reservoir-rock deformation: 'Reduction in well pressure also has a second serious effect on productivity. The fluid pressure in the well bore provides the horizontal component of stress in the immediate vicinity of a well perforation, so abrupt changes in pressure in the well-bore lead to abrupt changes in the horizontal components of stress in the adjacent rocks, causing localized increases in shear stress. Depending on the magnitude of this shear stress and the strength characteristics of the rock adjacent to the perforations, the rock may be so weakened as to fail by disaggregating, leading to excessive production of reservoir solids (rock fragments and mineral grains)'.

6.2.2 Deformation Types

As discussed in Geertsma (1973), compaction of reservoir formations or a reduction in their volume can be thought of as a decrease in the reservoir height, so it can be expressed as the vertical strain of the reservoir rocks. He expresses formation compaction as the vertical strain in the reservoir due to the reduction in its height. This reduction in height originates from a reduction in reservoir pressure, which he states as a

function of factors like the mobility, solubility, density and compressibility of the pore fluids and also the reservoir boundary conditions such as faults, edge or bottom water, *etc.* In addition, as reservoir compaction cannot be considered merely as a one-dimensional process – the contribution of lateral compliance of the formations in terms of an increase in the effective compressibility should be studied as well. Figure 6.1 illustrates the influence of the lateral compliance of reservoir formations on their compaction. Figure 6.2 shows how fracture closure can add to initial compaction in a reservoir, and how the adjacent rocks accelerate compaction in a reservoir due to their lateral compliance.

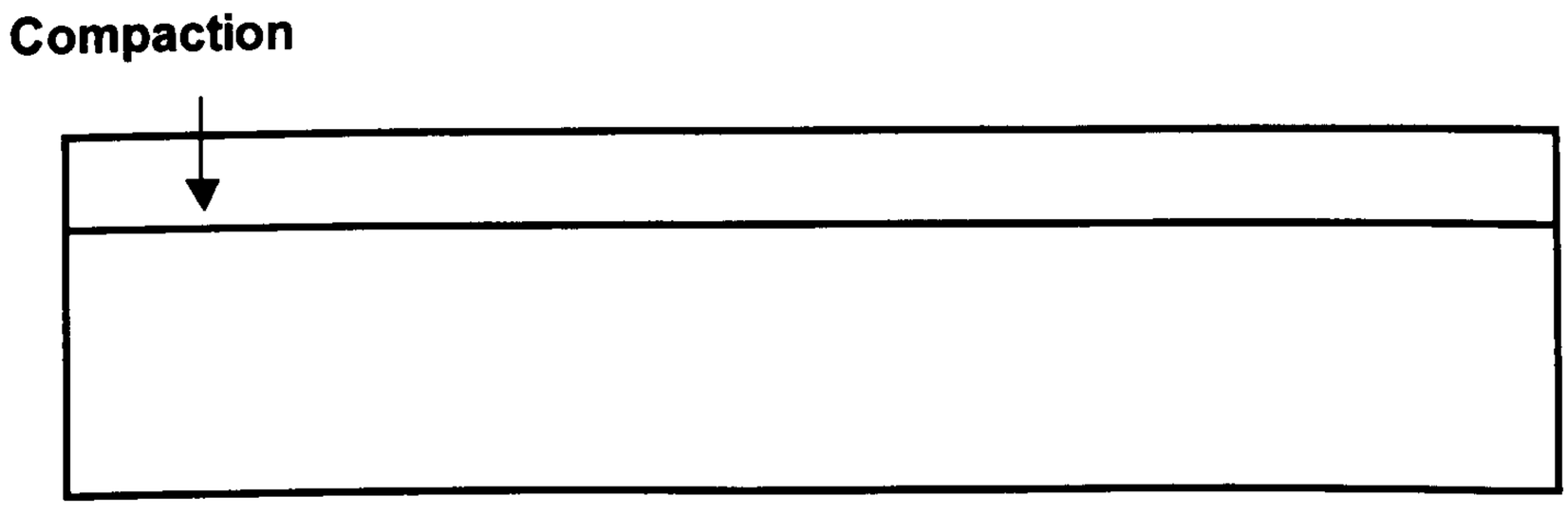

Figure 6.1: The reservoir compacts as a direct result of an increase in its vertical effective stress (top); this amount of compaction in a compressible reservoir is likely to be topped up by an additional compaction due to lateral compliance of the reservoir rocks (bottom), (Jones et al., 1992).

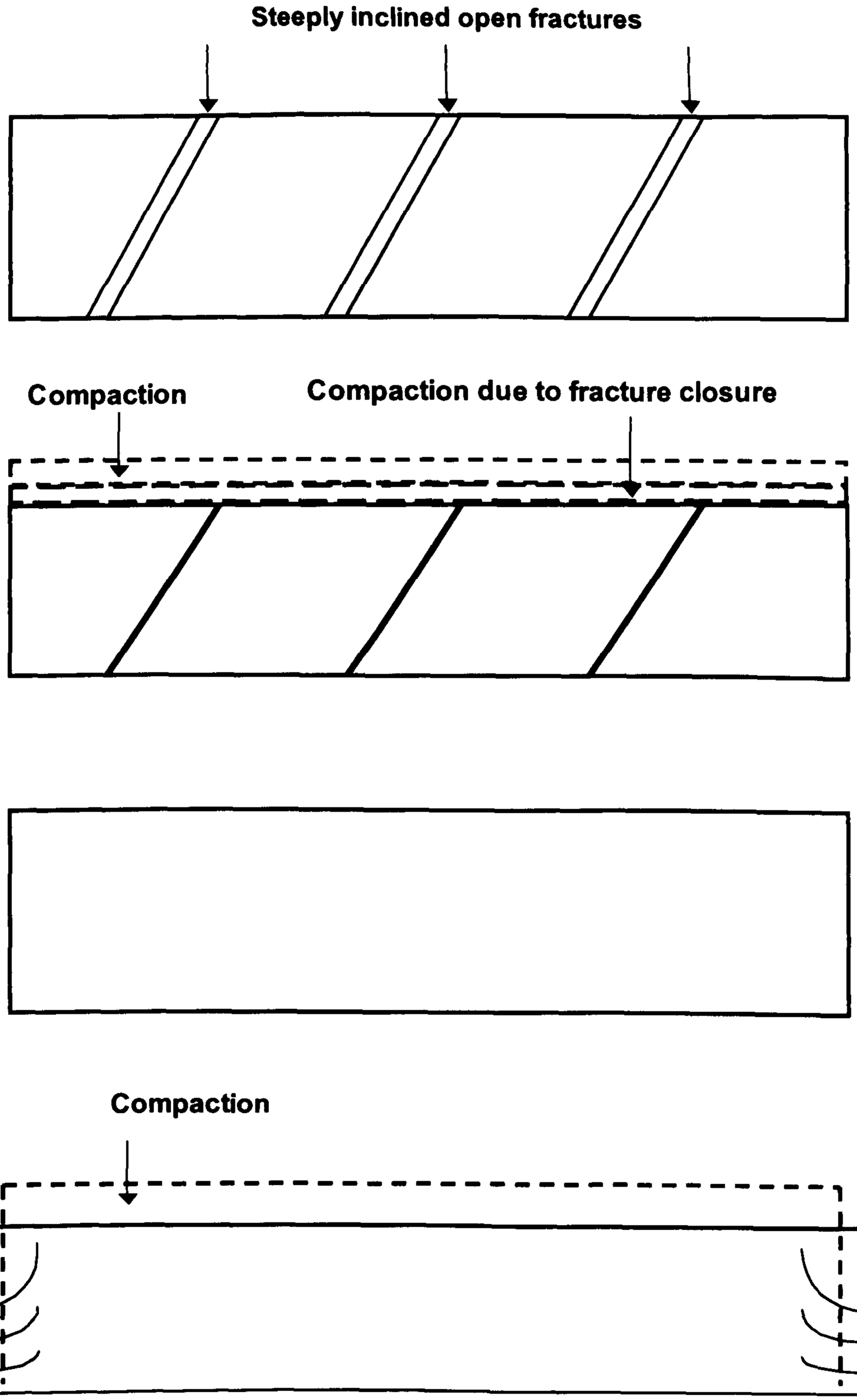

Figure 6.2: Fracture closure can add to initial compaction in a reservoir too (upper pair), or adjacent rocks can accelerate compaction in a reservoir because of their lateral compliance (lower pair), (Jones et al., 1992).

Not all compacting reservoirs cause surface or sea-floor subsidence, although subsidence is a consequence of reservoir compaction. The amount of such subsidence is proportional to the ratio of reservoir burial depth to its lateral extent. Geertsma (1973)

predicts an amount of subsidence equal to compaction for a reservoir at a depth of 1000 metres; provided that the reservoir has a surface area of 50 km^2 or more. Figure 6.3 illustrates the relationship of subsidence to compaction and reservoir size and depth.

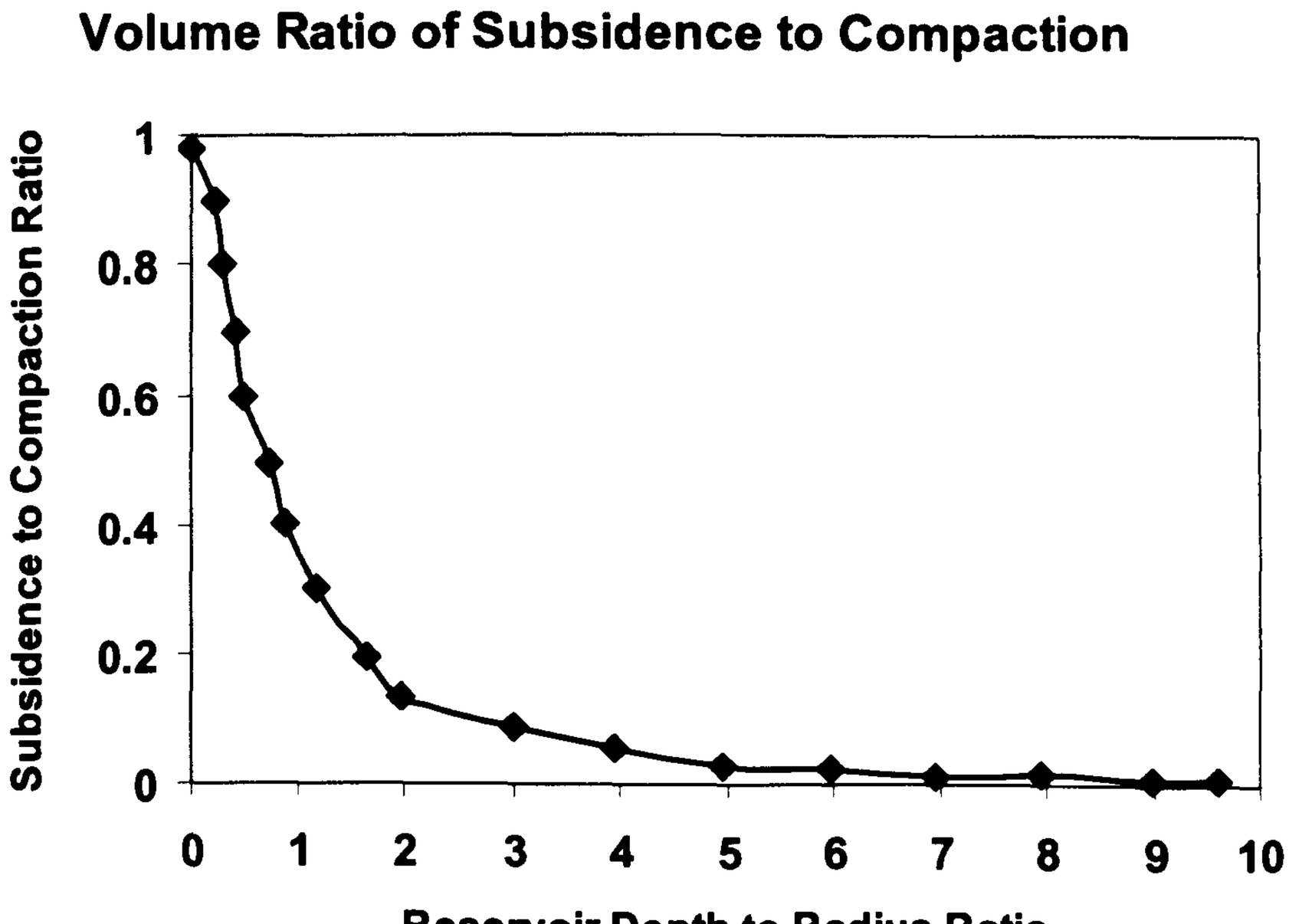

Figure 6.3: Subsidence to compaction ratio versus the ratio of reservoir depth to its radius (Xu, 2002).

6.3 A Review of Time-Lapse Methods for Estimating Compaction

Most hydrocarbon reservoirs range in depth from several hundred metres to few thousand metres; the overburden weight is supported partially by the reservoir-rock matrix and partially by fluid pressure or pore pressure. As a large amount of hydrocarbons are extracted from the reservoir during a long period of production, the pore pressure is depleted, and the reservoir formations fail to tolerate the overburden load and deform. This amount of strain expressed as a variation of the reservoir thickness to its original thickness ($\Delta h/h$) can give the magnitude of compaction. Different approaches have been used for estimating reservoir compaction, and I will summarize a few of these as follows.

Guilbot and Smith (2002) developed a method in which they constrained the commonly used depth conversion so that it could capture a time shift in the range of 12–16 ms in a time-lapse study of the Ekofisk Field between 1989 and 1999, and could compute reservoir compaction and sea-floor subsidence. The details can be found in Appendix 5. Hatchell *et al.* (2003) considered stress changes in a compacting reservoir, and computed the magnitude of compaction from the time shift in the two-way travel times of 4D studies. They took into account the stress relaxation above and below the compacting reservoir resulting from stress arching that translated into time delays in the time-lapse seismic, while the stress buildup on the sides of the reservoir was observed as a time pull-up.

Landrø and Stammeijer (2004) presented two separate methods: one based on near-offset and far-offset travel-time shifts from pre-stack data, and the other based on impedance changes and travel-time shifts from full stack data. Al-Naamani (2004) computed compaction in a reservoir model using zero-offset two-way travel time, which is followed and modified in this study and further extended to non-zero offset in order to investigate the effect of anisotropy on compaction estimation.

6.3.1 Two-Way Travel-Time Method

For a horizontal reservoir model (Figure 6.4) with initial thickness h_1, compressional-wave velocity V_{P1} and shear-wave velocity V_{S1}, the zero-offset P-wave two-way travel time is given by:

$$\tau_{PP1} = \frac{2h_1}{V_{P1}} \tag{6.1}$$

and, for converted shear waves:

$$\tau_{PS1} = h_1\left(\frac{1}{V_{P1}} + \frac{1}{V_{S1}}\right) \tag{6.2}$$

Therefore, for the compacted reservoir model (Figure 6.4) after Δh of compaction, the two-way travel times for compressional- and shear-waves are:

$$\tau_{PP2} = \frac{2h_2}{V_{P2}} \tag{6.3}$$

and

$$\tau_{PS2} = h_2\left(\frac{1}{V_{P2}} + \frac{1}{V_{S2}}\right) \tag{6.4}$$

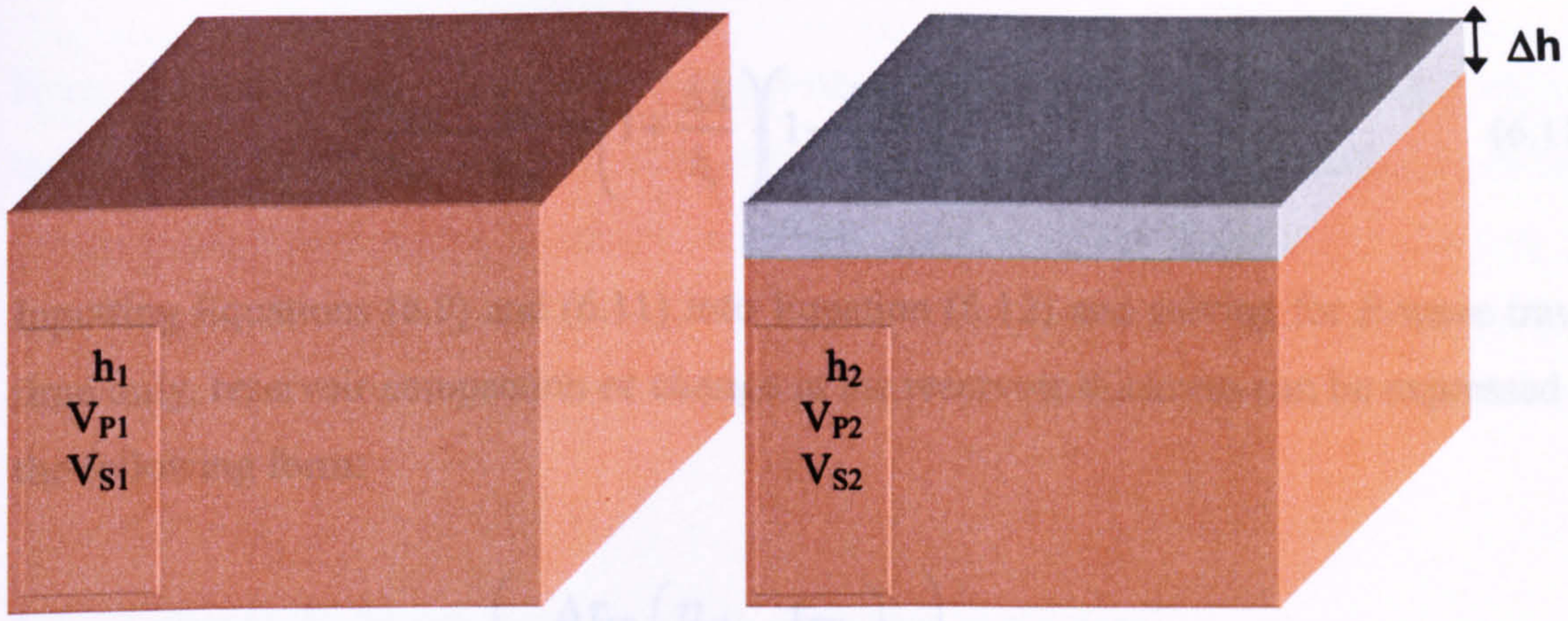

Figure 6.4: Horizontal reservoir model with properties before (left) and after (right) compaction.

Subscript 1 denotes the reservoir properties before compaction, and subscript 2 denotes the same properties for post-compaction scenarios. Changes in the above-mentioned properties can be listed as follows:

$$\Delta h = h_2 - h_1 \tag{6.5}$$

$$\Delta V_{\mathrm{P}} = V_{\mathrm{P2}} - V_{\mathrm{P1}} \tag{6.6}$$

$$\Delta V_{\mathrm{S}} = V_{\mathrm{S2}} - V_{\mathrm{S1}} \tag{6.7}$$

The relative change in the P-wave velocity can be expressed in the form of:

$$\frac{\Delta V_{\mathrm{P}}}{V_{\mathrm{P1}}} = \frac{\tau_{\mathrm{PP1}}}{\tau_{\mathrm{PP2}}}\left(1+\frac{\Delta h}{h_1}\right)-1 \tag{6.8}$$

and the relative change in the ratio of compressional-wave velocity to shear-wave velocity $\eta_r = V_{\mathrm{P}}/V_{\mathrm{S}}$, can also be approximated to the first order by:

$$\frac{\Delta \eta_r}{\eta_r} = \frac{\Delta V_{\mathrm{P}}}{V_{\mathrm{P}}} - \frac{\Delta V_{\mathrm{S}}}{V_{\mathrm{S}}} \tag{6.9}$$

By combining Equations (6.9) and (6.10), one can write the relative change in the converted shear-wave velocity as:

$$\frac{\Delta V_{\mathrm{S}}}{V_{\mathrm{S1}}} = \frac{\tau_{\mathrm{PP1}}}{\tau_{\mathrm{PP2}}}\left(1+\frac{\Delta h}{h_1}\right)-\left(1+\frac{\Delta \eta_r}{\eta_{r1}}\right) \tag{6.10}$$

So, by using Equations (6.3), (6.5), (6.6) and (6.8), to the first order and, in terms of both waves' travel time, we will have:

$$\frac{2\tau_{PS2}-\tau_{PP2}}{2\tau_{PS1}-\tau_{PP1}}=\left(1+\frac{\Delta h}{h_1}\right)\left(1-\frac{\Delta V_S}{V_{S1}}\right) \tag{6.11}$$

Inputting Equations (6.9) and (6.11) into Equation (6.12) and solving for P-wave travel time only, reservoir compaction or change in the reservoir thickness can be expressed in the following form:

$$\Delta h = h_1\left(\frac{\frac{\Delta\tau_{PP}}{\tau_{PP2}}\left(\frac{\eta_{r2}}{\eta_{r1}}-\frac{\tau_{PP1}}{\tau_{PP2}}\right)}{\frac{\tau_{PP1}}{\tau_{PP2}}\left(\frac{\eta_{r2}}{\eta_{r1}}-2\frac{\tau_{PP1}}{\tau_{PP2}}+1\right)}\right) \tag{6.12}$$

Similarly, solving a combination of Equations (6.9), (6.11) and (6.12) for the travel times of P- and S-waves leads to a more accurate estimation of reservoir compaction as follows:

$$\Delta h = h_1\left(\frac{\Delta\tau_{PP}}{2\tau_{PP2}}\right)\left(\frac{\frac{\eta_{r2}}{\eta_{r1}}-\frac{\tau_{PP1}}{\tau_{PP2}}}{\frac{\tau_{PP1}}{\tau_{PP2}}\left(\frac{\eta_{r2}}{\eta_{r1}}-2\frac{\tau_{PP1}}{\tau_{PP2}}+1\right)}+\frac{\frac{2\Delta\tau_{PS}-\Delta\tau_{PP}}{2\tau_{PS1}-\tau_{PP1}}}{\left(\frac{2\Delta\tau_{PS}-\Delta\tau_{PP}}{2\tau_{PS1}-\tau_{PP1}}-\frac{\Delta\tau_{PP}}{\tau_{PP2}}\right)}\right) \tag{6.13}$$

By using the relation of non-zero-offset two-way travel time (for example for initial reservoir case with subscript 1, Equation 6.14) as in Tsvankin and Thomsen (1997) or Grechka and Tsvankin (1998) Equation 6.12 approximates reservoir compaction while considering the whole range of offsets.

$$\tau_{PP1}(x)=\sqrt{\left(\frac{2h_1}{V_{P1}}\right)^2+\left(\frac{x}{V_{P1-NMO}}\right)^2-\frac{2\eta x^4}{\left(\frac{2h_1}{V_{P1}}\right)^2+\left(xV_{P1-HOR}\right)^2}} \tag{6.14}$$

Where x is offset and NMO velocity is defined as:

$$V_{P1-NMO}=V_{P1}\sqrt{1+2\delta_1} \tag{6.15}$$

Horizontal velocity reads:

$$V_{P1-HOR}=V_{P1}\sqrt{1+2\eta_1} \tag{6.16}$$

And NMO parametr is in form of:

$$\eta_1=\frac{\varepsilon_1-\delta_1}{1+2\delta_1} \tag{6.17}$$

Here, in order to apply the two-way travel-time method and illustrate the improvement that it offers to the estimation of compaction, I will utilize a dataset; study its porosity decline with stress; derive its stress-sensitivity parameters (as discussed in Chapter 3); and analyse its velocity variation with stress. Then, by using such variations in a reservoir model, I will compute its compaction after 10 years of production.

6.4 Laboratory Measurements on an Artificial Shaly Sand

As described in Xu *et al.* (2002) and Al-Naamani (2004), a dataset derived from laboratory measurements (Yin, 1993), on artificial clay sand is utilized in this section. The sand sample is made up of 70% clean Ottawa sand and 30% pure kaolinite powder, with an overall weight of 100 grams. Yin (1993) measured the porosity and velocities of compressional- and shear-waves of the sand during loading and unloading cycles. Figure 6.5 shows the loading and unloading trends for porosity variations of the sample. For example, during the loading process, the porosity of the sample decreases from 27% at 10 MPa effective stress to slightly less than 14% at 50 MPa effective stress.

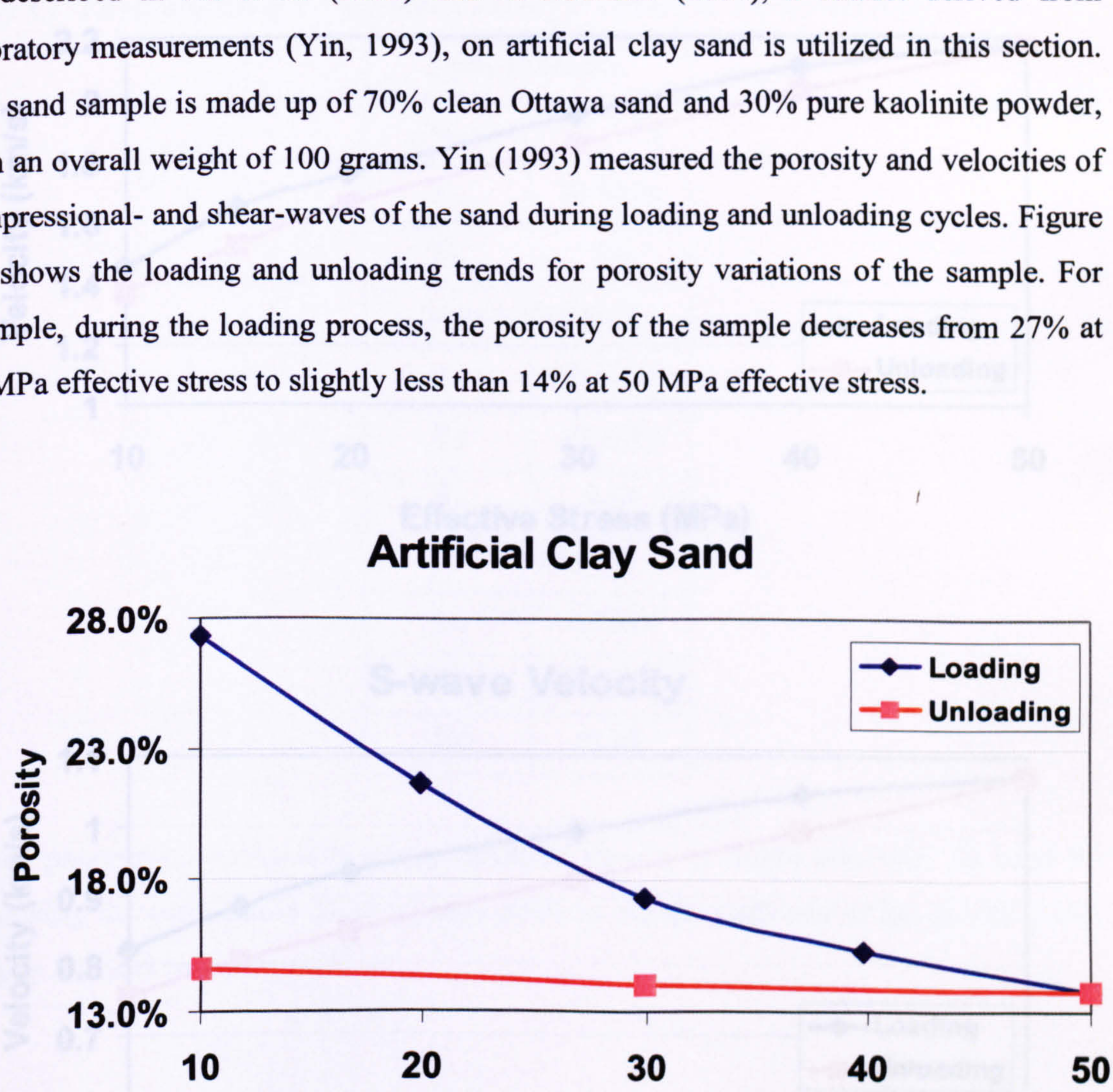

Figure 6.5: Measured values of porosity at different effective stresses in loading and unloading cycles on artificial clay sand (Xu et al., 2002).

The corresponding velocity increase for compressional waves produces values of around 1400 m/s to 2200 m/s, with the same effect, shear-wave velocity changes from an initial value of 800 m/s to 1100 m/s (Figure 6.6). As the unloading branch of the porosity changes of the sample with effective stress shows, there is a considerable irrecoverable porosity loss that can be partly the cause of a velocity drop observable in the unloading branches of both P- and S-waves.

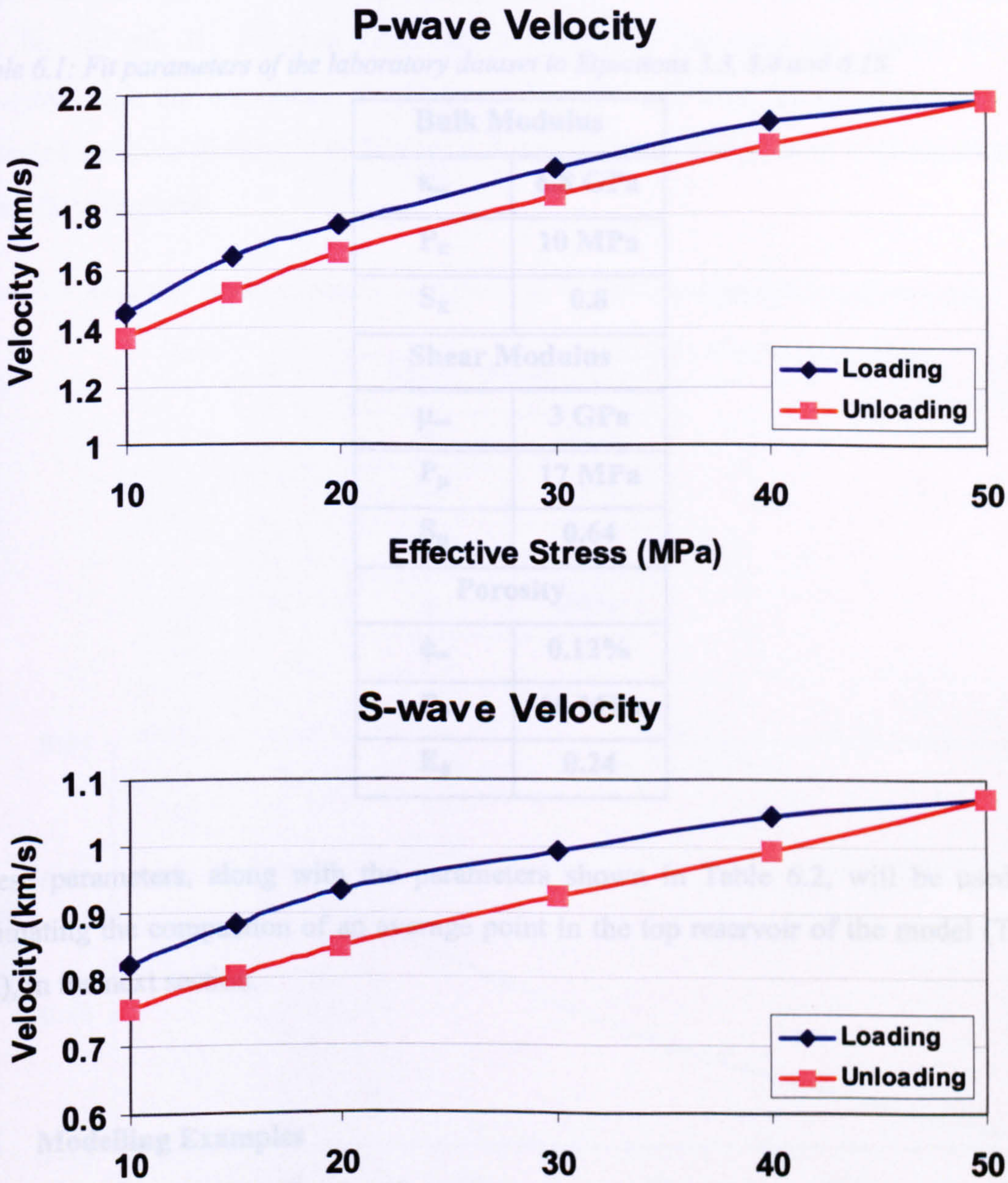

Figure 6.6: Loading and unloading cycles of velocity variations for compressional waves (top) and shear waves (bottom) of an artificial sample (Xu, 2002).

Here I will follow the work of Al-Naamani (2004), in order to recover bulk and shear moduli, utilizing porosity-dependent density (a matrix density of 2600 kg/m^3) and loading trends of compressional- and shear-wave velocities illustrated in Figure 6.6 and Equations 3.3 and 3.4. On the other hand, variations in porosity can be expressed as in the following exponential relationship:

$$\phi(P) = \phi_\infty + E_\phi e^{-P/P_\phi} \tag{6.18}$$

The corresponding fit parameters: ϕ_∞, E_ϕ and P_ϕ to the above equation and those to Equations 3.3 and 3.4 are given in Table 6.1.

Table 6.1: Fit parameters of the laboratory dataset to Equations 3.3, 3.4 and 6.18.

Bulk Modulus	
κ_∞	**6.8 GPa**
P_κ	**10 MPa**
S_κ	**0.8**
Shear Modulus	
μ_∞	**3 GPa**
P_μ	**17 MPa**
S_μ	**0.64**
Porosity	
ϕ_∞	**0.12%**
P_ϕ	**20 MPa**
E_ϕ	**0.24**

These parameters, along with the parameters shown in Table 6.2, will be used for estimating the compaction of an average point in the top reservoir of the model (Table 6.2), in the next section.

6.5 Modelling Examples

Here, to clarify our idea of estimating compaction by using the travel-time method, and also to investigate the effect of seismic velocity anisotropy, some examples of modelling for two isotropic and anisotropic divisions are presented.

6.5.1 Estimation of the Compaction for a Point in a Reservoir

A) Isotropic Reservoir

The model shown in Figure 6.4 is considered together with parameters derived from the previous section (Table 6.1). For a reservoir thickness of 120 metres, a 12-metre compaction (10%) is assigned. The rock is saturated with oil up to 85% and the water saturation is set to 15%. Porosity decline for a range of effective stress is displayed in Figure 6.7. The bulk and shear moduli of the reservoir model are obtained in the next step. Therefore, the velocities of compressional and shear waves for the dry-frame rock can be derived. By utilizing Gassmann's equations, corresponding values for oil-saturated rock are calculated. P-wave and S-wave velocities for dry-frame and oil-saturated rock are illustrated in Figures 6.8 and 6.9 respectively; both show an increase with effective stress.

Table 6.2: Reservoir model thickness, oil saturation, water saturation and initial porosity.

Model Parameters	
h	**120 m**
S_o	**85%**
S_w	**15%**
ϕ	**28%**

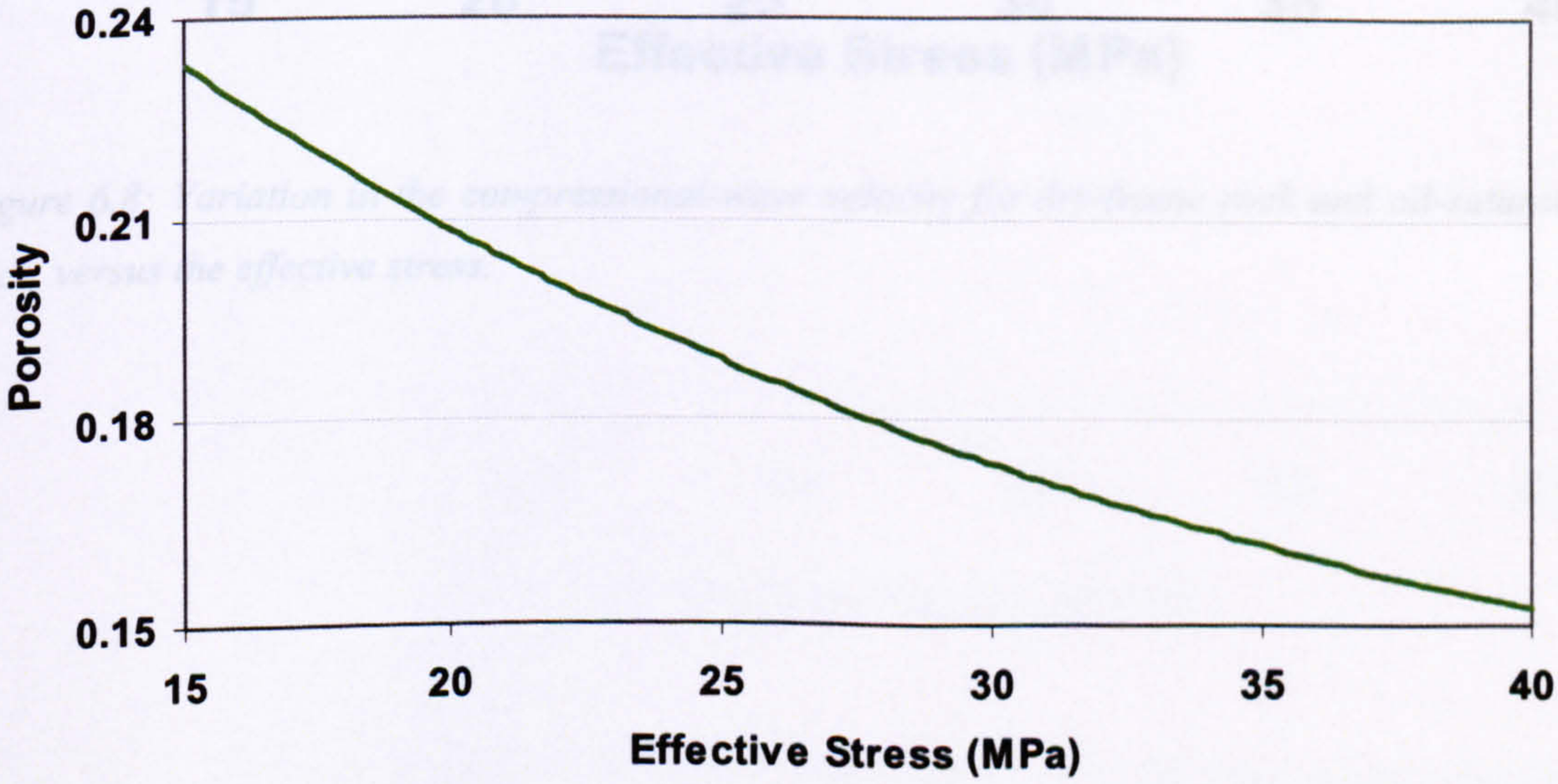

Figure 6.7: Porosity declines with effective stress as the rock matrix collapses and a decrease in volume occurs.

Figure 6.10 displays an approximately 24-ms decrease in two-way travel time for P-waves. These variations are next inputted to the methodology discussed in Section 6.3, in order to estimate the anticipated compaction of the model.

By using the porosity method presented by Guilbot and Smith (2002) (Appendix 5), another compaction estimation is made for the model to be displayed as a reference along with the estimate obtained from the two-way travel-time method. Results and the assigned or true compaction are plotted in Figure 6.11. Both of the estimated compaction curves display a good match to the curve for true compaction.

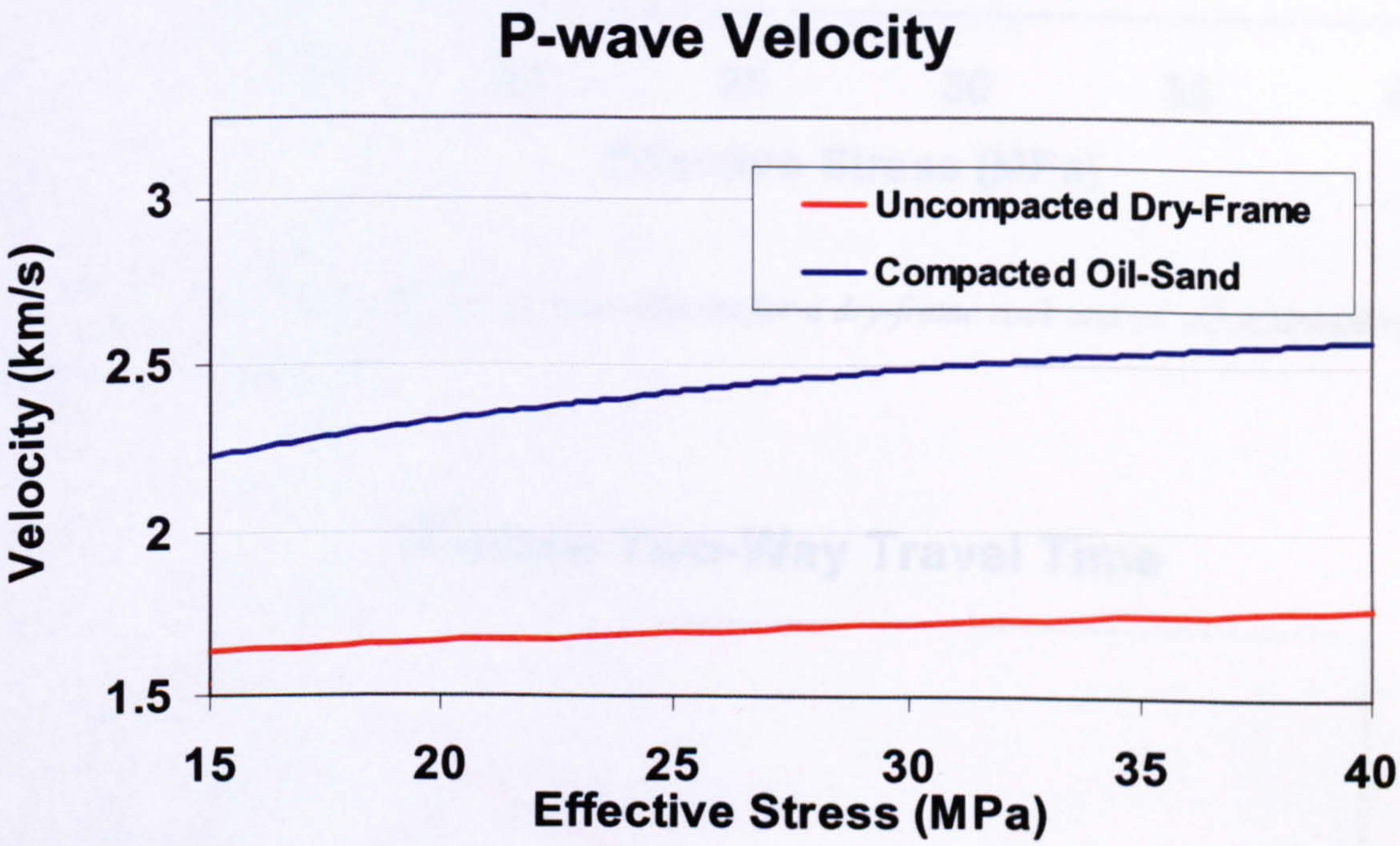

Figure 6.8: Variation in the compressional-wave velocity for dry-frame rock and oil-saturated rock, versus the effective stress.

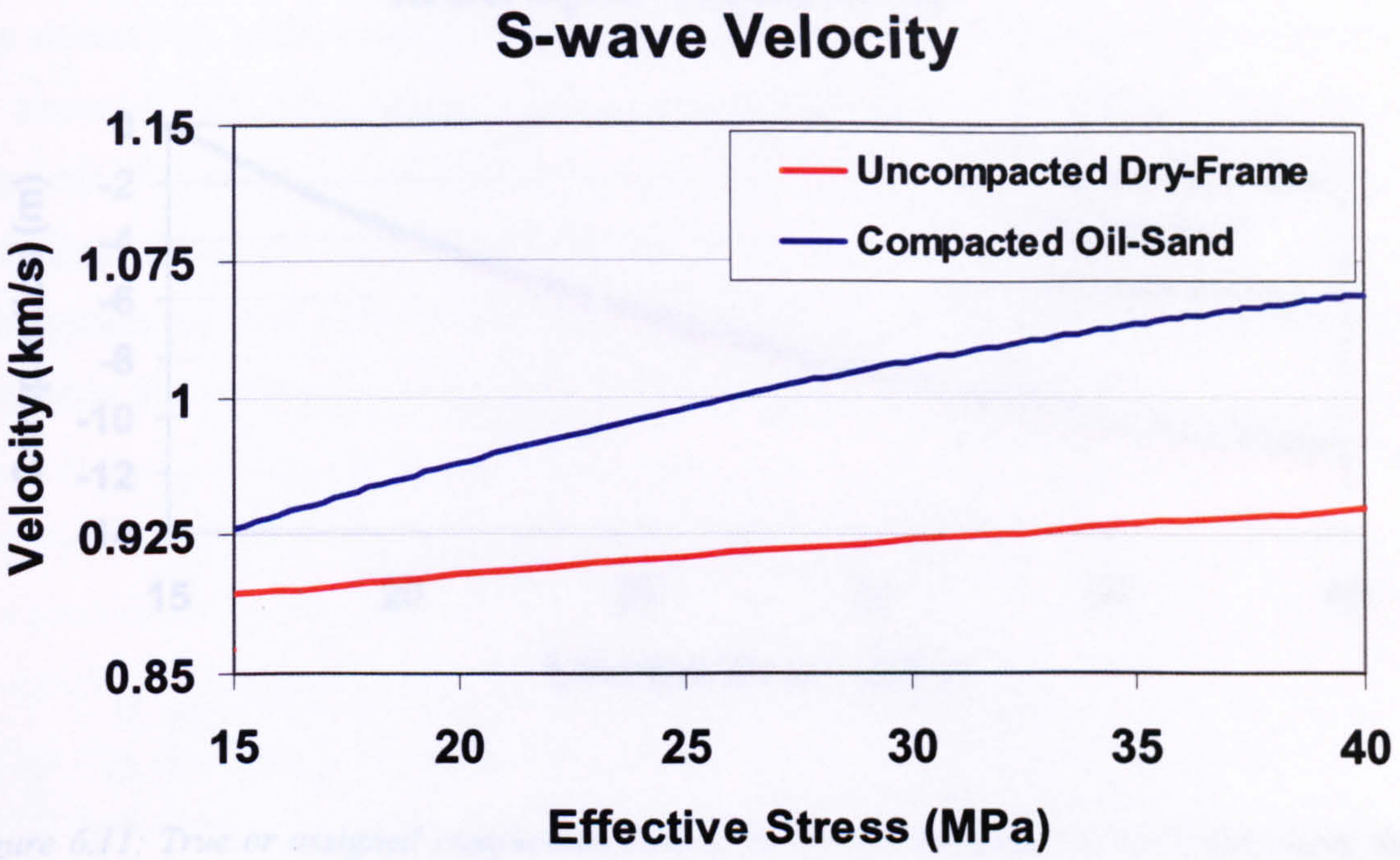

Figure 6.9: Variation in the shear-wave velocity for a dry-frame rock and an oil-saturated rock, versus the effective stress.

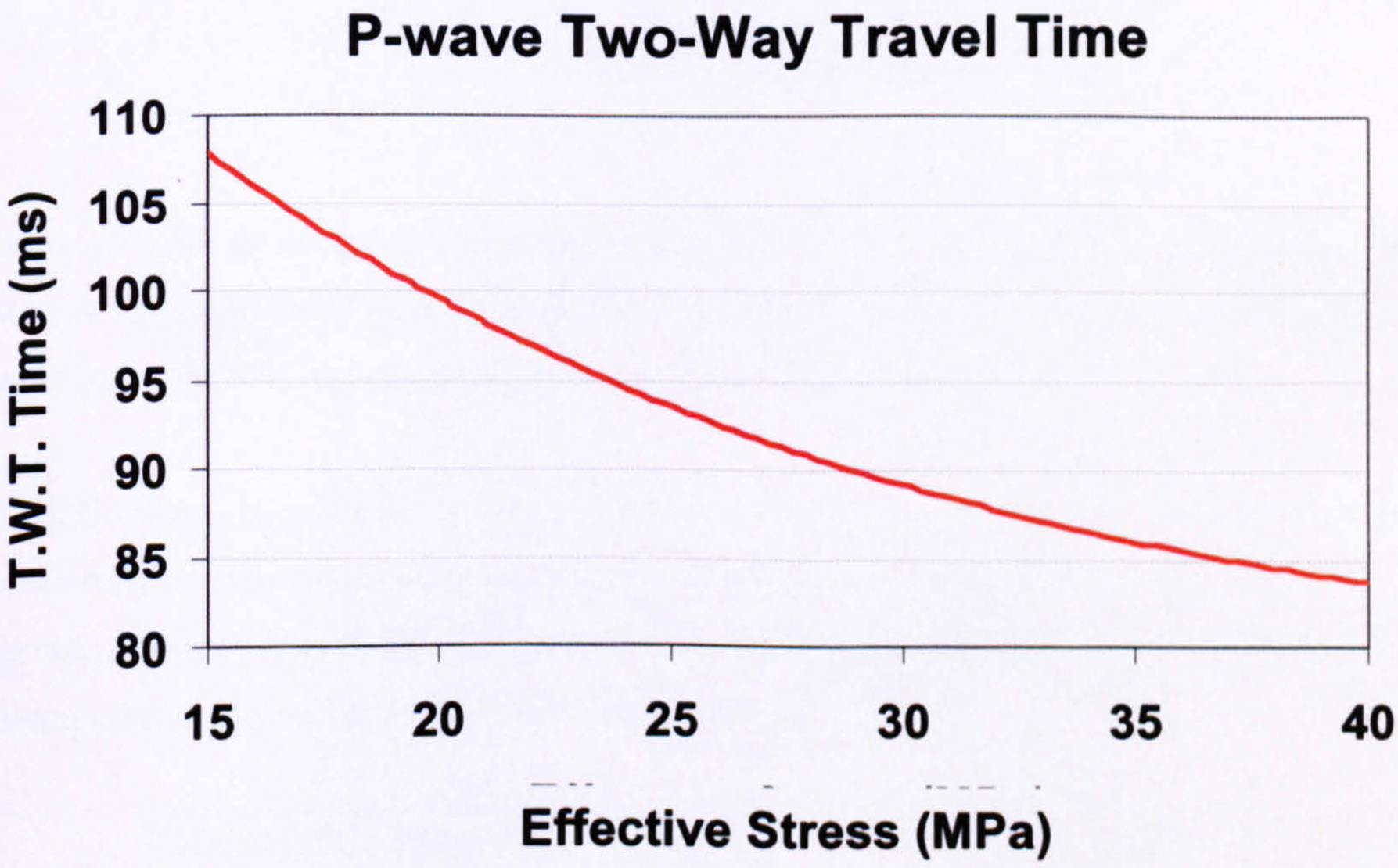

Figure 6.10: The two-way travel time for the compressional wave declines with an increase in the reservoir's effective stress.

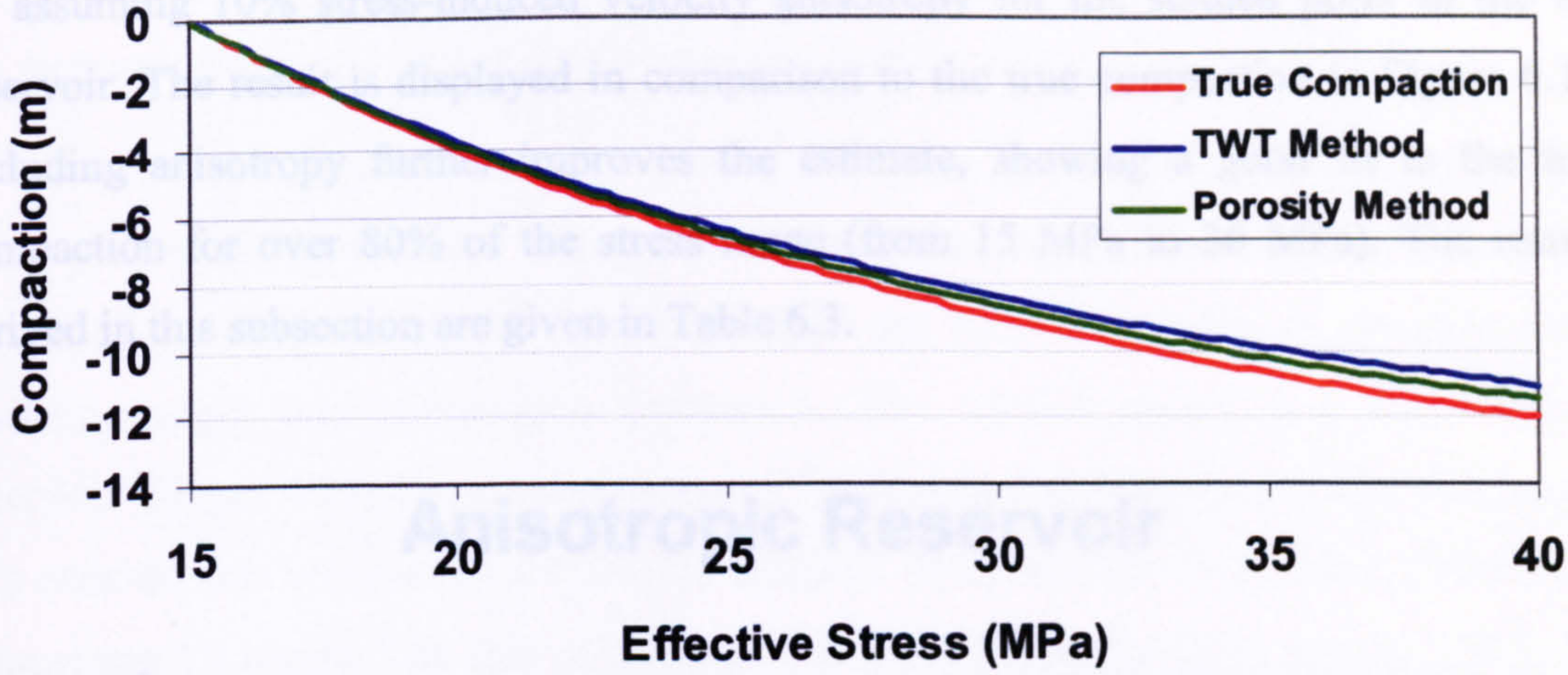

Figure 6.11: True or assigned compaction compared with the estimated compaction, using the two-way travel-time method and the porosity method as a reference. The reservoir is assumed to be isotropic.

B) *Anisotropic Reservoir*

In a similar way to the case of the isotropic reservoir model, the compaction is estimated by assuming 10% stress-induced velocity anisotropy for the studied point in the top reservoir. The result is displayed in comparison to the true compaction in Figure 6.12. Including anisotropy further improves the estimate, showing a good fit to the true compaction for over 80% of the stress range (from 15 MPa to 36 MPa). The results derived in this subsection are given in Table 6.3.

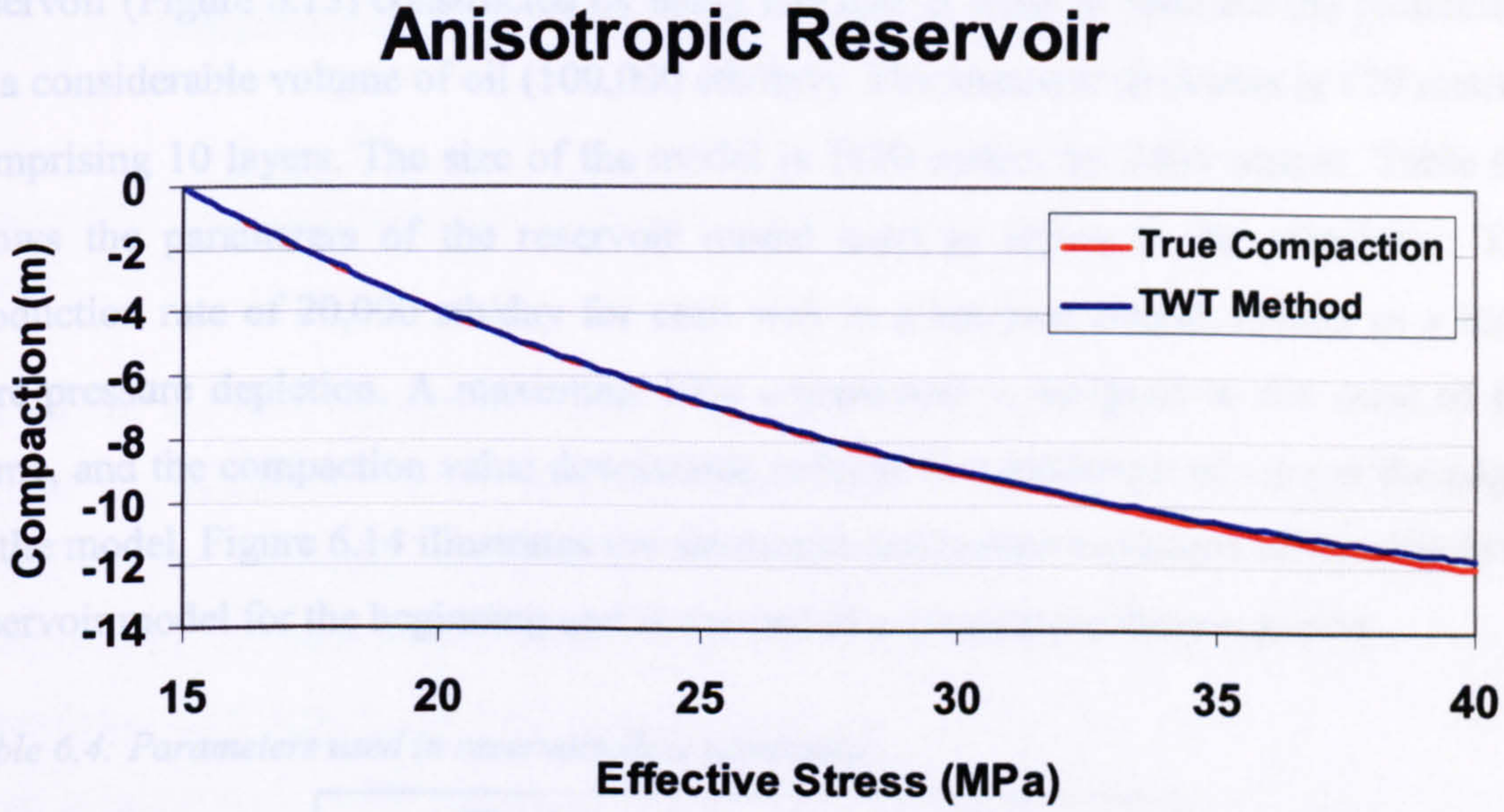

Figure 6.12: True or assigned compaction compared with the estimated compaction, using the anisotropic two-way travel-time method. The anisotropic travel-time method shows a result that is very close to the true compaction for 80% of the studied stress range.

Table 6.3: True compaction of the reservoir model, together with a set of compaction estimations. The estimation using the porosity method is mentioned here as a reference – by taking into account stress-induced anisotropy, the two-way travel-time method predicts a closer estimate to the maximum value of reservoir compaction.

Reservoir Compaction	**Metres**
True	**12**
Estimate Using the Porosity Method	**11.4**
Estimate Using the TWT Method – Isotropic	**11**
Estimate Using the TWT Method – Anisotropic	**11.9**

6.5.2 Estimation of the Compaction for the Whole Reservoir, Using Simulation Results

A) Isotropic Scenario – Isotropic Overburden and Reservoir

In this subsection, another set of modelling examples is presented, examples that have many parameters in common with those in the previous subsection. However, here the results of the reservoir model flow simulation are utilized in order to obtain a more realistic insight into compaction estimation. The studied model is a dome-shaped reservoir (Figure 6.13) constructed by using FloGrid in order to simulate the production of a considerable volume of oil (100,000 stb/day). The reservoir thickness is 120 metres, comprising 10 layers. The size of the model is 2400 metres by 2400 metres. Table 6.4 shows the parameters of the reservoir model used as inputs to the simulator. The production rate of 20,000 stb/day for each well in a ten-year period, results in a large pore-pressure depletion. A maximum 10% compaction is assigned to the crest of the dome, and the compaction value downwards reduces to a minimum of zero at the edges of the model. Figure 6.14 illustrates the saturation and pressure changes of the simulated reservoir model for the beginning and at the end of a 10-year production period.

Table 6.4: Parameters used in reservoir-flow simulation.

Thickness	**120 m**
So	**85%**
Sw	**15%**
ϕ	**28%**
X = Y	**2,400 m**
Z	**120 m**
Number of Wells	**5**
Production – Each	**20,000 stb/day**
Depth	**2,134 m (7,000 ft)**
Production Period	**10 years**

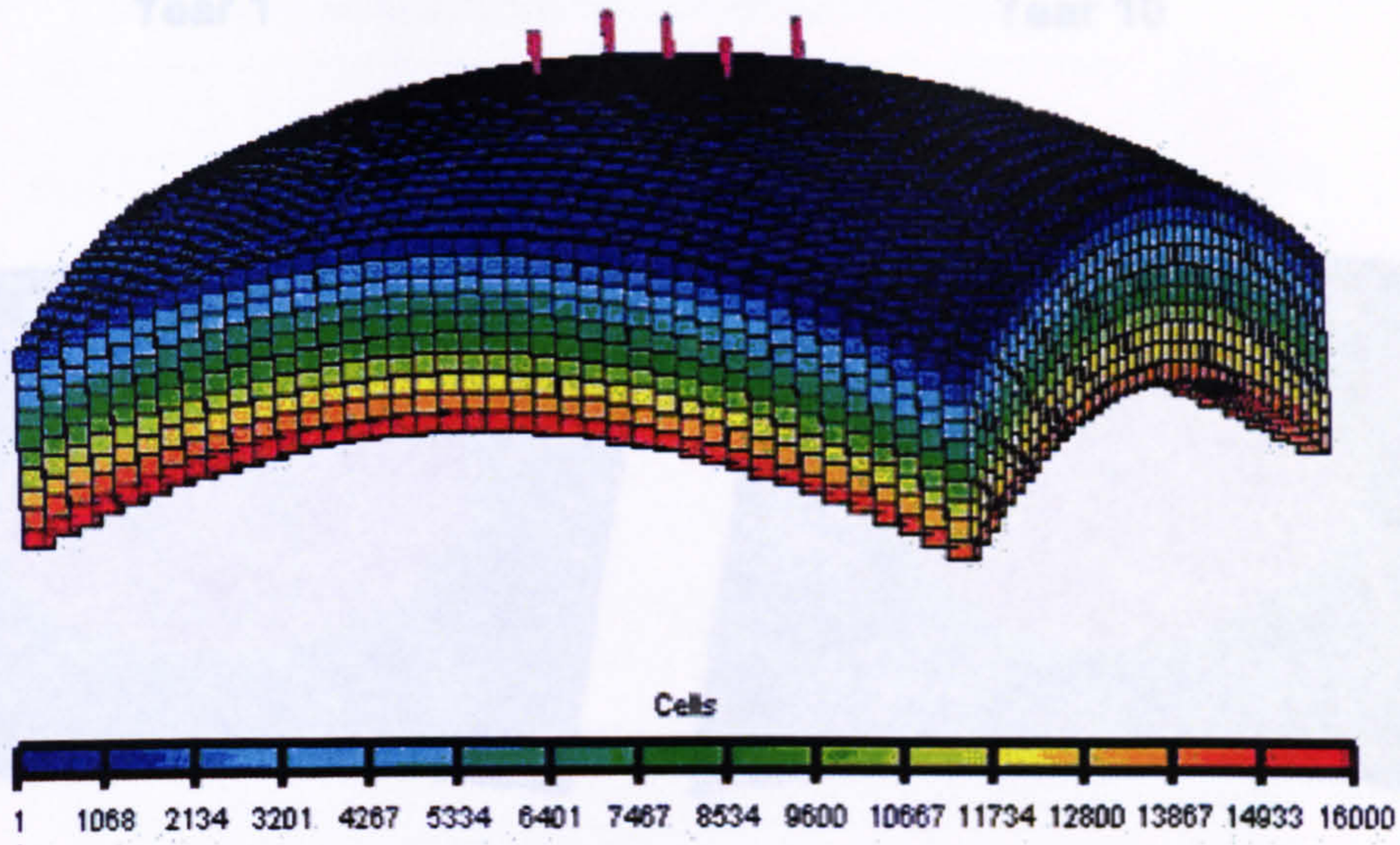

Figure 6.13: Output of the reservoir flow simulation illustrating different layers and producing wells.

As part of the flow simulation results, next the pressure and saturation values of each cell of the model can be fed into the petro-elastic model to obtain its velocity and density. Later, acoustic impedances and seismic reflectivities of P-wave can be computed by utilizing related formulae of, for example, Aki and Richards (1980). By convolving each reflectivity series with a 35-Hz zero-phase Ricker wavelet, a synthetic trace is generated. After repeating this process for all cells of the model, synthetic seismograms for the whole reservoir are made, so that, as in Figure 6.15, for example, the seismic section across the centre of the model can be displayed. Figure 6.15 illustrates the seismic section of the P-wave for pre-production (top), with slightly higher amplitude compared to the seismic section of post-production scenario (bottom), the difference between the amplitudes can be seen in the automatic scales of the plots.

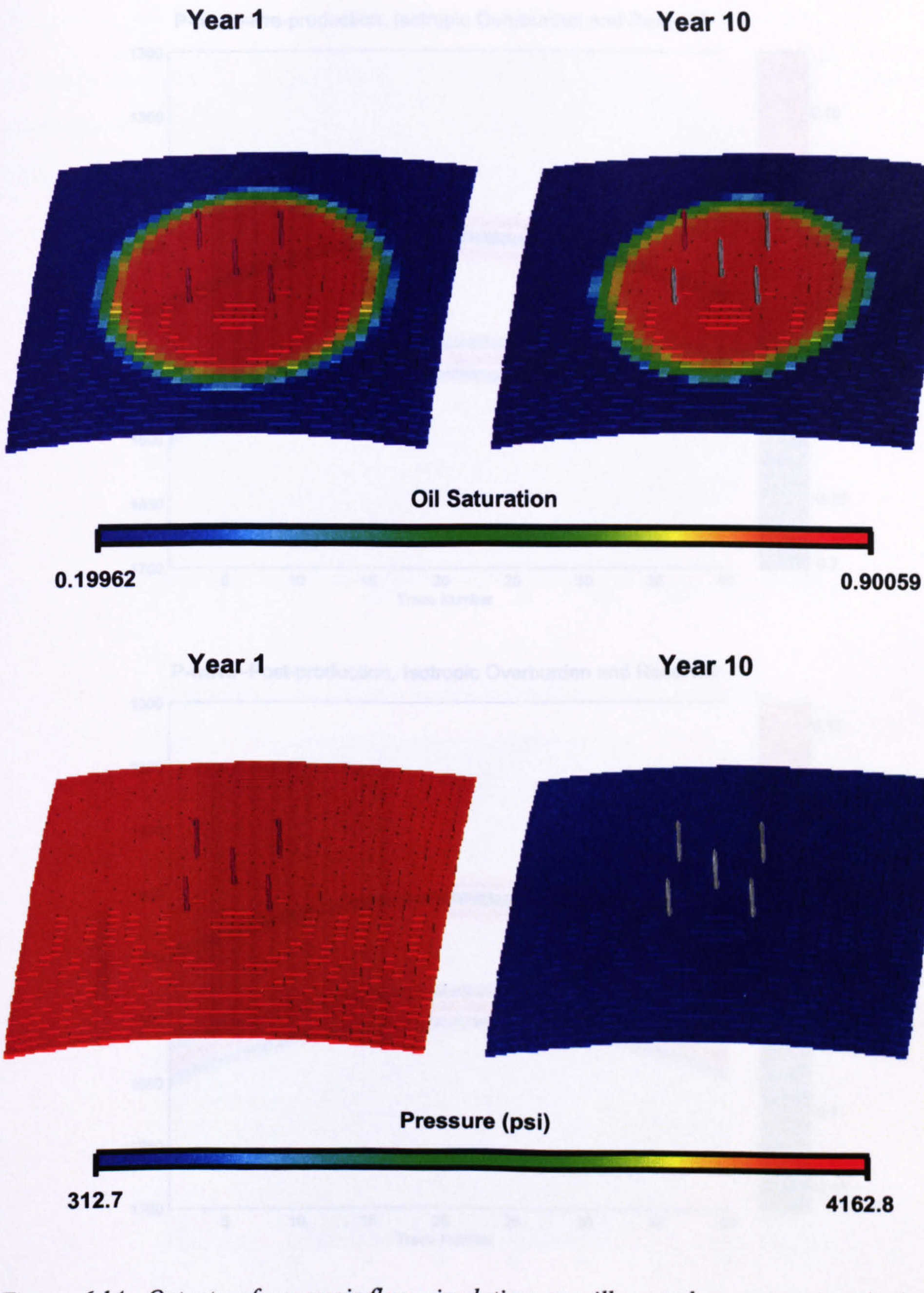

Figure 6.14: Outputs of reservoir-flow simulation are illustrated as saturation (top) and pressure (bottom) changes for pre-production (left) and post-production (right), depicting the observable decrease of oil saturation and the large pressure drop.

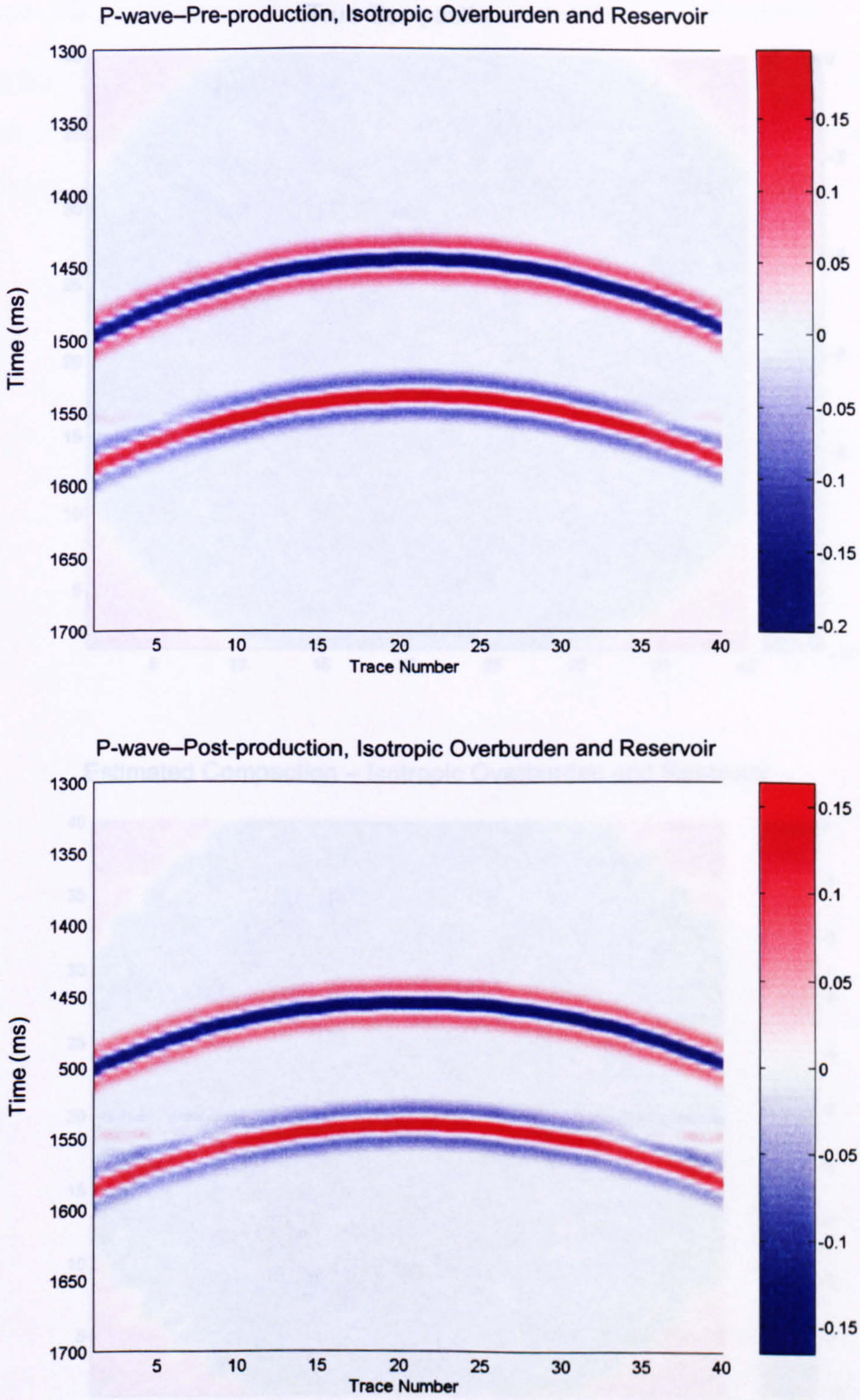

Figure 6.15: Synthetic sections for compressional waves using simulation results: before production (top) and after production (bottom). Scenario: isotropic overburden and reservoir.

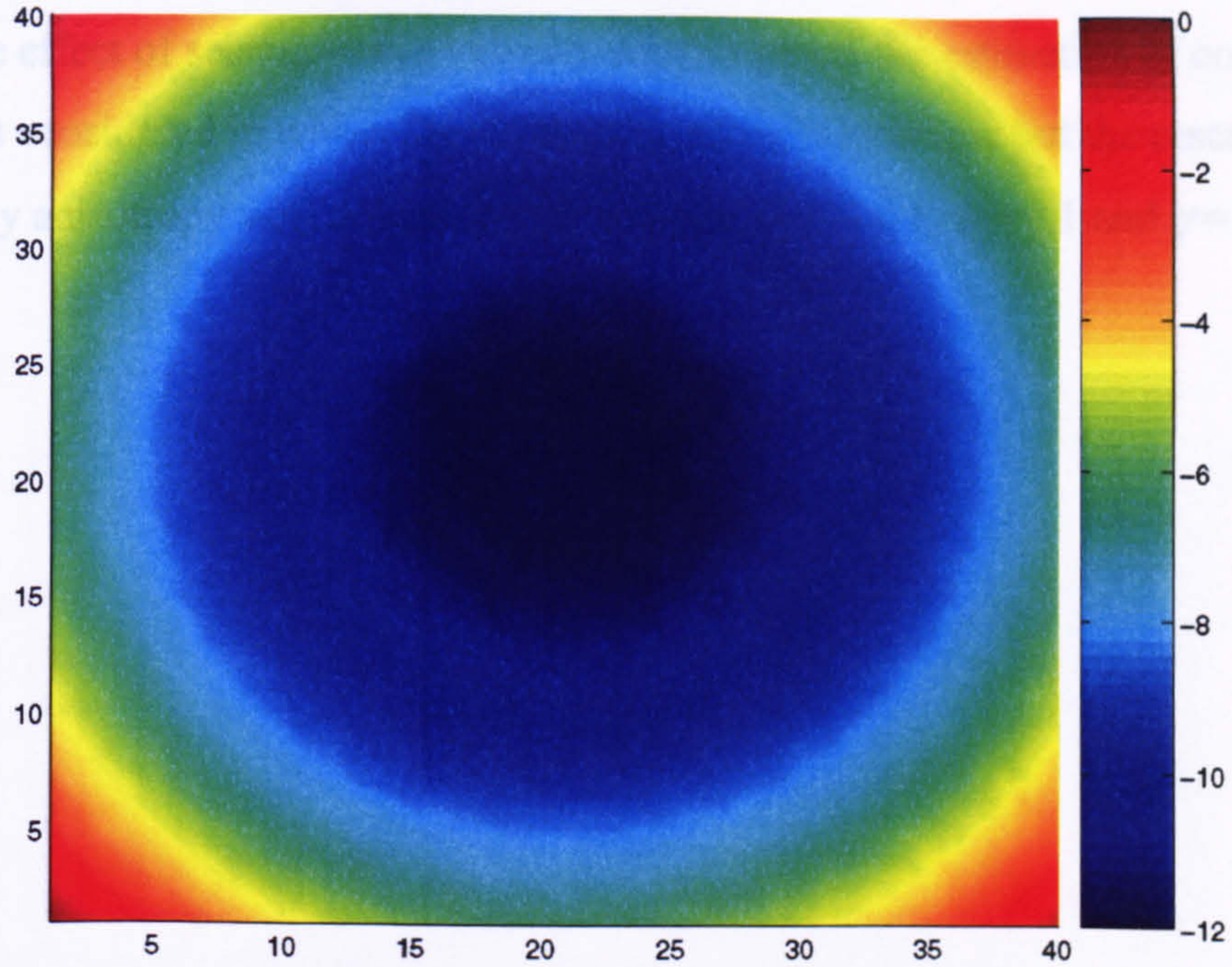

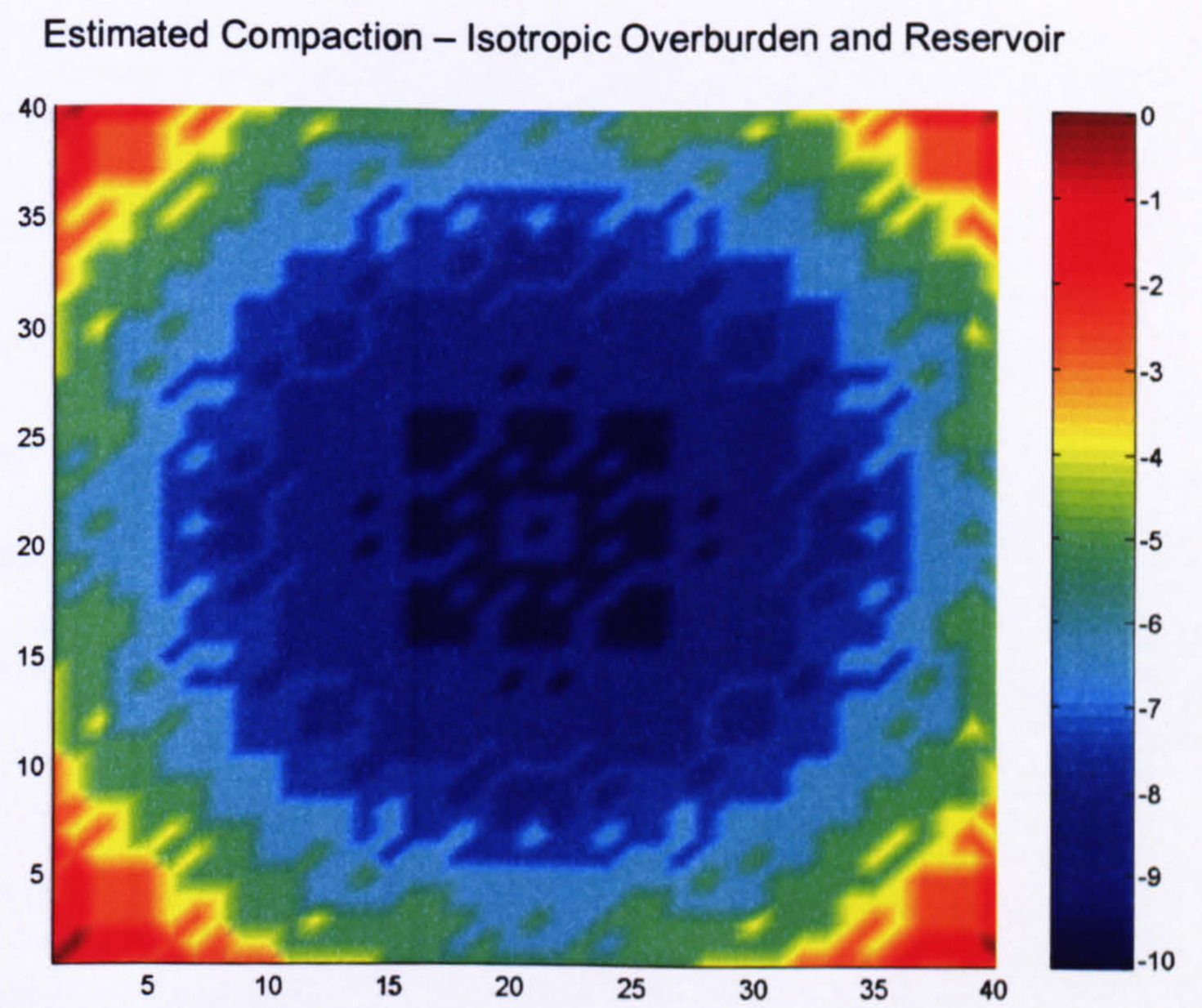

Figure 6.16: True or assigned compaction (top) and estimated compaction using the two-way travel-time method – isotropic assumption (bottom). Scenario: isotropic overburden and reservoir.

B) *Anisotropic Scenario – Isotropic Overburden and Anisotropic Reservoir*

To study the effect of seismic-wave velocity anisotropy on the estimation of compaction, a scenario is considered in which the overburden shale is isotropic but the reservoir has a 10% velocity anisotropy with anisotropy parameters of $\varepsilon = 0.1$, $\delta = 0.1$ and $\gamma = 0.1$.

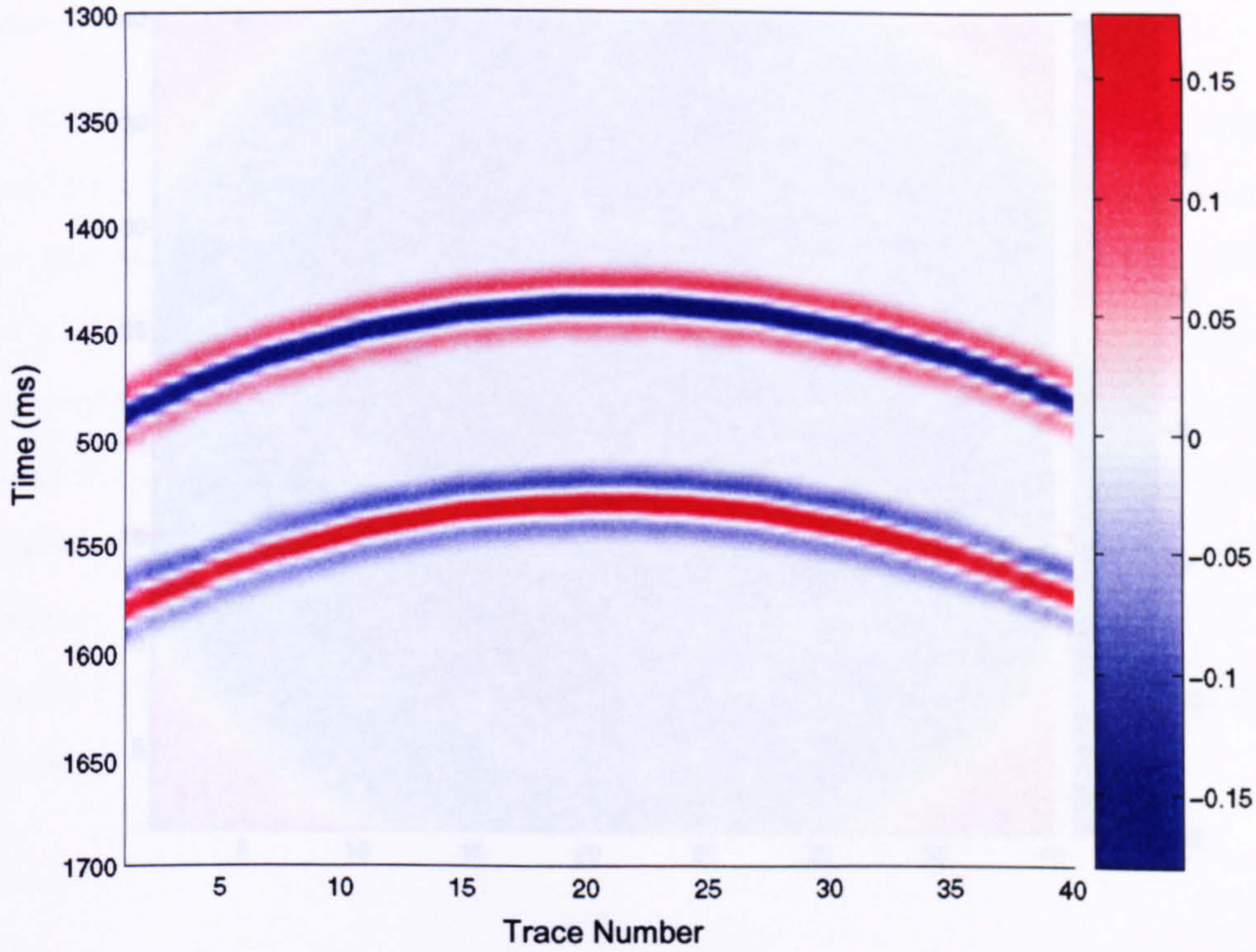

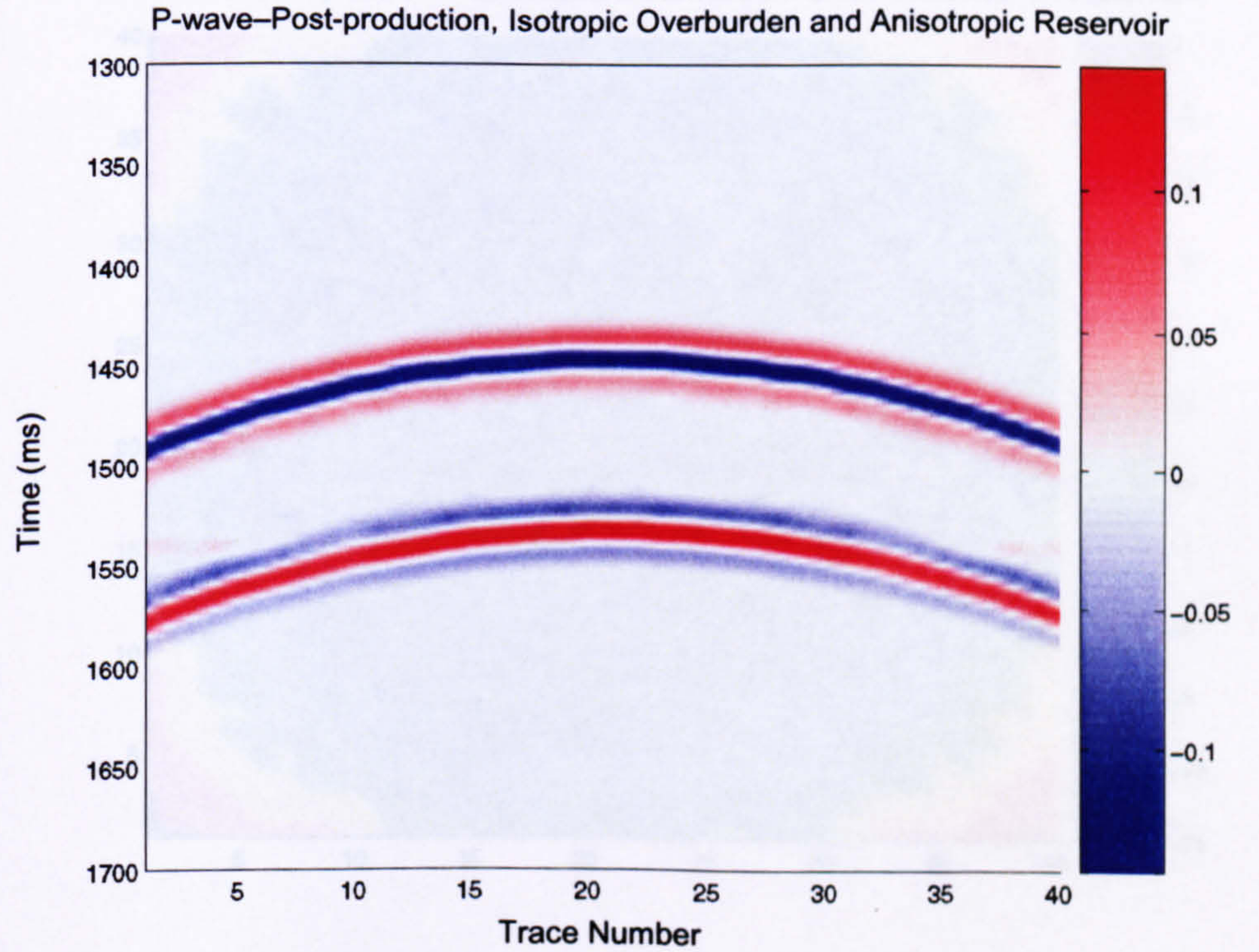

Figure 6.17: Synthetic sections for compressional waves, using simulation results – before production (top) and after production (bottom). Scenario: isotropic overburden and anisotropic reservoir.

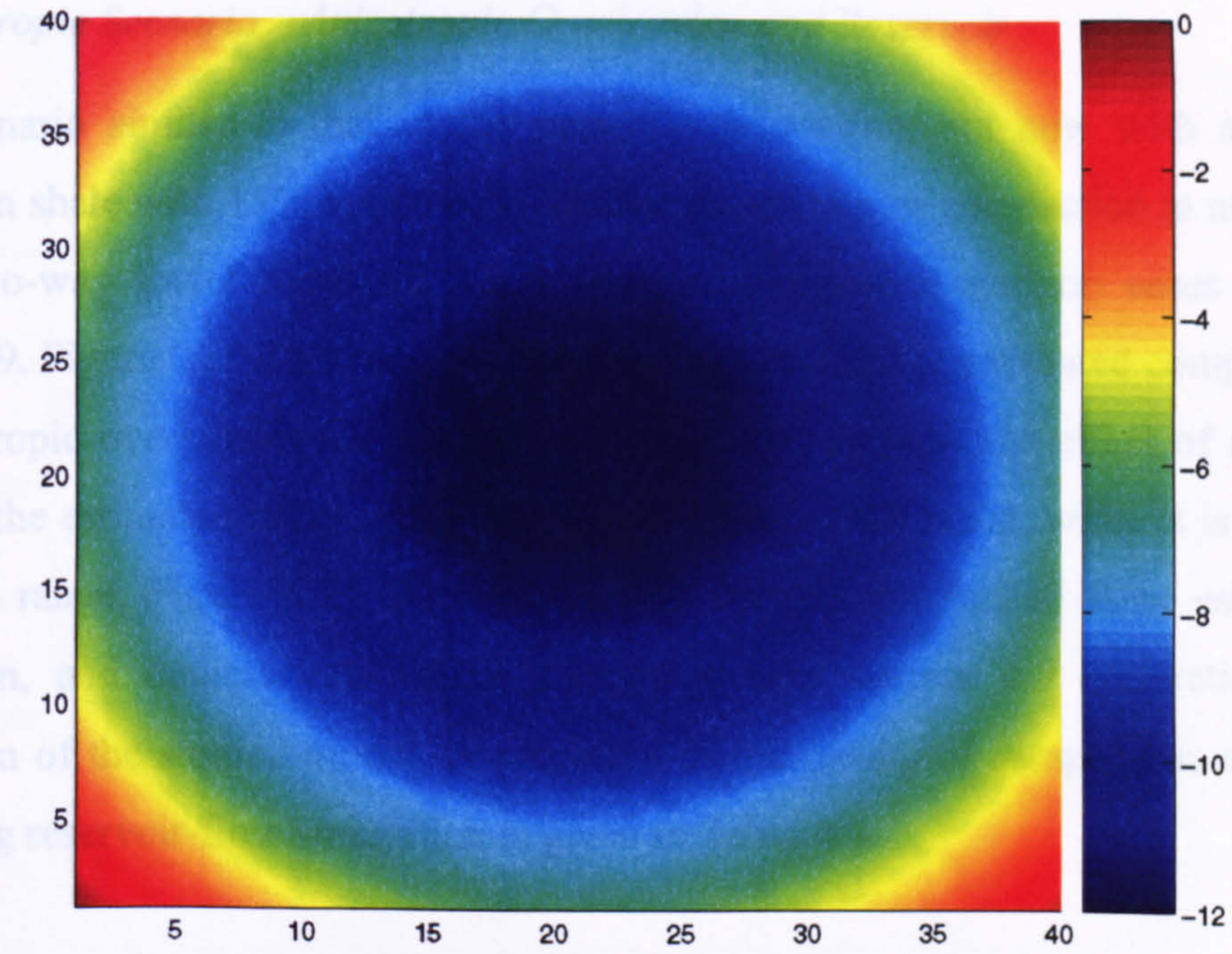

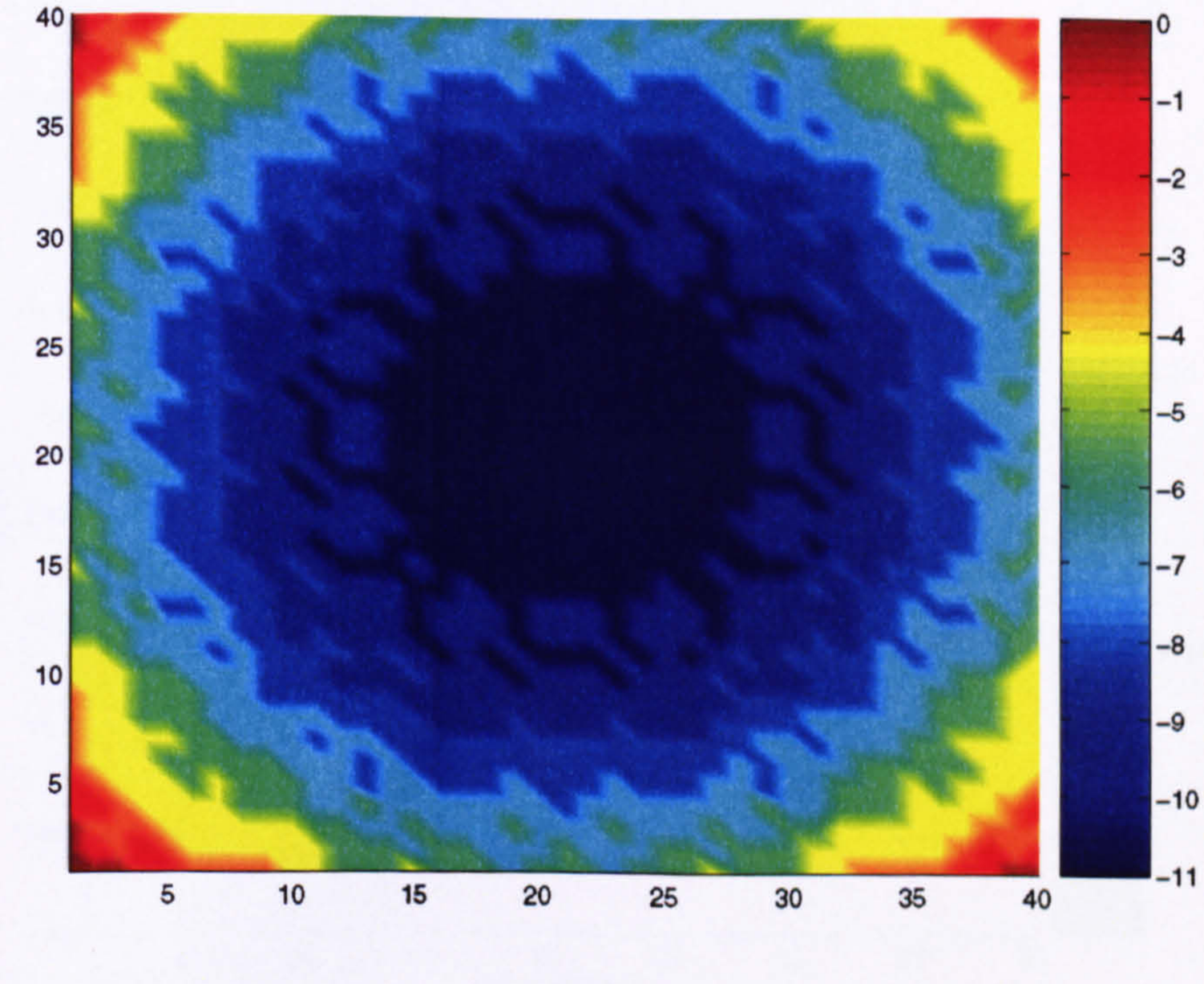

Figure 6.18: True compaction (top) versus estimated compaction from the anisotropic two-way travel-time method (isotropic overburden and anisotropic reservoir). Scenario: isotropic overburden and anisotropic reservoir.

C) Anisotropic Scenario – Anisotropic Overburden and Reservoir

For a scenario similar to that in the previous subsection, but now with anisotropic overburden shale with 15% anisotropy, another estimation of compaction is made based on the two-way travel times of pre-production and post-production cases shown in Figure 6.19. Figure 6.20 illustrates the true compaction and the estimated compaction for the anisotropic overburden and reservoir. Taking into account the effect of anisotropy improves the estimated result, although it overestimates the result, while it is still in an acceptable range. Figure 6.21 displays the true compaction and all three estimates of compaction, and depicts how much anisotropy may correct our estimation of the compaction of the studied model. A summary of the results of compaction estimations made using reservoir-flow simulation is given in Table 6.5.

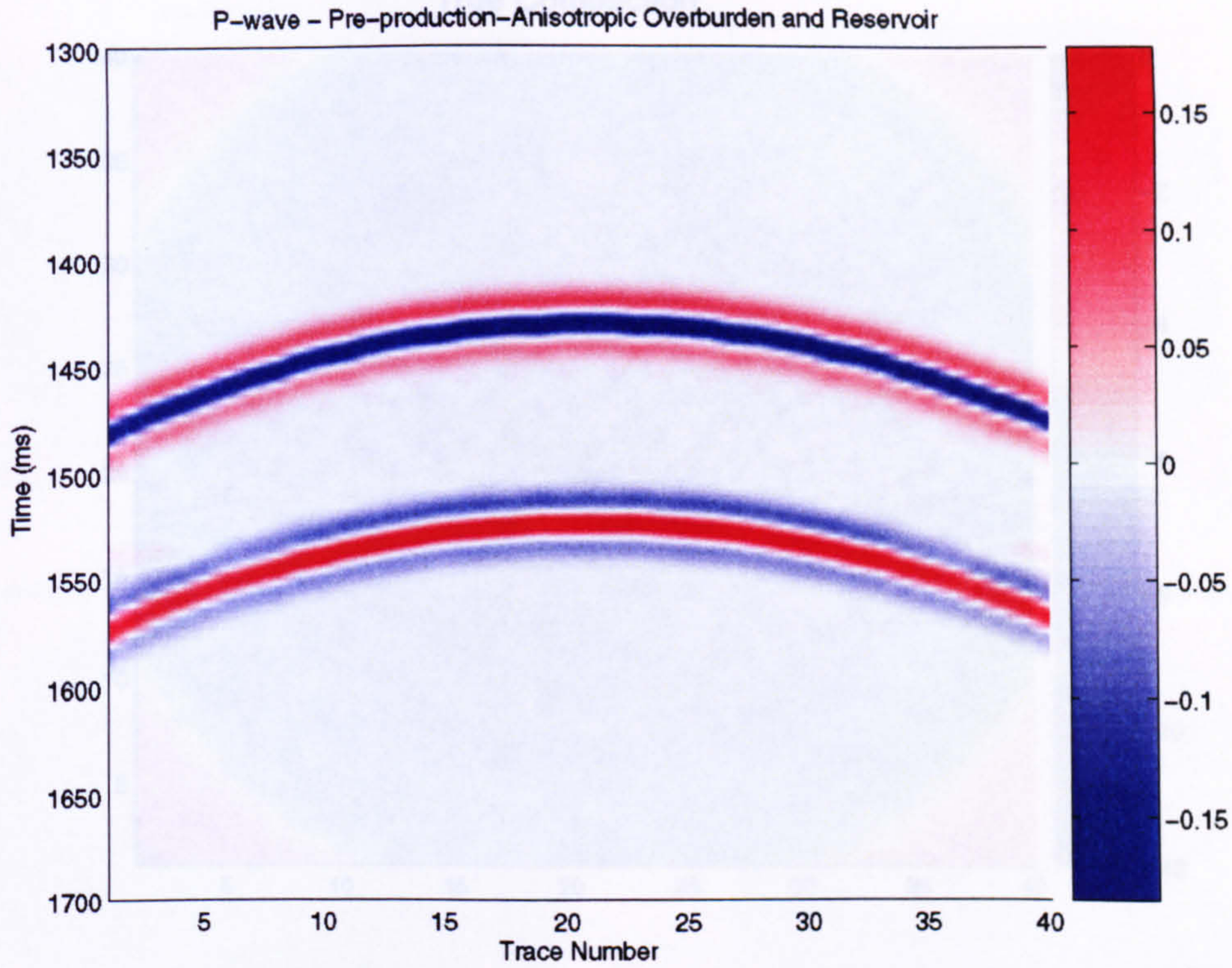

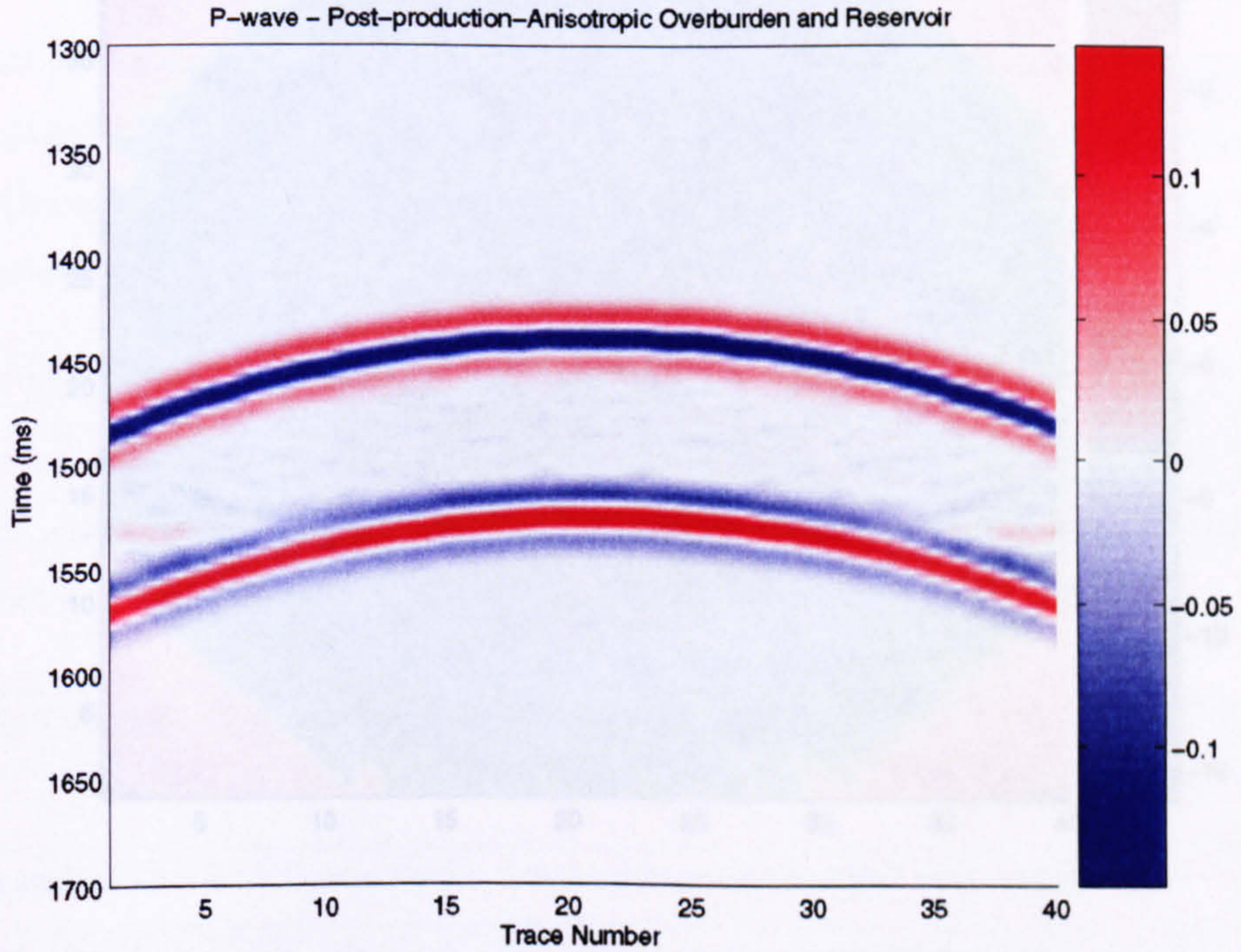

Figure 6.19: Synthetic sections for compressional waves, using simulation results – before production (top) and after production (bottom). Scenario: anisotropic overburden and reservoir.

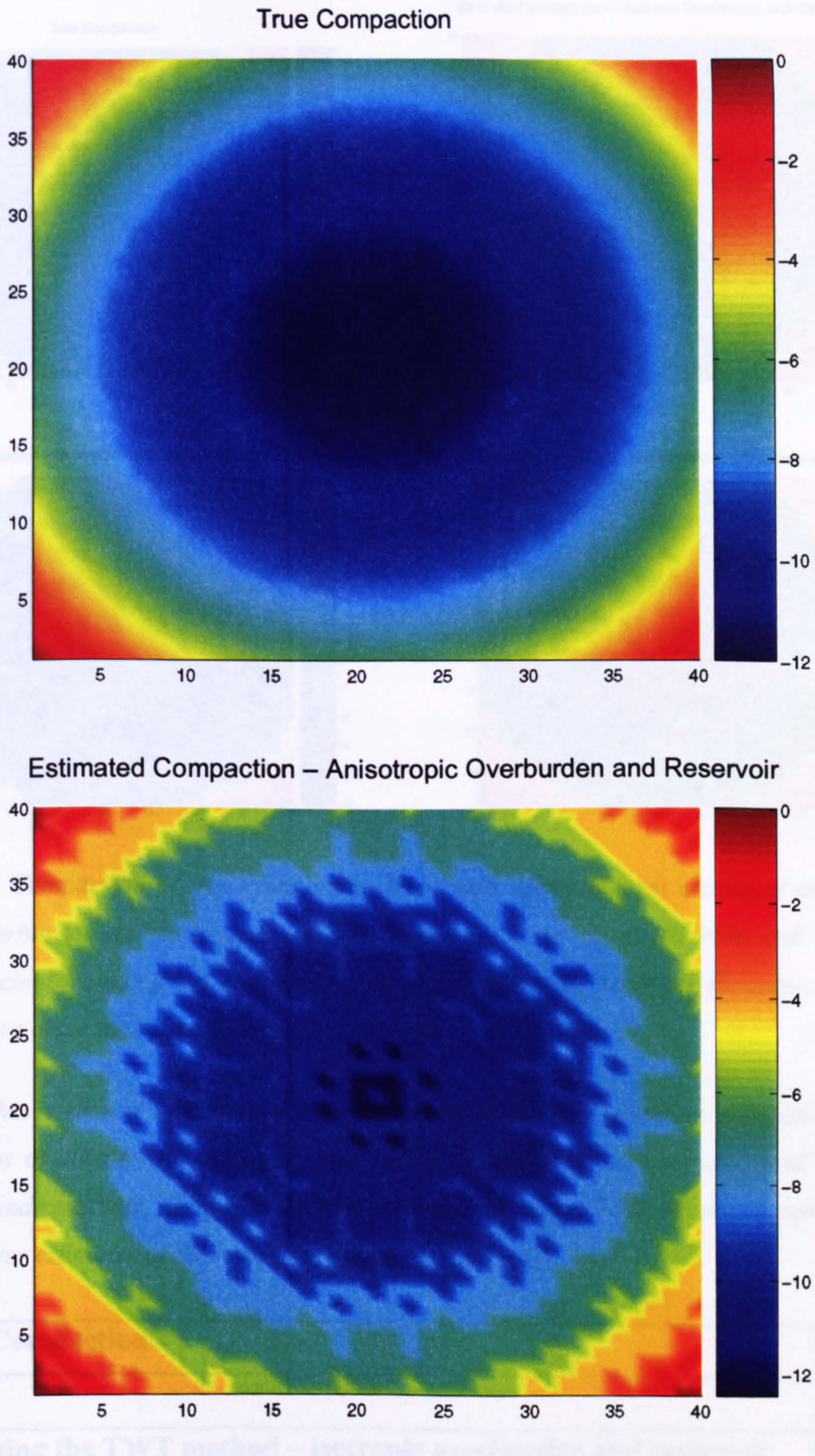

Figure 6.20: True compaction (top) versus compaction estimated from the anisotropic two-way travel-time method. Scenario: anisotropic overburden and reservoir.

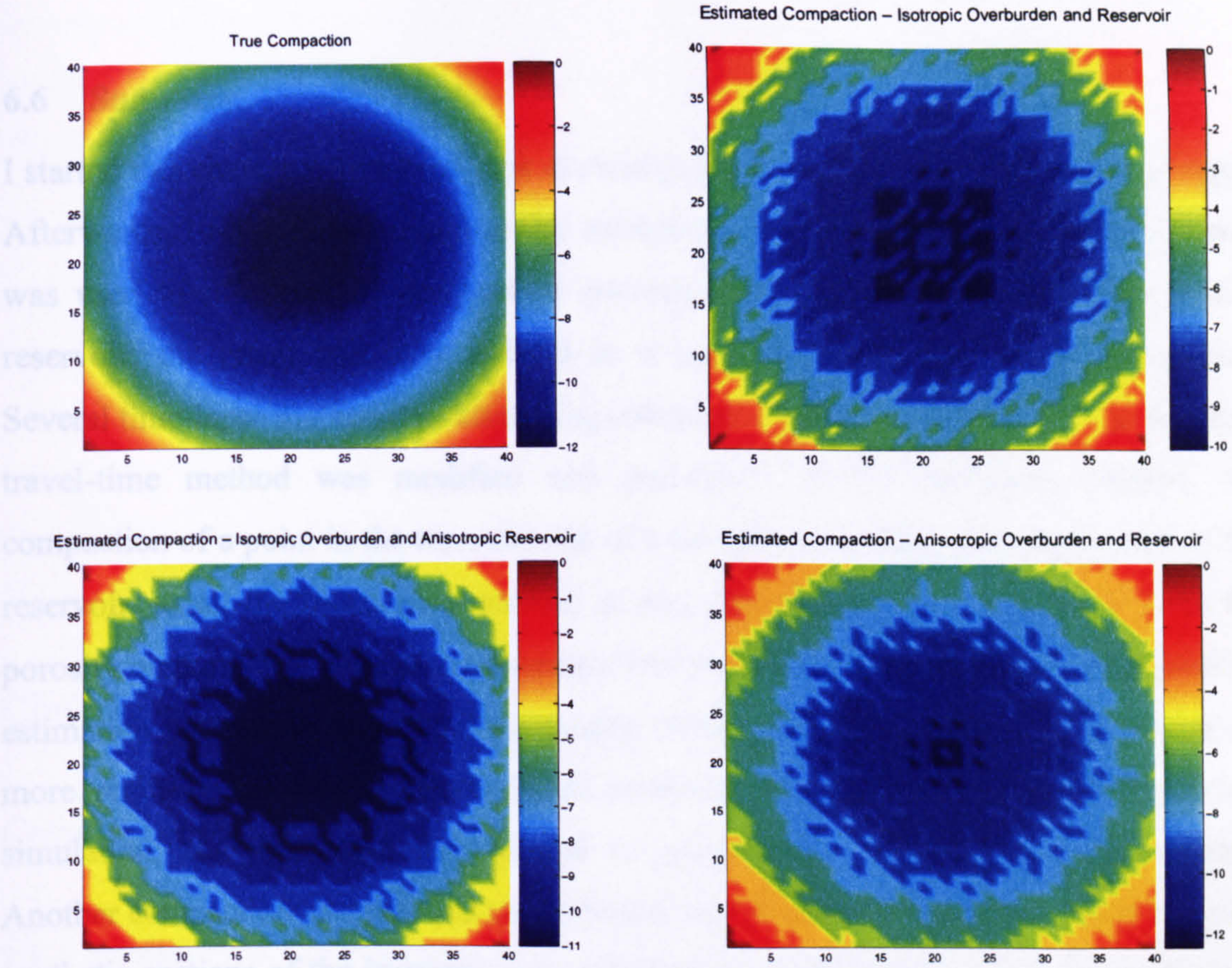

Figure 6.21: Comparison of true compaction (top) with three different estimated compactions, isotropic overburden and reservoir (second from top), isotropic overburden and anisotropic reservoir (second from bottom) and anisotropic overburden and reservoir (bottom), illustrating results that are close to the true value of compaction.

Table 6.5: This is similar to Table 6.4, but is taken from the reservoir-flow simulation and with two scenarios of anisotropy: isotropic overburden and anisotropic reservoir; and anisotropic overburden and reservoir, compared with the isotropic response. Here the anisotropic scenarios also give better estimates of the reservoir compaction.

Reservoir Compaction	**Metres**
True	**12**
Estimate using the TWT method – isotropic overburden and reservoir	**10**
Estimate using the TWT method – isotropic overburden and anisotropic reservoir	**11**
Estimate using the TWT method – anisotropic overburden and reservoir	**12.3**

6.6 Summary

I started this chapter with a brief look at reservoir deformation, its importance and types. Afterwards, I reviewed compaction and subsidence in more detail. A laboratory dataset was used to illustrate the decrease in porosity with hydrocarbon production from a reservoir; the result was later utilized as a basis to compute reservoir compaction. Several time-lapse methods for estimating compaction were mentioned, and the two-way travel-time method was modified and presented. In the modelling section, the compaction of a point in the top reservoir of a model was estimated as an average of the reservoir, using the travel-time method; it was also compared to the results from the porosity method. The impact of anisotropy was studied via another round of compaction estimation that further improved the quality of the isotropic estimate. To investigate a more realistic scenario, a dome-shaped reservoir was inputted into a reservoir-flow simulation, and the output was utilized to generate isotropic synthetic seismograms. Another compaction analysis was made, based on P-wave travel time computed from the synthetic sections of the isotropic case, which underestimated the value of compaction. Anisotropic synthetic seismograms were also generated in two scenarios: one scenario involving an isotropic overburden and an anisotropic reservoir, and the other with an anisotropic overburden and reservoir. Here again the estimates of compaction demonstrated improvements – now being closer to the true value of reservoir compaction. Considering the anisotropy of both the overburden and the reservoir, and hence taking its effect into account during the computation, appeared to correct the estimation of compaction.

Chapter 7

Conclusions

7.1 Summary of the Findings

To bring this thesis to a close, I will now briefly review the objectives of the study; seismic velocity anisotropy that is induced by either stress or fractures; and the most likely impacts on seismic studies, in order to assess how far my efforts have reached. Hence, the importance of stress to hydrocarbon reservoirs, and also the value that fractures add to reservoirs' productivity, was noted. Chapter 2 represented an attempt to refresh our ideas of the importance of stress and fractures to most aspects of reservoir management. It also introduced the topic of seismic-wave velocity anisotropy – including the necessary definitions and concepts, as well as providing a historical perspective of research into stress-induced anisotropy, followed by a description of fractures and fractured reservoirs and some of their important features, as well as the major effective medium and fracture theories.

Calculation of Stress-Induced Anisotropy (SIA) in Sandstone

In Chapter 3, a methodology was presented that could be used to compute the stress-induced anisotropy in sandstone reservoirs, utilizing both the published literature and the laboratory data. Based on the new findings, it was noted that a specific differential stress setting gave rise to a high induced anisotropy. Since including fluid saturation is more desirable and realistic with regard to reservoir studies, the induced anisotropy was

recomputed for different saturation scenarios, which had moderate to high magnitudes of anisotropy. At the end of the chapter, some exponential approximations were presented. These displayed a good fit to the computed anisotropy parameters.

Calculation of Fracture-Induced Anisotropy (FIA), and Comparing it with SIA

By using the same reservoirs as for Chapter 3, different cases of fracture-induced anisotropy were calculated – for dry-frame rocks, and rocks later saturated with gas, oil and brine. The fracture-induced anisotropy was observed to be high for less stress-sensitive reservoirs. In this study, the stress-sensitive reservoirs showed little fracture-induced anisotropy. The next challenge was to compare this type of anisotropy (FIA), with stress-induced anisotropy (SIA). It was observed that, in FIA, the parameter γ decreases with fluid saturation from gas to oil and brine, as the fluid bulk modulus increases, whereas it is unchanged in SIA. This depicts that the analysis of shear-wave velocity anisotropy could have the potential to discriminate between the two types of anisotropy. Other anisotropy parameters, ε and δ, exhibit different behaviours in different anisotropy types; they also add to the possibility of distinguishing one source of induced anisotropy from another. The modelling of a less stress-sensitive gas reservoir revealed that ε and δ increase almost linearly with fracture porosity, but that the growth of γ is exponential – an effect which is also smoothed to linear in stress-sensitive oil reservoirs. The magnitudes of FIA parameters are less than 2% for the oil–water contact, implying that FIA may not be able to detect such an interface. However, they are adequate to distinguish gas from water, due to the large differences between the corresponding values. The SIA seemed to be dimming in the less stress-sensitive reservoirs, but was observable to strongly developed in the stress-sensitive reservoirs, for all gas-, oil- and brine-saturated sandstones. As was mentioned for SIA the parameter γ increases with pressure, but shows no variations with fluid change hinting once again that the anisotropy in shear waves can provide information on distinguishing the role of stress from that of fractures, and also on fluid and pressure studies. It was illustrated that SIA produces a greater magnitude of anisotropy, and therefore it was chosen for further investigation in Chapters 5 and 6. Using several displays, it was shown that the AVO and AVAZ attributes could also contribute to indirectly distinguishing the role of stress from that of fractures.

Effects of SIA on Time-Lapse Studies

Chapter 5 gave a subtle comparison of the common industry approach to time-lapse seismic analyses *i.e.* based on the isotropic assumptions of the behaviour of reservoir formations versus their realistic anisotropic responses. As stress had earlier been shown to produce larger magnitudes of anisotropy, the corresponding procedure was utilized in both the initial case – or pre-production of an oil reservoir, and in the final case – or post-production. The SIA results of these scenarios were inputted into the modelling of compressional-wave reflectivity and synthetic seismograms. Variations of amplitude with offset and azimuth and 4D signatures were illustrated and interpreted. The results indicated the significance of including the effects of stress-induced anisotropy in such studies. An error in estimating the oil–water contact could be detected by taking the induced anisotropy into consideration.

Effects of SIA on the Estimation of Geomechanical Compaction

In Chapter 6, the stress-induced anisotropy was utilized for estimating reservoir compaction, after stressing the importance of geomechanical deformation to producing reservoirs, and reviewing the published methods of estimating compaction. The P-wave travel-time method was modified and illustrated in order to present an accurate estimate of compaction. Taking into account the velocity anisotropy of the overburden and reservoir rocks had the effect of further improving the estimate, producing a closer fit to the true compaction.

7.2 Recommendations for Future Research

As has already been shown, stress-induced anisotropy can be considerable, and so its implications deserve scrutiny with regard to a range of aspects important for reservoir exploration, production and management. For example, permeability is believed to be markedly affected by stress changes: hence, this type of velocity anisotropy may have a lot to offer to the reservoirs' permeability anisotropy (for example Almaskeri and MacBeth, 2005, Floricich *et al.*, 2005 and MacBeth, 2006).Wide-azimuth and wide-offset 3D seismic can give valuable information about stress regimes and also fracture distribution and density, allowing the reservoir manager to predict reservoir performance.

Shear-wave azimuthal anisotropy and its effects on travel time; phase; and amplitude; and also its splitting or birefringence, offer numerous opportunities to better understand and analyse the anisotropic behaviour of reservoirs. Information on lithology can also be obtained from the analysis of shear-wave data.

Stress-induced anisotropy was calculated based upon a setting most appropriate to the North Sea. However, different settings are recommended for research on other areas, in order to assess the accuracy of the observations and methodology used in Chapter 3.

The frequency dependence of induced anisotropy might add considerably to our understanding of the reservoirs' responses to time-lapse studies (for example Chapman, 2003, Liu *et al.*, 2003 and Maultzsch *et al.*, 2003). This would involve investigating attributes such as reflection coefficients, attenuation, azimuthal changes, variations of shear-wave time-delay with frequency, and also the polarization of fast and slow shear waves. Modelling scenarios used in the comparison of stress-induced anisotropy with fracture-induced anisotropy, and the results thus achieved can be further evaluated through their application to real seismic data.

With respect to the example of modelling illustrated in Chapter 5, the significance and limitations of the approach can be confirmed and revealed by testing it on time-lapse seismic data. This will involve acquiring time-lapse data for different azimuths.

Seismic velocity anisotropy was illustrated in order to enhance the estimation of geomechanical compaction using the compressional-wave travel-time method. Additional enhancement can be achieved by using the compressional- and converted-shear-wave (PS) travel-time method. This modelling can also be tested by using travel times taken from real data.

References

Adams, L.H. and Williamson, E.D., 1923. The compressibility of minerals and rocks at high pressure. *Journal of the Franklin Institute*, **195**, 475.

Aguilera, R., 1980. *Naturally Fractured Reservoirs*. Pennwell Publishing Company, Tulsa, OK, USA.

Aki, K. and Richards, P., 1980. *Quantitative Seismology – Theory and Method*. W.H. Freeman, New York, USA.

Alkhalifah, T., Tsvankin, I., Larner, K. and Toldi, J., 1996. Velocity analysis and imaging in transversely isotropic media: methodology and a case study. *The Leading Edge*, **15**(5), 371–378.

Almaskeri, Y., and MacBeth, C., 2005. Location and evaluation of flow barriers using 4D seismic. 75th Annual International Meeting, SEG, Expanded Abstracts , 2472-2475.

Al-Naamani, A.Y., 2004. *Time-lapse analysis of multi-component seismic data*. PhD thesis, Heriot-Watt University, Edinburgh, Scotland, UK.

Al-Sughayer, A.A.H., 1999. *Stress sensitivity of some reservoirs and its impact on well test analysis*. Ph.D. thesis, Heriot-Watt University, Edinburgh, Scotland, UK.

Amadei, B. and Stephansson, O., 1997. *Rock Stress and its Measurement*. Chapman and Hall, London, UK.

Angerer, E., Crampin, S., Li, X.Y. and Davis, T.L., 2002. Processing, modelling and predicting time-lapse effects of overpressured fluid-injection in a fractured reservoir. *Geophysical Journal International*, **149**, 267–280.

Ball, V. and Batzle M., 1994. Contrasting stress dependence of compressional and shear velocities: implications for laboratory, logging and seismic measurements. *SEG Technical Program Expanded Abstracts*, **13**, 1065–1068.

Batzle, M. and Wang, Z., 1992. Seismic properties of pore fluids. *Geophysics*, **57**, 1396–1408.

Bennion, D.B. and Thomas, F.B., 1999. Underbalanced drilling: a reservoir design perspective. *The 7th Annual Petroleum Society/SPE (Society of Petroleum Engineers) Conference on Horizontal Well Technology,* 3 November, Calgary, Canada, Hycal Energy Research Laboratories Ltd. www.hycal.com/index.php?s=file_download&id=97, 1-22.

Biot, M.A., 1962. Mechanics of deformation and acoustic propagation in porous media. *Journal of Applied Physics*, **33**, 1482–1498.

Borgerud, L. and Svare, E., 1995. In-situ stress field on the Norwegian margin, 62°–67° North. *Workshop on Rock Stresses in the North Sea*, Trondheim, Norway, February 13–14, SINTEF Rock and Mineral Engineering, 169-178.

Boyd-Gorst, J., Fail, P. and Pointing, L., 2001. 4D time lapse reservoir monitoring of Nelson Field, central North Sea: successful use of an integrated rock physics model to predict and track reservoir production. *The Leading Edge*, December, 1336–1350.

Brown, J.S. and Korringa, J., 1975. On the dependence of the elastic properties of a porous rock on the compressibility of the pore fluid. *Geophysics*, **40**, 608–616.

Bruno, M.S. and Winterstein, D.F., 1994. Some influences of stratigraphy and structure on reservoir stress orientation. *Geophysics*, **59**, 954–962.

Cabrera, P. and Davis, T.L., 2002. Use of time-lapse shear wave anisotropy for dynamic characterization of the San Andres carbonate reservoir. *AAPG Annual Meeting*, American Association of Petroleum Geologists, Tulsa, OK, USA.

Cardona, R., 2002. Two theories for fluid substitution in porous rocks with aligned cracks: 72nd Annual International Meeting, SEG, Expanded Abstracts, 173-176.

Castagna, J.P., Batzle, M.L. and Kan, T.K., 1993. Rock physics: the link between rock properties and AVO response. *In:* Castagna, J.P. and Backus, M.M. (eds), *Offset-dependent Reflectivity – Theory and Practice of AVO Analysis*, Society of Exploration Geophysicists, Tulsa, OK, USA, 135–171.

Chapman, M., 2003. Frequency dependent anisotropy due to meso-scale fractures in the presence of equant porosity. *Geophysical Prospecting*, **51**, 5, 369-379.

Cheng, C.H. and Toksöz, M.N., 1979. Inversion of seismic velocities for the pore aspect ratio spectrum of a rock. *Journal of Geophysical Research*, **84**, 7533–7543.

Chin, L.Y., Thomas, L.K., Pierson R.G. and Sylte J.E., 2003. Integrating geomechanics in full-field 3-D reservoir simulation – modeling techniques and field applications. *SPE Applied Technology Workshop*, Corpus Christi, Texas, USA. Available at: www.spe.org/specma/binary/files/156854203acor_session2_3chin.pdf.

Crampin, S., 1989. Suggestions for a consistent terminology for seismic anisotropy. *Geophysical Prospecting*, **37**, 753–770.

Crampin, S., 1998. Shear-wave splitting in a critical crust: the next step. *Revue de L'Institut Français du Petrole*, **53**(5), September–October, 749–764.

Crampin, S., 2001. Shear-wave anisotropy: a new window into the crack-critical rockmass. *CSEG Recorder*, September, 11–27.

Davis, T.L., Terrell, M.J., Benson, R.D. and Kendall, R.R., 2002. Seismic monitoring of the CO2 flood at Weyburn Field, Saskatchewan, Canada. EAGE 64th Conference and Exhibition, Florence, Italy, EAGE (European Association of Geoscientists and Engineers), Zeist, The Netherlands, also available at: geophysics.mines.edu/rcp/papers/Davis_EAGE_2002.PDF.

Dillen, M.W.P., Cruts, H.M.A., Groenenboom, J., Fokkema, J.T., and Duijndam, A.J.W., 1999. Ultrasonic velocity and shear-wave splitting behavior of a Colton sandstone under a changing triaxial stress. *Geophysics*, **64**, 1603–1607.

Duranti, L., 2001. *Time-lapse multicomponent seismic analysis of reservoir dynamics.* PhD thesis, Colorado School of Mines, Golden, Colorado, USA.

Dvorkin, J., Nur, A. and Chaika, C., 1996. Stress sensitivity of sandstones. *Geophysics*, **61**, 444–455.

Eaton, B., 1998. Using pre-drill seismic and LWD data for safe, efficient drilling. www.findarticles.com, Articles, World Oil, December.

Fett, T., 1991. Fracture evaluation in the Austin Chalk. Presented at *Houston Geological Society Conference on Fracture Evaluation* (Schlumberger Well Services).

Finkbeiner, T., 1998. *In-situ* stress, pore pressure, and hydrocarbon migration and accumulation in sedimentary basins. *Stanford Rock Physics and Borehole Geophysics Project. Thesis*, Vol. 73, Stanford University, Stanford, CA, USA.

Fjaer, E. and Holt, R.M., 1999. Stress and stress release effects on acoustic velocities from cores, logs and seismics. *SPWLA 40th Annual Logging Symposium*, May 30–June 3, paper WW (1-13).

Floricich, M., Alaskeri, Y. and MacBeth, C., 2005. Estimation of Horizontal Permeability Using Pressure Changes Derived from 4D Seismic Data: 67th Meeting, EAGE, Expanded Abstracts, C009.

Freund, D., 1992. Ultrasonic compressional and shear velocities in dry clastic rocks as a function of porosity, clay content, and confining pressure. *Geophysical Journal International*, **108**, 125–135.

Gaarenstroom, L., Tromp, R.A.J., de Jong, M.C. and Brandenburg, A.M., 1993. Overpressures in the Central North Sea: implications for trap integrity and drilling safety. *In:* Parker, J.R. (ed.), *Petroleum Geology of Northwest Europe.* Proceedings of the 4th Conference, Geological Society of London, UK, 1305–1313.

Gassmann, F., 1951. Elastic waves through a packing of spheres, *Geophysics,* **16**, 673–685.

Geertsma, J., 1973. Land subsidence above compacting oil and gas reservoirs. *Journal of Petroleum Technology*, June, 734-744.

Grechka, V. and Tsvankin, I., 1998. Feasibility of nonhyperbolic moveout inversion in transversely isotropic media. *Geophysics*, **63**, 957–969.

Gregory, A.R., 1976. Fluid saturation effects on dynamic elastic properties of sedimentary rocks. *Geophysics*, **41**, 895–921.

Grimm, R.E., Lynn, H.B., Bates, R., Philips, D.R., Simon, K.M. and Beckham, W.E., 1999. Detection and analysis of naturally fractured reservoirs: multiazimuth seismic surveys in the Wind River Basin, Wyoming. *Geophysics*, **64**, 1277–1292.

Guilbot, J. and Smith, B., 2002. 4D-constrained depth conversion for reservoir compaction estimation, application to the Ekofisk Field. *The Leading Edge*, **21**, 302–308.

Gurevich, B., 2002. Elastic properties of saturated porous rocks with aligned fractures. *SEG Expanded Abstracts, 72nd Meeting, Society of Exploration Geophysicists*, Tulsa, OK, USA, 2405–2408.

Hall, S., 2000. Rock fracture characterization and seismic anisotropy: application to ocean bottom seismic data. PhD Thesis, University of Leeds, UK.

Hansen, L., Davies, D., Garnham, J., McInally, A. and Boyd-Gorst, J., 2001. Time-lapse lithology prediction in the Nelson Field. *First Break*, **19**, 40–45.

Hatchell, P.J., van den Beukel, A., Molenaar, M.M., Maron, K.P., Kenter, C.J., Stammeijer, J.G.F., van der Velde, J.J. and Sayers, C.M, 2003. *Whole Earth 4D: Reservoir Monitoring Geomechanics*. SEG Expanded Abstracts, 1330–1333.

Heffer, K.J., Fox, R.J., McGill, C.A. and Koustabeloullis, N.C., 1997. Novel techniques show links between reservoir flow directionality, Earth stress, fault structure and geomechanical changes in mature waterfloods. SPE (Society of Petroleum Engineers) Paper No. 30711, 91-98.

Helbig, K., 1983. Elliptical anisotropy – its significance and meaning. *Geophysics*, **48**, 825–832.

Helbig, K., 1984. Anisotropy and dispersion in periodically layered media. *Geophysics*, **49**, 364–373.

Helbig, K., 1994. Foundations of Anisotropy for Exploration Seismics. Pergamon, New York, USA.

Helbig, K., 1996. Kelvin and early history of seismic anisotropy. *In:* Fjaer, E., Holt, R.M. and Rathore, J.S. (eds) *Seismic Anisotropy*, Society of Exploration Geophysicists, Tulsa, OK, USA, 15–36.

Holt, R.M. and Fjaer, E., 1987. Acoustic and mechanical behavior during failure. *57th Annual International Meeting, SEG, Expanded Abstracts*, *Session, BHG 1.5*, Society of Exploration Geophysicists, Tulsa, OK, USA,14–18.

Holt, R.M., Fjaer, E. and Furre, A.K., 1996. Laboratory simulation of the influence of earth stress changes on wave velocities. *In:* Rathore, J.S. (ed.), *Seismic Anisotropy*. Society of Exploration Geophysicists, Tulsa, OK, USA, 180–202.

Hudson, J.A, 1980. Overall properties of a cracked solid. *Mathematical Proceedings of the Cambridge Philosophical Society*, **88**, 371–384.

Hudson, J.A., 1981. Wave speeds and attenuation of elastic waves in material containing cracks. *Geophysical Journal of the Royal Astronomical Society*, **64**, 133–150.

Hudson, J.A., 1986. A higher order approximation to the wave propagation constants for a cracked solid. *Geophysical Journal of the Royal Astronomical Society*, **87**, 265–274.

Hudson, J.A., 1990. Overall elastic properties of isotropic materials with arbitrary distribution of circular cracks. *Geophysical Journal International*, **102**, 465–469.

Hudson, J.A., 1994. Overall properties of anisotropic materials containing cracks. *Geophysical Journal International*, **116**, 279–282.

Hudson, J.A., 2000. The effect of fluid pressure on wave speeds in a cracked solid. *Geophysical Journal International*, **143**, 302–310.

Hudson, J.A., Liu, E. and Crampin, S., 1996*a*. The mechanical properties of materials with interconnected cracks and pores. *Geophysical Journal International*, **124**, 105–112.

Hudson, J.A., Liu, E. and Crampin, S., 1996*b*. Transmission properties of a fault plane. *Geophysical Journal International*, **125**, 559–566.

Hudson, J.A., Liu, E. and Crampin, S., 1997. The mean transmission properties of a fault with imperfect facial contact. *Geophysical Journal International*, **129**, 720–726.

Ibekwe, I.A., Coker-III, O.D., Fuh, G.F. and Actis, S.C., 2003. Magnolia casing design for compaction. SPE (Society of Petroleum Engineers), Richardson, Texas, USA, Paper No. 79816, 1–11.

International Energy Agency, 1994. Monthly Oil Market Report, **9**, March, 9–19. Available at: *http://omrpublic.iea.org/supplyarchres.asp*

Jack, I., 1998. Time-lapse seismic in reservoir management. *Distinguished Instructor Short Course*, Society of Exploration Geophysicists, Tulsa, OK, USA.

Johnson, P.A. and Rasolofosaon, P.N.J., 1996. Nonlinear elasticity and stress-induced anisotropy in rocks: reflections on experiment results. *Journal of Geophysical Research*, **101**, 3113–3124.

Jones, M.E., Leddra, M.J., Goldsmith, A.S. and Edwards, D., 1992. The geomechanical characteristics of reservoirs and reservoir rocks. *Offshore Technology Report, OTH*, 90, 333.

Khaksar, A., Griffiths, C.M. and McCann, C., 1999. Compressional and shear-wave velocities as a function of confining stress in dry sandstones. *Geophysical Prospecting*, **47**, 487–508.

Kirstetter, O. and MacBeth, C., 2001. Compliance-based interpretation of dry frame pressure sensitivity in shallow marine sandstone. *71st Annual International Meeting: Society of Exploration Geophysicists*, 2132–2135.

Kirstetter, O., Jones, C., Somerville, J., Corbett, P. and Smart, B., 2000. Time-lapse feasibility study on a shallow marine sandstone reservoir analogue. *Proceedings of the EAGE/SEG Workshop: Petrophysics Meets Geophysics*, Paris, France, 6–8 November, EAGE (European Association of Geoscientists and Engineers).

Landrø, M., 2001. Discrimination between pressure and fluid saturation changes from time-lapse seismic data. *Geophysics*, **66**, 836–844.

Landrø, M. and Stammeijer, J., 2004. Quantitative estimation of compaction and velocity changes using 4D impedance and traveltime changes. *Geophysics*, **69,** 949–957.

Lefeuvre, F., 1993. Fracture related anisotropy detection and analysis; and if the P-waves were enough? *SEG Expanded Abstracts*, **64**, 942–945.

Li, X.Y., 1998. Processing PP and PS waves in multicomponent sea-floor data for azimuthal anisotropy: theory and overview. *Proceedings of the 8th International Workshop on Seismic Anisotropy*, Revue de L'Institut Français du Petrole, **53**, 607–620.

Liu, E., Crampin, S. and Booth, D.C., 1989. Shear-wave splitting in cross-hole surveys: modeling. *Geophysics*, **54**, 57–65.

Liu, E. and Crampin, S., 1990. Effects of the Internal Shear Wave Window: Comparison With Anisotropy Induced Splitting. *Journal of Geophysical Research*, **9.5**(B7), 11,275–11,281.

Liu, E., Hudson, J.A. and Pinter, T., 2000. Equivalent medium representation of fractured rock. *Journal of Geophysical Research*, **105** (B2), 2981–3000.

Liu, E., Queen, J.H., Li, X.Y., Chapman, M., Lynn, H.B. and Chesnokov, E.M. 2003. Analysis of frequency-dependent seismic anisotropy from a multicomponent VSP at Bluebell-Altamont field, Utah. *Journal of Applied Geophysics*, **54**, 319-333.

Lo, T., Coyner, K. and M., 1986. Experimental determination of elastic anisotropy of Berea sandstone. *Geophysics*, **51**, 164–171.

Love, A.E.H., 1934. *A Treatise on the Mathematical Theory of Elasticity*. Cambridge, Cambridge University Press, UK.

Lynn, H.B., 1991. Field measurements of azimuthal anisotropy: First 60 metres, San Francisco Bay Area, CA, and estimation of the horizontal stresses' ratio from V_{S1}/V_{S2}. *Geophysics*, **56**, 822–832.

Lynn, H.B. and Thomsen, L., 1990. Reflection shear wave data collected near the principal axes of azimuthal anisotropy. *Geophysics*, **55**, 147–156.

Lynn, H.B., Beckham, W.E., Simon, K.M., Bates, R., Layman, M. and Jones, M., 1999*a*. P-wave and S-wave azimuthal anisotropy at a naturally fractured gas reservoir, Bluebell–Altamont Field, Utah. *Geophysics*, **64**, 1312–1328.

Lynn, H.B., Campagna, D., Simon, K.M. and Beckham, W.E., 1999*b*. Relationship of P-wave seismic attributes, azimuthal anisotropy and commercial gas play in 3-D P-wave

multiazimuth data, Rulison Field, Piceance Basin, Colorado. *Geophysics*, **64**, 1293–1311.

Lynn, H.B., Weathers, L. and Beckham, W.E., 1999*c*. The mobile Onshore Texas 3D full-azimuth full-offset P-wave survey, 9th International Workshop on Seismic Anisotropy, www.seg.org, Meeting.

MacBeth, C., 1999. Azimuthal variation in P-wave signatures due to fluid flow. *Geophysics*, **64**, 1181–1192.

MacBeth, C., 2000*a*. Using P-wave data to distinguish between gas from water in fractures. *9th International Workshop on Seismic Anisotropy*, Society of Exploration Geophysicists, Tulsa, OK, USA, 1–15.

MacBeth, C., 2000*b*. Multicomponent VSP analysis for applied seismic anisotropy. *Handbook of Geophysical Exploration, Seismic Exploration Series*, Elsevier, Volume **26**.

MacBeth, C., 2002. The dry-frame pressure sensitivity of sandstone. *72nd Annual Meeting, Abstracts, Society of Exploration Geophysicists*, Tulsa, OK, USA, 1850–1853.

MacBeth, C., 2004. A classification for pressure sensitivity properties of a sandstone rockframe. *Geophysics*, **69**, 479–510.

MacBeth, C., 2006. Extraction of permeability from time-lapse seismic data: *Geophysical Prospecting*, **54**, 3, 333-349.

MacBeth, C. and Crampin, S., 1991. Processing of seismic data in the presence of anisotropy. *Geophysics*, **56**, 1320–1330.

MacBeth, C. and Lynn, H.B., 2001. Mapping fractures and stress using full-offset full-azimuth 3D PP data. 71st Annual International Meeting, San Antonio. *Expanded Abstracts, Society of Exploration Geophysicists*, Tulsa, OK, USA, 110-113.

MacBeth, C., Reid, F.L., McInally, A., Garnham, J. and Redondo-Lopez, T., 2002. 4D signatures of OWC movement in the Nelson Field -- modeling and interpretation. *72nd Annual International Meeting: Society of Exploration Geophysicists*, 1704–1707.

MacBeth, C., Stammeijer, J. and Omerod, M., 2006. Seismic monitoring of pressure depletion evaluated for a United Kingdom continental-shelf gas reservoir: *Geophysical Prospecting*, **54**, 1, 29-47.

McInally, A.T., Redondo-Lopez, T., Garham, J., Kunka, J., Brooks, A.D., Strenstrup-Hansen, L., Barclay, F. and Davies, D., 2003. Optimising 4D fluid imaging. *Journal of Petroleum Geosciences*, 91–101.

McLellan, P. and Hawkes, C., 2001. Borehole stability analysis for underbalanced drilling. *Journal of Canadian Petroleum Technology*, **40**(5), 1–8.

Matsushima, S., 1960. On the deformation and fracture of granite under high confining pressure. *Disaster Prevention Research Institute, Kyoto University, Bulletin*, **36**, 11.

Maultzsch, S., Chapman, M., Liu, E. and Li, X.Y., 2003. Modelling frequency dependent seismic anisotropy in fluid-saturated rock with aligned fractures: implication of fracture size estimation from anisotropic measurements. Geophysical Prospecting, **51**, 5, 381-392.

Mavko, G., Mukerji, T. and Godfrey, N., 1995. Predicting stress-induced velocity anisotropy in rocks. *Geophysics*, **60**, 1081–1087.

Mavko, G., Mukerji, T. and Dvorkin, J., 1998. *The Rock Physics Handbook: Tools for Seismic Analysis in Porous Media*. Cambridge University Press, Cambridge.

Nelson, R. A., 1985. *Geologic Analysis of Naturally Fractured Reservoirs*. Gulf Publishing Company, London, UK.

Nes, O.M., Holt, R.M. and Fjaer, E., 2000. The reliability of core data as input to reservoir monitoring studies. *SPE European Petroleum Conference, Paris*, Richardson, Texas, USA, SPE Paper No. 65180, 1-11.

Nur, A., 1971. Effects of stress on velocity anisotropy in rocks with cracks. *Journal of Geophysical Research*, **76**, 2022–2034.

Nur, A. and Simmons, G., 1969. Stress-induced velocity anisotropy in rock: an experimental study. *Journal of Geophysical Research*, **74**, 6667–6674.

Ohlson, F. and MacBeth, C., 1999. Elliptical anisotropy – regression or advance? *Annual Meeting Abstracts, Society of Exploration Geophysicists*, Tulsa, OK, USA, 1600–1603.

Olofsson, B., Probert, T., Kommedal, J.H. and Barkved, O.I., 2003. Azimuthal anisotropy from the Valhall 4C 3D Survey. *Leading Edge*, **22**(12), 1228–1235.

Ostrander, W.J., 1982. Plane-wave reflection coefficients for gas sands at non-normal angles of incidence. *52nd Annual International Meeting, Society of Exploration Geophysicists, Expanded Abstracts*, 216–218.

Ostrander, W.J., 1984. Plane-wave reflection coefficients for gas sands at non-normal angles of incidence. *Geophysics*, **49**, 1637–1648.

Postma, G.W., 1955. Wave propagation in a stratified medium. *Geophysics*, **20**, 780–806.

Prensky, S., 1992. Borehole breakouts and *in-situ* rock stress – a review. *Log Analyst*, **33**(3), 304–312.

Prioul, R., Bakulin, A. and Bakulin, V., 2004. Nonlinear rock physics model for estimation of 3D subsurface stress in anisotropic formations: theory and laboratory verification. *Geophysics*, **69,** 415–425.

Rasolofosaon, P., 1998. Stress-induced seismic anisotropy revisited. *Revue de L'Institut Français du Petrole*, **53**, 679–693.

Redpath, B.B. and Lee, R.C., 1986. *In-situ* measurements of shear-wave attenuation at a strong-motion recording site: sponsored by the USGS Contract No. 14-08-001-21823. Prepared by URSl, John A. Blume and Associates Engineers, San Francisco, CA, USA.

Rüger, A., 1996. *Reflection coefficients and azimuthal AVO analysis in anisotropic media*. Doctoral Thesis, Colorado School of Mines, Golden, Colorado, USA.

Rüger, A., 1998. Variation of P-wave reflectivity with offset and azimuth in anisotropic media. *Geophysics*, **63**, 935–947.

Rüger, A. and Tsvankin, I., 1995. Azimuthal variation of AVO response for fractured reservoirs. *Annual Meeting, Abstracts, Society of Exploration Geophysicists*, Tulsa, OK, USA, 1103–1160.

Rüger, A. and Tsvankin, I., 1997. Using AVO for fracture detection: analytic basis and practical solutions. *Leading Edge*, **10**, 1429–1434.

Saidi, A.M., 1987. Reservoir engineering of fractured reservoirs: Fundamental and practical aspects. TOTAL Edition Press, Paris, France.

Sarkar, D., Bakulin, A. and Kranz, R.L., 2002. Anisotropic inversion of seismic data for stressed media: theory and a physical modeling study on Berea sandstone. *72nd Annual Meeting, Expanded Abstracts, Society of Exploration Geophysicists*, Tulsa, OK, USA, 117–120.

Sayers, C.M., 2002. Stress-dependent elastic anisotropy of sandstones. *Geophysical Prospecting*, **50**, 85–95.

Sayers, C.M. and Kachanov, M., 1991. A simple technique for finding effective elastic constants of cracked solids for arbitrary crack orientation statistics. *International Journal of Solids Structure*, **12**, 81–97.

Sayers, C.M. and Kachanov, M., 1995. Microcrack-induced elastic wave anisotropy of brittle rocks. *Journal of Geophysical Research*, **100**(B3), 4149–4156.

Sayers, C.M., Van Munster, J.G. and King, M.S., 1990. Stress-induced ultrasonic anisotropy in Berea sandstone. *International Journal of Rock Mechanics*, **27**, 429–436.

Schoenberg, M.A., 1980. Elastic wave behavior across linear slip interfaces. *Journal of the Acoustical Society of America*, **68**, 1516–1521.

Schoenberg, M.A., 1999. Modeling rock behavior with linear slip deformation theory. *Annual Meeting, Abstracts, 61st EAGE Meeting*, Expanded Abstracts, European Association of Geoscientists and Engineers, Zeist, The Netherlands, 2-05.

Schoenberg, M. and Muir, F., 1989. A calculus for finely layered anisotropic media. *Geophysics*, **54**, 581–589.

Schoenberg, M. and Sayers, C.M., 1995. Seismic anisotropy of fractured rock. *Geophysics*, **60**, 204–211.

Schwartz, L.M., Murphy, W.F. and Berryman, J.G., 1994. Stress-induced transverse isotropy in rocks. *Annual Meeting, Abstracts, Society of Exploration Geophysicists*, Tulsa, OK, USA, 1081–1085.

Seiki, T., Aydan, O. and Kawamoto, T., 1997. The relation between geological features and the stress state of the earth's crust in Central Japan. *In:* Sugawara, K. and Obara, Y. (eds), *Rock Stress*, 385–390.

Shapiro, S. and Kaselow, A., 2002. On the stress dependence of seismic velocities in porous rocks. *72nd Annual International Meeting: Society of Exploration Geophysicists*, Tulsa, OK, USA, 1893–1896.

Shuey, R.T., 1985. A simplification of Zoeppritz Equations. *Geophysics*, **50**, 609–614.

Sinha, B.K. and Plona, T.J., 2001. Wave propagation in rocks with elastic--plastic deformations. *Geophysics*, **66**, 772–785.

Skomedal, E., Jostad, H.P. and Hettema, M.H., 2002. Effect of pore pressure and stress path on rock mechanical properties for HPHT application, SPE (Society of Petroleum Engineers), Richardson, Texas, USA, Paper No. 78152, 1–10.

Tao, G., King, M.S. and Nabi-Bidhendi, M., 1995. Ultrasonic wave propagation in dry and brine-saturated sandstones as a function of effective stress: laboratory measurements and modeling. *Geophysical Prospecting*, **43**, 299–327.

Teufel, L.W. and Farrell, H.E., 1992. Interrelationship between *in-situ* stress, natural fractures, and reservoir permeability anisotropy – a case study of the Ekofisk Field, North Sea, presented at: *Fractured and Jointed Rock Conference, ISRM Symposium*.

Thomsen, L., 1986. Weak elastic anisotropy. *Geophysics*, **51**, 1954–1966.

Thomsen, L., 1990. Poisson was not a geophysicist. *Leading Edge*, **9**(12), 27–29.

Thomsen, L., 1993. Weak anisotropic reflections, *In:* Castagna, J. and Backus, M. (eds), *Offset Dependent Reflectivity*, Society of Exploration Geophysicists, Tulsa, OK, USA.

Thomsen, L., 2002. Understanding seismic anisotropy in exploration and exploitation. *Distinguished Instructor Short Course Series*, No. **5**, Society of Exploration Geophysicists, Tulsa, OK, USA.

Tocher, D., 1957. Anisotropy in rocks under simple compression. *Transactions of the American Geophysical Union*, **38**(1), 89.

Tod, S., 2002. The effects of stress and fluid pressure on the anisotropy of interconnected cracks. Geophysical Journal International, **149**, 149-156.

Tsvankin, I., 1996. P-wave signatures and notation for transversely isotropic media: an overview. *Geophysics*, **61**, 467–483.

Tsvankin, I., 1997. Anisotropic parameters and P-wave velocity in orthorhombic media. *Geophysics*, **62**, 1292–1309.

Tsvankin, I. and Thomsen, L., 1994. Nonhyperbolic reflection moveout in anisotropic media. Geophysics, **59**, 1290-1304.

Tura, A. and Lumley, D., 1999. Estimating pressure and saturation changes from time-lapse AVO data. *69th Annual International Meeting, Expanded Abstracts*, Society of Exploration Geophysicists, 1655–1658.

Uhrig, L.F. and Van Melle, F.A., 1955. Velocity anisotropy in stratified media. *Geophysics*, **20**, 774–779.

Wang, Z., 2002. Seismic anisotropy in sedimentary rocks, Part 2: Laboratory data. *Geophysics*, **67**, 1423–1440.

Whyatt, M., Bowen, J.M. and Rhodes, D.N, 1992. The Nelson Field: a successful application of a development geoseismic model. *In*: Hardman, R.F.P. (ed.), *Exploration Britain: Geological Insights for the Next Decade.* Geological Society, London, Special Publications, **67**, 283–305.

Winkler, K.W., 1983. Contact stiffness in granular porous materials: comparison between theory and experiment. *Geophysical Research Letters*, **10**, 1073–1076.

Winkler, K.W. and Murphy, W.F., III, 1995. Acoustic velocity and attenuation in porous rocks. *In:* Ahrens, T.J.(ed) *Rock Physics and Phase Relations, A Handbook of Physical Constants*, *American Geophysical Union*, Washington DC, USA, **3**, 20–34.

Winterstein, D.F., 1990. Velocity anisotropy terminology for geophysicists. *Geophysics*, **55**, 1070–1088.

Winterstein, D.F., De, G.S. and Meadows, M.A., 2001. Twelve years of vertical birefringence in nine-component VSP data. *Geophysics*, **66**, 582–597.

Wiprut, D.J. and Zoback, M.D., 2000. Constraining the full stress tensor in the Visund Field, Norwegian North Sea: application to well-bore stability and sand production. *International Journal of Rock Mechanics and Mining Sciences*, **37**, 317–336.

Xu, H., Dvorkin, J. and Nur, A., 2002. Rock physics basis for determining porosity reduction due to production. *SEG 72nd Annual Meeting, Expanded Abstracts*, Tulsa, OK, USA, 1862-1865.

Yin, H., 1993. Acoustic velocity and attenuation of rocks; isotropy, intrinsic anisotropy, and stress-induced anisotropy. Ph.D. thesis, Stanford University, Stanford, CA, USA.

Yin, H. and Nur, A., 1992. Stress-induced ultrasonic velocity and attenuation anisotropy in rocks. *SEG Expanded Abstracts*, Tulsa, OK, USA, 1073–1076.

Zamora, M. and Poirier, J.P., 1990. Experimental study of acoustic anisotropy and birefringence in dry and saturated Fountainebleau sandstone. *Geophysics*, **55**, 1455–1465.

Zoback, M.D. and Peska, P., 1995. *In-situ* stress and rock strength in the GBRN/DOE pathfinder well, South Eugene Island, Gulf of Mexico. *Journal of Petroleum Technology*, July, 582.

Zoeppritz, K., 1919. Erdbebenwellen VII B, on the reflection and penetration of seismic waves through unstable layers. *Göttinger Nachrichten*, **1**, 66–84.

Appendices

Appendix 1: Stress–Strain Relations

The mathematical basis of elastic-wave propagation in an anisotropic medium has been discussed by Love (1934). Some physical laws are utilized as the basis of calculations of all categories of deformation in a continuum due to propagation of seismic waves These theorems of conservation include conservation of energy, conservation of mass, conservation of linear momentum, and conservation of angular momentum. Let x_1, x_2 and x_3 be spatial coordinates and u_1, u_2 and u_3 be the displacement components of an elastic wave in the rock. If the stress tensor is σ_{ij} and the normal strain tensor is related to the displacement u by:

$$\varepsilon_{ii} = \frac{\partial u_i}{\partial x_i}, \textit{for i = 1, 2 and 3.}$$

and for shear strain:

$$\varepsilon_{ij} = \frac{\partial u_i}{\partial x_j} + \frac{\partial u_j}{\partial x_i}, \textit{for i,j = 1, 2 and 3.}$$

The generalized Hooke's law is the starting point of our analysis. As shown by Aki and Richards (1980), a linearly elastic medium behaves such that each component of applied stress is linearly dependent on every component of strain. Or, in other words, an elastic medium possesses a constitutive relation between applied stress and resultant strain, which is one-to-one and time-independent. This relation can be defined as follows:

$$\sigma = F(\varepsilon)$$

Stressed sandstone treated in Hooke cell is expected to follow the stress–strain rule, assuming that there is no pre-stressing, *i.e.* $F(0) = 0$. By expanding the function in a power series, the constitutive relation will be in the form of:

$$\sigma_{ij} = C_{ijkl}\varepsilon_{kl} + D_{ijklmn}\varepsilon_{kl}\varepsilon_{mn} + \ldots$$

That can be approximated with adequate accuracy with:

$$\sigma_{ij} = C_{ijkl}\varepsilon_{kl}$$

where σ_{ij} is the second-order tensor of stress, ε_{kl} is the second-order tensor of strain, and C_{ijkl} is the fourth-order tensor of elastic modulus or stiffness. Writing the relation in the other way, the fourth-order compliance tensor emerges:

$$\varepsilon_{ij} = S_{ijkl}\sigma_{kl}$$

Compliance is the inverse of stiffness, *i.e.* $S_{ij} = C_{ij}^{-1}$.

$$\begin{bmatrix} \sigma_{11} \\ \sigma_{22} \\ \sigma_{33} \\ \sigma_{23} \\ \sigma_{13} \\ \sigma_{12} \end{bmatrix} = \begin{bmatrix} C_{1111} & C_{1122} & C_{1133} & C_{1123} & C_{1113} & C_{1112} \\ C_{2211} & C_{2222} & C_{2233} & C_{2223} & C_{2213} & C_{2212} \\ C_{3311} & C_{33322} & C_{3333} & C_{3323} & C_{3313} & C_{3312} \\ C_{2311} & C_{2322} & C_{2333} & C_{2323} & C_{23135} & C_{2312} \\ C_{1311} & C_{1322} & C_{1333} & C_{1323} & C_{1313} & C_{1312} \\ C_{1211} & C_{1222} & C_{1233} & C_{1223} & C_{1213} & C_{1212} \end{bmatrix} \begin{bmatrix} \varepsilon_{11} \\ \varepsilon_{22} \\ \varepsilon_{33} \\ \varepsilon_{23} \\ \varepsilon_{13} \\ \varepsilon_{12} \end{bmatrix}$$

Recalling that each component of the two-rank stress tensor is linearly proportional to every component of the two-rank strain tensor, we will have:

When $i = 1$ and $j = 1$, but $k = 1,2,3$ and $l = 1,2,3$ independently:

$$\sigma_{11} = C_{1111}\varepsilon_{11} + C_{1112}\varepsilon_{12} + C_{1113}\varepsilon_{13} + C_{1121}\varepsilon_{21} + C_{1122}\varepsilon_{22} + C_{1123}\varepsilon_{23} + C_{1131}\varepsilon_{31} + C_{1132}\varepsilon_{32} + C_{1133}\varepsilon_{33}$$

When $i = 1$ and $j = 2$, but $k = 1,2,3$ and $l = 1,2,3$ independently:

$$\sigma_{12} = C_{1211}\varepsilon_{11} + C_{1212}\varepsilon_{12} + C_{1213}\varepsilon_{13} + C_{1221}\varepsilon_{21} + C_{1222}\varepsilon_{22} + C_{1223}\varepsilon_{23} + C_{1231}\varepsilon_{31} + C_{1232}\varepsilon_{32} + C_{1233}\varepsilon_{33}$$

When $i = 1$ and $j = 3$, but $k = 1,2,3$ and $l = 1,2,3$ independently:

$$\sigma_{13} = C_{1311}\varepsilon_{11} + C_{1312}\varepsilon_{12} + C_{1313}\varepsilon_{13} + C_{1321}\varepsilon_{21} + C_{1322}\varepsilon_{22} + C_{1323}\varepsilon_{23} + C_{1331}\varepsilon_{31} + C_{1332}\varepsilon_{32} + C_{1333}\varepsilon_{33}$$

When $i = 2$ and $j = 1$, but $k = 1,2,3$ and $l = 1,2,3$ independently:

$$\sigma_{21} = C_{2111}\varepsilon_{11} + C_{2112}\varepsilon_{12} + C_{2113}\varepsilon_{13} + C_{2121}\varepsilon_{21} + C_{2122}\varepsilon_{22} + C_{2123}\varepsilon_{23} + C_{2131}\varepsilon_{31} + C_{2132}\varepsilon_{32} + C_{2133}\varepsilon_{33}$$

When $i = 2$ and $j = 2$, but $k = 1,2,3$ and $l = 1,2,3$ independently:

$$\sigma_{22} = C_{2211}\varepsilon_{11} + C_{2212}\varepsilon_{12} + C_{2213}\varepsilon_{13} + C_{2221}\varepsilon_{21} + C_{2222}\varepsilon_{22} + C_{2223}\varepsilon_{23} + C_{2231}\varepsilon_{31} + C_{2232}\varepsilon_{32} + C_{2233}\varepsilon_{33}$$

When $i = 2$ and $j = 3$, but $k = 1,2,3$ and $l = 1,2,3$ independently:

$$\sigma_{23} = C_{2311}\varepsilon_{11} + C_{2312}\varepsilon_{12} + C_{2313}\varepsilon_{13} + C_{2321}\varepsilon_{21} + C_{2322}\varepsilon_{22} + C_{2323}\varepsilon_{23} + C_{2331}\varepsilon_{31} + C_{2332}\varepsilon_{32} + C_{2333}\varepsilon_{33}$$

When $i = 3$ and $j = 1$, but $k = 1,2,3$ and $l = 1,2,3$ independently:

$$\sigma_{31} = C_{3111}\varepsilon_{11} + C_{3112}\varepsilon_{12} + C_{3113}\varepsilon_{13} + C_{3121}\varepsilon_{21} + C_{3122}\varepsilon_{22} + C_{3123}\varepsilon_{23} + C_{3131}\varepsilon_{31} + C_{3132}\varepsilon_{32} + C_{3133}\varepsilon_{33}$$

When $i = 3$ and $j = 2$, but $k = 1,2,3$ and $l = 1,2,3$ independently:

$$\sigma_{32} = C_{3211}\varepsilon_{11} + C_{3212}\varepsilon_{12} + C_{3213}\varepsilon_{13} + C_{3221}\varepsilon_{21} + C_{3222}\varepsilon_{22} + C_{3223}\varepsilon_{23} + C_{3231}\varepsilon_{31} + C_{3232}\varepsilon_{32} + C_{3233}\varepsilon_{33}$$

When $i = 3$ and $j = 3$, but $k = 1,2,3$ and $l = 1,2,3$ independently:

$$\sigma_{33} = C_{3311}\varepsilon_{11} + C_{3312}\varepsilon_{12} + C_{3313}\varepsilon_{13} + C_{3321}\varepsilon_{21} + C_{3322}\varepsilon_{22} + C_{3323}\varepsilon_{23} + C_{3331}\varepsilon_{31} + C_{3332}\varepsilon_{32} + C_{3333}\varepsilon_{33}$$

Conservation of angular momentum results in the symmetry of the stress tensor, hence:

$$\sigma_{ij} = \sigma_{ji}$$

and:

$$\varepsilon_{kl} = \varepsilon_{lk}$$

$\sigma_{ij} = C_{ijkl}\varepsilon_{kl}$, for i, j, k and l = 1, 2 and 3.

or:

$\varepsilon_{ij} = S_{ijkl}\sigma_{kl}$, for i, j, k and l = 1, 2 and 3.

in which σ_{ij} is the *ij*-element of the symmetrical second-order stress tensor; ε_{ij} is the *kl*-element of the symmetrical second-order strain tensor; C_{ijkl} is the *ijkl*-element of the fourth-order stiffness tensor; and S_{ijkl} (the inverse of C_{ijkl}) is the corresponding compliance tensor.

Appendix 2: Symmetry Systems

C_{ijkl} comprises 81(3^4 – three directions of x, y and z, and '4' because of the order) elastic constants. Because of the symmetries of stress $\sigma_{ij} = \sigma_{ji}$ and of strain $\varepsilon_{kl} = \varepsilon_{lk}$, the first and the second pairs of subscripts of the fourth-order tensor C_{ijkl} can be replaced by one another, *i.e.* $C_{ijkl} = C_{jikl} = C_{ijlk}$, reducing the 81 components of the tensor to 36. On the other hand, by using the law of conservation of energy $C_{ijkl} = C_{klij}$, the number of independent components is reduced to 21 components only, that represents a triclinic symmetry system.

Additionally, in order to translate a tensor to a matrix, one may map *ijkl* (i, j, k and l = 1,2,3) subscripts into *IJ* (I,J = 1,2,3,4,5,6) subscripts by utilizing the Voigt recipe that works as follows, $ij \rightarrow I$ or $kl \rightarrow J$:

11 ⇒ 1	**23 ⇒ 4**
22 ⇒ 2	**13 ⇒ 5**
33 ⇒ 3	**12 ⇒ 6**

Therefore the $3 \times 3 \times 3 \times 3$ tensor C_{ijkl} may be represented by a 6×6 matrix C_{IJ}:

$$C_{IJ} = \begin{bmatrix} C_{11} & C_{12} & C_{13} & C_{14} & C_{15} & C_{16} \\ C_{21} & C_{22} & C_{23} & C_{24} & C_{25} & C_{26} \\ C_{31} & C_{32} & C_{33} & C_{34} & C_{35} & C_{36} \\ C_{41} & C_{42} & C_{43} & C_{44} & C_{45} & C_{46} \\ C_{51} & C_{52} & C_{53} & C_{54} & C_{55} & C_{56} \\ C_{61} & C_{62} & C_{63} & C_{64} & C_{65} & C_{66} \end{bmatrix}$$

For a medium with triclinic symmetry, the stiffness matrix will be in the form of:

$$C_{IJ} = \begin{bmatrix} C_{11} & C_{12} & C_{13} & C_{14} & C_{15} & C_{16} \\ C_{12} & C_{22} & C_{23} & C_{24} & C_{25} & C_{26} \\ C_{13} & C_{23} & C_{33} & C_{34} & C_{35} & C_{36} \\ C_{14} & C_{24} & C_{34} & C_{44} & C_{45} & C_{46} \\ C_{15} & C_{25} & C_{35} & C_{45} & C_{55} & C_{56} \\ C_{16} & C_{26} & C_{36} & C_{46} & C_{56} & C_{66} \end{bmatrix}$$

The elements of the lower triangle of coefficients are equal to the upper triangle, reducing the independent coefficients from 36 elements to just 21 elements. In a triclinic system there are no symmetry planes. Crampin (1989) provided a detailed catalogue of anisotropic symmetry systems.

A2.1 Hexagonal Symmetry System, VTI Media

Shales, layering and thin-bed sequences can give rise to a VTI medium. To verify the C_{ijkl} of a hexagonal symmetry system, a VTI medium, one can assume a rotation of 60° ($\pi/3$) about the x_3-axis, which does not change the tensor components of the C_{ijkl} . So, for $\theta = \pi/3$, we have:

$$a_{ij} = \begin{bmatrix} \cos\theta & \sin\theta & 0 \\ -\sin\theta & \cos\theta & 0 \\ 0 & 0 & 1 \end{bmatrix} = \begin{bmatrix} 1/2 & \sqrt{3}/2 & 0 \\ -\sqrt{3}/2 & 1/2 & 0 \\ 0 & 0 & 1 \end{bmatrix}$$

$$C'_{ijkl} = a_{ip} a_{jq} a_{kr} a_{ls} C_{pqrs} = C_{ijkl}$$

For a case where *ijkl* equals 3333, the above relation leads to:

$$C'_{3333} = C_{3333}$$

For a case where *ijkl* equals 1333 or 2333:

$$C'_{1333} = a_{11} C_{1333} + a_{12} C_{2333} = C_{1333}$$

$$C'_{2333} = a_{21} C_{1333} + a_{22} C_{2333} = C_{2333}$$

That will result in:

$$C'_{1333} = C_{2333} = 0$$

Similarly, when *ijkl* equals 1313, 1323 and 2323, it produces:

$$C_{2323} = C_{1313}$$

$$C_{1323} = 0$$

$$C_{2233} = C_{1133}$$

$$C_{1233} = 0$$

In a case where *ijkl* equals 1113, 1213, 1123, 1223, 2213, and 2223, it gives:

$$C_{1113} = C_{1213} = C_{1123} = C_{1223} = C_{2213} = C_{2223} = 0$$

And finally, when *ijkl* equals 1111, 1112, 1122, 1212, 2212, and 2222, it results in:

$$C_{2212} = C_{1112} = 0$$

$$C_{1111} = C_{2222}$$

$$C_{1122} = C_{1111} - 2C_{1212}$$

So, the familiar stiffness tensor of a VTI medium emerges as:

$$C_{ijkl} = \begin{bmatrix} C_{1111} & C_{1111}-2C_{1212} & C_{1313} & 0 & 0 & 0 \\ C_{1111}-2C_{1212} & C_{1111} & C_{1313} & 0 & 0 & 0 \\ C_{1313} & C_{1313} & C_{3333} & 0 & 0 & 0 \\ 0 & 0 & 0 & C_{2323} & 0 & 0 \\ 0 & 0 & 0 & 0 & C_{2323} & 0 \\ 0 & 0 & 0 & 0 & 0 & C_{1212} \end{bmatrix}$$

Or, in two-subscript notation, therefore in a VTI (vertical transverse isotropy) medium, the elastic constant matrix takes the form of:

$$C_{IJ} = \begin{bmatrix} C_{11} & C_{11}-2C_{66} & C_{13} & 0 & 0 & 0 \\ C_{11}-2C_{66} & C_{11} & C_{13} & 0 & 0 & 0 \\ C_{13} & C_{13} & C_{33} & 0 & 0 & 0 \\ 0 & 0 & 0 & C_{44} & 0 & 0 \\ 0 & 0 & 0 & 0 & C_{44} & 0 \\ 0 & 0 & 0 & 0 & 0 & C_{66} \end{bmatrix}$$

where there are only five independent elements: C_{11}, C_{33}, C_{44}, C_{66} and C_{13}.

Thomsen's type anisotropy parameters of a VTI medium are as follows:

$$\varepsilon = \frac{C_{11} - C_{33}}{2C_{33}}$$

$$\delta = \frac{(C_{13} + C_{55})^2 - (C_{33} - C_{55})^2}{2C_{33}(C_{33} - C_{55})}$$

$$\gamma = \frac{C_{66} - C_{55}}{2C_{55}}$$

A2.2 HTI Media

Stress, vertically aligned fractures and vertically tilted beds are known to form an HTI medium. For an HTI medium, the stiffness tensor C_{IJ} can be written in the form of:

$$C_{IJ} = \begin{bmatrix} C_{11} & C_{13} & C_{13} & 0 & 0 & 0 \\ C_{13} & C_{33} & C_{33}-2C_{44} & 0 & 0 & 0 \\ C_{13} & C_{33}-2C_{44} & C_{33} & 0 & 0 & 0 \\ 0 & 0 & 0 & C_{44} & 0 & 0 \\ 0 & 0 & 0 & 0 & C_{66} & 0 \\ 0 & 0 & 0 & 0 & 0 & C_{66} \end{bmatrix}$$

Rüger (1998) gives relations to recover the HTI anisotropy parameters from the VTI ones:

$$\varepsilon_{\mathrm{HTI}} = -\frac{\varepsilon_{\mathrm{VTI}}}{1+2\varepsilon_{\mathrm{VTI}}}$$

$$\delta_{\mathrm{HTI}} = \frac{\delta_{\mathrm{VTI}} - 2\varepsilon_{\mathrm{VTI}}(1+\varepsilon_{\mathrm{VTI}}/f)}{(1+2\varepsilon_{\mathrm{VTI}})(1+2\varepsilon_{\mathrm{VTI}}/f)}$$

$$\gamma_{\mathrm{HTI}} = -\frac{\gamma_{\mathrm{VTI}}}{1+2\gamma_{\mathrm{VTI}}}$$

where f is a function of compressional-wave velocity V_{P} and shear-wave velocity V_{S} as:

$$f = 1-(V_{\mathrm{S}}/V_{\mathrm{P}})^2 .$$

Appendix 3: Sayers and Kachanov's (1991 and 1995) Approach to SIA

Seismic waves propagate with increasing velocities in sandstones under stress, because of internal flaws and discontinuities that deform as applied stresses increase. Still-open or partially open discontinuities gradually close, so that the sandstone can be considered as an anisotropic elastic body with an elastic compliance tensor $S_{ijkl;}$ that can be written in the form of:

$$S_{ijkl} = S^0_{ijkl} + \Delta S_{ijkl}$$

where $S_{ijkl}{}^0$ is the background compliance and ΔS_{ijkl} is the excess compliance of the rock. The latter can be written as:

$$\Delta S_{ijkl} = \frac{1}{4}\left(\delta_{ik}\alpha_{jl} + \delta_{il}\alpha_{jk} + \delta_{jk}\alpha_{il} + \delta_{jl}\alpha_{ik}\right) + \beta_{ijkl}$$

where δ_{ik} is delta Cronecker; and α_{ij} and β_{ijkl} represent a second-rank tensor and a fourth-rank tensor respectively, as:

$$\alpha_{ij} = \frac{1}{V}\sum_r B_T^{(r)} n_i^{(r)} n_j^{(r)} A^{(r)}$$

and:

$$\beta_{ijkl} = \frac{1}{V}\sum_r \left(B_{\mathrm{N}}^{(r)} - B_{\mathrm{T}}^{(r)}\right) n_i^{(r)} n_j^{(r)} n_k^{(r)} n_l^{(r)} A^{(r)}$$

α_{ij} and β_{ijkl} are of Pa^{-1} dimensions. $B_{\mathrm{N}}{}^{(\mathrm{r})}$, $B_{\mathrm{T}}{}^{(\mathrm{r})}$, $n_{\mathrm{i}}{}^{(\mathrm{r})}$ and $A^{(\mathrm{r})}$ show normal and shear compliances of the *r*th discontinuity, *i*th component of the normal to the discontinuity, and the area of the discontinuity respectively. If $B_{\mathrm{N}}{}^{(\mathrm{r})} = B_{\mathrm{T}}{}^{(\mathrm{r})}$, for all rock discontinuities, $\beta_{ijkl} = 0$, and ΔS_{ijkl} is verified by only α_{ij}, which leads to unrealistic results; thus one may relax this latest equality ($\beta_{ijkl} = 0$) in order to investigate the real compliance of the rock.

Appendix 4: Reservoir AVO and AVOAZ

The reflection coefficients of gas sands have been observed to vary anomalously with the angle of incidence. These variations have been used as a direct indicator in hydrocarbon detection (Ostrander, 1982, 1984). Analysis of amplitude versus offset has been successfully applied in different exploration and production studies. Variation of seismic amplitude with offset depends on intrinsic rock parameters like compressional-wave and shear-wave velocities, density, anisotropy and attenuation. Interrelationships among the rock properties and these parameters should be considered in any AVO studies. Castagna *et al.* (1993) discussed in detail the effects of rock properties such as lithology, porosity and pore fluid content on AVO responses. Stress and an accumulation of aligned vertical fractures in an isotropic background lead to azimuthal anisotropy. Rüger and Tsvankin (1995) showed that the differences between P-wave AVO gradients in two symmetry planes of an HTI medium will be a function of the S-wave anisotropy parameter $\gamma^{(v)}$ that is close to the crack density – one of the most important reservoir parameters.

In another work, Rüger and Tsvankin (1997) state that, the move-out parameter of anisotropy or $\gamma^{(v)}$ controls the P-wave AVO gradient too. They also conclude that the P-wave reflectivity is able to verify fracture orientation, predict crack density, and distinguish dry from fluid-filled cracks. MacBeth and Lynn (2001) studied several datasets from different locations, and found a good correlation between horizontal differential stress and open fractures in terms of move-out and internal velocities, and azimuthal variations of PP AVOA both in magnitude and direction.

*A*4.1 Isotropic AVO

Here, in order to investigate amplitude changes with offset in an isotropic medium, I will consider a simple model consisting of an overlying layer (indicated by subscript 1) and the lower layer (indicated by subscript 2) (Figure A4.1). The problem of seismic-wave reflection and transmission as a basic problem in geophysics has been dealt with by many authors (Zoeppritz, 1919; Aki and Richards, 1980; Castagna *et al.*, 1993; Rüger, 1996).

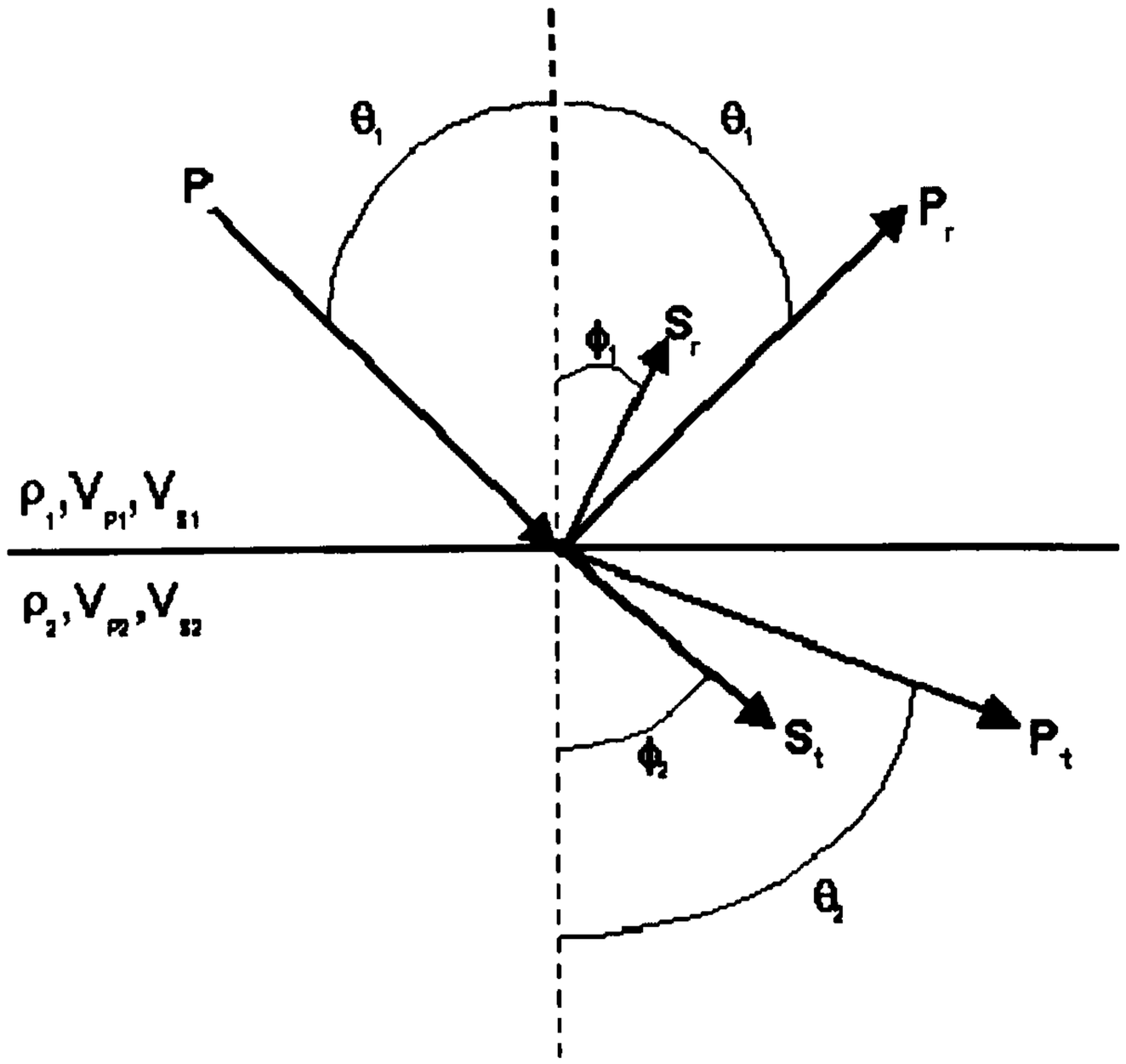

Figure A4.1: A compressional or primary wave generates two reflected waves (P_r and S_r) and two transmitted waves (P_t and S_t) upon interacting with the boundary between two media.

A normally incident wave (compressional or shear) will generate reflected and transmitted waves in the same mode only; whereas in non-normal incidence, for example, when a P-wave hits an interface with an angle of incidence θ_1, four different waves are generated: a reflected P-wave (P_r), a reflected S-wave (that is actually S_V) (S_r), a transmitted P-wave (P_t) and a transmitted S-wave (S_t). In a homogeneous medium, these body waves spread out as spherical wavefronts, the compressional wave with velocity $V_P = [(\kappa + 4\mu/3)/\rho]^{1/2} = [(\lambda + 2\mu)/\rho]^{1/2}$ and the shear wave with velocity $V_S = [\mu/\rho]^{1/2}$. The spherical wavefront is often approximated by a plane surface, as the wavefront radius is assumed to be far larger than the body-wave wavelength. In computing reflection and transmission coefficients of body waves leaving an interface such as that shown in Figure A4.1, two types of boundary conditions are construed: kinematic boundary conditions and dynamic boundary conditions. The former require continuity of displacement amplitudes, and the latter imply that the stress components due to traction across the boundary should be continuous. Aki and Richards (1980) provided exact relations for reflection and transmission coefficients of plane waves at an interface between two isotropic layers:

$$\begin{pmatrix} P^{\downarrow}P^{\uparrow} & S^{\downarrow}P^{\uparrow} & P^{\uparrow}P^{\uparrow} & S^{\uparrow}P^{\uparrow} \\ P^{\downarrow}S^{\uparrow} & S^{\downarrow}S^{\uparrow} & P^{\uparrow}S^{\uparrow} & S^{\uparrow}S^{\uparrow} \\ P^{\downarrow}P^{\downarrow} & S^{\downarrow}P^{\downarrow} & P^{\uparrow}P^{\downarrow} & S^{\uparrow}P^{\downarrow} \\ P^{\downarrow}S^{\downarrow} & S^{\downarrow}S^{\downarrow} & P^{\uparrow}S^{\downarrow} & S^{\uparrow}S^{\downarrow} \end{pmatrix} = M^{-1}N$$

where M and N are defined as functions of incidence angle θ_1, reflection angle ϕ_1, transmission angles θ_2 and ϕ_2, and also densities and velocities of layers ρ_1, ρ_2, V_{P1}, V_{S1}, V_{P2}, and V_{S2}.

$$M = \begin{pmatrix} -\sin\theta_1 & -\cos\phi_1 & \sin\theta_2 & \cos\phi_2 \\ \cos\theta_1 & -\sin\phi_1 & \cos\theta_2 & -\sin\phi_2 \\ 2\rho_1 V_{S1}\sin\phi_1\cos\theta_1 & \rho_1 V_{S1}(1-2\sin^2\phi_1) & 2\rho_2 V_{S2}\sin\phi_2\cos\theta_2 & \rho_2 V_{S2}(1-2\sin^2\phi_2) \\ -\rho_1 V_{P1}(1-2\sin^2\phi_1) & \rho_1 V_{S1}\sin 2\phi_1 & \rho_2 V_{P2}(1-2\sin^2\phi_2) & -\rho_2 V_{S2}\sin 2\phi_2 \end{pmatrix}$$

$$N = \begin{pmatrix} \sin\theta_1 & \cos\phi_1 & -\sin\theta_2 & -\cos\phi_2 \\ \cos\theta_1 & -\sin\phi_1 & \cos\theta_2 & -\sin\phi_2 \\ 2\rho_1 V_{S1}\sin\phi_1\cos\theta_1 & \rho_1 V_{S1}(1-2\sin^2\phi_1) & 2\rho_2 V_{S2}\sin\phi_2\cos\theta_2 & \rho_2 V_{S2}(1-2\sin^2\phi_2) \\ \rho_1 V_{P1}(1-2\sin^2\phi_1) & -\rho_1 V_{S1}\sin 2\phi_1 & -\rho_2 V_{P2}(1-2\sin^2\phi_2) & \rho_2 V_{S2}\sin 2\phi_2 \end{pmatrix}$$

In the matrix expression, each element comprises an incident wave and a reflected wave, with corresponding arrows showing the direction of propagation, for example $P^{\downarrow}P^{\uparrow}$ is the reflection coefficient of an incident downgoing P-wave and a reflected upcoming P-wave that is defined as follows:

$$R_{PP} = \left[\left(b\frac{\cos\theta_1}{V_{P1}} - c\frac{\cos\theta_2}{V_{P2}}\right)F - \left(a + d\frac{\cos\theta_1}{V_{P1}}\frac{\cos\phi_2}{V_{S2}}\right)Hp^2\right]/D$$

Likewise, $P^{\downarrow}S^{\uparrow}$ stands for R_{PS}, or the reflection coefficient of an incident downgoing P-wave and a reflected upcoming S-wave that reads:

$$R_{PS} = \left[-2\frac{\cos\theta_1}{V_{P1}}\left(ab + cd\frac{\cos\theta_2}{V_{P2}}\frac{\cos\phi_2}{V_{S2}}\right)pV_{P1}\right]/(V_{S1}D)$$

where p is the ray parameter, recalling Snell's law:

$$p = \frac{\sin\theta_1}{V_{P1}} = \frac{\sin\theta_2}{V_{P2}} = \frac{\sin\phi_1}{V_{S1}} = \frac{\sin\phi_2}{V_{S2}}$$

Other factors can be expressed in the following form:

$$a = \rho_2(1-2\sin^2\phi_2) - \rho_1(1-2\sin^2\phi_1)$$
$$b = \rho_2(1-2\sin^2\phi_2) + 2\rho_1\sin^2\phi_1$$
$$c = \rho_1(1-2\sin^2\phi_1) + 2\rho_2\sin^2\phi_2$$
$$d = 2(\rho_2 V_{S2}^2 - \rho_1 V_{S1}^2)$$
$$D = EF + GHp^2 = (\det M)/(V_{P1}V_{P2}V_{S1}V_{S2})$$
$$E = b\frac{\cos\theta_1}{V_{P1}} + c\frac{\cos\theta_2}{V_{P2}}$$
$$F = b\frac{\cos\phi_1}{V_{S1}} + c\frac{\cos\phi_2}{V_{S2}}$$
$$G = a - d\frac{\cos\theta_1}{V_{P1}}\frac{\cos\phi_2}{V_{S2}}$$
$$H = a - d\frac{\cos\theta_2}{V_{P2}}\frac{\cos\phi_1}{V_{S1}}$$

As it is obvious that the unwieldy equations that resulted from this matrix expression may not provide an intuitive insight into the reflection and transmission of plane waves, so simplifications and approximations to the exact solution will be of great practical use for most AVO and other seismic studies. Several such analytical approximations have been derived, based upon assumptions akin to the similarity of elastic properties of layers on both sides of a boundary; small changes of plane-wave velocities; and small angles of incidence. Among these simplifications is Shuey's (1985) work, which provides a simpler form of compressional-wave reflectivity in isotropic media. Here is Shuey's three-term formula:

$$R_{PP}(\theta) = A + B\sin^2(\theta) + C\sin^2(\theta)\tan^2(\theta)$$

where A is called the AVO intercept, which is the normal incidence reflection coefficient; B is the AVO gradient; and C is called the AVO curvature. Factors A, B and C are defined as follows:

$$A=\frac{1}{2}\left(\frac{\Delta V_P}{\overline{V}_P}+\frac{\Delta\rho}{\overline{\rho}}\right)=\frac{1}{2}\frac{\Delta Z}{\overline{Z}}$$

$$B=-2\left(1-\frac{\overline{\nu}}{1-\overline{\nu}}\right)A-\frac{1}{2}\frac{1-3\overline{\nu}}{1-\overline{\nu}}\frac{\Delta V_P}{\overline{V}_P}+\frac{\Delta\overline{\nu}}{(1-\overline{\nu})^2}$$

$$C=\frac{1}{2}\frac{\Delta V_P}{\overline{V}_P}$$

although, in many seismic-data analyses, the two-term formula is utilized:

$$R_{PP}(\theta)=A+B\sin^2(\theta)$$

V_P is compressional-wave velocity, Δ indicates the difference between the properties of the upper and lower layers (for example $\Delta V_P = V_{P2} - V_{P1}$) and the super-score shows the average of a property (for example, $\overline{V}_P = (V_{P2} + V_{P1})/2$). The compressional-wave impedance is denoted by $Z = \rho V_P$, G is the vertical shear modulus: $G = \rho V_S^2$, and ν is the Poisson's ratio.

Thomsen (1990) presents a simpler form of Shuey's three-term relation and expresses the P-wave reflection coefficient in the form of:

$$R_P(\theta)=\frac{1}{2}\frac{\Delta Z}{\overline{Z}}+\frac{1}{2}\left[\frac{\Delta V_P}{\overline{V}_P}-\left(\frac{2\overline{V}_S}{\overline{V}_P}\right)^2\frac{\Delta G}{\overline{G}}\right]\sin^2\theta+\frac{1}{2}\frac{\Delta V_P}{\overline{V}_P}\sin^2\theta\tan^2\theta$$

Reflection coefficients of shear waves S_H and S_V can be expressed in the same way:

$$R_{S_H}(\phi)=-\frac{1}{2}\left(\frac{\Delta\rho}{\overline{\rho}}+\frac{\Delta V_S}{\overline{V}_S}\right)+\frac{\Delta V_S}{\overline{V}_S}\sin^2\phi+\frac{1}{2}\frac{\Delta V_S}{\overline{V}_S}\sin^2\phi\tan^2\phi$$

$$R_{S_V}(\phi)=-\frac{1}{2}\frac{\Delta Z_S}{\overline{Z}_S}+\left(2\frac{\Delta\rho}{\overline{\rho}}+\frac{7}{2}\frac{\Delta V_S}{\overline{V}_S}\right)+\frac{\Delta V_S}{\overline{V}_S}\sin^2\phi-\frac{1}{2}\frac{\Delta V_S}{\overline{V}_S}\sin^2\phi\ \tan^2\phi$$

where Z_S is shear-wave impedance ($Z_S = \rho V_S$).

*A*4.2 Anisotropic AVO and AVOAZ

Because, in reality, rocks are not isotropic, their properties differ from the simplified isotropic responses, and therefore the propagating elastic waves behave differently. Amplitude variations with offset are also affected by the anisotropic response of the rocks. Rüger (1996) modified Thomsen's (1993) approximation to the reflection

coefficient of compressional waves in a VTI medium. The phase velocities of compressional- and shear-waves in VTI media can be expressed in terms of Thomsen's anisotropy parameters as follows:

$$V_{\mathrm{P}}(\theta)=V_{\mathrm{P0}}\left[1+\delta\sin^2\theta\cos^2\theta+\varepsilon\sin^4\theta\right]$$

$$V_{\mathrm{S_V}}(\theta)=V_{\mathrm{S0}}\left[1+\left(\frac{V_{\mathrm{P0}}}{V_{\mathrm{S0}}}\right)^2(\varepsilon-\delta)\sin^2\theta\cos^2\theta\right]$$

$$V_{\mathrm{S_H}}(\theta)=V_{\mathrm{S0}}\left[1+\gamma\sin^2\theta\right]$$

V_{P0} and V_{S0} are normal incidence (vertical, or when $\theta = 0$) velocities. As in Rüger (1996), the reflection and transmission coefficients of body waves in HTI media are identical to those of VTI media, for example, the reflection coefficient of the compressional wave propagating in the symmetry-axis plane of an HTI medium comprising an overlying anisotropic layer with ρ_1, V_{P1}, V_{S1}, ε_1, δ_1 and γ_1 as well as an anisotropic lower layer with ρ_2, V_{P2}, V_{S2}, ε_2, δ_2 and γ_2, reads as:

$$R_{\mathrm{P}}^{\mathrm{sym}}(\theta)=\frac{1}{2}\frac{\Delta Z}{\bar{Z}}+\frac{1}{2}\left[\frac{\Delta V_{\mathrm{P}}}{\bar{V}_{\mathrm{P}}}-\left(\frac{2\bar{V}_{\mathrm{S}}}{\bar{V}_{\mathrm{P}}}\right)^2\left(\frac{\Delta G}{\bar{G}}-2\Delta\gamma\right)+\Delta\delta\right]\sin^2\theta$$
$$+\frac{1}{2}\left(\frac{\Delta V_{\mathrm{P}}}{\bar{V}_{\mathrm{P}}}+\Delta\varepsilon\right)\sin^2\theta\tan^2\theta$$

When the variation of azimuth is also taken into account, as seismic surveys can be shot in different azimuths or arbitrary azimuth other than symmetry-axis direction of the field, the P-wave reflection coefficient is defined as a function of incidence angle θ and azimuth ϕ, as follows:

$$R_{\mathrm{P}}(\theta,\phi)=\frac{1}{2}\frac{\Delta Z}{\bar{Z}}+\frac{1}{2}\left[\frac{\Delta V_{\mathrm{P}}}{\bar{V}_{\mathrm{P}}}-\left(\frac{2\bar{V}_{\mathrm{S}}}{\bar{V}_{\mathrm{P}}}\right)^2\frac{\Delta G}{\bar{G}}+\left(\Delta\delta+2\left(\frac{2\bar{V}_{\mathrm{S}}}{\bar{V}_{\mathrm{P}}}\right)^2\Delta\gamma\right)\cos^2\phi\right]\sin^2\theta$$
$$+\frac{1}{2}\left[\frac{\Delta V_{\mathrm{P}}}{\bar{V}_{\mathrm{P}}}+\Delta\varepsilon\cos^4\phi+\Delta\delta\sin^2\phi\cos^2\phi\right]\sin^2\theta\tan^2\theta$$

Appendix 5: Estimating Compaction

*A*5.1 A Review of Methods for *Estimating* Compaction

Most hydrocarbon reservoirs range in depth between several hundred metres and a few thousand metres .The overburden weight is supported partially by the reservoir-rock matrix and partially by fluid pressure or pore pressure. As large amounts of hydrocarbons are extracted from the reservoir during a long period of production, the pore pressure is depleted and reservoir formations can no longer bear the overburden load, so they deform. This amount of strain, expressed as the variation of the reservoir thickness from its original thickness ($\Delta h/h$), can give the magnitude of compaction. Different approaches have been used to estimate reservoir compaction. I will summarize a few of these as follows.

Geertsma (1973) expressed formation compaction as the vertical strain in the reservoir due to its height reduction. This reduction in height originates from a reduction in the reservoir pressure, which he states is a function of factors like the mobility, solubility, density and compressibility of the pore fluids, and also the reservoir boundary conditions such as faults, edge or bottom water, *etc.*

Guilbot and Smith (2002) developed a method in which they constrained the common-practice depth conversion so that it can capture the time-shift in the range of 12–16 ms in a time-lapse study from the Ekofisk Field between 1989 and 1999, and computed reservoir compaction and sea-floor subsidence. The details can be found in the next subsection.

Ibekwe *et al.* (2003) utilized the stiffness (Young's modulus) contrast between the reservoir sand and overburden to calculate reservoir compaction; they also presented a methodology for predicting overburden stretch.

Hatchell *et al.* (2003) considered the stress changes in a compacting reservoir and computed the magnitude of compaction from the time-shift in the two-way travel times of 4D studies. They took into account the stress relaxation above and below the compacting reservoir – a stress relaxation resulting from stress arching that is translated into time-delays in the time-lapse seismic, while the stress buildup on the sides of the reservoir is observed as time pull-up.

Landrø and Stammeijer (2004) presented two separate methods: one based on near-offset and far-offset travel-time shifts from pre-stack data, and the other based on impedance changes and travel-time shifts from full stack data.

Al-Naamani (2004) computed the compaction in a reservoir model using zero-offset two-way travel time, which is followed and modified in this study, and is further extended to non-zero offset in order to investigate the effect of anisotropy on estimating compaction.

*A*5.2 Guilbot and Smith's Method

Guilbot and Smith (2002) introduced a model-driven approach to couple two depth models from the Ekofisk Field, one as a depth model for 1989 and the other as a depth model for 1999. The water depth in the depth model for 1989 is denoted by z_0, z_1, z_2 and z_3, indicating the depths of Layer 1 (overburden), Layer 2 (upper reservoir) and Layer 3 (lower reservoir) respectively. Similarly, the corresponding P-wave velocity of each layer is shown by V_1, V_2 and V_3. The 'prime' symbols give corresponding model parameters for the depth model of 1999. For the base of the reservoir, they assume that, $z_3' = z_3$, implying that the depth of the base reservoir has not changed between 1989 and 1999. Then, the simple expressions of vertical seismic travel times at the base and top of Layer 3 in 1989 (t_3 and t_2) and in 1999 (t'_3 and t'_2) are used:

$$t_3 = t_2 + \frac{z_3 - z_2}{V_3}$$

and:

$$t_3' = t_2' + \frac{z_3' - z_2'}{V_3'}$$

Thickness and porosity changes are related, and follow the uniaxial constraint given by:

$$\frac{H_3}{H_3'} = \frac{1-\phi_3'}{1-\phi_3}$$

then:

$$H_3' = H_3 \frac{1-\phi_3}{1-\phi_3'}$$

where:

$$H_3 = z_3 - z_2$$

and:

$$H'_3 = z'_3 - z'_2$$

Subtracting the travel time of Layer 3 in 1999 (t'_3) from the travel time of Layer 3 in 1989 (t_3) and using the linear porosity–velocity relationship observed on the well logs and valid at the seismic scale:

$$\phi = \alpha + \beta V$$

for V'_3 and combining with the equation of H'_3:

$$-K\beta V_3'^2 + (1-\alpha)K_3 V_3' - (1-\phi_3)H_3 = 0$$

where:

$$K_3 = \Delta t_3 - \Delta t_2 = \frac{H_3}{V_3}$$

$$\Delta t_3 = t'_3 - t_3$$

and:

$$\Delta t_2 = t'_2 - t_2$$

Computing the velocity of Layer 1 requires an estimation of the depth of the water bottom (the reference is in mean sea-level) in 1989 and in 1999. Such data are available through regular bathymetry surveys, from which the seabed subsidence is estimated. Starting from the vertical seismic travel times at the water bottom and the top of Layer 2 in 1989 (t_0 and t_1), and in 1999 (t'_0 and t'_1):

$$t_1 = t_0 + \frac{z_1 - z_0}{V_1} \text{ and } t'_1 = t'_0 + \frac{z'_1 - z'_0}{V'_1}$$

and also:

$$t_0 = \frac{z_0}{V_0} \text{ and } t_0' = \frac{z_0'}{V_0'}$$

where V_0 is the velocity of the seawater, and, by introducing the seabed subsidence (WBS (Water Bottom Subsidence) = $z'_0 - z_0$) the velocity is given by:

$$V_1' = \frac{z_1' - z_0'}{\Delta t_1 + \frac{z_1 - z_0}{V_1} - \frac{z_0' - z_0}{V_0}}.$$